DIRECT FIBER LASER FREQUENCY COMB STABILIZATION VIA SINGLE TOOTH SATURATED ABSORPTION SPECTROSCOPY IN HOLLOW-CORE FIBER

by

SHUN WU

B.S., Beijing Normal University, 2005

M.S., Michigan Technological University, 2007

AN ABSTRACT OF A DISSERTATION

submitted in partial fulfillment of the
requirements for the degree

DOCTOR OF PHILOSOPHY

Department of Physics
College of Arts and Sciences

KANSAS STATE UNIVERSITY
Manhattan, Kansas

2014

Abstract

Portable frequency references are crucial for many practical on-site applications, for example, the Global Position System (GPS) navigation, optical communications, and remote sensing. Fiber laser optical frequency combs are a strong candidate for portable reference systems. However, the conventional way of locking the comb repetition rate, f_{rep}, to an RF reference leads to large multiplied RF instabilities in the optical frequency domain. By stabilizing a comb directly to an optical reference, the comb stability can potentially be enhanced by four orders of magnitude. The main goal of this thesis is to develop techniques for directly referencing optical frequency combs to optical references toward an all-fiber geometry.

A big challenge for direct fiber comb spectroscopy is the low comb power. With an 89 MHz fiber ring laser, we are able to optically amplify a single comb tooth from nW to mW (by a factor of 10^6) by building multiple filtering and amplification stages, while preserving the comb signal-to-noise ratio. This amplified comb tooth is directly stabilized to an optical transition of acetylene at $\sim$ 1539.4 nm via a saturated absorption technique, while the carrier-envelope offset frequency, f_0, is locked to an RF reference.

The comb stability is studied by comparing to a single wavelength (or CW) reference at 1532.8 nm. Our result shows a short term instability of 6×10^{-12} at 100 ms gate time, which is over an order of magnitude better than that of a GPS-disciplined Rb clock. This implies that our optically-referenced comb is a suitable candidate for a high precision portable reference. In addition, the direct comb spectroscopy technique we have developed opens many new possibilities in precision spectroscopy for low power, low repetition rate fiber lasers.

For single tooth isolation, a novel cross-VIPA (cross-virtually imaged phase array) spectrometer is proposed, with a high spectral resolution of 730 MHz based on our simulations.

In addition, the noise dynamics for a free space Cr:forsterite-laser-based frequency comb are explored, to explain the significant f_0 linewidth narrowing with knife insertion into the intracavity beam. A theoretical model is used to interpret this f_0 narrowing phenomenon, but some unanswered questions still remain.

DIRECT FIBER LASER FREQUENCY COMB STABILIZATION VIA SINGLE TOOTH SATURATED ABSORPTION SPECTROSCOPY IN HOLLOW-CORE FIBER

by

SHUN WU

B.S., Beijing Normal University, 2005

M.S., Michigan Technological University, 2007

A DISSERTATION

submitted in partial fulfillment of the
requirements for the degree

DOCTOR OF PHILOSOPHY

Department of Physics
College of Arts and Sciences

KANSAS STATE UNIVERSITY
Manhattan, Kansas

2014

Approved by:

Major Professor
Kristan L. Corwin

Copyright

Abstract

Portable frequency references are crucial for many practical on-site applications, for example, the Global Position System (GPS) navigation, optical communications, and remote sensing. Fiber laser optical frequency combs are a strong candidate for portable reference systems. However, the conventional way of locking the comb repetition rate, f_{rep}, to an RF reference leads to large multiplied RF instabilities in the optical frequency domain. By stabilizing a comb directly to an optical reference, the comb stability can potentially be enhanced by four orders of magnitude. The main goal of this thesis is to develop techniques for directly referencing optical frequency combs to optical references toward an all-fiber geometry.

A big challenge for direct fiber comb spectroscopy is the low comb power. With an 89 MHz fiber ring laser, we are able to optically amplify a single comb tooth from nW to mW (by a factor of 10^6) by building multiple filtering and amplification stages, while preserving the comb signal-to-noise ratio. This amplified comb tooth is directly stabilized to an optical transition of acetylene at $\sim$ 1539.4 nm via a saturated absorption technique, while the carrier-envelope offset frequency, f_0, is locked to an RF reference.

The comb stability is studied by comparing to a single wavelength (or CW) reference at 1532.8 nm. Our result shows a short term instability of 6×10^{-12} at 100 ms gate time, which is over an order of magnitude better than that of a GPS-disciplined Rb clock. This implies that our optically-referenced comb is a suitable candidate for a high precision portable reference. In addition, the direct comb spectroscopy technique we have developed opens many new possibilities in precision spectroscopy for low power, low repetition rate fiber lasers.

For single tooth isolation, a novel cross-VIPA (cross-virtually imaged phase array) spectrometer is proposed, with a high spectral resolution of 730 MHz based on our simulations.

In addition, the noise dynamics for a free space Cr:forsterite-laser-based frequency comb are explored, to explain the significant f_0 linewidth narrowing with knife insertion into the intracavity beam. A theoretical model is used to interpret this f_0 narrowing phenomenon, but some unanswered questions still remain.

Table of Contents

List of Figures

List of Tables

Acknowledgements

The person that has the greatest influence on my PhD education is my dissertation advisor, Dr. Kristan Corwin. I appreciate her for giving me the opportunity to join her group, where I have had wonderful experiences over the past six years and a half. I was always inspired by her passionate in research. She is not only an excellent mentor, but also a good friend of mine. This dissertation could not have been completed without her encouragement and guidance.

Special thanks to Dr. Brian Washburn. He gave me numerous helpful suggestions in group meetings. In his area of expertise, I was mostly under his guidance when building fiber ring lasers as well as amplifiers. He is always trying to help students as much as he could.

I would like to thank all the colleagues I have been pleasure to work with over my PhD years. Rajesh Thapa is the first person who showed me the lab. Aaron Pung taught me how to use the arc splicer to splice fibers. Karl Tilmman has taught me a lot of instrumentation skills on the Cr:forsterite laser. He could spent an hour answering my questions as a fresh PhD. I really appreciate his help work with me on fixing the laser during one Christmas break. I worked closely with Kevin Knabe for nine months. He taught me how to run the saturated absorption setup. He helped me with powerpoint animations and correcting mistakes for my first public scientific seminar. I was always thankful for his kind group dinner invitations. Andrew Jones had been a great colleague to work with. He was always willing to help whenever I needed him and more than once had brilliant ideas to solve my problem. Jinkang Lim is such a nice and hard-working person. His passion in research always inspired me. I appreciate the numerous valuable discussions with Rajesh Kadel and Chenchen Wang. I would like to thank undergraduate students who have worked in our group: Daniel Moeder, Stephen Meinhardt and Jordan Nesley, for their continuous effort

on making the servo amplifiers. Big thanks to my current colleagues Neda Dadashzadeh, Mary Harner and Turghun Matniyaz. Thank you all for being around and work in a group like families.

I appreciate our collaborators Dr. Fetah Benabid's group, especially Coralie, for making the special hollow-core fibers for this work.

Special thanks to our visiting scholars Dr. Yishan Wang, and Xiaohong Hu from Xi'an Institute. Dr. Wang made the initial efforts for building the NPR laser, which I used later for my work. During his stay in the US, Xiaohong Hu had been a nice colleague to work with.

I would like to thank all the JRM staff for their help on lab machining work. Mike Wells is the person I always turn for help whenever I need to borrow tools or had vacuum problems. Scott Chainey spent his valuable time helping me with questions regarding electronics. Al Rankin helped me machine the aluminium block that used in my Fabry-Perot cavity, which substantially improved the cavity stability. Russ Reynolds taught me how to run machines in the mechanical shop and always was around when I ran into trouble. Special thanks to Peter Nelson for lending me his equipment from time to time.

Special thanks to Matthew Kirchner at National Institute of Science and Technology for helpful email conversations about Fabry-Perot cavity design. Thank you so much for the long detailed emails.

In the end, I would like to thank the Air Force Office of Scientific Research (AFOSR), who has given me the financial support of this work (Current contract No. FA 9550-11-1-0096).

Dedication

This work is dedicated to my family. To my mother, Xiaorong Liu, and father, Guozhu Wu, who have taught me the importance of education and given me the courage to pursue the life I want, to my mother-in-law, Cuiyun Zhu, who strongly supported us by providing years of daycare in a foreign country for a pair of my precious children, to my husband, Wei Cao, who has shared all my pain as well as happiness throughout the past six years and a half, and to my daughter and son, Grace and Lucas, whose smiling faces always drive away my stress and unhappiness.

List of Publication

PEER REVIEWED JOURNAL PUBLICATIONS

1) K. Knabe, **S. Wu**, J. Lim, K. A. Tillman, P. S. Light, F. Couny, N. Wheeler, R. Thapa, A. M. Jones, J. W. Nicholson, B. R. Washburn, F. Benabid, and K. L. Corwin., "10 kHz accuracy of an optical frequency reference based on $^{12}C_2H_2$-filled large-core kagome photonic crystal fibers", *Optics Express*, Vol. **17**, Issue 18, pp. 16017-16026 (2009).

2) K. A. Tillman, R. Thapa, K. Knabe, **S. Wu**, J. Lim, B. R. Washburn, and K. L. Corwin. "Stabilization of a self-referenced, prism-based, Cr:forsterite laser frequency comb using an intracavity prism", *Applied Optics*, Vol. **48**, Issue 36, pp. 6980-6989 (2009).

3) V. K. Kayastha, **S. Wu**, J. Moscatello, and Y. K. Yap, "Synthesis of vertically aligned Single- and double-walled carbon nanotubes without etching agents", *Journal of Physical Chemistry Letters*, Vol. **111**, Issue 28, pp. 10158-10161 (2007).

4) **S. Wu**, C. Wang, C. Fourcade-Dutin, B. R. Washburn, F. Benabid and K. L. Corwin., "Direct fiber comb stabilization to a gas-filled hollow-core photonic crystal fiber", *Optics Express*, Vol. **22**, Issue 19, pp. 23704-23715 (2014).

5) **S. Wu**, K. A. Tillman, B. R. Washburn and K. L. Corwin., "Investigation of carrier-Envelope offset frequency linewidth narrowing in a prism-based Cr:forsterite frequency comb", in preparation.

PEER REVIEWED CONFERENCE SUBMISSIONS

6) **S. Wu**, C. Wang, C. Fourcade-Dutin, B. R. Washburn, F. Benabid and K. L. Corwin., "Direct comb stabilization to an $^{12}C_2H_2$-filled hollow-core fiber via single tooth saturated absorption spectroscopy", oral presentation delivered at CLEO conference, San Jose, CA, June 2014.

7) C. Wang, **S. Wu**, C. Fourcade-Dutin, B. R. Washburn, F. Benabid, and K. L. Corwin., "Toward an all-fiber based optically referenced frequency comb", oral presentation delivered at CLEO conference, San Jose, CA, June 2014.

8) **S. Wu**, C. Wang, C. Fourcade-Dutin, B. R. Washburn, F. Benabid, and K. L. Corwin., "Direct Stabilization of a frequency comb to a $^{12}C_2H_2$-filled hollow-core photonic crystal fiber", oral presentation delivered at OSA annual meeting, Orlando, FL, October 2013. *I was selected a finalist for the* ***2013 Emil Wolf Outstanding Student Paper Competition*** *based on this work.*

9) **S. Wu**, C. Wang, C. Fourcade-Dutin, B. R. Washburn, F. Benabid, and K. L. Corwin , "Sub-Doppler intrafiber spectroscopy of $^{12}C_2H_2$ using amplified frequency comb lines directly", oral presentation delivered at CLEO conference, San Jose, CA, June 2013.

10) **S. Wu**, K. Tillman, B. R. Washburn, K. L. Corwin., "Noise dynamics of a prism-based Cr:forsterite laser frequency comb", poster delivered at DAMOP conference, Houston, TX, May 2010.

Acronyms

AC trace = autocorrelation trace

AM = amplitude modulation

AOM = Acousto-optic modulator

ASE = amplified spontaneous emission

BPF = band pass filter

BW = bandwidth

CW = continuous wave (monochromatic color laser source)

Cr:f = Cr:forsterite

CSO = Cryogenic sapphire oscillator

DFB = distributed-feedback diode laser

ECDL = external-cavity diode laser

EDF = erbium-doped fiber

EDFA = erbium-doped fiber amplifier

EOM = Electro-optic modulator

PD = Photodetector

FFT-SA = Fast Fourier Transform spectrum analyzer

FM = frequency modulation

FP cavity = Fabry-Perot cavity

FSR = Free-spectral range

FWHM = Full-width at half-maximum (halfwidth)

GDD = group delay dispersion

GHz = gigahertz (10^9 Hz)

GVD = group velocity dispersion

HC-PCF = Hollow-core photonic crystal fiber

IR = infrared ($\lambda > 3$ μm)

JILA = The institute formerly known as the "Joint Institute for Laboratory Astrophysics", located in Boulder, Colorado

MHz = megahertz (10^6 Hz)

NIR = near-infrared ($0.76 < \lambda < 3$ μm)

NIST = National Institute of Standards and Technology

RAM = residual amplitude modulation

SAS = saturated absorption spectroscopy

SBS = stimulated Brillouin scattering

SHG = second harmonic generation

SMF = single mode fiber (standard fiber for telecommunication)

SOA = Semiconductor optical amplifier

THz = Terahertz (10^{12} Hz)

PDH = Pound-Drever-Hall locking

VIPA = virtually-imaged phase array spectrometer

WDM = wavelength division multiplexer

Chapter 1

Introduction

Throughout history, humankind has ceaselessly pursued improved methods of timekeeping. From the earliest solar time scale in the Middle Ages, which uses the rotation of the earth to determine time, to the invention of the pendulum and wrist watches in early 20^{th} century, until today's atomic clock, the accuracy of time measurement has increased incredibly by over fifteen orders of magnitude.

Although personal watches seem to be accurate enough for common people's daily life, and the need for keeping time to an accuracy of one second over 100 million years is not obvious, the precision in time is actually crucial for many daily activities of the general public, and also plays a vital role in current scientific investigations, which I will address in the following Sections 1.1.1 and 1.1.2. Without realizing it, the ability for more precise time measurement has greatly influenced the progress of advanced techniques and led to many exciting scientific discoveries, which in turn has enabled the development of better clocks that can be used to explore new scientific frontiers. In this Chapter, I will first introduce the close relationship between time and frequency standards, followed by some motivations for the obsession of researchers in frequency metrology with the ever-increasing frequency accuracy. As more and more applications of frequency standards described below are close enough to impact our daily life, portable frequency references that are accurate and

precise have become more and more important in these applications. Next, I will introduce a new generation of frequency standards in the optical frequency domain, which potentially have stability over four orders of magnitude better than our current microwave standards. Progressing through this Chapter, the need for an optical frequency comb to realize these optical standards will become clear. We will then take a glance at the current state of the art frequency combs, and see how the accuracy and precision of a standard improves as the system becomes more complex. Finally, I will introduce the general procedures and techniques of how to realize these frequency standards. These guidelines will be integrated more specifically in later Chapters as I discuss how we built portable optical frequency references.

1.1 Introduction to Frequency References

1.1.1 Relationship between Time and Frequency

The heart of a *clock* relies on certain physical processes that can provide a periodic "tick". A good example would be quartz crystal oscillators, which are inside most wrist-watches and household clocks. By counting the number of ticks over a certain time period, the duration of a time interval can be measured. *Frequency* is defined as the inverse of a time interval. By counting the number of "ticks" per second, we can measure frequency. A *frequency reference* refers to a device that can produce this periodic "tick", such as the quartz crystal oscillator. An important quantity to evaluate the quality of a frequency reference is the fractional uncertainty, which is given by the ratio between the uncertainty in the measured frequency and its nominal frequency.

$$\sigma_\nu = \frac{\delta\nu_{\text{measured}}}{\nu_{\text{nominal}}} \tag{1.1}$$

Among the seven basic SI units listed in Table 1.1 [14], time interval and frequency are

SI Base Unit	Physical Quantity	Uncertainty
Second	Time interval	1×10^{-15}
Meter	Length	1×10^{-12}
Kilogram	Mass	1×10^{-8}
Ampere	Electric current	1×10^{-8}
Mole	Amount of substance	1×10^{-8}
Kelvin	Temperature	1×10^{-7}
Candela	Luminous intensity	1×10^{-4}

Table 1.1: *Uncertainties of the seven base SI units [14].*

now the most precisely measurable quantities. For this reason, many physical parameters are preferred to be read out by frequency measurement for the best attainable precision. Therefore, the uncertainty of a frequency measurement has a direct impact on the measurement resolution in these experiments. In the following section, a few applications of high precision frequency references will be given. Although these applications are from different areas, they all share one thing in common, that is, improving the precision of the references used in these experiments is the key to improving the measurement resolution in their research areas, which after all enhances the capability of discovering the finest details of nature.

1.1.2 Motivations for Precise Frequency References

The fact that the second is currently the most accurately measured unit leads to the first application I would like to talk about here. That is, the definition of many other units have been changed based on the definition of the second. The current definition for the second is based on the Caesium atomic clock, which is the time duration of 9,192,631,770 cycles of oscillation corresponding to the transition between the two hyperfine levels of the ground state of the Cs atom. In 1983, the meter was redefined as the distance travelled by light in a time interval of 1/299,792,458 of a second. Other units like ampere and volt also rely on the definition of the second. One of the proposed definitions for the kilogram is also

based on the second [15]. Because of the reliance on time for the definition of several units, the ability to achieve highly accurate time and frequency measurements becomes extremely important.

A second application is that a high precision frequency reference enables the capability to test some of the foundations of physics, such as the search for variations of fundamental constants on a cosmological time scale. Experimental results may be found to be in violation of Einstein's equivalence principle and may imply spatial and temporal dependencies of the fundamental coupling constants. These topics are exciting to physicists because they may open a window for new physics towards a deeper theoretical understanding. For example, the comparisons between current optical clocks in the laboratory put an new upper bound on the relative variation of the fine structure constant α having an uncertainty of $\Delta\alpha/\alpha \sim 10^{-17}$/yr [16]. However, recent astrophysical observations suggests an observable variation of 10^{-19}/yr in the laboratory [17]. A new generation of optical clocks will be necessary to observe this effect.

Astronomical physicists have particular interests in high precision frequency references for wavelength calibration [18]. In the search for extrasolar planets, the presence of the planet can be confirmed by the variations in the radial velocity of the star with respect to earth. Since this radial velocity can be deduced from the shift of the parent star's spectral lines due to the Doppler effect, wavelength calibration for astronomical telescopes is essential to detect subtle displacements for the spectral lines. Highly precise calibration is also beneficial for direct measurements of expansion of the universe, which can be made by observing the real time evolution of the spectral line shift from distant objects.

An important application for precise frequency measurement is the Global Positioning System (GPS). The GPS system uses 24 satellites that orbit the earth to transmit signals. A GPS receiver on earth that receives signals from multiple satellites can determine its distance to each satellite by comparing the frequency of the received signals to the receiver's internal frequency reference, thereby pinpointing its exact location on earth. GPS plays

an essential role in numerous scientific fields. Geological scientists use GPS for digitally mapping the geological features of the earth. Information such as crustal deformations and continental drifts can be obtained and analyzed. GPS helps civil engineers to monitor any changes of manmade structures over time and do land surveys. GPS has proved particularly effective for the navigation of ships, airplanes, and even family cars. It is crucial to have a highly accurate GPS during sea rescue operations and in situations such as Antarctic expeditions where navigating by traditional landmarks is impossible. The current GPS signal in space provides an accuracy of at least 7.8 meters at a 95 % confidence level [19]. In a foreseeable future, the accuracy can be improved to be within a few centimeters for real-time positioning, and even reach the millimeter level if longer averaging time is allowed. This level of precision will stimulate a lot more applications, such as automatic guiding of a personal vehicle on the road without direct human guidance.

Frequency references have many more military applications [20, 21]. In a modern battle, positive identification of friend and foe (IFF) is critically important when the sky is filled with aircraft from both sides. Current IFF systems spread encoded interrogation signals for identification recognition. The interrogation signal received by a friend is supposed to result in the "correct" code sent back. The "correct" code must change frequently to prevent a foe from recording and transmitting that code (so-called "repeat jamming") and appearing as a friend. The better the clock accuracy, the shorter time it takes for changing the code, the less vulnerable the system is to repeat jamming. Similar requirements exist in electronic warfare applications. One method of locating radio and radar emitters is to measure the time difference of arrival of the same signal at widely separated locations. This method depends on the availability of highly accurate clocks, and on highly accurate methods of synchronizing clocks that are widely separated.

Telecommunication industry is another application that has an impact on the life of a common person, which relies on accurate frequency references. This covers all forms of distant communications, such as radio, television, telephony, mobile phone, and com-

puter networking. Current optical communication systems convert the original information (voice, music video, or data) into electronic signals at different frequencies. For a maximum transmission capacity, dense wavelength division multiplexing (DWDM) is implemented to transmit signals through multiple frequency channels over a single optical fiber. Frequency references ensure the signal frequencies are measured correctly and are packed into their corresponding channels. The size and spacing of these frequencies (or channels) are determined by the international telecommunication union (ITU). For instance, the ITU-T G.694.1 frequency grid covers the frequency range 191.7 THz to 196.1 THz with 100 GHz spacing. An improvement in the current telecom frequency references potentially narrows the current channel spacing, therefore allowing more channels to be added to the ITU wavelength bands, allowing a larger data transmission capacity.

Among the numerous applications of frequency references, only a few are listed above. Although the high performance standards such as the Cs atomic clock offer great stability and accuracy, these systems are usually complex and expensive and therefore not very useful for many practical on-site measurements. In this case, the development of a portable frequency reference with comparable performance is necessary. The goal of this work is to develop a fiber-based optical frequency reference system with combined features of high precision and portability. But before we talk about how to realize this fiber-based system, it is necessary to know some basic concepts about frequency references, which is what I describe next.

1.1.3 Characterization of References

A perfect frequency reference should repeatably and reliably produce oscillations as an ideal sine wave. The frequency of this sine wave is called the *nominal frequency* of this reference. A frequency reference can be characterized in two respects, namely, *stability* and *accuracy*. *stability* refers to how well the reference can produce the same frequency signal over a given time interval. *Accuracy* is the degree of conformity of a measured or calculated value to

its definition [14]. Stability of a reference does not tell whether the frequency is right or wrong, but only indicates whether it is consistent when being measured multiple times. In contrast, accuracy of a references indicates how well can it be set to a particular frequency.

Accuracy of a frequency source can be measured in either the frequency domain or the time domain. A common frequency domain measurement involves *frequency counters* which can directly measure the frequency by comparing with their internal (or external) frequency references. The accuracy of the frequency source is determined by

$$Accuracy = \frac{\nu_{\text{measured}} - \nu_{\text{nominal}}}{\nu_{\text{nominal}}} \tag{1.2}$$

Similarly, accuracy measurements in the time domain involve a phase comparison over a certain time period between the source and the reference. It is given by

$$Accuracy = \frac{\Delta t}{T} \tag{1.3}$$

where Δt is the amount of deviation in time between the source and the reference, and T is the time period for the measurement.

Stability is the statistical estimation of the frequency/time fluctuations with respect to its mean frequency/time offset. It also can be measured in both frequency domain and time domain [22], while the time domain estimates are more widely used.

There are mainly two characterization methods in the time domain. One is to measure the phase noise spectrum by integrating over a range of Fourier frequencies, which reveals the phase deviation within that interval with respect to the starting point. The integrated phase noise represents the coherence of the source.

The other method involves how the frequency fluctuations of the reference vary as a function of time. Frequency counters with certain sampling gate time are often used to measure the frequency of the source in this type of measurement, giving a set of frequency measurements y_i that consists of n number of individual frequency measurements, y_1, y_2,

y_3 ... y_n. Classical statistics such as standard deviation can be used to measure scatter of the y_i's as a measure of oscillator noise. But a more commonly used method is named *Allan deviation*, which is what we use to characterize our reference in this work. It differs from the standard variance in that the point to point deviations are analyzed instead of the deviations from the mean, and can be expressed as

$$\sigma_y(\tau) = \sqrt{\frac{1}{2}\sum_{n=1}^{N}(y_{n+1} - y_n)^2} \tag{1.4}$$

where y_{n+1} and y_n are two adjacent data points taken at time t and $t+\tau$, with τ the sampling gate time, assuming no electronics dead time for the frequency counter. For averaging times that are integer multiples of τ, denoted as $m\tau$, the Allan deviation can be either directly measured or calculated by forming a new set of N/m frequency values from the original set of N values. This is done by dividing the original data into N/m adjacent subsets of data. Each subset gives an average frequency value forming one data point in the new set of N/m frequency values. The fractional uncertainty of the frequency reference under test can then be given by

$$\mathrm{FS} = \frac{\sigma_y(\tau)}{\nu_{\mathrm{nominal}}} \tag{1.5}$$

Figure 1.1 shows an example of a frequency stability plot for a quartz crystal oscillator in wristwatches based on Allan deviation. It shows an improvement in the stability as the averaging period, or gate time, gets longer. This is because some types of noise can be removed by averaging. Eventually, the stability will reach the *noise floor* when further averaging no longer improves the results. The Allan deviation stability plot is useful for frequency reference characterization because it reveals what type of noise contributes to the system [3, 23], and also how long we need to average to get rid of the noise. For example, if $\sigma_y(\tau) \propto \tau^{-1}$ then white phase noise is dominant in the system. Whereas, $\sigma_y(\tau) \propto \tau^{-1/2}$ indicates white frequency noise is dominant. However, it always takes a short period of time

for the system to respond before it takes the next measurement, which is defined as *dead time*. For example, the frequency counter we used in our lab has a typical dead time of 24 ms for an one second gate time measurement. For a reliable indication, it is important that there should be no dead time between the successive frequency data measurements, because dead time destroys the coherence between consecutive frequency measurements.

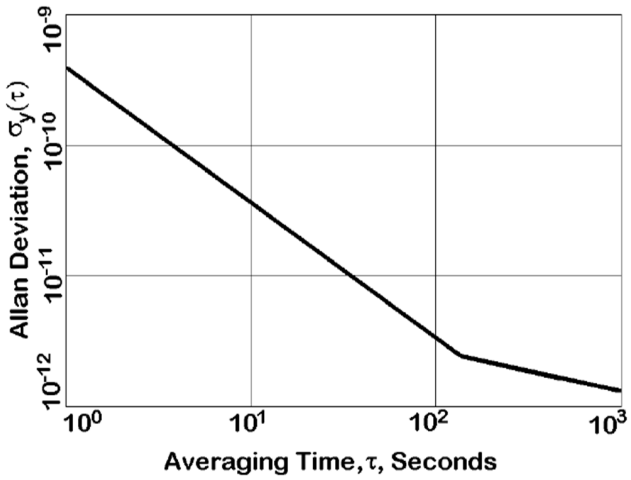

Figure 1.1: *Frequency stability plot of quartz crystal oscillator in wristwatches [1].*

Another important concept is *short-term* and *long-term* stability. Short-term stability refers to the stability for gate times less than 100 s. Long-time stability is for gate time longer than 100 s, and often even more than 24 hours. The short-term stability is important, especially for portable frequency references when some on-site measurements cannot take advantage of averaging over long periods of time.

It is evident that reducing the fractional uncertainties of current frequency references is crucial in many fields. Currently, the second is defined based on the hyperfine splitting of the Cs atom with a resonance frequency of about 9 GHz, with an uncertainty on the order of 10^{-16}. The next generation of clocks will be orders of magnitude better than the current Cs standard at least in terms of stability, as I will talk about in the next section.

1.1.4 From Microwave to Optical References

An obvious way to improve the fractional frequency uncertainty, $\delta\nu/\nu_{\text{nominal}}$, is to use a transition with a higher frequency ν_{nominal}, assuming comparable uncertainty $\delta\nu$. A Cs atomic reference is based on a GHz microwave transition. If the definition could move to an optical frequency, which is in the terahertz (> 100 THz) range, the uncertainty of the optical frequency references could potentially be reduced by at least four orders of magnitude over the Cs atomic reference, under the condition that the center of the transition can be determined with comparable uncertainty. Such an optical frequency reference can be developed by stabilizing a laser to an optical frequency transition or an optical cavity.

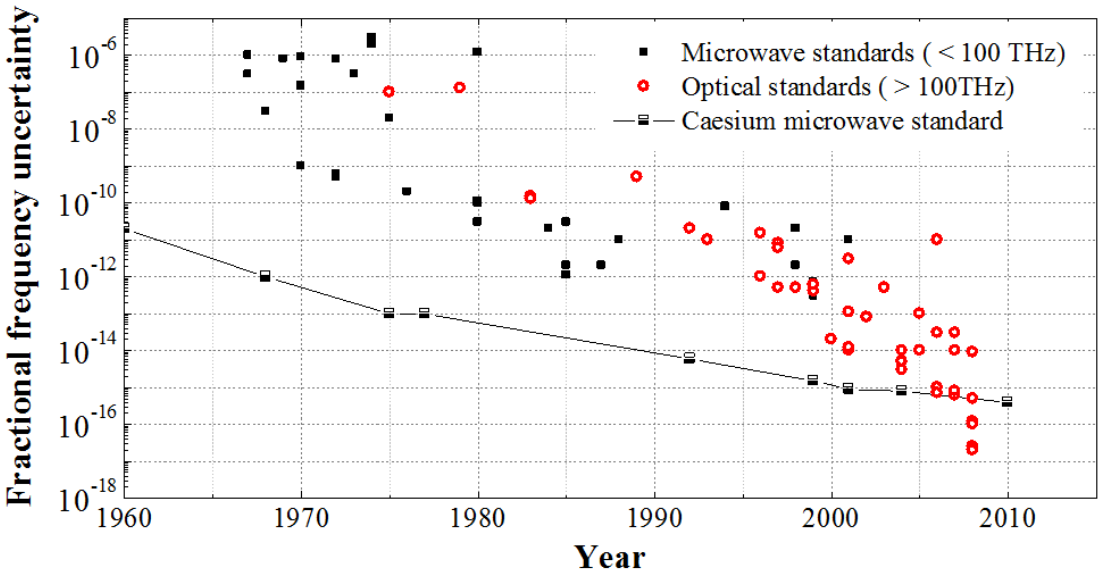

Figure 1.2: *Fractional frequency uncertainty of selected microwave and optical frequency standards versus time [2–5].*

Figure 1.2 shows the development of the fractional frequency uncertainty for both microwave references and optical references as a function of time. It is noticeable that only a few measurements were made at frequencies greater than 100 THz prior to the year 1990. It was not until the year 2000 when the femtosecond laser frequency comb was invented that the measurements for optical references became commonplace.

The major obstacle for developing optical frequency references in the early days comes from the frequency readout system. Unfortunately, the response of electronics, i.e. in a frequency counter, is limited to the ns level, corresponding to a maximum measurable frequency of up to only a few GHz. This allows for direct electronic counting of microwave signals, but is not fast enough to keep up with the optical frequency oscillations (THz). This means that a phase-coherent link must be invented to connect the optical frequencies to the measurable microwave frequencies.

For this reason, harmonic phase-locked frequency chains [2] were invented. Successive steps of frequency multiplication and offset-locking are created to phase-coherently link the optical frequency oscillators to the harmonics of lower-frequency references. One can imagine the technical difficulties in optimizing locks for up to 15 separate frequency offsets simultaneously in the chain, which requires rooms of equipment and also experts that master a variety of technologies for different wavelengths. In the end, these efforts only result in the measurement of one specific optical frequency. This is partly because some of the oscillators in the chain have limited tunability. It is also because of the difficulty in operating such a complex chain. Due to the system complexity, a limited number of chains were built in national labs across the world, covering only a few discrete frequency lines in the optical spectrum [24–27].

Other approaches have been developed to measure optical frequencies [28]. One relies on difference-frequency generation, which involves dividing the optical frequency into smaller portions that can be measured. Another method is related to the generation of a 30 THz wide optical frequency comb by modulating an intracavity electro-optic modulator (EOM). However, this method suffers from the limited comb bandwidth due to cavity dispersion and modulation efficiency.

Thanks to the advances in laser science and nonlinear fiber optics, the first phase-stabilized optical frequency comb was realized from a mode-locked Ti:sapphire laser by J. L. Hall's group at JILA in 2000 [29]. This major progress is because of the invention

of a specially designed highly nonlinear fiber that could broaden the laser spectrum to a full optical octave, allowing the generation and stabilization of the carrier-envelope offset frequency of the comb. At the same time, Bellini and Hänsch demonstrated for the first time that two white-light continuum pulses from a mode-locked laser can generate interference fringes, indicating a phase-coherent relationship between comb teeth from mode-locked lasers [30].

The realization of an optical frequency comb provides a direct link between optical and microwave frequencies, which is a milestone in the development of optical frequency references. Due to their contributions, Hall and Hänsch were together awarded half the Nobel prize in 2005. Since then, phase-stabilized mode-locked lasers based on fibers have been demonstrated [31], which will allow the frequency comb to move out of the laboratory into commercial devices. In the following section 1.2, I will introduce what a frequency comb is and the performance for some of the state of the art combs.

1.2 Introduction to Optical Frequency Combs

1.2.1 Basics of Frequency Combs

Before we introduce frequency combs, let's first take look at the difference between a continuous wave, or CW laser, and a pulsed laser in two different representations: both the time and frequency domain, which are related by the Fourier transform (Figure 1.3). A CW laser is a single frequency laser, and has constant power output versus time. In contrast, a pulsed laser is a train of regularly separated pulses with certain spectral bandwidth. For a given average power, the shorter the pulses are, the higher the peak power of the pulses.

A frequency comb is a phase-stabilized pulsed laser. The constant time separation between successive pulses is the round trip time for the laser cavity. In the frequency domain, it is a spectrum of discrete frequencies, which are cavity modes satisfying certain boundary conditions [32]. These modes are separated by a consistent spacing, namely, the repetition

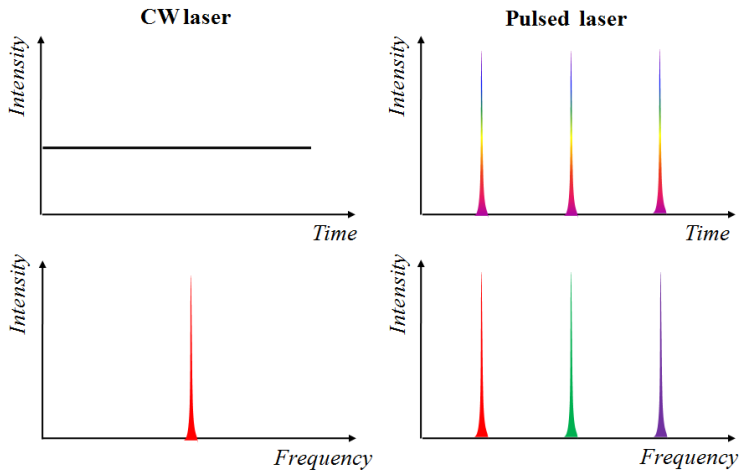

Figure 1.3: *Comparison of output power for a continuous wave (CW) laser and a pulsed laser in time and frequency representations.*

rate f_{rep} in a plot of the comb spectrum (lower right quadrant of Figure 1.3). Each frequency is referred to as a distinct comb mode, or comb tooth. The name "frequency comb" comes from the fact that the comb modes resemble the teeth of a comb.

In order to produce a periodic train of pulses, the cavity modes need to have a constant phase relationship, such that they can all interfere with each other constructively at certain times. This is essentially called mode-locking. In contrast, with a random phase relationship, all cavity modes will oscillate independently giving a constant CW output. This idea is illustrated in Figure 1.4. n represents the number of cavity modes that are coherently added up. A larger n corresponds to a larger spectral bandwidth of the comb. It is clear to see that the pulse duration is inversely proportional to the spectral bandwidth.

The frequency comb in a frequency domain is shown in Figure 1.5. The frequency of each comb tooth can be determined by the comb equation

$$\nu_n = n \times f_{\text{rep}} + f_0 \tag{1.6}$$

where f_0 is the carrier-envelope offset frequency, which originates from the pulse to pulse

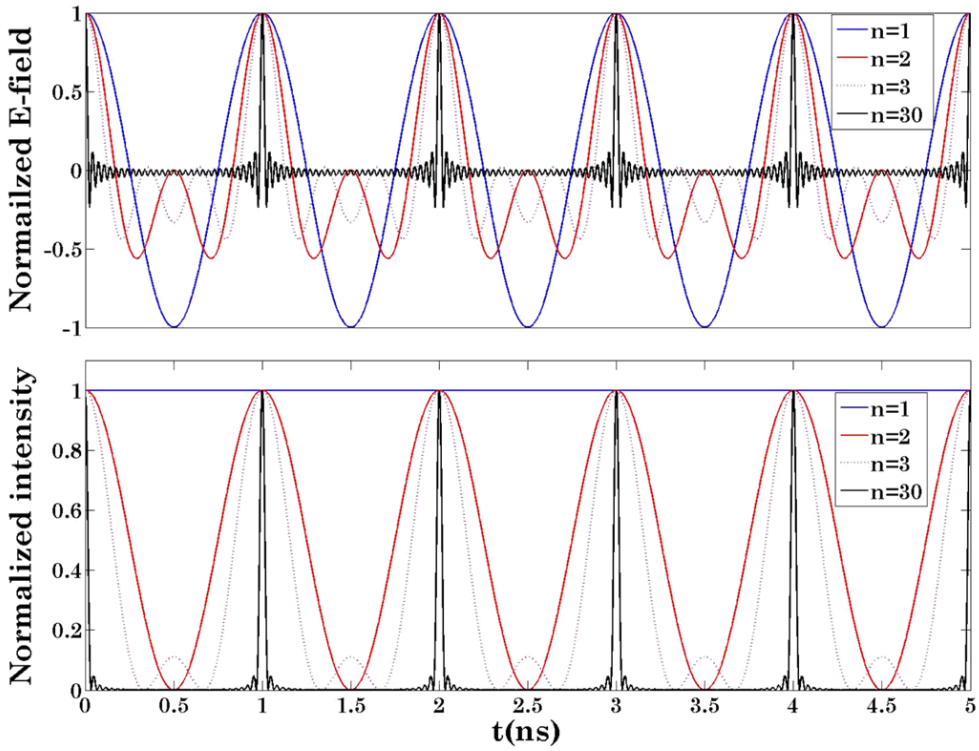

Figure 1.4: *Amplitude of electric field (top) and intensity (bottom) as a function of time when n number of cavity modes are added up coherently.*

electric field phase slip between the carrier and envelope [32]. n must be a large integer for f_n to reach optical frequencies. For telecom wavelengths around 1.5 μm, n is on the order of 2,000,000 for a rep rate frequency of 100 MHz.

A phase-stabilized frequency comb requires the stabilization of two comb parameters: f_0 and f_{rep}. Both f_0 and f_{rep} can stabilized directly to RF references, but in our work f_{rep} is stabilized by locking a single comb tooth f_n to an optical reference. f_{rep} can be determined easily by detecting the laser pulse train on an RF photodetector. The generation of the f_0 signal is a little bit tricky. A common method is the self-referencing technique. It involves three steps depicted in Figure 1.5: first, generation of an octave-spanning spectrum (or the so-called *supercontinuum, SC*) from the fiber laser. Second, frequency-doubling a comb tooth in the long wavelength portion ($f_n = f_0 + \text{n}f_{\text{rep}}$) of the SC. Third, optical heterodyne beating the frequency-doubled signal ($f_{2n} = 2f_0 + 2\text{n}f_{\text{rep}}$) against another comb tooth in

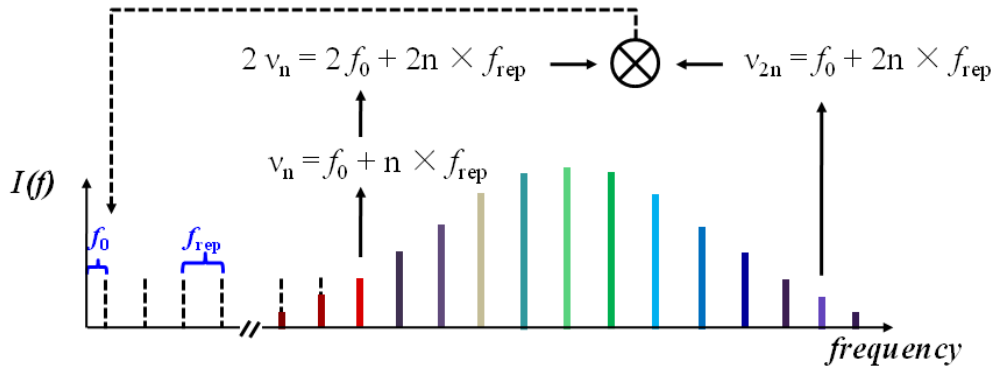

Figure 1.5: *Self-referencing technique for f_0 stabilization for an optical frequency comb.*

the short wavelength portion ($f_{2n} = f_0 + 2nf_{\text{rep}}$) to produce the desired f_0 signal. Since every tooth can be precisely known based on the two stabilized comb parameters, a phase-stabilized frequency comb can serve as a spectral ruler for measuring any unknown optical frequencies.

1.2.2 State of the Art Combs

To evaluate the frequency stability of an optical frequency comb, it is important to keep in mind that the stability of a comb depends on that of the references being used for comb stabilization. Table 1.2 lists a few state of the art or commonly used oscillators for comb stabilization.

The general trend in terms of cost and portability shown in Table 1.2 is that references with better stability are more expensive and less portable. The technologies for microwave, or RF, references have been well-developed in the past few decades. Caesium fountain clocks have the best performance in terms of both accuracy and stability and thereby serve as the primary standard of time and frequency. Cryogenic sapphire oscillators (CSOs) [39] are currently the most stable microwave frequency sources for short time scales. Optical lattice clocks based on single ion or neutral atoms have stability surpassing that of a Cs clock, but worse accuracy. Therefore, they were announced to be "secondary representations of

Oscillator Type	Nominal Frequency	Stability in 1 s	Ref	Cost	Portability
Quartz Wristwatch	RF	1×10^{-9}	[1]	$ 100	★★★★★
Rubidium	RF	5×10^{-11}	[1]	$ 5 k	★★★
Hydrogen maser	RF	1×10^{-12}	[1]	$ 250 k	★★★
Caesium fountain	RF	4×10^{-16}	[33]	$ 50 k	★
Cryogenic sapphire	RF	2×10^{-16}	[34]	$ 250 k	★
Ion/neutral atoms	Optical	8.6×10^{-18}	[35]	$ >250 k	★
High performance optical cavity	Optical	1×10^{-17}	[36]	$ >250 k	★★
Acetylene-filled power build up cavity	Optical	1×10^{-11}	[37]	$ >70 k	★★★
Gas-filled fiber cell	Optical	1×10^{-12}	[38]	N/A	★★★★

Table 1.2: *Stability of a selection of references.*

the second" by CIPM in 2006 [32]. Optical cavities have proven to have excellent stability approaching the thermal noise limit [36]. However, all these systems mentioned have their own requirements which restrict their implementation to laboratory environments. For example, the Cs atom and sapphire crystal need to be cooled to a temperature close to absolute zero, and optical cavities require isolation from thermal and acoustic noise. These requirements make them less appealing for a portable system.

In our lab, we have chosen a commercial GPS–disciplined Rb clock as an RF reference, which has the short-term stability of a Rb atomic clock and long-term stability of the GPS satellite network. A GPS-Rb reference is a good candidate for a portable frequency comb in terms of stability and cost, but it needs to be in contact with several satellites and it takes a few days to achieve maximum stability and accuracy. In contrast, an acetylene-filled CW fiber reference, a fiber-based system developed in our group [40], offers both good short-term and long-term stability without accessing the GPS network. The experimental details and performance of such a CW reference is further addressed in Chapter 2. An integrated version of this CW reference using two solid-core fibers on both ends to trap low pressure acetylene inside hollow-core fiber, namely the fiber cell reference, further improves the portability with compromised stability performance [38]. This type of design could serve

as the ideal optical reference for a portable comb system.

Current frequency combs can be classified into two categories based on the types of laser: solid-state and fiber-based laser frequency combs. The stability of a few state of the art combs in both categories are listed in Table 1.2.2. Ti: Sapphire laser-based frequency combs are so far the gold standard exhibiting the best performance in terms of frequency stability, f_0 linewidth, and accumulated carrier-envelope phase fluctuations, etc. One drawback of Ti: Sapphire combs is that the laser spectrum is centered at around 800 nm and does not extend into the telecommunications wavelength, which is around 1550 nm. Although telecom wavelengths can be frequency doubled into the Ti: Sapphire band, such implementation is not suitable for a portable system.

Fiber-based lasers have the advantages of being compact and more portable, alignment free, and less expensive with low power assumption compared with solid-state systems. Gain fibers doped with various rare earth elements cover a wide spectral range from near-infrared to the mid-infrared (1 - 3 μm). At telecom wavelengths, erbium-doped fiber lasers have been demonstrated to have sub-mHz linewiths [48], with stability comparable to Rubidium oscillators. Therefore, an erbium-doped fiber frequency comb is an ideal source for a portable optical frequency reference.

The goal of this project is to build a portable optical frequency reference system in the telecom wavelength (~ 1.5 μm). An erbium-doped fiber laser frequency comb is an excellent candidate to fit into a portable system. Since the ultimate performance of the frequency comb is set by the stability of its reference standard used for comb stabilization, the reference(s) for the comb also demand both high stability and portability. From Table 1.2, the most stable references are the most expensive and least portable. Therefore, compromises need to be made among the stability, portability and cost. The acetylene-filled fiber cells can serve the purpose of a portable and stable optical reference for the erbium-doped fiber laser frequency comb. In this work, as an initial step for this portable system, an erbium-doped fiber comb is optically referenced to an acetylene-filled vacuum-chamber-based CW

Laser	Stabilization Method	Optical stability	Compared to	Year	Ref
Ti: S	tooth→CW ref@657 nm$^{(a)}$ f_0→RF	6×10^{-17}@1 s (900 nm)	Dual comb beat$^{(d)}$	2004	[41]
Ti: S	tooth→CW ref@657 nm$^{(a)}$ f_0→RF	10^{-19}@ 1×10^{4} s	CW ref@657 nm$^{(e)}$	2007	[42]
Ti: S	tooth→atomic ref@780 nm$^{(b)}$ f_{rep}→H maser	7×10^{-12}@1 s (800 nm)	Dual comb beat$^{(d)}$	2009	[43]
Er comb	tooth→CW ref@1550 nm$^{(a)}$ f_0→RF	5×10^{-18}<100 s (1200-1720 nm)	Dual comb beat$^{(d)}$	2006	[44]
Er comb	f_{rep}→CSO$^{(c)}$ f_0→H maser	6×10^{-14}<100 s	CW ref@778 nm$^{(e)}$	2007	[34]
Er comb	tooth #1→CW ref@1550 nm$^{(a)}$ tooth #2→CW ref@1535 nm	5×10^{-15}@1 s (1536 nm)	Dual comb beat$^{(d)}$	2008	[45]
Er comb	tooth→CW ref@578 nm$^{(a)}$ f_0→RF	3.7×10^{-16}@1 s	slave CW laser$^{(f)}$ @1064 nm	2010	[46]
Er comb	tooth→CW ref@1062 nm$^{(a)}$ f_0→RF	6.7×10^{-16}@1 s	CW ref@1542 nm$^{(e)}$	2014	[47]

Table 1.3: *Stability of a selection of optical frequency combs.*

$^{(a)}$ Locking is achieved by stabilizing the heterodyne beatnote between the comb and the CW ref to an RF reference. $^{(b)}$ Locking is achieved by direct stabilization of a comb tooth to an atomic transition. $^{(c)}$ Cryogenic Sapphire Oscillator with stability of 1×10^{-14} at 1 s gate time. $^{(d)}$ Two combs are stabilized in the same way. By performing dual comb heterodyne beat, the optical stability at certain wavelength is the RF beatnote linewidth divided by the nominal frequency of the comb tooth involved in the heterodyne beat. $^{(e)}$ The optical stability is the RF beatnote linewidth between the comb and the CW ref laser divided by the nominal frequency of the CW ref. $^{(f)}$ Two combs are stabilized in the same way. A slave laser is phase locked to one of the two combs, and heterodyne beat against the other comb. The optical stability of the second comb is measured by the beatnote linewidth divided by the nominal frequency of the slave laser.

fiber reference (Chapter 4). The vacuum chambers could eventually be replaced by an acetylene-filled fiber cell (Chapter 7.2).

1.3 Introduction to the Techniques

Free-running lasers usually have large intrinsic noise, and are not suitable for being a frequency reference directly. Therefore, we need to *"lock"* the laser frequency to an external

reference which gives a frequency signal with high stability and accuracy. The ultimate performance of the laser is determined by the external reference(s) being used in the system.

Laser stabilization is a fairly complex topic. In general, there are two types of locking: *frequency lock* and *phase lock*. The former involves the frequency stabilization of a laser to a fixed value. However, the laser linewidth remains the same as the intrinsic linewidth. Phase locking gives a more rigorous lock by precisely controlling the phase of the electric field. The resulting laser linewidth can be reduced to the sub-Hz level from a MHz diode laser [49, 50]. Both locking techniques are used in our system, and will be discussed in later chapters. In this section, we will be mainly focused on a general description of the multiple steps needed for laser stabilization. Our goal here is to familiarize the reader with some of the terminologies. A more detailed description of each step will be further explained in Section 2.6, 4.4 and 4.5.

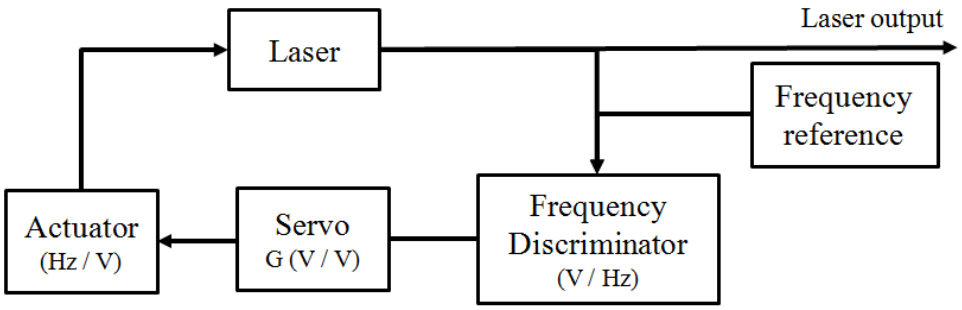

Figure 1.6: *Schematic of laser frequency stabilization feedback loop.*

The topic of laser stabilization itself is embedded in a much larger field of *"Control Theory"*, which is of great interest to engineers for controlling physical systems, for example, the cruise control feature on a car. The key point is to create a physical mechanism that gives proper corrections to the target when it deviates from the set point. Usually, this is called a *servo system*, or a *feedback loop*. The structure of a general laser frequency stabilization feedback loop is depicted in Figure 1.6, which includes several parts: (1) the

target, in our case is the laser frequency, which is something we want to control; (2) an *actuator*, which changes the state of the target. For precise frequency control, the actuator varies depending on different laser systems. It could be a piezoelectric transducer (PZT) of a fiber laser [40], or the pump current of a diode laser [51], or the end mirror of a filtering cavity [52], all of which should able to change the laser's frequency; (3) the *error signal* for locking, or *frequency discriminator*. This electronic error signal is created by comparing the instantaneous laser frequency with a frequency reference, and is proportional to the difference between the two frequencies, and usually has the phase information to tell which direction the laser is deviating from the reference. Therefore, the error signal usually has an odd symmetry; and (4) the *servo*, or the *loop filter*, which is a high-bandwidth low noise electronic amplifier. The gain of the servo is properly designed, such that when the error signal is amplified by the servo and fed back to the laser actuator, the frequency noise of the free-running laser can be greatly suppressed. The purpose of the feedback loop is to correct the laser frequency, with respect to the reference, within the servo electronic bandwidth.

Once we decide which reference the laser locks to, in order to reach optimal results, one has to make the best choices for all system parameters. This includes the choice of frequency discriminator and actuator, and design of the servo that fits into our system. In the following paragraphs, we will talk about each of these steps one by one. For each step, we will describe briefly the pros the cons for some of the common options.

1.3.1 Choosing the Reference

There are multiple options for an optical reference to which a laser can be locked, such as ultra-stable optical cavities or interferometers, trapped ions or neutral atoms. Both offer good short term stability, but the systems are expensive and bulky, and thus not very portable. A less expensive and potentially more portable option is to lock a laser to a natural resonance, i.e. an atomic or molecular transition, which gives good long-term stability. For the telecommunication industry, a few molecular gases have been used for

wavelength referencing, as shown in Figure 1.7.

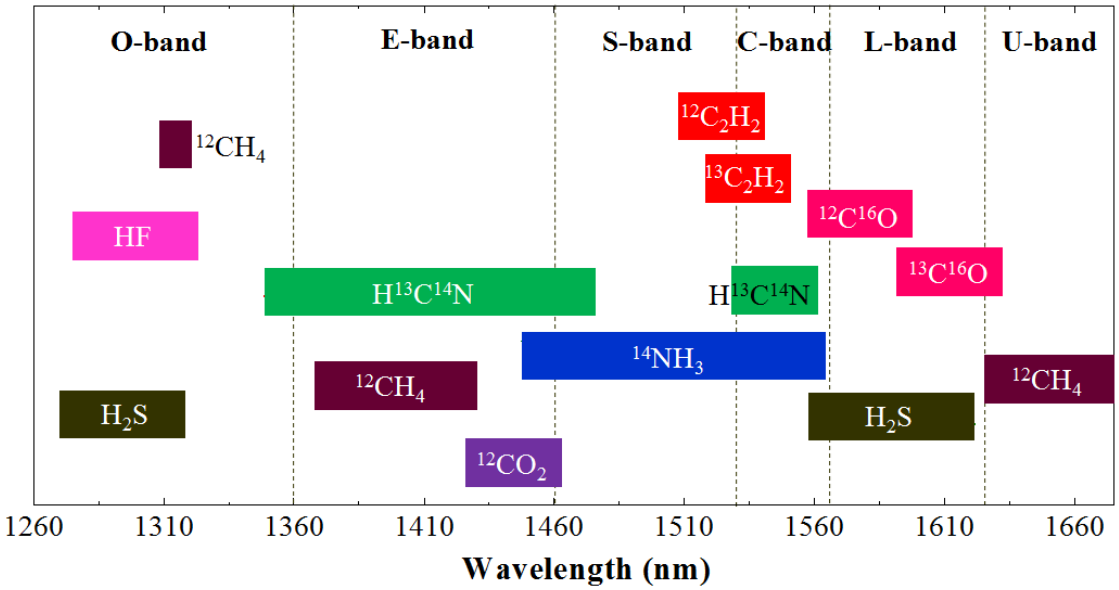

Figure 1.7: *Common gases for referencing the wavelengths for telecommunication industry [6, 53–58]*

Acetylene has a series of well separated overtone transitions that conveniently occur in the 1500-1600 nm range. These transitions (for both $^{12}C_2H_2$ and $^{13}C_2H_2$) have strong absorption strengths and one has been selected by BIPM (Bureau International des Poids et Mesures) as a wavelength reference in the near infrared. In our work, we choose to use $^{12}C_2H_2$. The spectrum of $\nu_1+\nu_3$ overtone transitions for $^{12}C_2H_2$ are shown in Figure 1.8.

So far, the accuracies of the best optical references based on acetylene realized research laboratories is $\sim$ 1 kHz using saturated absorption spectroscopy technique [7, 59–61], which will be discussed in Section 2.1. They are based on multi-pass power build up cavities for long interaction lengths. But those cavities are alignment sensitive and difficult to integrate into a commercial portable reference. A recently developed commercial acetylene stabilized diode laser (Model number: C2H2LDS-1540, by Neoark, Japan) has frequency uncertainty of about 20 kHz at 1542.38 nm with a market price of $ 70,000 [37]. The less expensive and portable optical references made by NIST (National Institute of Standards and Technology)

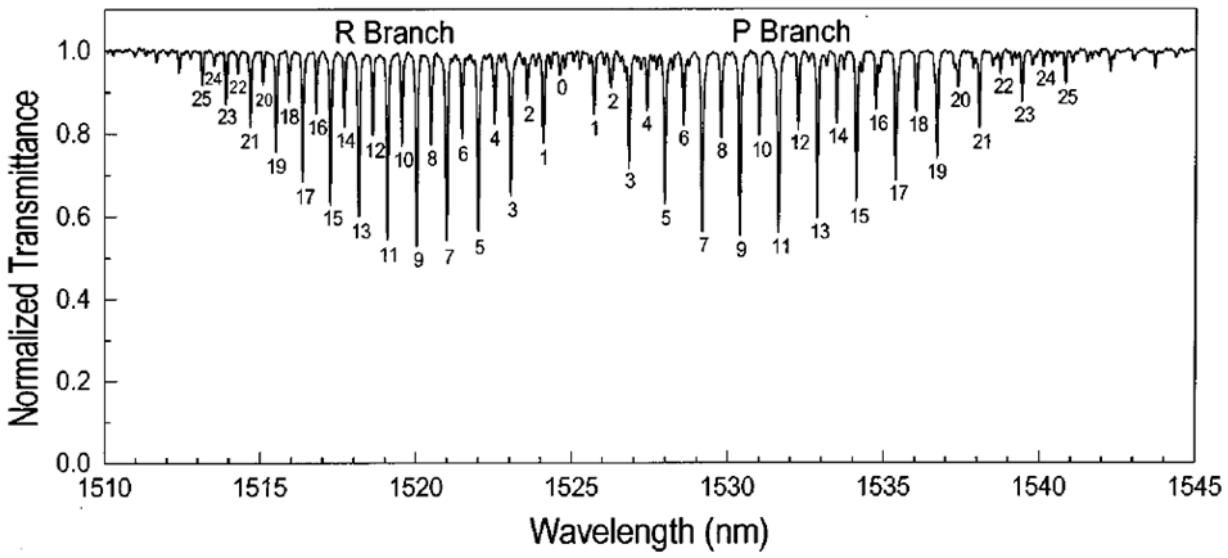

Figure 1.8: *Spectrum for acetylene ($^{12}C_2H_2$) $\nu_1+\nu_3$ overtone transition [7].*

have accuracies on the order of 100 MHz [7]. In this work, we show hollow-core fibers offer a potential alternative to free-space cavity setups.

Since their invention in 2003, hollow-core photonic crystal fibers have been demonstrated in many areas for nonlinear light-gas interactions. They are also suitable for replacing power build up cavities for making portable optical references for the following reasons. Their uniquely designed hollow-core structure allows light to be confined at high intensities in the core, where gas can be filled in, with very low loss. Since long interaction length can be easily realized in these fibers, sufficiently low pressures can be used for a minimized collisional broadening. In this case, the linewidth of the sub-Doppler feature is then mainly determined by the transit-time and power broadening effect. Large fiber core size and low pump power gives narrower sub-Doppler features. Knabe *et al.* have demonstrated 10 kHz accuracy of such a CW acetylene reference with large-core kagome fiber installed in vacuum chambers [40]. A more portable version of this reference can be made by sealing both ends of the hollow-core fiber with solid-core telecommunication single mode fibers (SMFs) through fusion splicing, which can serve as a portable optical reference for comb stabilization.

1.3.2 Derivation of Frequency Discriminator

Once we have created a resonance (e.g. the sub-Doppler feature) that the laser can be locked to, we need to produce a voltage signal that changes with laser frequency, that is the so-called *error signal* (or *frequency discriminator*). It should give zero voltage at the desired lock point. As the laser frequency deviates from the lock point, the error signal should give either a positive or negative voltage depending on which way the laser frequency drifts away with respect to the lock point. This error signal will be further processed by the following feedback circuitry for locking the laser to the resonance of interest.

1.3.3 The Feedback Circuitry

The last part of the feedback loop is accomplished by the electric feedback circuitry, sometimes also called *the loop filter* or *servo circuit*. It connects the error signal to the laser. The error signal is amplified by the servo and fed back to the laser actuator to cancel the frequency noise, in order to drive the error signal to zero. For optimal behaviour, when the laser is locked, the locking bandwidth, in other words, the correction speed of the feedback loop, should only be limited by the laser actuator's resonance frequency. Thermal fluctuations or mechanical noise at low frequencies (DC to kHz level) should all be corrected as much as possible by the servo circuit.

There are commercially available products to serve the purpose, such as the servo controller box from Newport [12]. It is a standalone box having a number of adjustment knobs, which gives certain flexibility to shape the overall servo gain for one's needs. With some basic servo design theory, one can also build a servo circuit that works for a particular system. Section 2.7 gives a tutorial for building such a servo box.

1.4 Thesis Outline

The work of the thesis is aimed at building a high precision, portable optical frequency reference system in the telecom wavelength ($\sim$ 1.5 μm) for practical applications. This portable system consists two major parts: One is the erbium-doped fiber laser frequency comb, the other is the optical CW reference for the stabilization of a single comb tooth.

Before we introduce the techniques for single comb tooth stabilization, Chapter 2 describes the stabilization of a CW fiber laser, or the CW reference, which is a CW fiber laser locked to an acetylene transition inside a hollow-core fiber using the saturated absorption spectroscopy (SAS) technique. The same technique applies to the single tooth SAS. Chapter 3 focuses on the implementation of an erbium-doped fiber laser frequency comb. For the isolation of a single comb tooth, a GHz repetition rate comb is generated by using an external filtering cavity. Chapter 4 talks about how we realized single comb tooth stabilization to the CW optical reference we developed in Chapter 2. Multiple amplification stages have been built to amplify a single comb tooth from nW to mW (a factor of 10^6 power amplification!) while preserving the comb signal-to-noise ratio, in order to perform SAS. Chapter 5 shows the comb stability results by comparing the optically-referenced comb to a second CW reference at a different wavelength from the stabilized single tooth. Chapter 6 presents a separate project in which I was involved. It is about the noise analysis of a prism-based Cr:forsterite laser frequency comb. A summary and outlook of this work is included in Chapter 7. In appendix A, a novel cross-VIPA (cross-virtually imaged phase array) spectrometer is proposed for single tooth isolation, with a high spectral resolution of 730 MHz based on our simulations.

We believe this work to be the first demonstration of an optically referenced comb system based on a fiber laser using direct comb saturated absorption spectroscopy. This work represents the first isolation and amplification of a single tooth directly from a sub-100 MHz fiber laser for saturated absorption spectroscopy. The comb amplification technique developed opens many possibilities for direct comb spectroscopy using low power, low repetition rate

(< 100 MHz) fiber laser frequency combs. In addition, the fiber comb optically referenced to a gas-filled fiber reference represents a large step towards an all-fiber portable frequency metrology system with low short-term instability, independent of the global positioning system (GPS).

Chapter 2

CW Laser Saturated Absorption Spectroscopy

As an initial step toward stabilizing a single comb tooth to an absorption line of acetylene, this Chapter describes how to stabilize a CW fiber laser to that absorption line. This is achieved by filling the hollow-core photonic crystal fibers with low pressures ($\sim$ 100 mtorr or 10^{-4} atm) of acetylene and then performing the pump-probe saturated absorption spectroscopy (SAS) to realize a narrow absorption transition, the sub-Doppler feature. This work was initially demonstrated [40] by Kevin Knabe, a previous group member. In Chapter 4, the CW fiber laser is replaced by an amplified single comb tooth, and the same SAS technique will be applied in a second identical setup. Section 2.2 presents the experimental SAS setup. Section 2.3 describes the hollow-core photonic crystal fibers used for filling the acetylene gas. A noise reduction technique is used in the experiment by shifting the probe frequency from the pump using an acousto-optic modulator (AOM), explained in Section 2.4. Section 2.6 details the frequency modulation (FM) technique used to produce the error signal from the sub-Doppler feature for locking purpose. As the last part of the feedback loop, Section 2.7 talks about simple servo designs and how we use servo boxes to lock the CW fiber laser to the sub-Doppler feature.

2.1 Introduction to Saturated Absorption Spectroscopy

The disadvantage of using a natural resonance as the optical reference is the linewidth broadening of these transitions at room temperature with respect to their natural linewidth due to various effects. The most dominant effect is the Doppler broadening, while others are collision broadening, transit-time broadening, saturation and power broadening, etc [62]. Therefore, a lot of methods have been developed to reduce or eliminate these effects to reduce the linewidth, including laser cooling and trapping. These methods are good for producing high stability atomic/molecular references, but are restricted to research laboratories due to complicated cooling and trapping techniques. Saturated absorption spectroscopy (SAS) is a convenient technique developed in the 1960s [63–66] that allows the observation of linewidths below the Doppler limit at room temperature with a simple experimental setup.

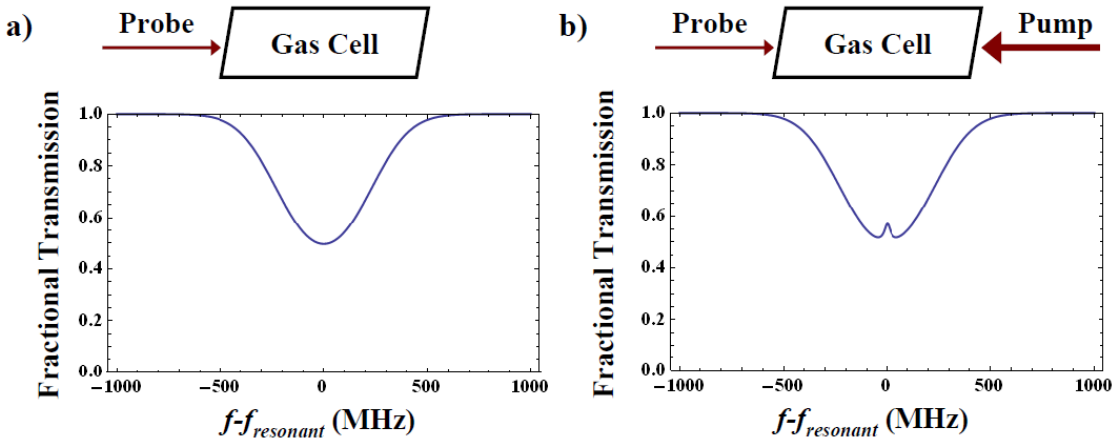

Figure 2.1: *Fractional transmission of light through a gas cell versus frequency (a) when only a probe beam is present, and (b) when both a pump and probe beam are present [8].*

The SAS setup involves two counter-propagating beams, namely, the pump and probe beam, interacting with molecules inside a gas cell. Both beams are from the same laser and thus have the same frequency. The probe beam is too weak to significantly alter the molecules' populations in the ground and excite states. However, the pump beam is strong enough to significantly affect the populations. The Doppler effect can be described as the

following: molecules travelling at different velocities see different frequencies from the same incoming laser. These frequencies are Doppler shifted from the laser's nominal frequency. The amount of the Doppler shift depends on the velocity of that particular molecule. This is to say, a laser at a certain frequency will only be in resonance with molecules that belong to a certain velocity class. If we scan the frequency of the probe beam, it will interact with molecules from a number of velocity classes, but one at each time. For a pump-probe scheme, although both beams are scanned at the same frequency, because they are counter-propagating, the pump and probe will always be interacting with molecules from two different velocity classes, except when both beams are on resonance with the zero velocity class. When the zero velocity class molecules are excited by the strong pump beam, the probe can transmit through the cell without being absorbed, thus giving a local maximum peak on the photodetector, shown in Figure 2.1 (b).

2.2 Setup Overview

The overview experimental setup for saturated absorption spectroscopy (SAS) is shown in Figure 2.2. The CW fiber laser is split into two counter-propagating pump and probe beams. The pump light is amplified by a commercial CW Erbium-doped fiber amplifier (EDFA) (Model number: HWT-EDFA-B-PM-C27X, by Manlight) up to 200-250 mW with preserved linear polarization. Then both beams are directed into the opposite ends of a hollow-core photonic crystal fiber (HC-PCF), with each fiber end installed in one of the two separate vacuum chambers. Details of the fiber will be described in Section 2.3. An acousto-optic modulator (AOM) is implemented for noise reduction, which will be explained in Section 2.4. Modulation techniques are used on both the probe and the pump beam for frequency modulation (FM) techniques, and will be described in details in Section 2.6. In Figure 2.2, mirrors and focusing lenses are used to achieve a maximum coupling efficiency from free space to the fiber, which is about 60-65% for both pump and probe including

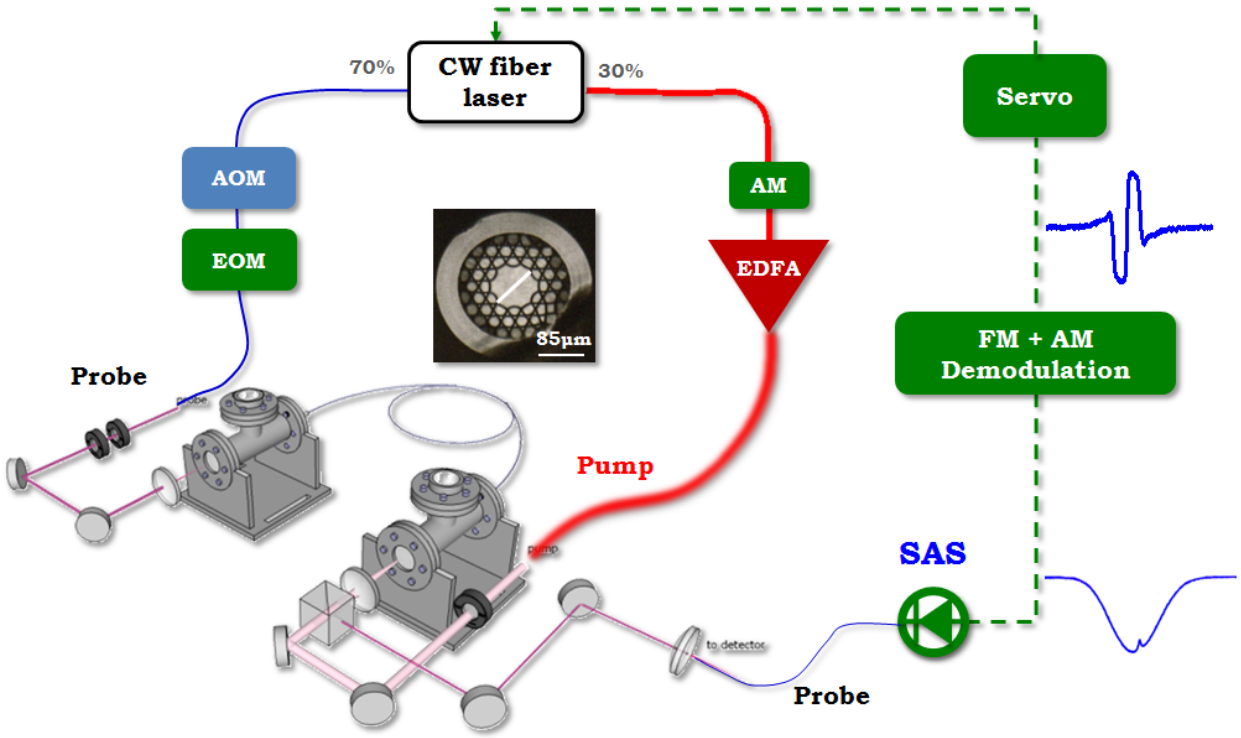

Figure 2.2: *Schematic setup for Saturated Absorption Spectroscopy (SAS). AOM: acousto-optic modulator, EOM: electro-optical modulator, AM: amplitude modulator, FM+AM: frequency and amplitude modulation.*

the fiber loss. The polarization state of pump and probe are carefully controlled to be orthogonal to each other using waveplates, such that the probe beam out from the fiber can be separated from the input pump beam using a polarization beam splitter (PBS). The probe after exiting the PBS is focused and coupled into a multi-mode fiber (MMF) and detected by a 125 MHz fast detector [Model 1811 by New Focus].

As we apply a ramp voltage to the fiber laser's piezo-electric transducer (PZT), the laser's frequency is scanned almost linearly over the P(13) acetylene transition at $\sim$ 1532.8 nm. Figure 2.3 gives an example of the resulting absorption spectrum [8]. The blue curves at the bottom of Figure 2.3 are the transmission from a fiber ring cavity (FRC) as we scan the laser frequency for frequency calibration purposes. The free spectral range (FSR) of the FRC is 48.01 $\pm$ 0.01 MHz.

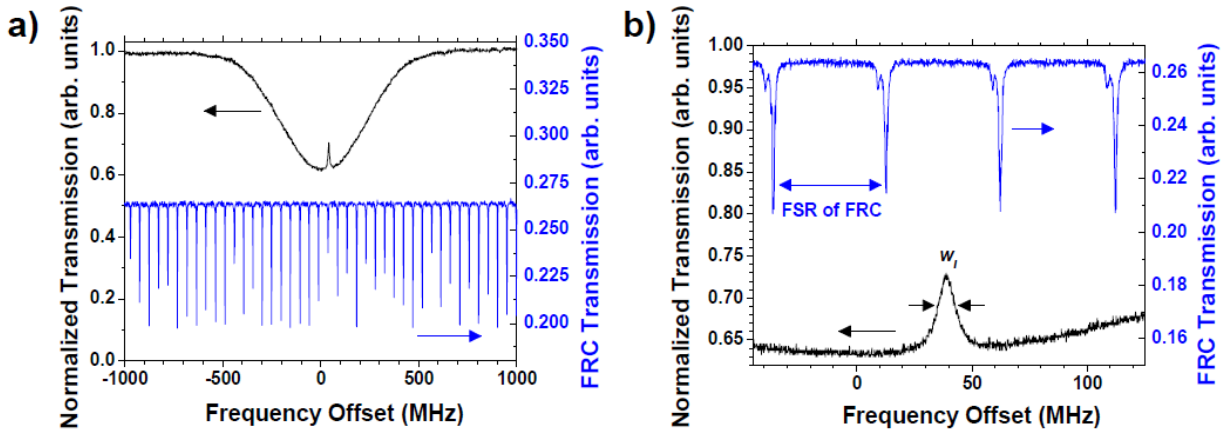

Figure 2.3: *Saturated absorption spectrum versus frequency with interferometer frequency calibration. a) The zoom out picture shows the Doppler-broadened feature. (b) The zoom in picture shows the sub-Doppler feature [8].*

2.3 The Hollow-Core Fiber

We have two identical vacuum-chamber-based reference setups in our lab, denoted as Ref I and Ref II in this thesis. Both setups have similar hollow-core photonic crystal fibers (HC-PCFs) installed. These HC-PCFs are specially fabricated by our collaborator Dr. Fetah Benabid's group in X'lim Institute, France. The SEM images of the cross section of both fibers are shown in Figure 2.4. The specs for both fibers are listed in Table 2.1.

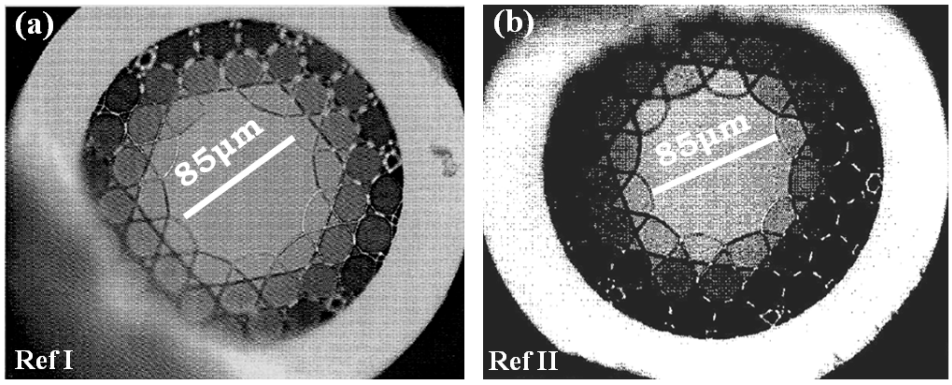

Figure 2.4: *SEM images for the Hollow-core Photonic Crystal fiber we used in two reference setups, from Dr. Benabid's group.*

Ref setup #	Ref I	Ref II
Part number	110727-CFD-K7C3R-C11J11	110727-CFD-K7C3R-C3J16
Loss	122 dB/km	32 dB/km
Length	7.9 m	6.8 m
Diameter	300 μm	300 μm
Core size	85/93.75 μm	85/93.75 μm
Pitch	18.75 μm	22.5 μm

Table 2.1: *Hollow-core Photonic Crystal fibers for (a) reference I, and (b) reference II setups.*

Ref I uses the HC-PCF on the left. It is used for the single tooth Saturated Absorption experiment, which will be discussed in Chapter 4. We lock an amplified comb tooth at $\sim$ 1539.4 nm to the P(23) overtone transition of $^{12}C_2H_2$. The $^{12}C_2H_2$ pressure loaded inside the fiber is $\sim$ 140 mtorr, which gives $\sim$ 50% fractional transmission.

For diagnostic purposes, which will be further described in Chapter 5.2, we stabilize a CW fiber laser to the P(13) overtone transition of $^{12}C_2H_2$ at $\sim$ 1532.8 nm to test the comb stability. Ref II setup, with the HC-PCF on the right, serves as the CW reference. For a $\sim$ 50% fractional transmission, the $^{12}C_2H_2$ pressure inside the fiber is $\sim$ 70 mtorr. Both setups have about the same fiber coupling efficiency. In principle, it does not matter which setup is used for single tooth or CW fiber laser locking.

2.4 The Acousto-optic Modulator

For noise reduction purposes, the probe beam is frequency shifted slightly from the pump by tens of MHz using an Acousto-optic modulator (AOM) (Figure 2.2). This results in any unwanted interference between the probe beam and any pump beam reflections occurring at one half the AOM frequency ($f_{\mathrm{AOM}} \sim$ 45-55 MHz) instead of at DC, which can be easily filtered out electronically.

An AOM is a device that can be used to modulate either the intensity or frequency (in our case) of a laser beam with an electrical drive signal, based on the acousto-optic effect.

The driver produces an RF signal at the piezoelectric transducer's resonant frequency (tens of MHz). The transducer then converts the RF energy into acoustic energy and produces acoustic waves inside the crystal. As a result, the crystal will experience a periodic change in the refractive index and acts as a sinusoidal grating. When an incident laser beam passes through this grating, it will be diffracted into several orders, each of which has different intensity and frequency. In this case, light is scattering from moving planes. The frequency of the diffracted beam in order m will be Doppler-shifted by an amount equal to the frequency of the acoustic wave.

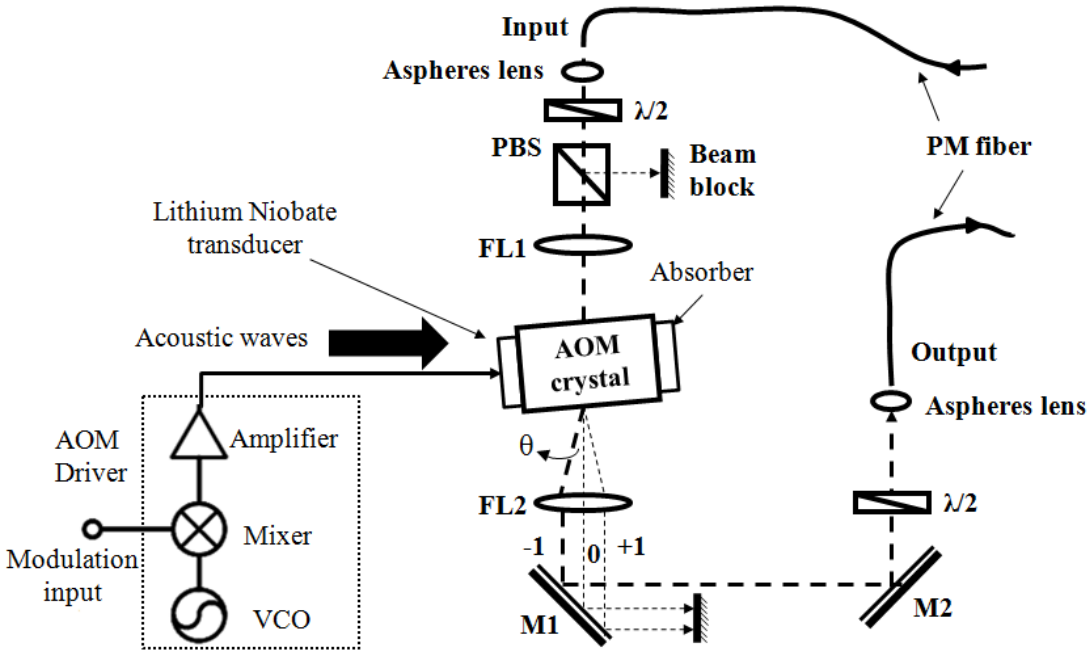

Figure 2.5: *Schematic setup for Acousto-optic modulator (AOM). PBS: polarization beam splitter FL: focusing lens, PM fiber: polarization-maintaining fiber.*

An important parameter of the AOM is the efficiency, that is the ratio between the optical power of the diffracted and incident laser beam. By positioning the AOM crystal at an appropriate angle, the highest efficiency can be achieved in the first order beam. This requires the angle between the laser light and the axis of acoustic propagation in the crystal to be Bragg's angle. The diffracted angle θ, between the incident and diffracted laser beam,

is then twice the Bragg angle. The theoretical maximum efficiency for an AOM given by NEOS [67] is:

$$\eta = \sin^2\left(1.57\sqrt{\frac{2}{\lambda^2}\left(\frac{L}{H}M_2 Pa\right)}\right) \tag{2.1}$$

where Pa is the acoustic power, M_2 is the figure of merit of the optical material, and L/H is the electrode's geometric factor. It should be noted that the efficiency is inversely proportional to the square of the wavelength λ.

In our AOM setup shown in Figure 2.5, the linearly polarized laser beam from a polarization-maintaining (PM) fiber is collimated into free space using an aspheric lens with a focal length of 18 mm. It passes through a half waveplate followed by a polarization beam splitter (PBS) to produce linearly polarized light, with its polarization axis perpendicular to the paper plane. The AOM we use is from NEOS with a 2 mm window (Model number 46055-1-1.55-LID). The collimated light is then focused into the crystal center with a beam waist of $\sim$ 200 μm. With an RF driving power of 2 Watts at $\sim$ 50 MHz, the first order beam can achieve an high efficiency of $\sim$ 70%, close to the AOM spec. The first order beam is then re-collimated and coupled back into another PM fiber as output.

2.5 Useful Techniques to Produce Error Signal

There are basically two types of techniques to produce error signal depending on if the laser is frequency modulated or not. In general, the modulated techniques have better performance over the non-modulated ones. The three techniques that are introduced in the following subsections are either non-modulated or slow-modulation techniques. The fast frequency modulation technique will be discussed in the next section, which is what we implemented in our experiment.

Side Locking

A straightforward way to derive an error signal is to have the laser tuned to the side of the resonance [68]. This method is called "side-lock". The steep slope of the resonance feature serves as the error signal for the servo loop. The slope is essentially the change in the absorption signal with laser frequency, and thus can be used to convert the laser frequency noise to the amplitude information, which can be easily detected by a photodetector. Side-locking to this slope can be accomplished by controlling the laser frequency so that the saturated absorption signal is maintained at a particular level.

Although this technique has advantages of being modulation-free and easy to implement, it suffers from several serious disadvantages. Firstly, because it is modulation-free, the error signal detected is at DC, where there can be significant amplitude noise. This results in a huge loss in SNR. Secondly, any perturbations in beam alignment or fluctuations in laser intensity can alter the lock point and cause drift in the laser frequency. If a sudden perturbation drives the laser to the opposite side of the resonance, the feedback loop will push the laser further away from resonance, due to the wrong sign of the slope. Thirdly,the side-lock has a very small capture range, which means that the laser frequency needs to be tuned very close to the resonance frequency before the system will lock. Once locked, small perturbations can knock the system out of lock.

There are two more limitations in the case of locking the laser to optical cavity fringes. Since the laser is locked to the side of the cavity resonance rather than the peak, the optical power of the transmitted light is only a fraction of the full power. In addition, the speed of the lock is limited by the cavity storage time, because the error signal generated is based on the light transmitted from the cavity. In contrast, error signals developed by reflection techniques, such as polarization-lock and Pound-Drever-Hall lock discussed in later paragraphs, are not limited by the cavity storage time.

Polarization Locking

Polarization locking is another modulation-free technique that was initially developed for locking a laser to an optical cavity [9], shown in Figure 2.6. Here, a polarizer or Brewster plate is inserted inside the optical cavity to cause a frequency dependent elliptical polarization. The light out from the cavity can be decomposed into two orthogonal linearly polarized components, either parallel or perpendicular with respect to the incident linearly polarized light. The perpendicular component is simply reflected by the cavity, and serves as a reference, while the parallel component enters the cavity and experiences a frequency-dependent phase shift in reflection. Any relative phase change between the two components will make the resulting beam elliptically polarized, which can be analyzed using a polarizing beam splitter and a pair of identical photodetectors.

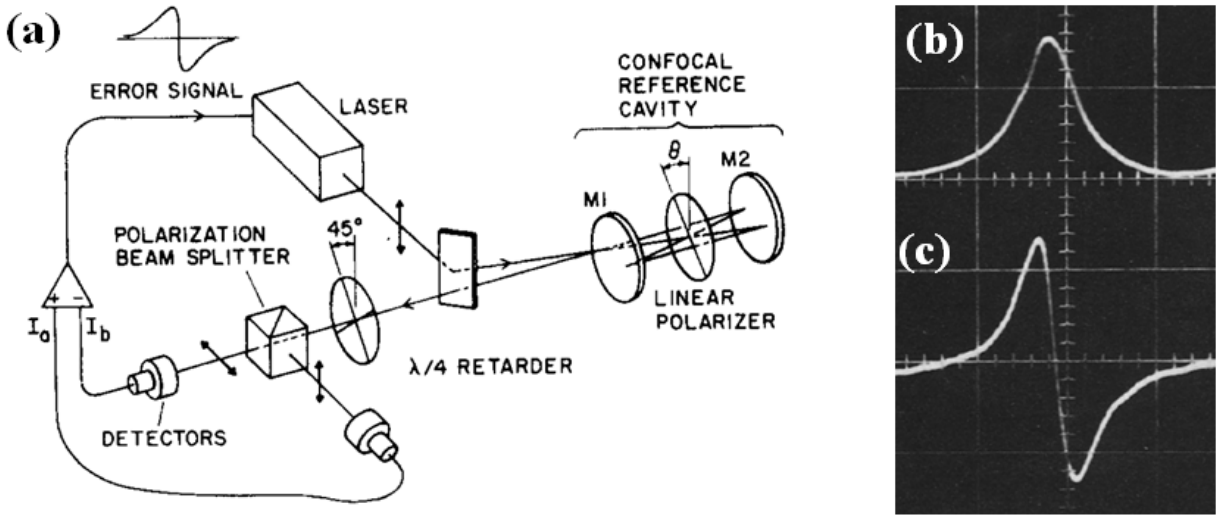

Figure 2.6: *Polarization locking technique for locking a laser to an optical cavity [9]. (a) Experimental setup, (b) Transmitted intensity from a 2 GHz confocal cavity, (c) Resulting polarization spectroscopy signal based on the difference between the two photodiodes.*

Similar ideas can also be applied to a pump-probe saturated absorption spectroscopy setup [10]. Figure 2.7 shows the experimental setup, as an example. The (nearly) counter-

propagating pump and probe beams overlap in a Rb vapour cell. The linear polarization of the probe is controlled by a half-waveplate. The weak probe beam interacts with a strong circularly polarized pump beam inside the Rb cell. The probe beam out from the cell is decomposed into two orthogonal linearly polarized components by the beam splitting cube, and the difference in intensity of the two components gives a dispersion-shaped, polarization spectroscopy signal, being the derivative of the sub-Doppler linewidth.

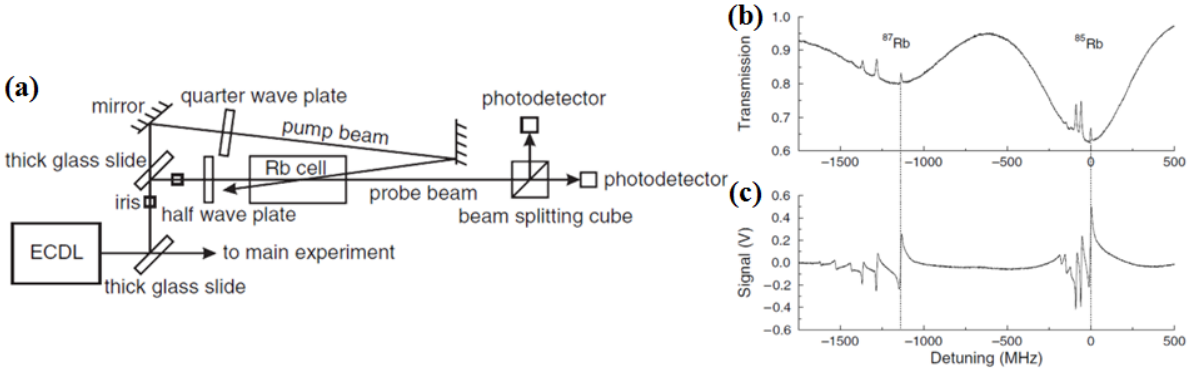

Figure 2.7: *Polarization locking technique for saturated absorption spectroscopy [10].(a) Experimental setup, ECDL: extended cavity diode laser. (b) Absorption spectrum for the transitions in ^{87}Rb (left) and for ^{85}Rb (right).(c) Resulting polarization spectrum.*

There are a few advantages for polarization spectroscopy. First, there is no modulation. Second, the homodyne detection between the two beams can reveal an extremely small level of absorption-induced changes of light polarization, resulting in a highly sensitive detection. The attainable sensitivity is limited by the finite extinction ratio of the intracavity polarizer. Third, it also has a very broad capture range, extending to nearly the cavity free spectral range ($\sim$ 2 GHz in the example above). Lastly, it is a reflection technique, so the response of the error signal is not limited by the storage time of the cavity.

One major disadvantage is its sensitivity to beam alignment. This is because the error signal depends on the balance between two detectors and their incident optical intensities. Small fluctuations in beam intensity have a large impact on the lock point. Similar to side-lock, polarization-lock also bears the disadvantage of being a DC technique, suffering from

low-frequency noise from both the laser and detectors. Moreover, polarization techniques do have long-term drifts associated with polarizing optics. A further disadvantage is that intracavity components increase system losses, resulting in a reduced cavity finesse ($\mathcal{F}$).

Dither Locking

Dither locking, known as the *slow* modulation technique, is one of the two modulation techniques that could be used. The other is frequency modulation spectroscopy, being the *fast* modulation technique, which will be discussed in the next subsection. Here we will only talk about the basic idea of the these two techniques and their relative advantages. A more detailed conceptual picture will be discussed in Section 4.4.

The purpose of frequency modulating the laser is to tell which side of resonance the laser is on by how the light intensity changes on the detector. For dither locking, the laser frequency is sinusoidally modulated, or dithered, at some slow modulation frequency ("slow" compared to the resonance linewidth, typically on the order of kHz level), producing a voltage signal oscillating at the modulation frequency. A dispersion-shaped error signal can be produced by comparing this voltage signal with the reference dither frequency. A typical experimental setup for dither lock is shown in Figure 2.8.

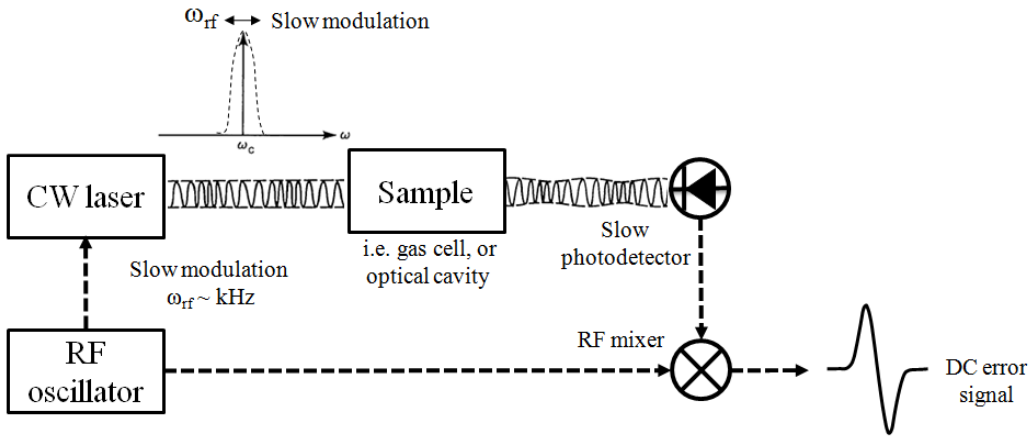

Figure 2.8: *Typical setup for dither locking.*

This low-frequency operation has two disadvantages. First, it results in a limited servo bandwidth, that is, how fast the servo loop can control the system, which is less than the slow modulation frequency. This is probably not a problem for some of the very stable lasers, but would become intractable for lasers with broad intrinsic noise. Second, the demodulated error signal is still partly contaminated by the low frequency technical noise, and the achievable SNR is thereby limited.

Another problem arises when we use dither locking to lock a laser to an optical cavity. The light transmitted from the cavity is still under slow modulation. This can interfere with processes afterwards, such as heterodyne beats with other lasers, and frequency counting. However, people have developed various ways to remove this modulation, such as an externally implemented device based on an AOM [69].

2.6 Frequency Modulation Spectroscopy

Frequency modulation (FM) spectroscopy [70] circumvents most of the drawbacks for all the techniques discussed above. This has been achieved through phase-modulating the laser at a frequency (tens to hundreds of MHz) much larger than the linewidth of the resonance of interest. The frequency modulation process basically generates a carrier optical frequency (ω_c) plus two RF modulation sidebands ($\omega_c \pm \omega_m$) with opposite phase, illustrated in Figure 2.9. The beam is then passed through the sample of interest and detected by a fast photodetector.

There are three advantages from this high frequency modulation. First, it allows each individual sideband to probe the resonance of interest and thereby preserves the high resolution capability from the narrow-linewidth laser source. In contrast, the slow modulation in dither locking results in a broader laser linewidth (Figure 2.8), which leads to a lower spectroscopic resolution because the spectral feature is probed by a noisier laser. Second, the useful signal can be moved to a high frequency region where the low frequency noise

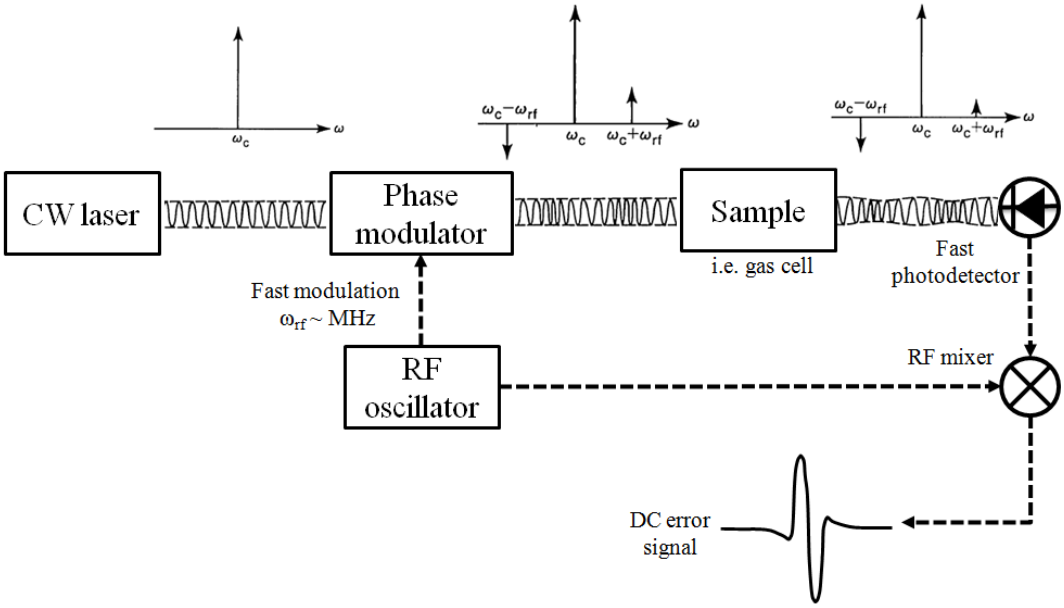

Figure 2.9: *Typical setup for Frequency Modulation (FM) spectroscopy.*

from the laser intensity fluctuations becomes negligible, allowing a high detection sensitivity approaching the quantum (shot noise) limit [71]. Third, fast modulation enables a rapid signal recovery, leading to a high sampling rate necessary for a high bandwidth servo loop. This can be understood in a simplified picture: if the laser is modulated slowly, say 100 Hz, then laser noise beyond 100 Hz cannot be compensated by the servo loop because we are not probing that fast. An additional advantage is the high SNR compared with dither locking. The error signal is generated in a similar way as the dither locking technique, by comparing the pure FM spectrum with the spectrum after the sample. When no absorbing sample is present, the pure FM signal will generate no photo-current in the high-speed detector (at the modulation frequency), resulting in a near-zero background. When a resonance feature is present, this FM balance is destroyed, producing phase-sensitive error signal.

For the reasons above, FM spectroscopy has become a powerful spectroscopic technique for high resolution, high sensitivity, and high-speed detection. However, in practical systems, the sensitivity of FM spectroscopy is limited by residual amplitude modulation (RAM)

instead of detector shot noise [72]. This gives a slowly drifting background on the error signal. A common source for RAM comes from residual etalon effects, for example, imperfect coatings for phase modulators (i.e. electro-optic modulators, or EOM), windows of the photodetector, or windows of the vapour cell. A number of techniques have been developed to overcome these problems [11], such as a careful control on the stress and temperature on the EOM crystal, and building a faster loop using an amplitude stabilizer [73]. The etalon fringe effect can be minimized by various optical or electronic methods [74]. A two-tone FM technique [75] can be used to reduce drifts and interference.

Here we use this technique to generate the error signal for locking a CW fiber laser to the sub-Doppler feature of the $^{12}C_2H_2$ overtone transitions (specifically, the P(13) line). In the next paragraphs, I will first talk about the physics of performing FM spectroscopy in an absorption case, and how we apply this general model to our saturated absorption setup. Then I will explain the induced offset problem caused by the Doppler background, and how we remove the offset by adding amplitude modulation (AM) on the pump beam. In the end, I will show the electronics circuits including both FM and AM demodulation we use for producing the error signal in our experimental setup.

2.6.1 The Physics of FM Spectroscopy

The essence of FM spectroscopy is to understand the effect of modulating the laser frequency on the intensity of light transmitted through the gas sample. For a fairly low modulation frequency, the physics picture of FM spectroscopy can be illustrated in a conceptual model shown in Figure 2.10 [76]. When the laser frequency is scanned over the absorption feature of interest, the slow dithering of the laser frequency causes the absorption to modulate at the same time. In other words, the frequency modulation of the laser is mapped into an amplitude modulation by the absorption, which can be easily detected by the photodetector. Figure 2.10 (a-c) illustrates the cases when the laser is scanned around the vicinity of the resonance. It is also important to note that the phase of this FM to AM conversion at a

certain frequency depends on the slope of the absorption at that frequency, shown in 2.10 (d). By mixing the photodetector RF output with the original driving signal, a dispersion feature with odd symmetry can be produced, which is used as the error signal for locking purposes.

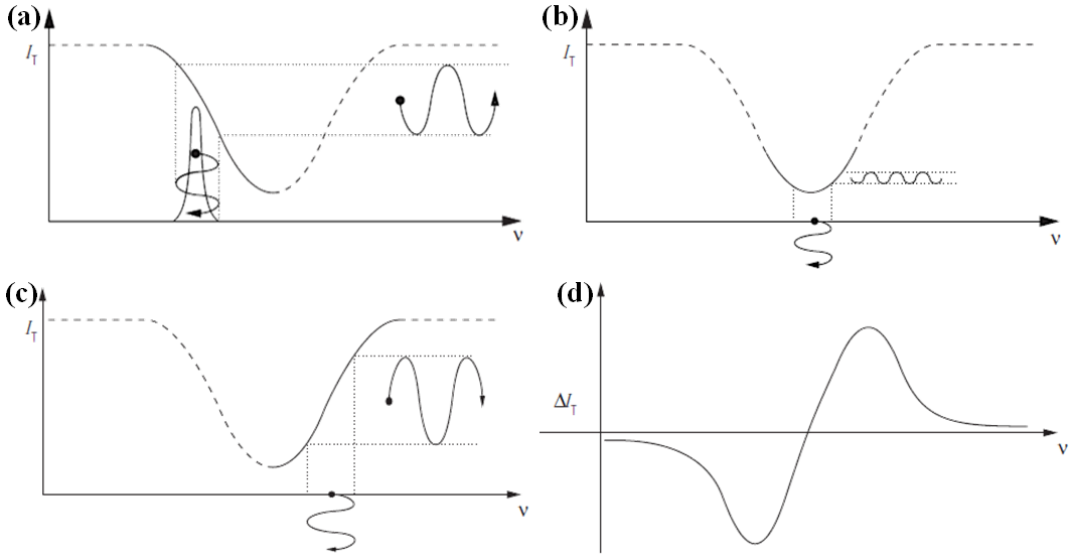

Figure 2.10: *A conceptual model to illustrate frequency modulation (FM) spectroscopy [76].*

The theory of FM spectroscopy has been well studied in vapor cells [70, 77]. If the modulation frequency ω_m is larger than half width of the spectral feature of interest, such that only one side-band probes the spectral feature, the intensity of the beam impinging on the photodetector can be expressed as [70]:

$$I_3(t) = \frac{cE_0^2}{8\pi} e^{-2\bar{\delta}} \times (1 - \Delta\delta M \cos(\omega_m t) + \Delta\phi M \sin(\omega_m t)). \tag{2.2}$$

where c is the speed of light, E_0 is the electric field amplitude of the original laser beam, $\bar{\delta}$ is the constant background loss, and $\Delta\delta$ and $\Delta\phi$ are deviations of loss and phase shift, respectively, from the background values caused by the spectral feature. The $\cos(\omega_m t)$ and $\sin(\omega_m t)$ components are then proportional to the absorption and dispersion, respectively, induced by the spectral feature. For many applications, the spectral feature of interest has

a Lorentzian lineshape. In Ref. [70] a dimensionless attenuation δ is defined as:

$$\delta(\omega) = \delta_{\text{peak}}(\frac{1}{R(\omega)^2 + 1}) \tag{2.3}$$

$$R(\omega) = \frac{\omega - \Omega}{(\Delta\Omega/2)} \tag{2.4}$$

where δ_{peak} is the peak attenuation at line center, Ω is the line center frequency, and $\Delta\Omega$ is the full width at half maximum.

2.6.2 Apply the Theory to SAS setup

However, things gets more complicated when we apply this idea in our Saturated absorption Spectroscopy (SAS) setup, because the ∼10 MHz sub-Doppler feature we are interested in is on top of a ∼ 500 MHz Doppler-broadened background. The modulation frequency we choose is 22 MHz. This number is larger than half of the sub-Doppler feature, but much smaller than the Doppler background. If we incorporate the loss due to the Voigt Doppler background [62], Equation 2.3 can be modified to:

$$\delta(\omega)_D = \delta_{\text{peak}} \times e^{-\frac{(\omega - \omega_c)^2}{0.36\omega_D^2}} (1 - \frac{1}{R(\omega)^2 + 1}) \tag{2.5}$$

where ω_D is the Doppler width.

The phase shift $\delta(\phi)_D$ induced by the sub-Doppler feature and Doppler background can then be calculated based on the Kramers-Kronig relations [78, 79]. With both terms (the loss and phase shift) known, the absorption ($\cos(\omega_m t)$) and dispersion ($\sin(\omega_m t)$) induced by the sub-Doppler feature can be calculated numerically.

Once a SAS signal is obtained from the fast photodetector, it is time to *demodulate* the error signal. The frequency modulation process *encodes* the laser frequency fluctuations around the modulation frequency, rather than at DC. The effect of demodulation is to *decode*

this error information by mixing it down to DC. This can be done by mixing the RF error signal with the FM driving signal, which allows the observation of either an absorption ($\Delta\delta$) or dispersion ($\Delta\phi$) component.

2.6.3 Producing Error Signal

As discussed in Section 2.6, one disadvantage of FM spectroscopy is the residual amplitude modulation (RAM) [71], which gives an offset on the produced error signal. In our case, this

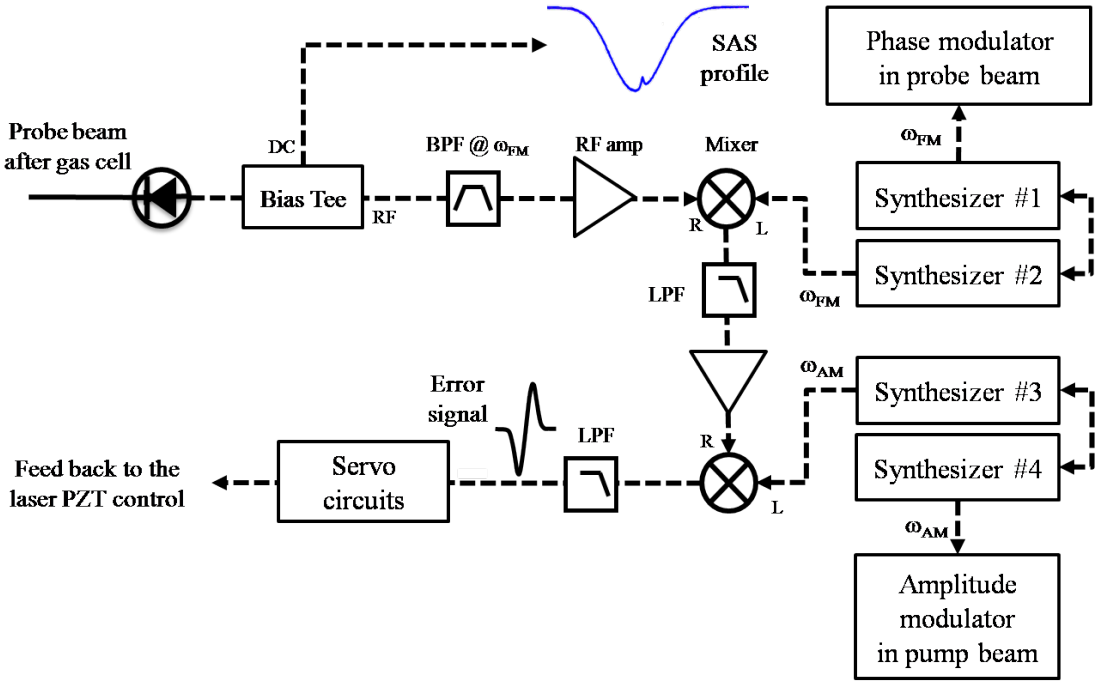

Figure 2.11: *Electronics circuit for FM and AM demodulation. The FM and AM modulation frequencies are 22 MHz and 900 kHz, respectively.*

is caused by the variation in laser intensity due to gas absorption over the FM range [40]. This background signal can be reduced by amplitude modulating the pump beam at 900 kHz, which essentially turns the pump beam on and off at a rate of 900 kHz, producing a signal which is the difference between when the pump is on and off.

Figure 2.11 shows the RF electronics setup for FM and AM demodulation. A 125

MHz photodetector (New Focus 1811-FC) is used to detect the probe light (under FM modulation) after passing through the $^{12}C_2H_2$-filled hollow-core fiber. The RF component of the photodetector output is filtered, amplified, and mixed at both FM and AM frequencies. The produced error signal after FM and AM demodulation, from a CW fiber laser, is shown in Figure 2.12 [8].

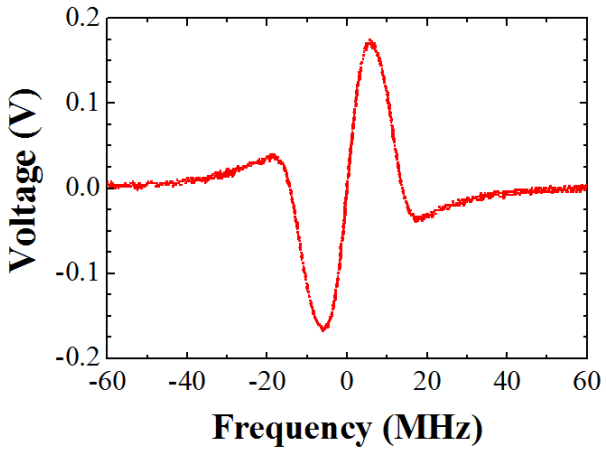

Figure 2.12: *Sub-Doppler error signals generated from a CW fiber laser for locking the CW laser to $^{12}C_2H_2$ overtone transitions P(13) at 1532.8 nm.*

A few precautions need to be taken for an optimized sub-Doppler error signal. First, the bandwidth of the RF band-pass filter should not be too narrow. In our case, the bandwidth is a few MHz around the FM modulation frequency of 22 MHz. If the filter bandwidth is too narrow, phase shifts would be induced that will limit the servo bandwidth [80]. Secondly, the power level of the two RF components (denoted as RF and LO in Figure 2.11) before the mixer should match the mixer's power level. This can be done by using appropriate RF amplifiers and attenuators to achieve the power level required. Thirdly, the lineshape of the FM (or AM) error signal at the mixer output depends on the relative phase between the RF signal with respect to the LO. For a maximized amplitude of the error signal, the RF and LO need to be 90° out of phase.

2.7 The Servo

In the last section, an error signal from a CW fiber laser is produced from FM and AM demodulation. This section describes the following servo system that takes the error signal and stabilizes the laser to an acetylene overtone transition of interest. For CW fiber laser stabilization, the servo output goes to the PZT of the fiber laser which adjusts the laser wavelength to the desired value.

In this section, we will first introduce a few terminologies for servo design, followd by a short tutorial guide. Then, as a concrete example, we will present two home-made servo boxes built based on Proportional-Integral (PI) amplifier circuits. For comparison, the performance of a commercial servo controller box [12] (Model number: LB1005, by Newport) will also be shown. In the end, we will show the locking result for the CW laser stabilization using the commercial servo box.

In our work, this servo box has been used for a few different locking schemes: (1) a CW fiber laser locked to a molecular transition (Section 2.7); (2) carrier-envelope offset frequency (f_0) and repetition rate (f_{rep}) of a fiber-based frequency comb locked to RF references (Section 5.2). With some basic servo design theory, one can also build a servo circuit that works for a particular system. Here, we will give a very simple introduction to the method we use for servo design. Two simple servo circuits will be presented in section 2.7 as concrete examples.

2.7.1 Basic Terminologies

Frequency Response Method

There are several important building blocks for a servo, including low-noise amplifiers, integrators, differentiators, lag and lead compensators, etc. The goal is to arrange them in an appropriate way to give us a desired shape of gain as a function of frequency, or the so-called *transfer function*. The most common method used is the *frequency response technique*, while

other useful methods are *Nyquist diagram* and *Rootlocus method* ([81], Section 5.2). The term *frequency response* refers to how a system responds to a sinusoidal input. By comparing the output to the input, we are basically looking at two things: (1) *amplitude response*, that is, the ratio between the output and input amplitudes; and (2) *phase response*, that is, how much the output lags behind the input in time.

The measurement of course can be done manually by feeding a sine wave at a certain frequency to the system, recording the output amplitude and phase information with respect to the input, and then repeating the same measurement at a number of different input frequencies. An alternative and easier way is to use the *swept sine* function available from a FFT spectrum analyzer. The source channel outputs a sinusoidal wave that is split into two portions. One portion goes directly to one of the two receivers on the spectrum analyzer, which serves as the reference channel. The other portion goes to the device under test, in this case, the servo circuit under design. The device output then goes to the second receiver. By starting the acquisition process, the spectrum analyzer will sweep the source signal across a frequency range, and measure the amplitude and phase as a function of frequencies, by comparing the reference channel to the signal output from the device under test.

Bode Plot

One of the most intuitive ways to display the frequency response is called *Bode plot*, developed by H. W. Bode at Bell Laboratories between 1932 and 1942 [73]. An example Bode plot of a low-pass filter is shown in Figure 2.13. The amplitude and phase response versus frequency (in log scale) is plotted in the upper and lower figures, respectively. The unit for amplitude response is in *decibels* (dB). In communications, it is standard to measure power gain in decibels:

$$|G_{\mathbf{power}}|_{dB} = 10 \log_{10} \frac{P_2}{P_1} \tag{2.6}$$

However, if we measure voltage gain, there is a factor of two difference because power is the square of the voltage. Thus, the voltage gain is:

$$|G_{\mathbf{voltage}}|_{dB} = 20 \log_{10} \frac{V_2}{V_1} \tag{2.7}$$

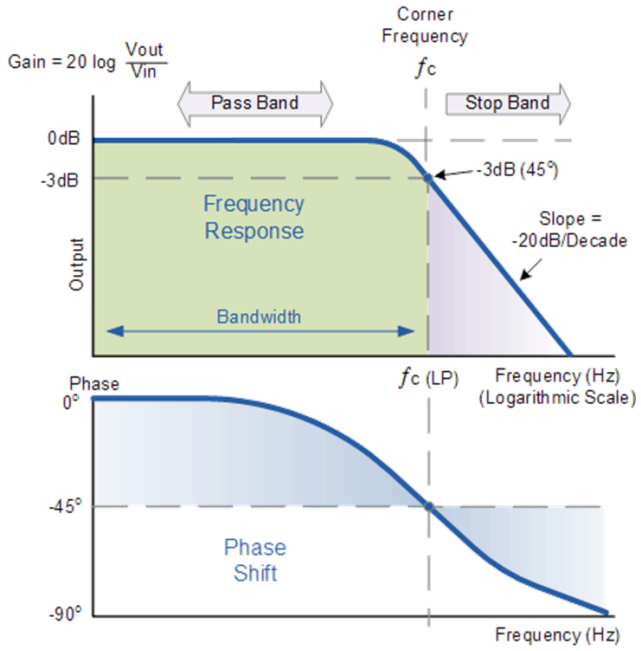

Figure 2.13: *Bode plot of a low pass filter with corner frequency f_c. Picture taken from: http://www.electronics-tutorials.ws/filter.*

Here, *corner frequency* is the frequency at which the amplitudes drops by 3 dB (or 50%). This frequency is also called the *3 dB bandwidth* of the device. It is shown in Figure 2.8 that the amplitude is flat at low frequencies and starts to drop at the corner frequency with a constant slope of 20 dB/decade (or 6 dB/octave for first-order filter, second-order filter drops faster, 40 dB/decade or 12 dB/octave). This is exactly what we would expect for a low pass filter, which passes the low frequency components, and attenuates high frequency components. A noticeable phase shift associated with the amplitude attenuation starts at one-tenth of the corner frequency, and stops accumulating at ten times the corner frequency.

By then, the filter output phase is delayed by 90° with respect to the input.

In general, for the response of any servo design, a 180° phase shift will happen at a high enough frequency. This indicates that the correction signal will turn the system from a useful *negative feedback* into an unwanted *positive feedback*. In this case, the amplified error signal is not effectively used to pull the laser frequency back to the set point, but pushes it away instead.

Closed-loop Gain and Open-loop Gain

By now, it is important to introduce two terms: closed-loop gain and open-loop gain. The *closed-loop gain* refers to the overall gain of the feedback loop that goes from the laser to the detector, then to servo electronics, and back to the laser. It can be measured by breaking the loop as shown in Figure 2.14 (a) via the swept sine measurement. We can feed the servo input with a sine wave, and look at the error signal as output, as indicated by the red arrows in Figure 2.14 (a).

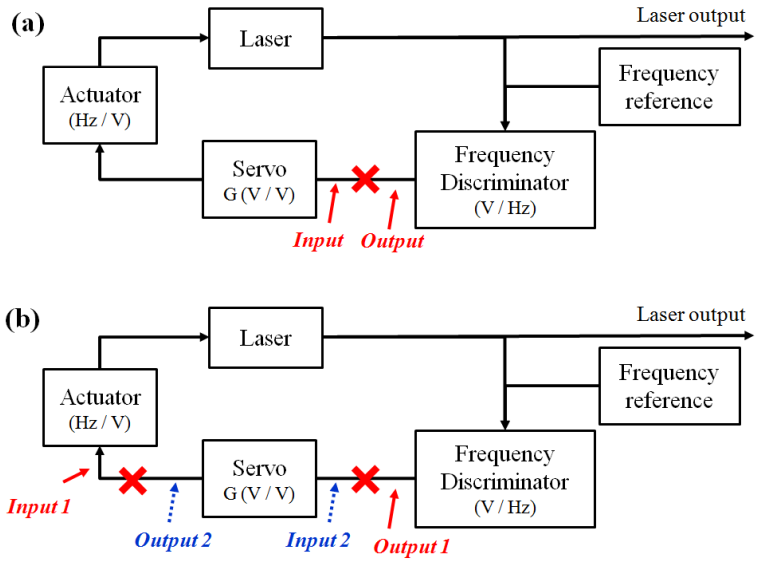

Figure 2.14: *Illustration of (a) Closed-loop gain, and (b) open-loop gain swept sine measurement. 1 and 2 are for open-loop laser and servo response, respectively.*

Open-loop gain refers to the gain for part of the feedback loop. For an optimum design of a servo circuit, we usually start off by measuring the open-loop gain of the laser response. Then, we try to match the open-loop gain of the servo circuit to the laser response. Both open-loop gains can be measured using the same swept sine method, with inputs and outputs shown in Figure 2.14 (b). Solid and dash arrows are for laser and servo response, respectively.

2.7.2 Servo Design Tutorial

We have already discussed a few terminologies in Section 1.3.3, such as transfer function, frequency response, Bode plot, closed-loop and open loop gain. If the reader is not familiar with those terms, it is suggested read Section 1.3.3 first before you start with this tutorial. This tutorial will be for a very simple servo design. More complicate design may lead to better performance in terms of stability and noise suppression, but requires more effort for the design. At the end of this tutorial, additional references are recommended for readers who are interested in more complicate servo designs.

A common class of servos are known as *PID controllers* [82], which are built based on three types of gain controls: 1) a *proportional* term, 2) *integral* term, and 3) a *derivative* term. The *proportional* term linearly amplifies the error signal, and provides immediate negative feedback to the system. For systems with pure proportional control, there is a non-zero steady state error for each unit of time. This accumulated error can get larger and larger for longer times. Higher proportional gain helps reducing this error, but turning up the gain makes the system more likely to oscillate. Therefore, an *integral* term is usually included to eliminate any residual offsets that accumulate over time, and force the error signal back to zero. The integral action is usually slow for correcting small errors because the error signal needs to be integrated for some time before the servo can tell which way to correct it. Higher integral gain will give a faster response, but again this leads to an oscillatory system. When there is sudden perturbation occurring to the system, both proportional and integral term will act and may exceed its desired steady state value. A *derivative* term is

usually used to avoid the overcorrection. The derivative action helps improve the overall closed-loop system stability but slows down the reaction as the derivative gain is increased.

In general, for laser stabilization, only a Proportional-Integral (PI) control loop is necessary, which is what we will introduce in this tutorial. For readers not familiar with the operational amplifier (or *"op amp"*) circuits, the basic building blocks we will use for a servo, Table 2.2 shows the circuit and frequency response for a few of these building blocks. The explanation of how the following circuits works can be found in any electronics books for op-amp application [83].

The first step for any servo design is to find out the *"mechanical resonances"* of the system. This can be done by measuring the open-loop gain of different parts of the system. For example, a PZT that drives the laser frequency usually has a resonance of tens of kHz. Since significant phase shift will be introduced at resonances, which could easily cause system oscillation, usually our feedback control has to occur below the system resonant frequency. For a more complicated servo design, one can do tricks such as adding lag/lead compensators [11] to compensate the phase roll-off, but this design technique would be beyond the scope of this tutorial.

Noise such as thermal fluctuations and vibrations are more predominant in the low frequency region (below 1 kHz). The system drifts greater at low frequencies (as we wait longer). Thus large gains are required at low frequencies (or on long time scales) to keep the laser frequency near the lock point. At high frequencies beyond the resonant frequency, phase shift will be introduced, which increases with frequency. The gain has to be less than one (0 dB), or *unity gain*, such that the error signal will be suppressed to avoid system oscillation. Therefore, the shape of the servo loop response will basically look like what's shown in Figure 2.15, based on a PI amplifier circuit. The slope of the gain is usually a constant (either 20 dB/decade or 40 dB/decade, depending on whether 1^{st} or 2^{nd} order filters are used). The cutoff frequency can be varied by using different combinations of resistors and capacitors. The proportional gain setting adjusts the offset for the overall gain curve.

Building Block	Circuits	Frequency Response
Inverting op-amp (linear amplifier)	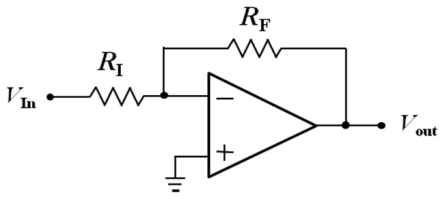	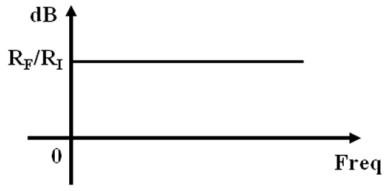
Integrator	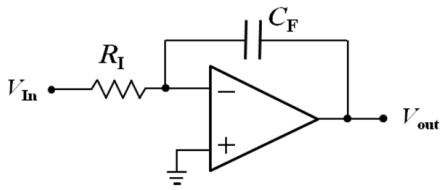	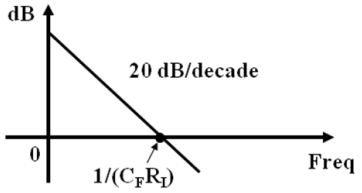
AC integrator with prop gain	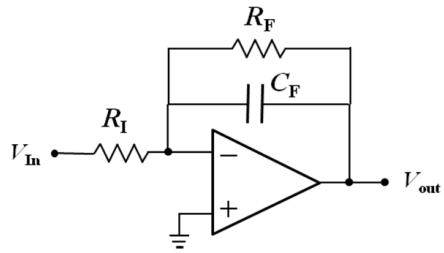	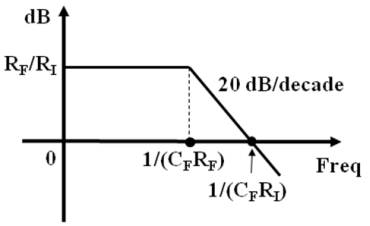
Differentiator	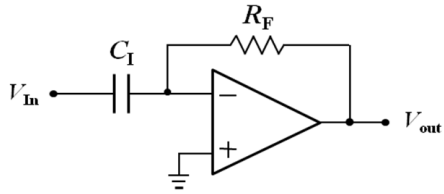	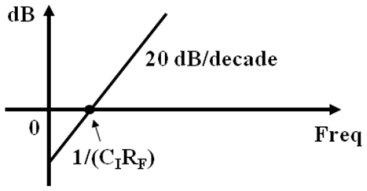
AC differentiator with prop gain	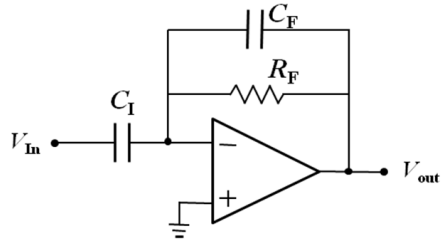	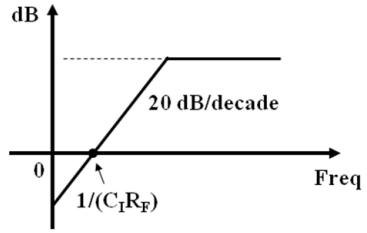
Modified AC differentiator	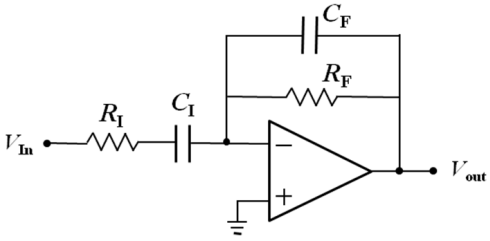	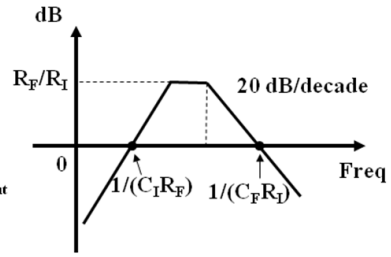

Table 2.2: *A few basic circuit blocks and their frequency response for servo design.*

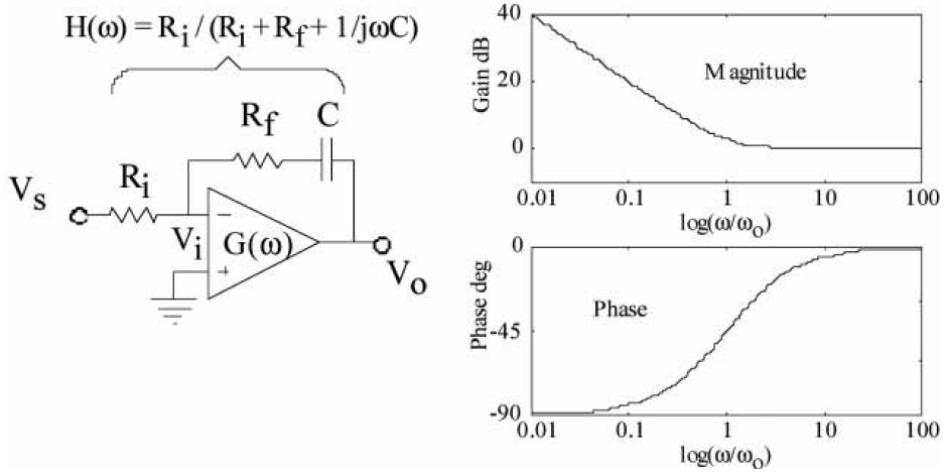

Figure 2.15: *Bode plot of a Proportional-Integral (PI) amplifier circuit [11].*

It is necessary to talk a little bit about servo feedback bandwidth, that is how fast the servo can respond to the error signal. In principle, a high feedback bandwidth is preferable, in that it allows the system to track rapidly varying changes. However, one will not benefit from too much bandwidth, because at large enough frequencies, positive feedback can turn into negative feedback.

For stability concerns, it is important to introduce two stability margins [84]. The *"phase stability margin"* is the phase lag at the unity-gain frequency. The *"gain margin"* is defined as the factor by which the gain has to be increased to have instability, at the frequency where the phase lag is 180°. A good rule of thumb is that the gain margin has to be at least a factor of 2, and phase margin at least 30°. If the gain margin is too small, the servo correction to the system responds slowly to perturbations. Similarly, if the phase margin is too small, the system will become *underdamped* to external perturbations, meaning that it overshoots the lock point and comes back. In contrast, an *overdamped* system approaches more slowly than is required to not overshoot. A *critically damped* response, which means approaching the lock point as fast as it can without overshooting, corresponds to a phase margin of 90°.

It should be clear by now that the key to a servo design is to have the right amount

of frequency-dependant gain required for a particular system. Insufficient gain could easily bring the unity-gain point to the slope portion of the gain curve and result in an unstable system. On the other hand, too much gain could push the unity-gain point to a higher frequency with insufficient phase margin, which again will make the system unstable. Section 1.4.2 in Ref. [80] gives a method to calculate the required gain at a particular frequency for a given system, based on two factors: one is the slope of the error signal in volts/Hz, while the other is the deviation of the laser frequency in Hz/volt, under a certain frequency modulation. The multiplication of the two yields a dimensionless loop gain at this particular modulation frequency.

Once we use this single gain point to scale the overall transfer function for the loop, we will have a better idea of what resistor and capacitor values to use for the servo circuit, in order to have the desired gain and the right cutoff frequency. Later modification is always necessary after we try the servo in our actual setup.

To summarize, a few key principles of a servo design are:

1) Maximum gain at low frequencies (1 kHz and below).

2) Minimize gain and phase shift at high frequencies (above the resonance frequency of the laser system).

3) To avoid system instability, the unity gain frequency needs to be below the resonance frequency, and the phase shift at the unity gain point has to be 90° *or below. Another way to look at it is, the phase margin needs to be at least* 30°*, and the gain margin has to be at least a factor of two. A rule-of- thumb is that at the unity-gain point, the slop of the loop transfer function may not be decreasing by much more than 20 dB/decade of frequency [80].*

For readers interested in knowing more about servos beyond this tutorial, a few references are suggested here. For basic concepts of feedback control, most text books and literatures introduce well-developed but complicate control theory that are suitable for engineering students. Text books such as Ref. [81, 85, 86] are good but need a lot of effort to understand. Ref. [84] written by John Bechlhefer is a good tutorial essay that describes feedback control more from a physicist's point of view. Ref. [11] gives an overview of current laser stabilization methods. Section 27.2 talks specifically about servo design principles, and gives an example of a PID controller design. For a more practical example of servo design for laser stabilization, Ref. [80] discusses the details of how to stabilize a diode laser to an optical cavity, a more complicated servo circuit design is presented in Section 1.4.3.

2.7.3 Home-made servo: Single-channel feedback

Figure 2.16 shows the circuit diagram of a home-made servo box with a single output. This type of servo design is used in our experiment for (1) filtering cavity locking, and (2) single tooth locking to an acetylene transition. It is a relatively simple servo based on a proportional-integral (PI) control, where the gain drops 20 dB per decade (due to the integrator) for low frequencies and is constant (or proportional) for high frequencies.

The circuit consists of a few components. First, the *inverter* chooses the right polarity of the error signal through switch 1 (SW1). Second, the *input offset* fine adjusts the error signal to be centered at zero volts by tuning the potentiometer R10, which is followed by a summing circuit (U2). The output of the sum is split into two parts: one output is the *error monitor*, which is basically the input error signal plus an offset voltage. The other part goes to the amplification stage, firstly by an *integrator* (U3), then a *proportional gain* control (U4). The cutoff frequency of the servo is determined by the RC constant of this integrator R16 and C9. With SW3 closed, it is AC integrator with constant DC gain (Table 2.2), which is the so-called *lock off* situation. With SW3 open, it becomes a pure integrator. The flat DC gain becomes a sloped line. A high DC gain is enabled, corresponding to the *lock on*

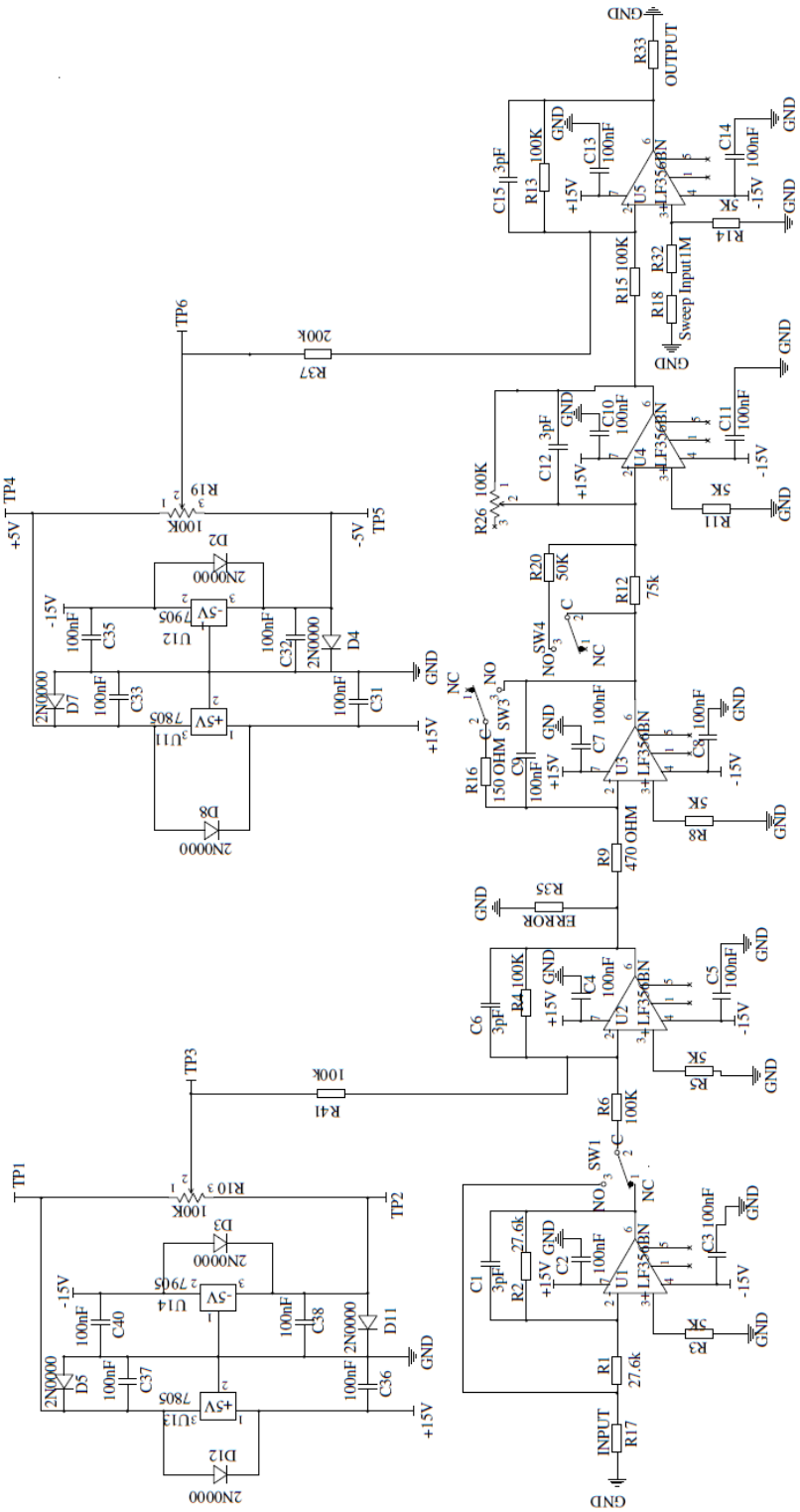

Figure 2.16: *Servo circuit diagram based on Proportional-Integral (PI) control.*

case. SW4 selects either "high" or "low" setting for the following proportional gain. With SW4 open, the proportional gain is on "low", with the gain being the ratio between R26 and R20. Similarly, with SW4 closed, R12 and R20 are in parallel, the proportional gain is on "high", with the gain being the ratio between R26 and the total resistance for parallel resistors R20 and R12. The proportional gain can be fine controlled by potentiometer R26. The final part is another summing circuit that adds an *output offset* within +/- 15 volts to the amplified signal, as the servo output. The *sweep* function takes an external scan voltage, and sweeps the servo output over the locking point. This is used when one wants to optimize the error signal.

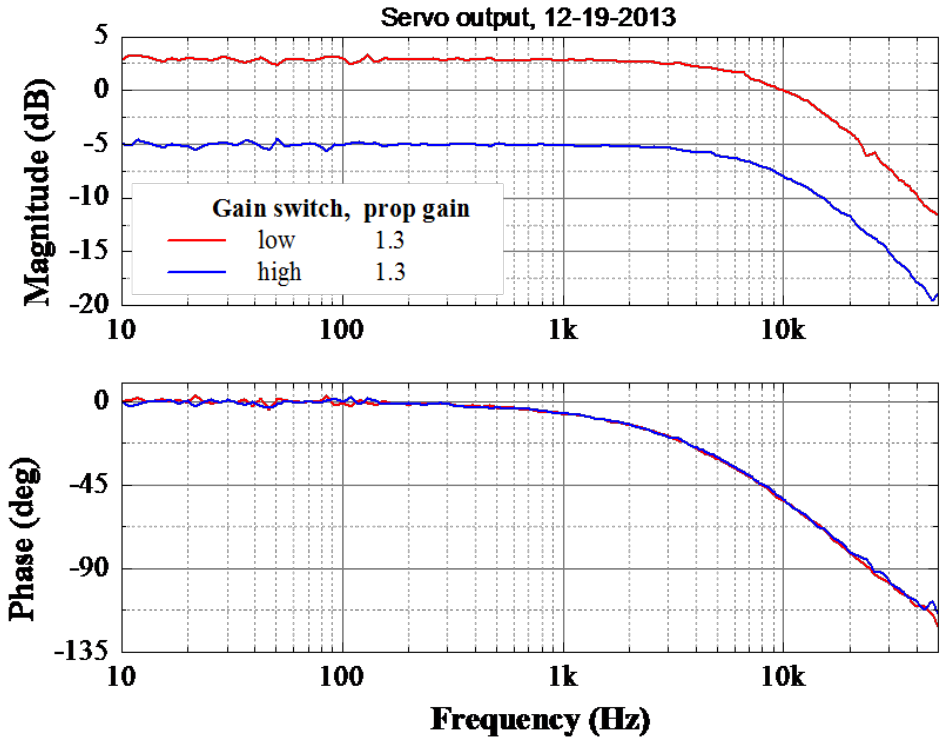

Figure 2.17: *Bode plot of a servo based on Proportional-Integral (PI) control.*

The Bode plot of the circuit in the *lock off* situation is shown in Figure 2.17. It has a low frequency gain limit of 3 dB, and cutoff frequency of about 9 kHz. The unity gain point is at 10 kHz, which is the resonance frequency of the filtering cavity in the feedback loop.

The *lock on* Bode plot is not able to be measured using the FFT spectrum analyzer in our lab because the DC gain is too high. However, it can be estimated from the slope that the gain should be around 80 dB at 1 Hz.

2.7.4 Home-made servo: Two-channel Feedback

In some cases, a servo circuit can be designed to have two outputs: a slow output compensates the slow variations of the system, while a fast output allows rapid corrections to suppress the fast noise of the system. An example of this is the stabilization of a diode laser. The slow channel goes to the PZT, and the fast channel goes to the laser's injection current. The advantage of this configuration is that we can have large gain to the PZT at low frequencies, while keeping the laser current nearly constant, which is necessary because large gain at low frequencies will cause large current changes, which will result in laser mode-hopping and can easily make the laser jump out of lock. Figure 2.18 is the circuit diagram of such a servo for Santec diode laser (model number: TSL-210) stabilization.

The slow feedback has the same structure as the previous servo design (Figure 2.15), with a few resistors and capacitors having different values. Here, an extra portion is split from the output of the first summing circuit (U2), which serves as the input of the fast feedback servo (third line of the circuit diagram). The capacitor C25 effectively filters out the DC signal, leaving only the AC signal going to the following PI amplification stage, which is essentially the same as the slow feedback design. It goes through in a sequence of: integrator (U8), inverter (SW2), and proportional gain control (U7). Potentiometer R27 varies the proportional gain. Diodes 9 and 10 are used to limit the output voltage within +/- 3 volts from the fast servo, due to the current limitation of the diode laser design.

Figure 2.19 shows the Bode plots of both the slow and fast feedback, with lock off in both cases. The slow channel has a cutoff frequency of about 18 Hz at unity gain, which is slightly below the PZT resonance frequency ($\sim$ 20 Hz). When the lock is on, the DC gain is estimated to be about 30 dB at 1 Hz based on the slope (not shown in the plot). The fast

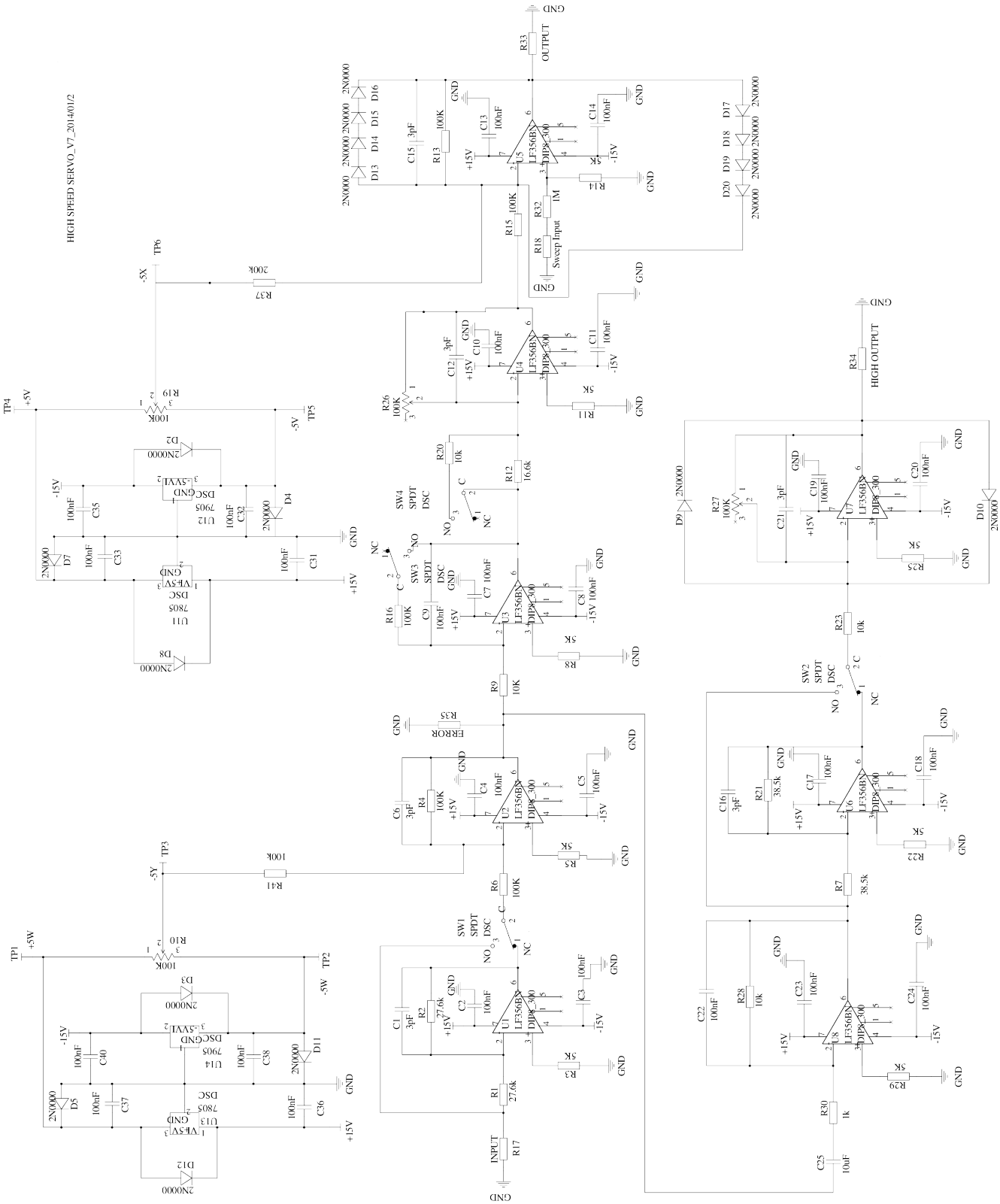

Figure 2.18: *Servo circuit diagram with both slow and fast feedback control.*

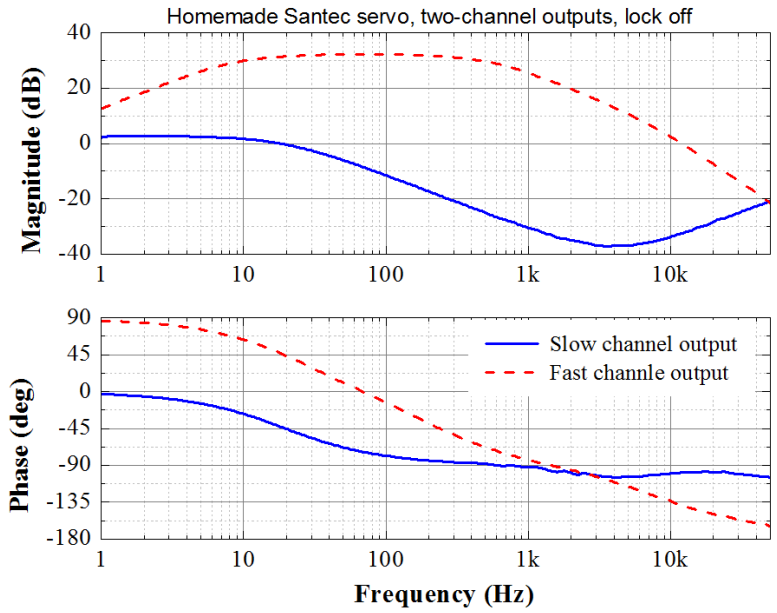

Figure 2.19: *Bode plot of a servo with both slow and fast feedback control.*

channel has a 3-dB turn-on frequency of about 10 Hz, turn-off frequency at 556 Hz, and a maximum gain of 30 dB at around 100 Hz.

2.7.5 The Commercial Servo

Another commercial servo box LB1005 from Newport [12] used in our experiment is also based on PI control. It has a high bandwidth of 10 MHz, and adjustable knobs that allow one to shape the gain curve in two aspects: (1) the 3-dB frequency beyond which proportional gain dominates over integral gain, named the *PI corner frequency*, and (2) the gain limit for low frequencies, as measured from the proportional gain value, named *low frequency gain limit*. Both terms are labeled in the gain curve plot shown in Figure 2.20.

A practical problem with this servo is the gain-dependent offset. As one changes the proportional gain, the error signal is offset slightly from zero volts. The amount of offset varies for different proportional gain settings, from a few mV to over a hundred mV. This offset can be corrected by fine adjusting the input offset of the servo, as one locks the system

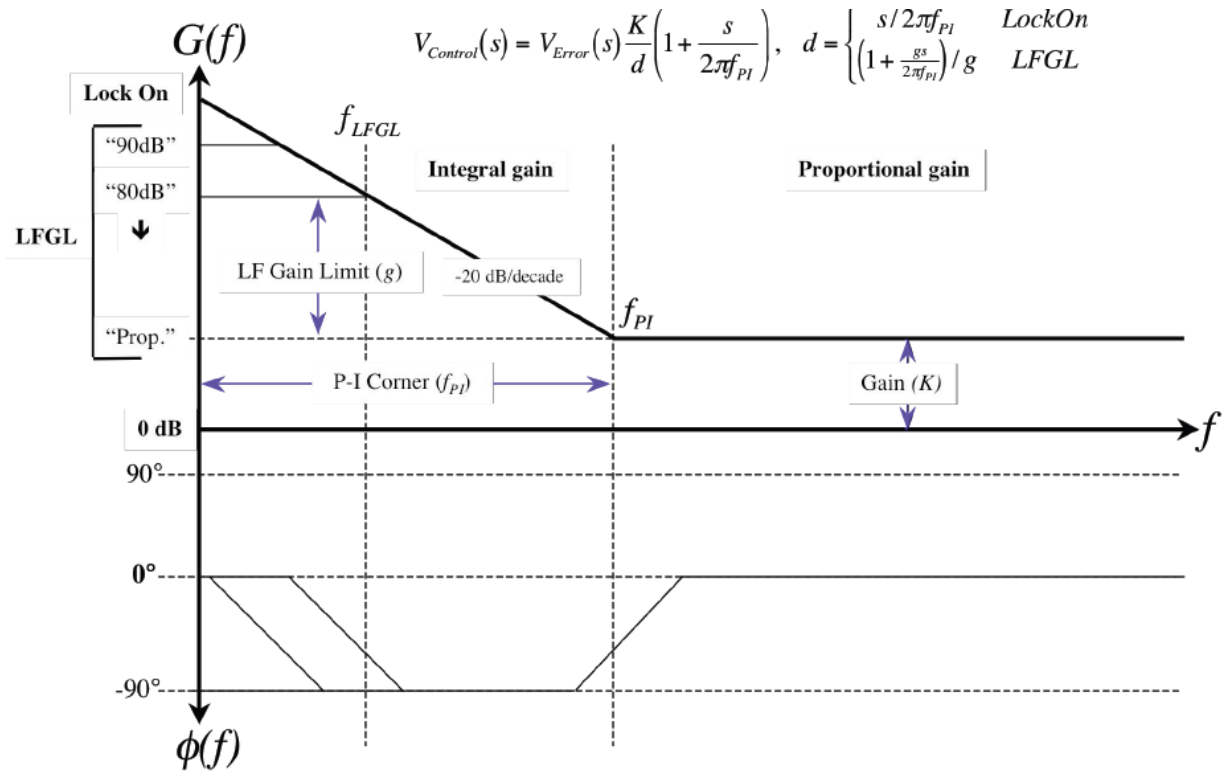

Figure 2.20: *Bode plot of LB1005 servo controller from Newport [12].*

initially.

2.7.6 Locking Results

The CW fiber laser can be locked to the P(13) transition of acetylene at 1532.8 nm using the commercial Newport servo controller. Figure 2.21 (a) shows saturated absorption (SAS) signal (yellow) as well as the sub-Doppler error signal (blue) as we scan the CW laser's frequency over the target transition by scanning the PZT voltage of the laser. An indication of the lock point is when the oscillation amplitude of the SAS signal is maximized due to amplitude modulation, as shown in Figure 2.21 (b). When the laser is locked, the error signal is centered at zero with a minimized noise of about 5 mV using a 60 kHz low pass filter before the servo, corresponding to a fractional stability of 2.2×10^{-12} $Hz^{-1/2}$ by comparing to the slope of the sub-Doppler error signal (22 MHz/V) within 60 kHz bandwidth.

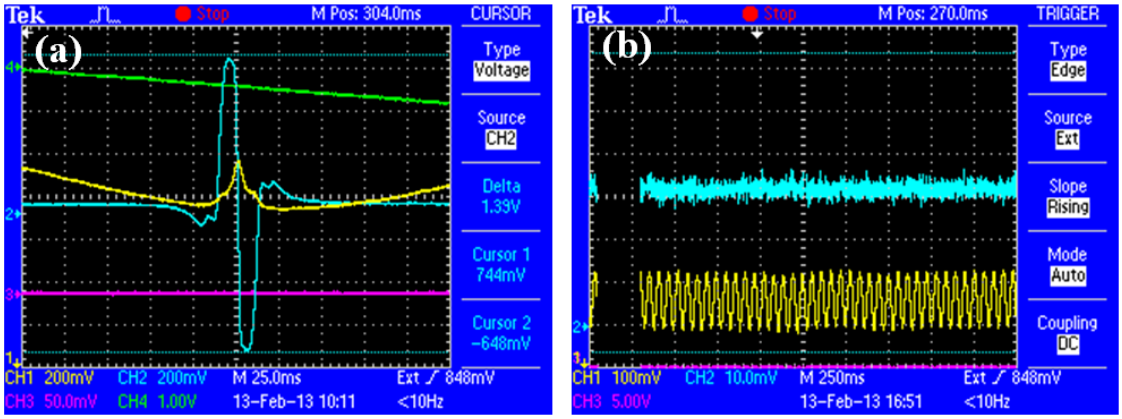

Figure 2.21: *Time domain sub-Doppler error signal (blue curve) when the CW fiber laser source is (a) scanned over, and (b) locked to the P(13) transition of acetylene at 1532.8 nm. Yellow curves represents the saturated absorption (SAS) signal in Figure 2.11. An indication of the lock point is when the oscillation amplitude of the SAS signal is maximized due to amplitude modulation.*

Chapter 3

GHz Repetition Rate Comb Generation

The typical repetition rate for a fiber laser is about 100 MHz (or below). The spectral resolution of current commercial grating spectrometers or filters are usually at least tens of GHz. Therefore, it is difficult to resolve individual comb teeth directly from the fiber laser oscillator. In this chapter, I will present how we generate a GHz repetition rate comb by implementing an external Fabry-Perot filtering cavity to the sub-100 MHz fiber laser. In combination with a narrow bandwidth fiber Bragg grating, single comb tooth isolation can be realized. Section 3.1 reviews a few methods for GHz comb generation. Section 3.2 presents a 89 MHz erbium-doped fiber ring oscillator. Section 3.3 introduces guidelines for an external filtering Fabry-Perot cavity design. Section 3.4 represents experimental implementation of two filtering cavities.

3.1 Review Methods for GHz Comb Generation

A high repetition laser requires a short cavity length. For a GHz laser, the cavity length is only a few centimeters. While this is less challenging for a free space solid-state laser,

i.e. a Ti: Sapphire laser. It is difficult to realize in a fiber-based laser system. One reason is the minimum fiber length needed for splicing the laser cavity components. Hence, free space sections are often integrated into such short cavities. In addition, a high gain fiber and a high finesse (low loss) cavity are also required for a short cavity. A few groups have built such lasers with repetition rates ranging from 1-10 GHz [87–89] using either SESAM or carbon nanotubes for mode-locking. However, besides the integrated free space section which makes the laser less portable and vulnerable to environmental perturbations, these designs share the same drawbacks of low output power of a few mW and narrow spectral bandwidth of less than 5 nm, and some are even below 1 nm [89].

GHz fiber lasers are difficult to phase stabilize. This is because a high repetition rate in the frequency domain means more pulses in the time domain. The resultant low pulse energy is not sufficient to generate an octave-spanning spectrum (supercontinumm, or SC) required for carrier-envelope offset frequency stabilization. In 2012, Ippen's group for the first time successfully phase stabilized a GHz fiber laser with 7 nm bandwdith [90]. Their system also has free space optics in the laser cavity. A special customized highly-nonlinear fiber (HNLF) is used to generate SC.

One way to generate a GHz fiber laser comb is to utilize repetition rate multiplication by implementing an external Fabry-Perot filtering cavity to an existing low rep rate fiber comb. High repetition rate, broad bandwidth fiber combs are generated in this way for astronomical calibration purposes [91, 92]. To compensate the power loss during the filtering process, optical amplification of the comb becomes necessary. The challenge of this method is to amplify the comb optical power without degrading the signal-to-noise ratio while maintaining a high side mode suppression [93, 94]. We were able to use this method to isolate a single tooth for direct comb spectroscopy.

Another type of GHz fiber laser oscillator is based on harmonic mode-locking [95, 96]. Because the mode-locking is achieved by actively locking a MHz ring laser to a Fabry-Perot etalon with a stabilized cavity free spectral range of a few GHz, the laser repetition rate is

not limited to the cavity length. Locking electronics are required to synchronize the fiber laser cavities to the integrated Fabry-Perot etalon, thus adding system complexity. Another drawback lies in the difficulty for the carrier-envelope offset frequency stabilization. Because the comb teeth are referenced to the etalon transmission modes, the absolute positions for the comb teeth are unknown and the carrier-envelope offset frequency cannot be tuned to an arbitrary value.

There are also parametric techniques that use microresonators to generate combs with large spacing, typically at least tens to hundreds of GHz [97]. Although octave-spanning spectra have been generated from these microresonator combs, large noise in the f_0 and f_{rep} beatnote still hinders the comb stabilization.

3.2 Low Rep Rate Fiber Frequency Comb

3.2.1 The Mode-locked Erbium Fiber Laser

The schematic setup for the NPR fiber laser oscillator developed in our lab is illustrated in Figure 3.1 (a). The name of the NPR laser comes from its modelocking mechanism, which is the *nonlinear-polarization rotation* (NPR) technique. When a linearly polarized intense pulse propagates in an optical fiber, the polarization state changes into elliptical and experiences rotation by a intensity-dependent angle. This is partly caused by the birefringence in the fiber, but for intense pulses, it is also due to the nonlinear effects such as self-phase and cross-phase modulation. By placing a polarizer afterwards, the power throughput of the system is intensity dependent. A single polarization is selected by the intracavity polarization-sensitive isolator and the polarization controllers on each side of the isolator such that the maximum transmission (minimum loss) of the system occurs for the highest possible optical intensity. A piece of 64 cm long erbium-doped fiber (Liekki Er110) is forward-pumped by a 300 mW diode at 980 nm. A hybrid wavelength division multiplexer, or WDM (HYBW-98-2-1-B-1-0 by AFW Fiber Optics) is used in this ring configuration,

which includes a 980/1550 nm WDM, single-stage isolator and a 90/10 output coupler. The WDM combines the pump and signal at different wavelengths. All fiber components in the oscillator are fusion spliced, except the phase shifter, which has FC/APC connectors on both ends. The phase shifter serves as a PZT stretcher, allowing feedback control for the cavity length. Figure 3.1 (b) shows the actual laser in a Styrofoam box in our lab.

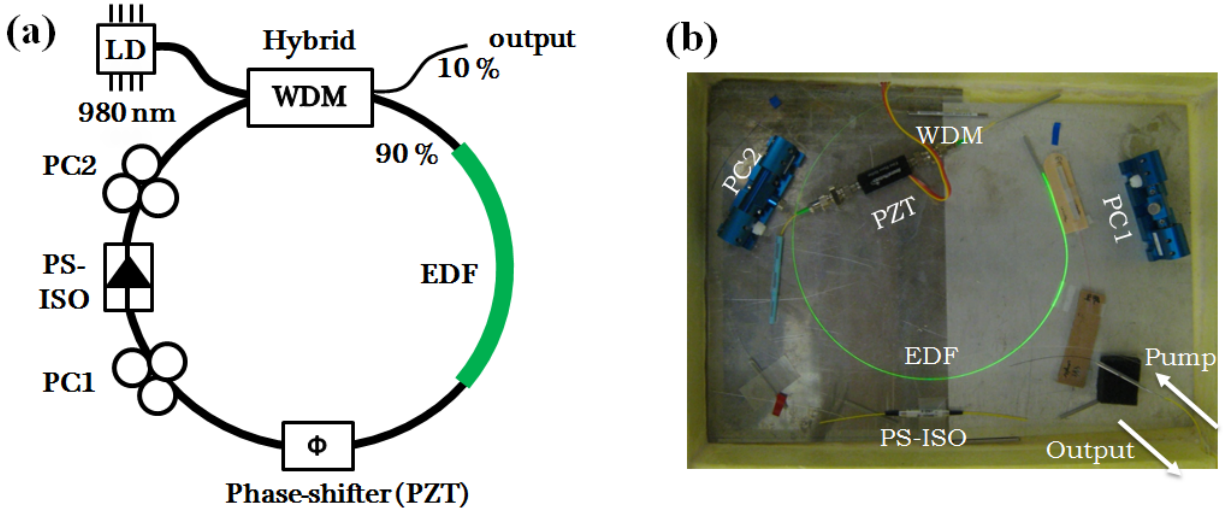

Figure 3.1: *(a) Schematic diagram of the all-fiber NPR laser oscillator. (b) NPR laser oscillator in the lab.*

There are two types of fibers in the oscillator: the erbium-doped fiber (EDF) and the standard single mode fiber (SMF), with opposite dispersion signs. There are two modelock regimes: *soliton regime* and *streched-pulse regime*, roughly classified according to the net cavity dispersion of the laser cavity. Figure 3.2 shows the lasing transition from one regime to the other, as we cut back the SMF in the laser cavity. The net cavity dispersion increases from a negative value to a less negative value closer to zero. If the net cavity dispersion is slightly negative, the laser tends to lase in the solitonic regime, resulting in spectra that exhibit the typical feature of *Kelly sidebands*, shown in Figure 3.2 (a)-(d). The origin of the Kelly sidebands is as follows: in a ring fiber laser, a solitonic pulse experiences periodic perturbation as it travels a complete cavity round trip each time. A perturbed soliton tends

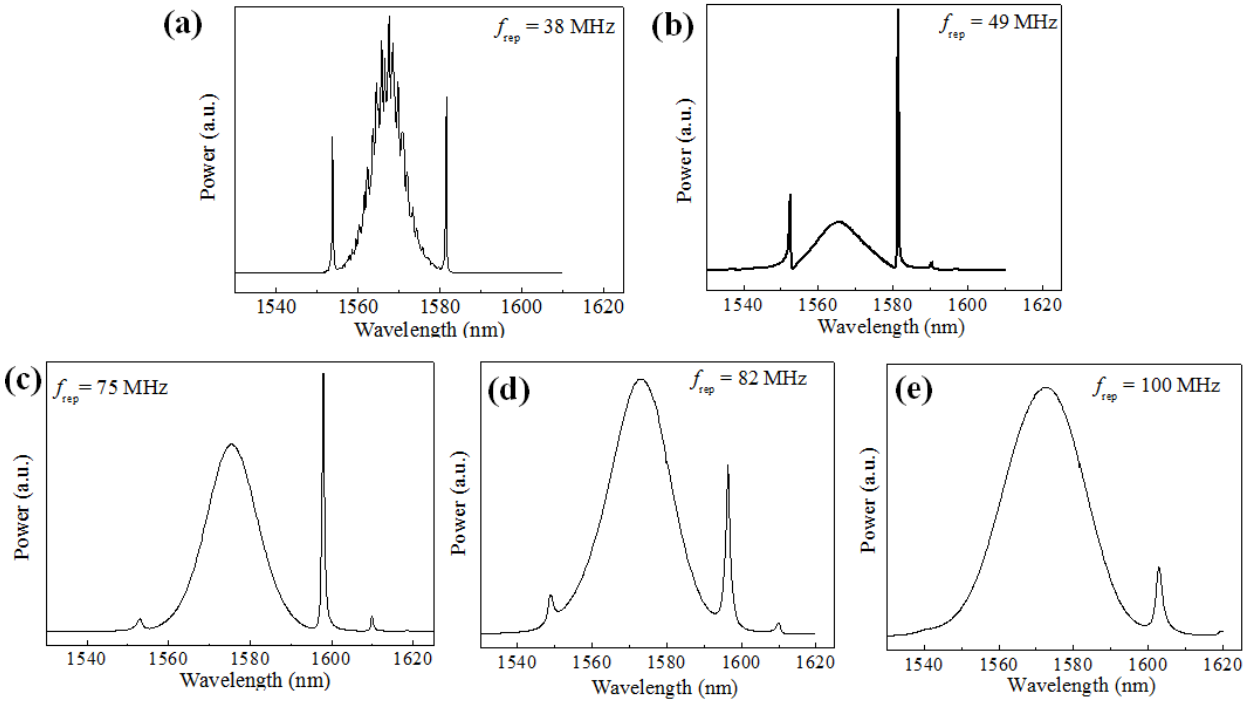

Figure 3.2: *The modelock spectrum of the NPR fiber laser as we cut back SMF length to increase repetition rate.*

to shed dispersive waves in order to readjust itself into a new soliton. These dispersive waves are phase matched at certain wavelengths and accumulate as sharp spectral sidebands. As the net cavity dispersion increases from negative toward zero, the laser tends to lase during the stretched-pulse regime, as shown in Figure 3.2 (e).

In the stretched-pulse regime, the Kelly-sidebands disappear and spectral bandwidth increases. It is noticeable that the 3 dB spectral bandwidth increases from 10 nm to almost 30 nm from (a)-(e). However, the laser is more difficult to mode-lock in the streched-pulse regime. Therefore, the final length of SMF is optimized to give a repetition rate of 89.9 MHz, resulting in an estimated net cavity dispersion of -0.030 ps^2. Figure 3.3 shows the pump diode calibration curve and the final laser output spectrum. The spectrum is centered at 1562 nm with 30 nm bandwidth, with a total output power of 3.8 mW.

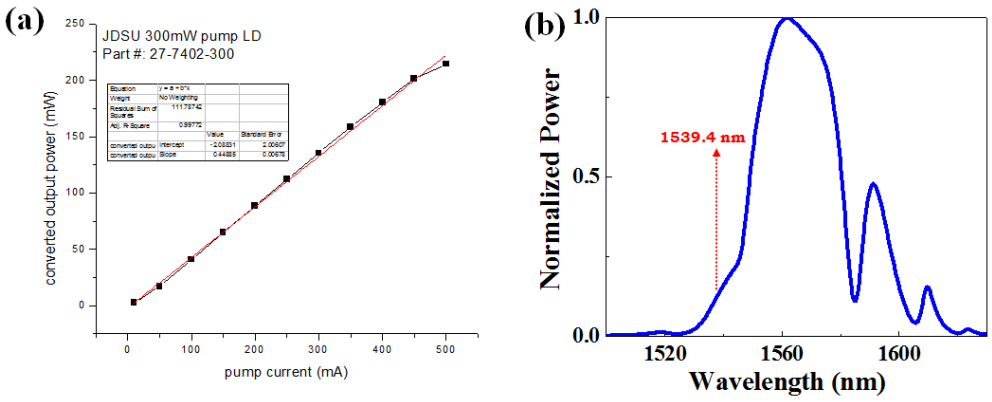

Figure 3.3: *(a) Pump diode output power as a function of pump current. (b) NPR laser oscillator typical output spectrum.*

3.2.2 f_0 Stabilization of Mode-locked Fiber Laser

Phase stabilization of a frequency comb requires the stabilization of two comb parameters: the carrier-envelope offset frequency f_0 and repetition rate frequency f_{rep}. For conventional RF referenced combs, both two parameters are locked to RF references. In this work, f_{rep} is stabilized by locking a single optical comb tooth, while f_0 is locked to an RF reference. Now we will be mainly focused on the f_0 detection and stabilization. Single tooth stabilization will be discussed in Chapter 4.

A common method to generate f_0 is the self-referencing technique, as discussed in Section 1.2.1. Figure 3.4 shows the experimental setup for self-referenced f_0 generation. It contains four stages: (1) laser power amplification in an erbium-doped fiber amplifier (EDFA), (2) pulse compression to increase the pulse peak power, (3) supercontinuum (SC) generation inside highly-nonlinear fiber (HNLF), and (4)a collinear f-2f interferometer for f_0 generation using the self-referencing technique. All these four stages were initially designed and optimized by our previous group member Jinkang Lim for another carbon nanotube laser in our lab, which degraded after years of use. For my work, I replaced the degraded laser by the newly-built NPR laser. Since the pulse duration and peak power from the oscillator were changed, I had to make a few changes in later stages for an optimized f_0 beatnote. My main

efforts were re-optimizing: (1) the EDFA pump currents, (2) the SC spectrum by optimizing the oscillator spectrum and polarization states during the power amplification and spectral broadening process, (3) the temporal delay for the f-2f interferometer to achieve a f_0 beanote signal, and (4) the optical alignment of the f-2f interferometer.

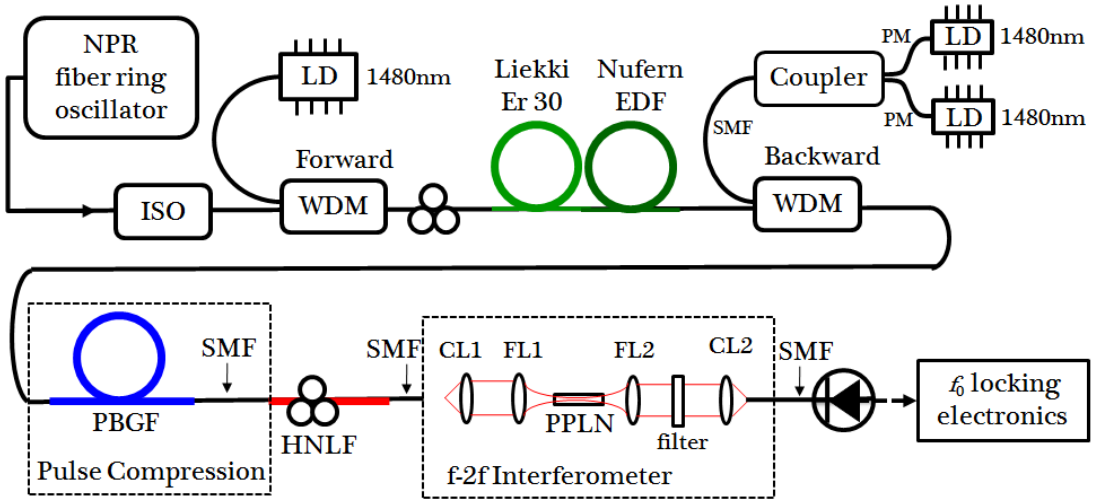

Figure 3.4: *Schematic setup for f_0 generation.*

Here, I will only briefly introduce some of the details for each of the four stages based on Jinkang's previous work [51]. For laser power amplification, the 10.5 m of EDF is composed of 4.7 meter Liekki Er 30 and 5.8 meter Nufern EDF. An inline dual stage isolator (ISO) is used to avoid any reflection from the interface between the laser oscillator and the amplifier. The amplified pulses are later compressed using a 2.9 meter hollow-core photonic bandgap fiber (PBGF), made by J. C. Knight's group at the University of Bath, UK. It has the GVD of -2.55 $\times$ 10^{-5} fs^2/nm at 1550 nm. Since direct splicing of PBGF to the following HNLF causes high loss of more than 6 dB, a short piece (14 cm) of SMF is used as the bridge fiber to reduce the splice loss. The SC was generated from 1.0 μm to 2.2 μm with a 40 cm length of OFS HNLF, shown in Figure 3.5 (a).

For second harmonic generation (SHG), a periodically poled lithium niobate ($LiNbO_3$, or PPLN) crystal (by Stratophase) is used to double the frequency at 2060 nm. The name

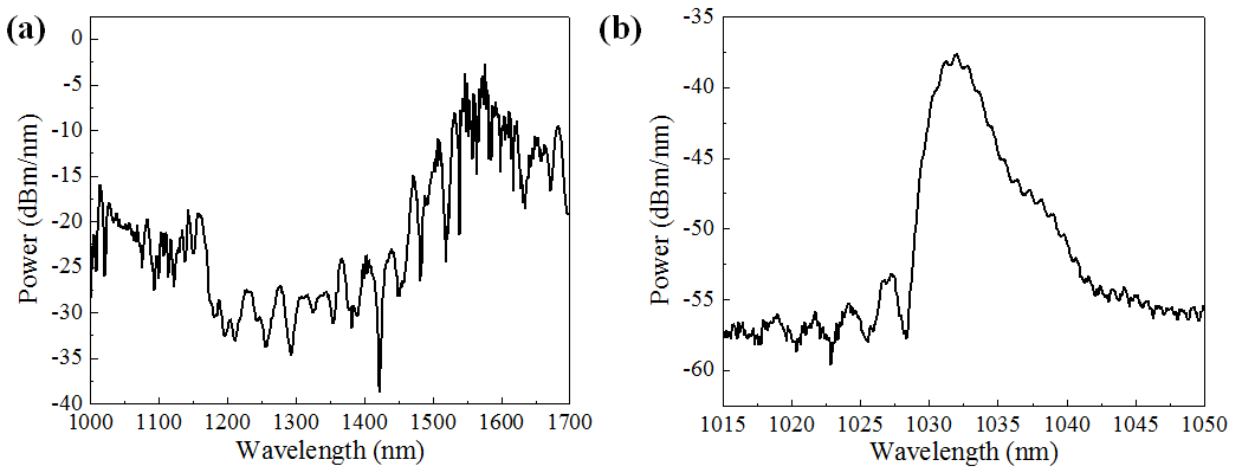

Figure 3.5: *(a) Supercontinuum generation from the NPR fiber laser. (b) Second harmonic generation from the collinear f-2f interferometer setup for 2060 nm.*

"periodically poled" refers to the fact that the orientation of the crystal is engineered to be periodically inverted, or poled, for a maximum conversion efficiency. The inverted portions generate photons that are 180° out of phase compared with the photons that would have been created if the crystal had not been poled. By choosing the correct periodicity, the newly generated photons will always interfere constructively with previously generated photons as light travels down the crystal, resulting in a high conversion efficiency of generating frequency-doubled photons. The PPLN crystal used in our setup has a physical dimension of 10 mm × 10 mm × 0.5 mm, with seven poling periods from 29.5 to 32.5 μm in steps of 0.5 μm for different phase matching purposes. A few aspheric lenses are used to focus a free space Gaussian beam into the crystal for SHG, illustrated in Figure 3.4. CL1 is a collimating lens to collimate diverging light out from a SMF to free space. FL1 focuses the beam to the center of the PPLN crystal. FL2 and CL2 collimate the diverging beam from the crystal and focus it back into a SMF as the output. The focal length of these lenses are chosen based on the compromise between two preferences: a tight focus (or a small beam waist) inside the crystal is preferred to achieve a high conversion efficiency because high pulse intensity facilitates the nonlinear effects. But if the beam waist is too small, yielding

a Rayleigh range shorter than the crystal length, part of the beam will be cut by the crystal since the beam diverges too fast. The resulting beam waist is measured to be $\sim$ 10 μm inside the crystal, yielding a maximum SHG peak power of -38 dBm/nm obtained in a SMF (with a 1030 nm optical bandpass filter before the SMF), as shown in Figure 3.5 (b). The poling period we used was 32.0 μm under a crystal temperature of 110°C.

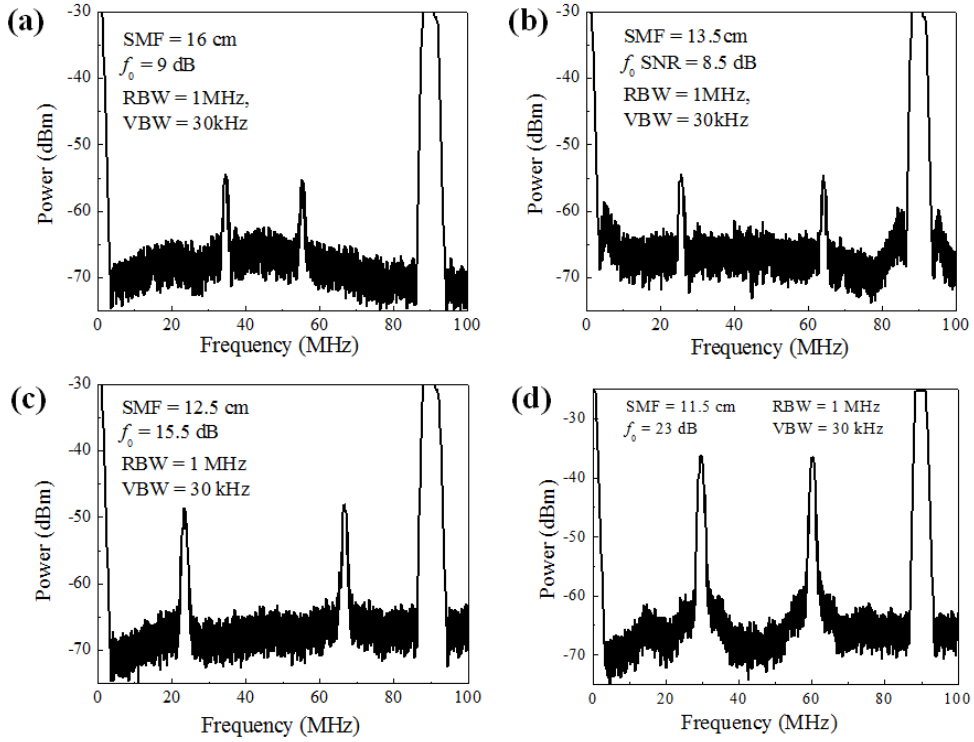

Figure 3.6: *(a)-(d): Optimization of temporal delay by cutting back SMF after HNLF for f_0 beanote generation. f_0 SNR from 9 dB to 23 dB observed on the RF spectrum analyzer.*

In order to have beanote occur between 1030 nm (f_{2n}, namely the "fundamental component") and the second harmonic of 2060 nm (f_n, namely the "second harmonic component"), we need both components to arrive at the photodetector at the same time. In other words, we need to compensate the temporal delay between the two components caused by fiber dispersion. For our collinear setup, this has been done by adding a short piece of SMF right after the HNLF. The length of the SMF is optimized by maximizing the SNR of the f_0 beatnote. Figure 3.6 shows the RF spectrum of the f_0 beatnote generated. The signal at 90

MHz is the repetition rate signature. A pair of f_0 beatnotes (one at f_0, the other at f_{rep} - f_0) are observed in Figure 3.6 (a)-(d), with an increasing SNR as we cut back the SMF length. When the SMF length is 11.5 cm, the optimized f_0 has a SNR of 23 dB with 1 MHz RBW and peak power of -37 dBm.

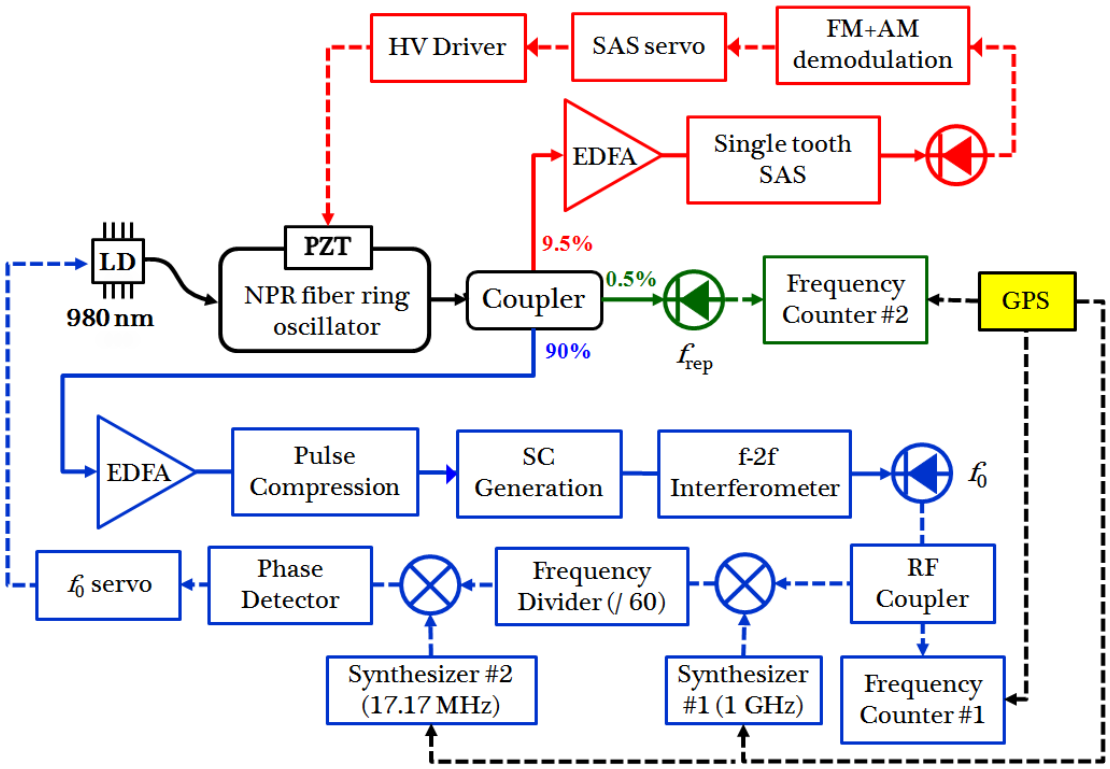

Figure 3.7: *Overview schematic setup for NPR comb stabilization, including both f_0 and single comb tooth stabilization.*

Figure 3.7 shows the overview phase stabilization of the NPR comb. A total output of 3.8 mW from the NPR oscillator is split into three portions: (1) the majority (90%) of light goes for f_0 generation, which is stabilized to an RF reference as we will discuss shortly, (2) a small portion (9.5%) of the output is optically amplified for single comb tooth saturated absorption spectroscopy (SAS), discussed in detail in Chapter 4, and (3) the last portion (0.5%) is for repetition rate monitoring.

For f_0 stabilization, the f_0 signal from the f-2f interferometer is first mixed with a 1 GHz

reference signal and bandpass filtered at the difference frequency of 1030 MHz for an f_0 locked to 30 MHz. This signal is then frequency divided by 60 to improve the servo capture range,

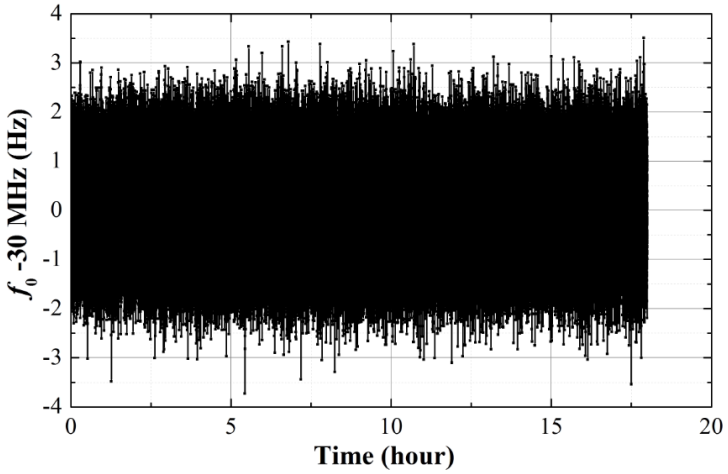

Figure 3.8: *Plot of f_0 stability measurement at 100 ms gate time.*

and compared with a second reference signal at 17.17 MHz in a phase-sensitive detector. The resulting error signal is DC-coupled into a servo filter (LB1005 by Newport), which drives the pump current to control the pump power of the fiber oscillator. All synthesizers used in the setup are externally referenced to our GPS-disciplined Rb oscillator. This approach allows f_0 to be independently stabilized to a level of a few Hz at 30 MHz for over ten hours with 100 ms gate time, as shown in Figure 3.8.

3.3 Fabry-Perot Filtering Cavity Design

3.3.1 The Ideal Fabry Perot Cavity

A basic Fabry-Perot (FP) cavity consists of two reflective mirrors separated by a distance L with light incident from the left, as shown in Figure 3.9. The reflectors can be curved or flat, giving different stability characteristics, which I will talk about in Section 3.3. For now, we just look at a simple model with two flat mirrors.

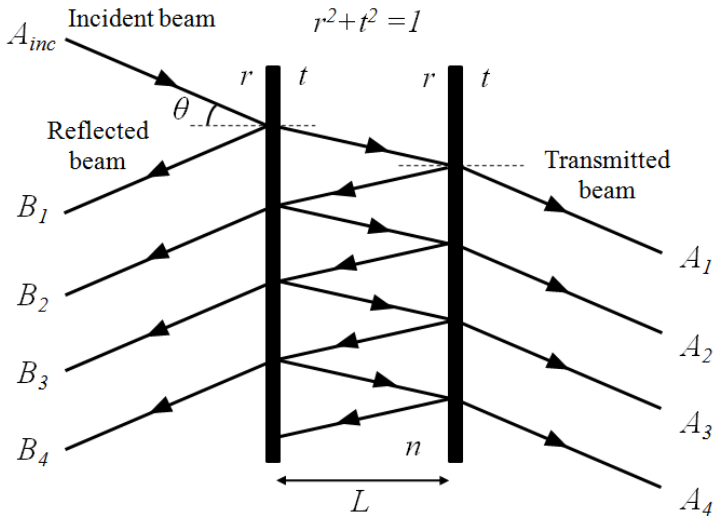

Figure 3.9: *Schematic diagram of a Fabry-Perot as a multiple beam interferometer.*

The cavity is approximated as a pair of identical ideal flat mirrors, each with amplitude reflectivity coefficient r and transmission coefficient t, where $r^2 + t^2 = 1$. The amplitude of the incident electric field can be approximated by a perfect plane wave.

$$A_{inc} = A_0 e^{i\omega t} \tag{3.1}$$

If we denote the reflected amplitude from the first mirror by B_i, and the partially transmitted amplitude from the second interface by A_i, the amplitudes of each of the transmitted waves can thus written as:

$$A_1 = TA_{inc} = t^2 A_0 e^{i\omega t} \tag{3.2}$$

$$A_2 = r^2 A_1 e^{-i\delta} = r^2 t^2 A_0 e^{i(\omega t - \delta)} \tag{3.3}$$

$$A_3 = r^2 A_2 e^{-i\delta} = r^4 t^2 A_0 e^{i(\omega t - 2\delta)} \tag{3.4}$$

... ...

$$A_n = r^{2(n-1)} t^2 A_0 e^{i(\omega t - (n-1)\delta)} \tag{3.5}$$

where δ is the optical phase acquired by the light on one round trip due to the different path lengths, which is given by

$$\delta = 4\pi nL\cos\theta/\lambda \tag{3.6}$$

where n is the index of refraction, θ is the incident angle, and λ is the wavelength of the laser. Therefore, the sum of all transmitted wave amplitudes, A_t, can be calculated as:

$$A_t = A_0 e^{i\omega t}\left(\frac{t^2}{1-r^2e^{i\delta}}\right) \tag{3.7}$$

The fractional output intensity, or power transmission, from the FP cavity is given by:

$$\frac{I_t}{I_{\text{inc}}} = \frac{A_t(A_t)^*}{A_{\text{inc}}(A_{\text{inc}})^*} = \frac{(1-r^2)^2}{(1-r^2)^2 + 4r^2\sin^2(\delta/2)} \tag{3.8}$$

Sometimes, the power transmission ratio is written as

$$\frac{I_t}{I_{inc}} = \frac{1}{1+F\sin(\delta/2)} \tag{3.9}$$

where F is known as the coefficient of finesse, and is given by

$$F = \left(\frac{2r}{1-r^2}\right)^2 = \frac{4R}{(1-R)^2}, \;\; with\, R = r^2 \tag{3.10}$$

R is introduced as the power transmission of the mirror. Eqn 3.9 is known as the *Airy function*. We can see that maximum transmission occurs when

$$\delta = \frac{4\pi nL\cos\theta}{\lambda_m} = 2m\pi, \;\; \text{where}\, m = \text{any integer}. \tag{3.11}$$

A more useful expression for the locations of maximum transmission is given in terms of frequency

$$\nu_m = m\frac{c}{2nL\cos\theta}, \;\; \text{where}\, m = \text{any integer}. \tag{3.12}$$

We can notice that the frequency separation between successive peaks is a constant value for a given FP cavity and incident beam, known as the *free spectral range* (FSR) of the FP cavity:

$$\text{FSR} = \nu_{m+1} - \nu_m = \frac{c}{2nL\cos\theta}, \quad \text{where}\, m = \text{any integer}. \tag{3.13}$$

The ratio I_t/I_i is plotted as a function of FSR in Figure 3.10 for mirror pairs with different

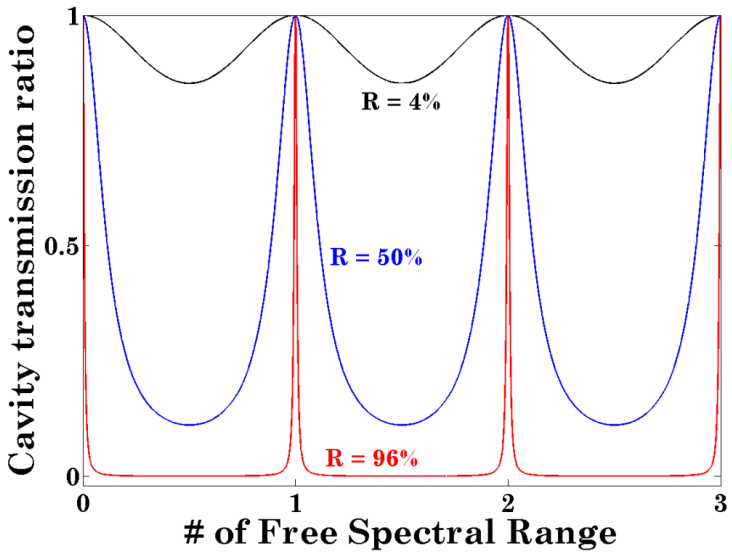

Figure 3.10: *Fabry-Perot cavity transmission ratio as a function of cavity free spectral range. Plotted for mirror reflectivity R = 4 %, 50 % and 96 %.*

power reflectivity R. As R increases, the transmission window becomes narrower. A common feature to characterize the shape of the cavity transmission is called *Finesse* $\mathcal{F}$, which is defined as

$$\mathcal{F} = \frac{\pi\sqrt{R}}{1-R} \tag{3.14}$$

However, a more useful expression for the finesse is written in terms of the cavity resonance linewidth ($\Delta\nu$) and the cavity FSR

$$\mathcal{F} = \frac{FSR}{\Delta\nu} \tag{3.15}$$

A similar quantity to describe the quality of a cavity is called the quality factor, or

Q-factor, which is defined as

$$Q = \frac{\nu}{\Delta\nu} \tag{3.16}$$

Here, I will spend a few words to explain the highly reflective case (blue curve) in Figure 3.10. It tells us two facts about an ideal FP cavity ($R + T = 1$) with an R close to 1. If the frequency of the incident beam lies within the frequency width $\Delta\nu$ of the cavity resonance, in which case we say the incident light is *in resonance* with the cavity, light will be transmitted completely ($I_t/I_{\text{inc}} = 1$). Otherwise, when the incident light is *off resonance* with the cavity, light will be reflected off the first cavity mirror completely.

The first fact is somewhat surprising given the fact that both mirrors have equally high reflectivity but no light is reflected off the mirrors. This puzzling phenomenon can be explained by the destructive interference between the waves leaking out from inside the cavity (T is small, but > 0) and the reflected waves. Meanwhile, the waves inside the FP cavity exhibit constructive interference leading to a build-up of intra-cavity intensity such that the intensity transmitted through the second mirror equals the initial beam intensity. For $R = 0.9999$ the intra-cavity intensity is 10,000 ($1/T$) times higher than the incident beam intensity.

If the light source is suddenly shut off, it will take some time for the energy stored inside the FP cavity to dissipate. This temporal decay time τ, or the *storage time*, also determines the time it takes for the cavity to be fully operational after the light source is switched on again. An important fact about the cavity storage time is that processes occurring on a faster time scale than the cavity storage time, such as the intensity or frequency fluctuations of the incident light, can be filtered by the FP cavity.

The cavity storage time is inversely proportional to the resonance bandwidth. The time for a $1/e$ fraction (≈ 0.368) of the initial energy to remain inside the FP cavity is given by:

$$\tau = \frac{1}{2\pi\delta\nu} \tag{3.17}$$

3.3.2 The Real Fabry Perot Cavity

The real Fabry-Perot cavity differs from the ideal cavity in two aspects. One is the cavity finesse, the other is the cavity loss.

A high quality FP cavity exhibits both a high finesse and a high cavity Q-factor. However, in reality, the finesse of a free space cavity is typically 100-200. The limitations of cavity finesse are from the mirror imperfections and beam alignment. An effective finesse $\mathcal{F}_{\text{eff}}$ can be calculated by [98–100]

$$\frac{1}{\mathcal{F}_{\text{eff}}^2} = \frac{1}{\mathcal{F}_R^2} + \frac{1}{\mathcal{F}_{\text{Defect}}^2} + \frac{1}{\mathcal{F}_{\text{Mode}}^2} \tag{3.18}$$

where $\mathcal{F}_R$ is the reflective finesse calculated by Eqn 3.14, $\mathcal{F}_{\text{Defect}}$ is the finesse associated with surface defects and is determined by the optical quality of the mirror substrate, while $\mathcal{F}_{\text{Mode}}$ is the finesse due to the mismatch of the wavefront and the surface, which can be optimized with a precise beam alignment. Take the plano cavity in Ref. [100] for example, the identical mirrors they used have a surface quality of $\lambda/10$ at 633 nm, with high reflectivity of $R = 99.0\% \pm 0.1\%$. The measured cavity finesse is $\mathcal{F} = 275 \pm 19$, while the calculated finesse is $\mathcal{F}_R = 312 \pm 30$ based on the mirror reflectivity. However, with special mirror fabrication techniques, ultra-stable FP cavities with finesses of up to 150,000 are able to be realized [101, 102].

The other factor that makes the real FP cavity different from the ideal ones is the cavity loss, resulting in the cavity transmission ratio I_t/I_{inc} less than unity. The loss is mainly due to the fact that light bouncing back and forth inside the cavity experiences losses due to absorption or scattering on the mirror surface. For a fixed cavity finesse of 200, the total transmission can be as low as 50% even though the loss per bounce may be only 1%.

Another factor that may significantly increase the cavity loss is non-perfect mode-matching, especially for spherical cavities. This means that the wavefront curvature needs to be perfectly matched with the spherical curvatures of the cavity mirrors for a high cavity

transmission. If the input beam is not mode-matched to the cavity, the transmitted intensity of any given mode will be fairly low.

3.3.3 Stability Concerns

An optical cavity consisting of two mirrors is called "stable" when an incident beam launched inside the cavity parallel to the optical axis remains inside the cavity after an infinite number of bounces. The lack of the self-reproduction of spherical waves inside the cavity results in an "unstable" cavity [103].

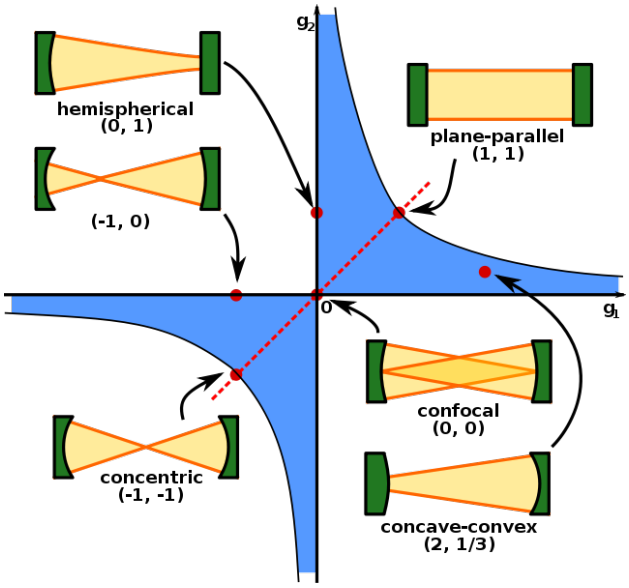

Figure 3.11: *Stability diagram for an optical cavity [104].*

By introducing g_1 and g_2

$$g_i = 1 - \frac{L}{\rho_i}, \quad \text{where}\, i = 1,\, 2. \tag{3.19}$$

where ρ_i is the radius of curvature of either of the two cavity mirrors, which is a positive value for a concave mirror and negative value for a convex mirror, the condition for a stable

resonator is

$$0 < g_1 g_2 < 1 \tag{3.20}$$

This condition can be visualized in the stability diagram, or the g-diagram, shown in Figure 3.11. In this diagram, an optical cavity with certain configurations is represented by a point in a g_1-g_2 plane. The shaded area represents the choices of g_1 and g_2 for a stable resonator. Both the confocal cavities (mirror radius of curvature equals cavity length) and plano cavities are commonly used. Confocal cavities have less alignment sensitivity, and are usually considered as a stable resonator. However, the FSR of a confocal cavity is only half of that of a plano cavity given the same cavity length. This is due to the degeneracy of the transverse modes inside the cavity [103]. As a result, the mode spacing will be half of $c/2L$.

3.3.4 Transverse Modes

For a stable resonator, the field distributions for steady-state can be found by solving the Kirchhoff integral equation analytically [102]. The solutions represent the eigenmodes of the optical resonator. In principle, there exist an infinite number of eigenmodes.

Due to the boundary conditions set by the cavity mirrors with a finite size, those eigensolutions can exhibit different symmetries depending on the mirror shape. Rectangular mirrors lead to a number of eigensolutions called Gauss-Hermite modes, which have rectangular symmetry. In most cases, round mirrors are used, which have Gauss-Laguerre modes with circular symmetry as solutions, shown in Figure 3.12 [105].

These Gauss-Laguerre modes are labeled by TEM_{pl}, where p and l are integers labeling the radial and angular mode orders, as shown in Figure 3.12. This figure shows the transverse mode profiles. The longitudinal profile of the mode is a standing wave inside the cavity, which has n number of nodes. Various modes in the cavity have different resonant frequencies, and are represented by different n, p and l numbers.

In both rectangular and circular symmetries, the TEM_{00} mode has the same round shape

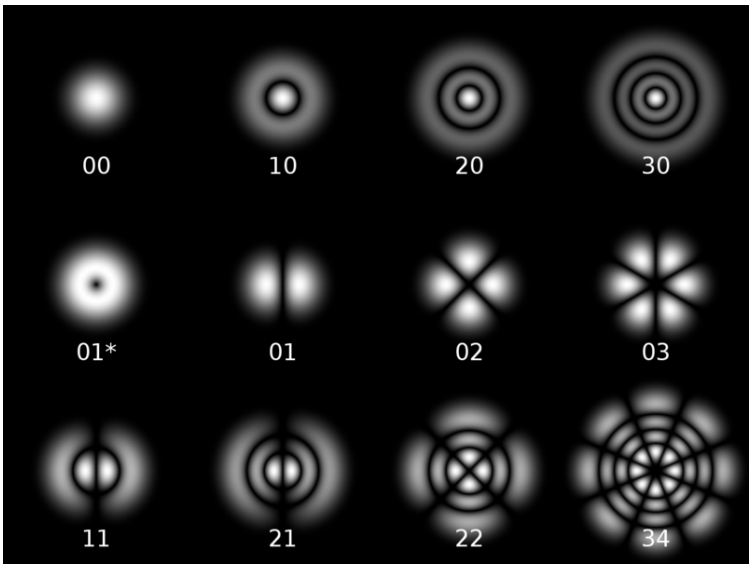

Figure 3.12: *Gauss-Laguerre modes inside a Fabry-Perot cavity [105].*

with a Gaussian intensity distribution, which is the mode with the smallest size that can oscillate in a stable resonator. The TEM_{00} is often referred to as the *fundamental mode*, and is the mode we want to excite inside the cavity. Other transverse modes are referred to as the *higher order modes*, which we want to avoid exciting in the cavity.

3.3.5 Filtering a Comb

The principle for comb filtering using a Fabry-Perot cavity is illustrated in Figure 3.13. If we adjust the Fabry-Perot cavity free spectral range (FSR) such that the separation between successive transmission peaks is exactly m times the comb repetition rate, i.e.

$$mf_{\text{rep}} = \text{FSR} = \frac{c}{2L}, \quad \text{where}\, m = \text{any integer}, \tag{3.21}$$

then only those comb teeth that are overlapped with the cavity transmission peaks will transmit through the cavity. Comb teeth that lies in between the transmission peaks, or the *side modes*, are suppressed.

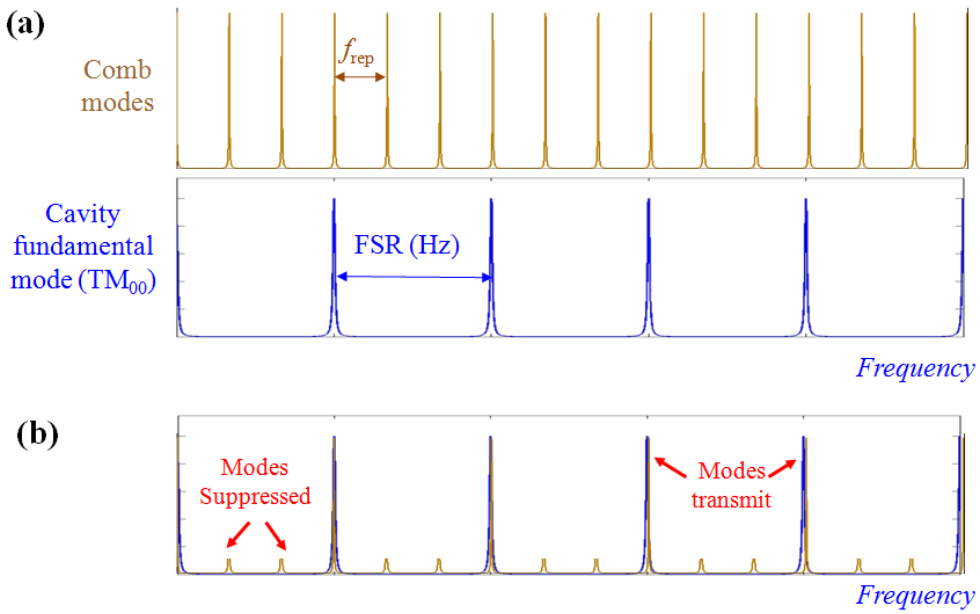

Figure 3.13: *Illustration of comb filtering using Fabry-Perot cavity. (a) A frequency comb and cavity fundamental mode before filtering (shown in frequency domain). (b) Suppressed comb after passing through the cavity. FSR: free spectral range of the cavity.*

The side-mode suppression ratio is an important characteristic for comb filtering, which is defined as the residual power transmitted versus the original power for the side modes. Now we will try to derive the mathematical expression for the suppression ratio.

The fractional power transmission from the FP cavity is given by Eqn 3.8. Considering an air-filled FP cavity, for normal incident beam, Eqn 3.8 can be re-written in terms of frequency f instead of wavelength

$$T(f, R, L) = \frac{I_t}{I_{\text{inc}}} = \frac{(1-R)^2}{(1-R)^2 + 4R\sin^2(\frac{2\pi f L}{c})} \tag{3.22}$$

Now the side-mode suppression ratio ρ can be obtained by replacing f in Eqn 3.22 with

f_{rep}.

$$\rho = T(f_{\text{rep}}, R, L) = \frac{(1-R)^2}{(1-R)^2 + 4R\sin^2(\frac{2\pi f_{\text{rep}} L}{c})} = \frac{(1-R)^2}{(1-R)^2 + 4R\sin^2(\frac{\pi}{m})} \tag{3.23}$$

The above Eqn 3.23 gives the expression for a single-pass two-mirror FP cavity. Note that the suppression ratio is only determined by the mirror reflectivity and the selection ratio $m = \text{FSR}/f_{\text{rep}}$ based on this expression. By designing the cavity in a double-pass, or triple pass configuration, with the same mirror separation L, the suppression ratio can be greatly improved [106]. The suppression ratio plotted in dB scale in Figure 3.14 is the calculated value for three types of configurations, under the assumption of perfect spatial mode coupling of the comb to the cavity fundamental mode. When the selection ratio m = 20, for a moderate cavity finesse of 200, a high suppression ratio of 60 dB is expected from a double-pass cavity. In the single-pass case, the same suppression ratio would require a high finesse of 10,000. For a triple-pass cavity, the same suppression ratio is given by an even lower finesse but at the cost of setup complexity. For these reasons, we initially chose to use the double-pass configuration for our comb filtering. Later, we had to modify it into a single-pass configuration (for higher cavity transmission power) with higher FSR to avoid mode competition in the injection locking process (Section 4.4.2).

To decide what cavity mirrors to use and the cavity FSR for comb filtering, we would like to avoid the situation in which higher order transverse modes of the cavity coincide with the comb teeth we want to suppress. This will not only transmit the unwanted comb teeth, but also destroy the mode-matched coupling and reduces the cavity transmission significantly. Therefore, a theoretical calculation is necessary to help select appropriate values of the mirror radius of curvature (ROC) and cavity length (L) for a given comb repetition rate. The goal here is to make suitable choices such that the cavity higher order transverse modes are located in between comb teeth.

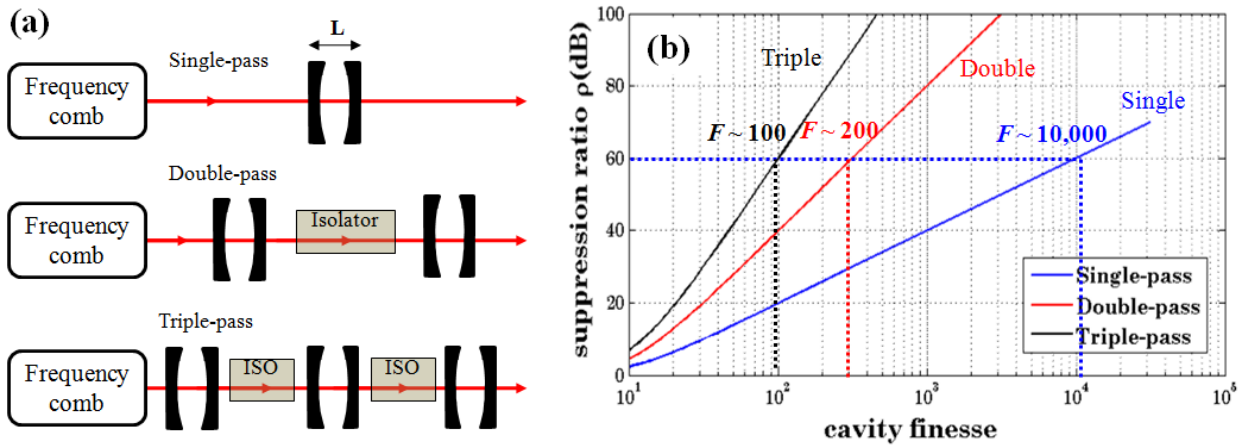

Figure 3.14: *(a) Schematic setup for a linear single, double, and triple-pass cavity configuration. (b) Side-mode suppression ratio (in dB) for multi-pass cavity configuration, selection ratio $m = 20$.*

According to Ref. [106], the resonant frequencies of a cavity are given by

$$\nu_{n,p,l} = \frac{c}{2L}(n + \frac{1+p+l}{\pi}\arccos(\sqrt{g_1 g_2})) \tag{3.24}$$

where n, p and l are the longitudinal and transversal mode numbers, as described in Section 3.3.4, and g_1 and g_2 are the g-parameters defined by Eqn 3.19.

Figure 3.15 displays the calculated comb filtering scheme. The vertical lines in both plots represent comb teeth, and the curves in the figure are the higher order cavity transverse modes (only $p + l = 1, 2, 3, 4, 5$ are included in the calculation). Figure 3.15 (a) shows two sets of cavity transverse modes based on different choices of mirror parameters, plotted in black and grey, respectively. The black curve avoids overlapping between the high order transverse modes and comb teeth, only allowing the major teeth to transmit (at $f_{\text{rep}} = 0$ and 10), which is what we want. However, a few peaks in the grey curve coincide with a number of comb teeth (at $f_{\text{rep}} = 1, 2, 3, 4$). Thus this set of mirror parameters is an unfavourable choice.

In our case, we would like to filter a comb with a repetition rate of about 100 MHz.

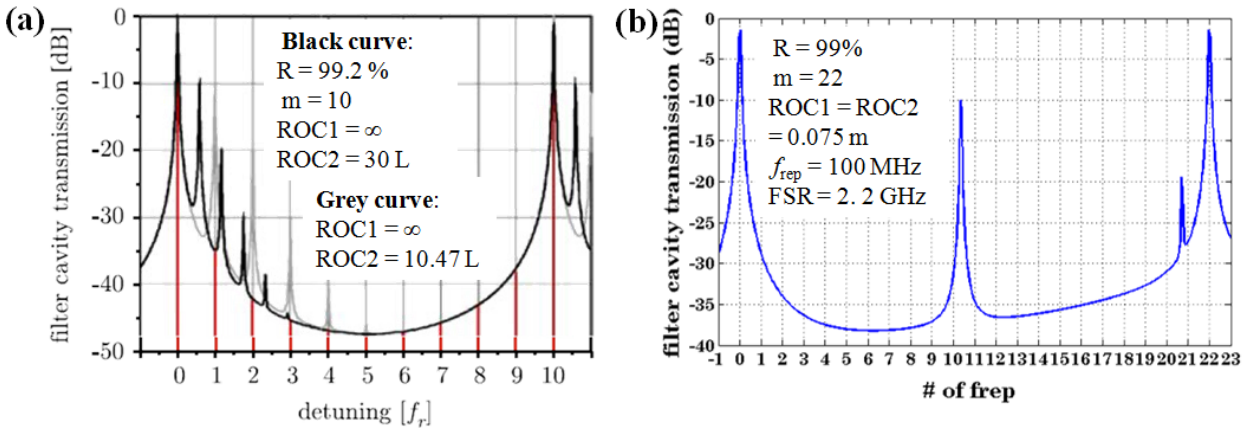

Figure 3.15: *Calculated comb filtering scheme. The cavity high order modes (curves) should be arranged in between comb teeth (red vertical lines). (a)Black and grey curves represent favourable and unfavorable choices, respectively [106]. (b)One set of cavity parameters giving cavity high order modes that are not overlapped with comb teeth.*

Figure 3.15 (b) shows the resulting filtering scheme for one possible set of mirror parameters. Both mirrors have identical radii of curvature of 7.5 cm. The cavity FSR is about 2.2 GHz. In later Section 3.4.1, I will talk about how to align such a FP cavity.

3.3.6 Mode-Matching

As discussed in Section 3.3.2, for a maximum cavity transmission, the wavefront curvature of the incident laser beam needs to be matched to the fundamental mode of the FP cavity. This is called *mode-matching*. Non-perfect mode-matching may result in significant cavity loss. Figure 3.16 shows the basic schematic of a double-pass cavity setup. A retro-reflector is added for creating the second-pass laser beam. For now, we only want to focus on the Gaussian beam propagation in the setup. Therefore, necessary polarization optics required for a double-pass design are omitted in this simplified picture.

For a given pair of cavity mirrors, we need to decide: (1) the focal length f_1 and location x_1 of the focusing lens FL3 before the cavity, and (2) the radius of curvature (R_r) and location x_2 of the retro-reflector. Since we already know the ROC of the mirrors and

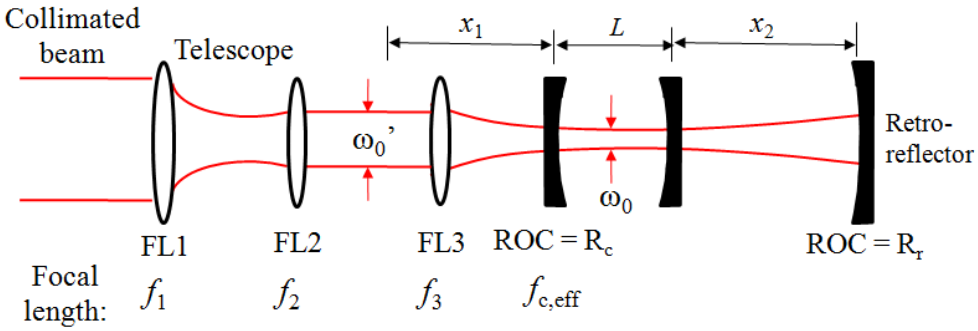

Figure 3.16: *Mode-matching schematic for a double-pass Fabry-Perot cavity.*

cavity length, we will start by solving the Gaussian beam parameters inside the cavity, then extend its propagation outside the cavity. The Rayleigh range of the Gaussian beam inside the cavity can be calculated by

$$z_R = z\sqrt{\frac{ROC(z)}{z} - 1} = \frac{L}{2}\sqrt{\frac{ROC(z = L/2)}{L/2} - 1} \tag{3.25}$$

For a 2.2 GHz cavity, the cavity length $L = 6.82$ cm. At $z = L/2$, ROC is 7.5 cm. Plugging these values into Eqn 3.25, we have $z_R = 3.74$ cm. At our wavelength of 1550 nm, the beam waist inside the cavity can be calculated to be $\omega_0 = 136$ μm by equation

$$\omega_0 = \sqrt{\frac{z_R \lambda}{\pi}} \tag{3.26}$$

With the intracavity beam parameter known, it is now straightforward to calculate the beam propagation outside the cavity. To decide which retro-reflector and focusing lens (FL3) to use, one can use the ABCD matrix method and solve the equations for a precise result, which I will briefly discuss at the end of this section. An alternative and easier way is to use ray optics equations for a good estimation. With either method, there exist multiple solutions. One should choose a suitable solution considering the physical spacing of the setup and availability of optics.

For the choice of FL3, assuming light propagates from FL3 (Figure 3.16) and is focused at the intracavity beam waist, the curved mirror acts like a diverging lens. Using the thick lens equation, the effective focal length of the cavity mirror is

$$1/f_{c,\text{eff}} = (n-1)[\frac{1}{R_{c,1}} - \frac{1}{R_{c,2}} + \frac{(n-1)d}{nR_{c,1}R_{c,2}}] \tag{3.27}$$

where $n = 1.5$ is the refractive index of the mirror substrate, $R_{C,1} = \infty$ and $R_{C,2} = 7.5$ cm are the radii of curvature of the front and back surfaces, and d is the mirror thickness. Therefore, we have the first cavity effective focal length $1/f_{c,\text{eff}}$ = -15 cm. The combined effective focal length for FL3 and the first cavity mirror is then

$$\frac{1}{f_{3+c,\text{eff}}} = \frac{1}{x_1 + L/2} = \frac{f_3 \times f_{c,\text{eff}}}{f_3 + f_{c,\text{eff}} - x_1}. \tag{3.28}$$

In Eqn 3.28, there are two unknowns: f_3 and x_1. In principle, one can choose an arbitrary f_3 and calculate for x_1. But it is preferred to choose a large focal length f_3 for a collimated beam with long Rayleigh range. This also affects the beam size reduction ratio for the telescope lenses before FL3. We do not want this ratio to be too big, because the reflected beam from the first cavity used for later locking purposes will be expanded by the same ratio. It would be hard to couple the expanded beam back into the fiber if the beam size is larger than the aperture of the aspheric lens (AL1, Figure 3.17). For the 1.9 GHz double-pass cavity, the focal length we chose for FL3 is 150 mm, with the calculated $x_1 = 13.24$ cm. The collimated beam size before FL3 can be calculated based on the Gaussian beam focusing equation:

$$\omega_0' = \frac{\lambda f_{3+c,\text{eff}}}{\pi \omega_0}. \tag{3.29}$$

With $f_{3+c,eff} = 17$ cm, $\lambda = 1550$ nm, we have $\omega_0' = 617$ μm, close to the measured value of 642 μm. The telescope ratio we chose is about 3.27, with the focal length of FL1 and FL2 to be 50 mm and 15.29 mm, respectively.

The parameters of the retro-reflector can be calculated in a similar way. Again, there is more than one choice. The further away the reflector is from the cavity, the larger ROC is required, resulting in a larger beam size. With a 20 cm ROC reflector, the position is calculated to be about 19 cm away from the intracavity beam waist, with a beam diameter of 1.4 cm incident on the reflector. This is a proper length considering the insertion for other components in between the second cavity mirror and the reflector, i.e. a Faraday rotator and a polarizer, as shown in Figure 3.17.

Finally, as an example, I will briefly show how to calculate the parameters for the retro-reflector using the ABCD matrix method. Starting from the cavity waist Figure 3.16, as the beam propagates to the retro-reflector and is then bounced back into the cavity waist again, the ABCD matrix for this trip is

$$\begin{aligned}\begin{pmatrix} A & B \\ C & D \end{pmatrix} = &\begin{pmatrix} 1 & L/2 \\ 0 & 1 \end{pmatrix} \begin{pmatrix} thick & lens \\ curved & front \end{pmatrix} \begin{pmatrix} 1 & x_2 \\ 0 & 1 \end{pmatrix} \begin{pmatrix} 1 & 0 \\ \dfrac{1-n}{R_r n} & \dfrac{1}{n} \end{pmatrix} \\ &\begin{pmatrix} 1 & x_2 \\ 0 & 1 \end{pmatrix} \begin{pmatrix} thick & lens \\ flat & front \end{pmatrix} \begin{pmatrix} 1 & L/2 \\ 0 & 1 \end{pmatrix} \\ with \quad &\begin{pmatrix} thick & lens \\ curved & front \end{pmatrix} = \begin{pmatrix} 1 & 0 \\ 0 & n \end{pmatrix} \begin{pmatrix} 1 & d \\ 0 & 1 \end{pmatrix} \begin{pmatrix} 1 & 0 \\ \dfrac{1-n}{R_c} & \dfrac{1}{n} \end{pmatrix} \\ and \quad &\begin{pmatrix} thick & lens \\ flat & front \end{pmatrix} = \begin{pmatrix} 1 & 0 \\ \dfrac{n-1}{R_c} & n \end{pmatrix} \begin{pmatrix} 1 & d \\ 0 & 1 \end{pmatrix} \begin{pmatrix} 1 & 0 \\ 0 & \dfrac{1}{n} \end{pmatrix}\end{aligned} \tag{3.30}$$

Here, R_c and R_r are the radius of curvature of the cavity mirror and retro-reflector, L is the cavity length, $n = 1.5$ is the refractive index of the lens substrate. The matrix elements A, B, C, and D can be expressed with the two unknowns x_2 and R_r. The q-parameter for the beam at the intracavity waist is

$$\frac{1}{q_0} = -i\frac{\lambda}{\pi\omega_0^2} \tag{3.31}$$

This beam parameter does not change after this trip, therefore we have

$$q_0 = \frac{Aq_0 + B}{Cq_0 + D} \tag{3.32}$$

By solving Eqn A.23, we can find the value of x_2 for any given R_r.

3.3.7 Summary

Designing a Fabry-Perot filtering cavity requires careful selection of a couple of cavity parameters. To summarize, below are a few general guidelines that help with the design.

(1) For comb filtering purposes, a high suppression ratio ($>$ 40 dB) is always desired. This requires high cavity finesse ($>$ 1,000) in a typical single-pass cavity, which is practically difficult. However, by using a double-pass configuration, a high suppression ratio can be achieved using a relative low finesse cavity ($\sim$ 100).

(2) In general, high cavity finesse is preferred as it gives a high cavity suppression ratio. However, there are a few concerns about a high finesse cavity. First, if the finesse is too high such that the transmission peaks are narrower than the comb linewidth, part of the comb teeth cannot be transmitted, which results in a reduced cavity power transmission. Second, sharper transmission peaks make the cavity more sensitive to dispersion, leading to a limited transmission bandwidth [91]. Every time the beam is reflected by the cavity mirror, the phase changes slightly giving an ununiform spacing between comb teeth. As this phase walk-off is cumulated large enough (within certain spectral bandwidth), comb teeth can not be overlapped with the cavity transmission peaks any more. Therefore, the cavity transmission is only limited to a certain spectral bandwidth. This spectral limitation would be an important factor to consider only if one wanted to transmit a large bandwidth ($>$ tens of nms) comb. Since we are only filtering a comb with a narrow bandwidth of 50

GHz around 1532.8 nm, dispersion concern is beyond our needs. Third, a narrow resonance linewidth means a longer cavity storage time. For cavity stabilization techniques that rely on cavity transmission signals, a long cavity storage time slows down the response of the entire servo loop. However, in our case, a reflection technique is used for our cavity locking (will be discussed in Section 3.4.2), which should not be limited by the cavity storage time.

(3) Regarding the selection of the cavity length and radius of curvature of the cavity mirrors, one first needs to satisfy the stability condition, which can be discerned from the *stability diagram* (Section 3.3.3). To ensure proper comb filtering, it is better to have the higher order cavity transverse mode not coincide with any of the comb teeth that one wants to suppress. Theoretical calculations can be done for any given sets of mirror parameters. In general, the smaller the selection ratio $m = \mathrm{FSR}/f_{\mathrm{rep}}$ is, the more easily one can make the choice. Because the suppressed comb teeth are less dense for small m, it is easier to avoid overlapping with the high order modes.

(4) For high cavity transmission and finesse, mode-matching the wavefront curvature of the incident Gaussian beam with the cavity mirror curvature is essential. Non-perfect mode-matching due to either using the inappropriate optics or misalignment can result in huge cavity loss.

3.4 Filtering Cavity Implementation

3.4.1 Cavity Alignment

Figure 3.17 displays the schematic diagram for the initial 1.9 GHz double-pass Fabry-Perot cavity we built for comb filtering. Later, we had to modify it into a 9.4 GHz single-pass cavity to avoid mode competition in the injection locking process (Section 4.4.2). Here, I will talk about cavity alignment techniques using the double-pass cavity as an example.

The idea of this double-pass configuration comes from Ref. [52]. A narrow bandwidth frequency comb is optically amplified using an erbium-doped fiber amplifier (EDFA) and coupled into free space through a fiber-based circulator into a collimated beam using an aspheric lens (AL1). With proper polarization control inside the fiber, this collimated beam has a linear polarization. The beam size is reduced by a factor of three using a telescope which consists of a pair of focusing lenses to achieve the required beam size for optimum mode-matching. The beam is then focused into the FP cavity with FL3 (focal length = 150 mm), resulting in an intra-cavity beam waist of 136 μm. Any reflection from the first cavity mirror is coupled back into the fiber along the incoming beam trajectory and exits through the fiber circulator port 3 for cavity locking purposes. The light that enters the

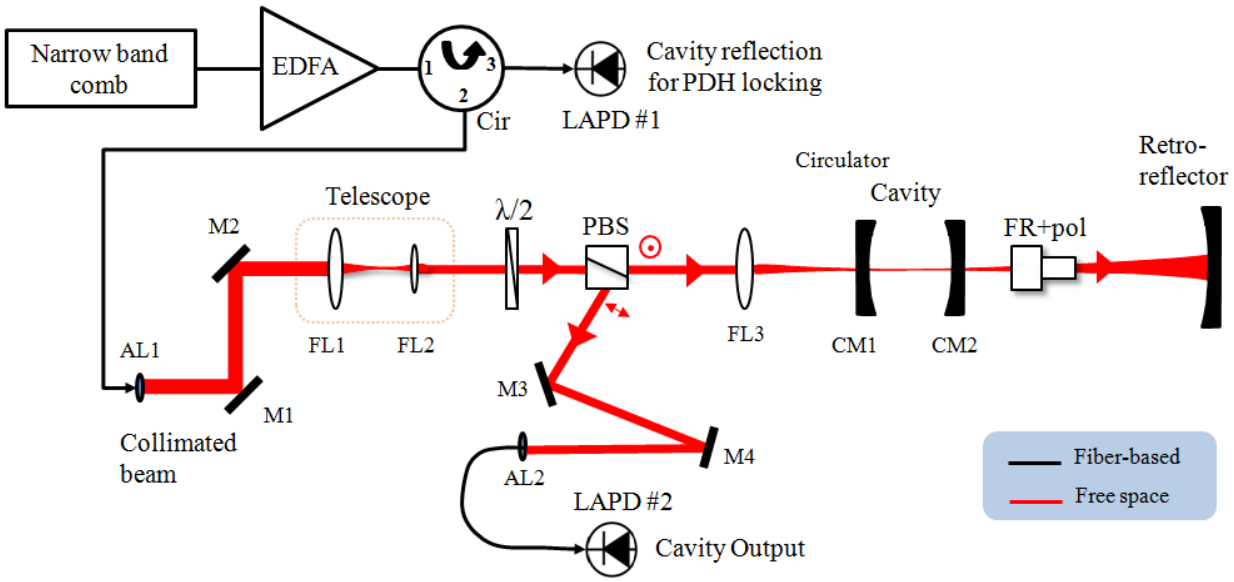

Figure 3.17: *Schematic for a double-pass Fabry-Perot filtering cavity. EDFA: erbium-doped fiber amplifier, Cir: circulator, PDH: Pound-Drever-Hall, LAPD: large-area photodetector, PBS: polarization beam splitter, AL: aspheric lens, FL: focusing lens, FR: Faraday rotator, Pol: linear polarizer.*

cavity experiences a number of bounces by the two highly-reflective mirrors before it exits the cavity, forming the first-pass beam. The first-pass output then goes through a Faraday rotator and thus experiences a polarization rotation of 45°. The light bouncing back from

the retro-reflector experiences another 45° rotation inside the Faraday rotator and forms the second-pass beam entering the cavity with a linear polarization orthogonal to the first pass. Again, after a number of intra-cavity bounces, the second-pass beam exits the polarization beam splitter as the final cavity output.

Before we setup the optics, we need to first glue the PZT to one of the cavity mirrors for later locking purposes. Both cavity mirrors have a diameter of 0.5 inch and thickness of 0.375 inch. The PZT we used is a ring actuator (CMAR03 by Noliac) with an inner diameter of 6 mm and the outer diameter matched to the cavity mirror. The major concern for gluing the PZT to the mirror is that we would like to have a PZT frequency response as high as possible, since in most cases the PZT response (typically tens of kHz) is the limiting factor in a servo loop. An appropriate choice of glue and clamping the two pieces together while the glue is curing are the two keys that help achieve a high frequency response. To choose the glue, a soft epoxy is preferred, as hard epoxy (i.e. 5 min super glue) tends to cause piezo deformation, which will limit the PZT performance and in the worst case can damage the piezo. The epoxy we used (Epo-Tek305 by Fiber Optic Center Inc.) has a Shore D hardness of 66 (while super glue has a Shore D hardness of 85) and a long curing time for a couple of hours. While the glue is curing, it is recommended by the PZT manufacturer that a 2-5 MPa pressure should be applied, corresponding to at least 40 pounds of weight on top of our cavity mirror considering the mirror size. The pressure ensures a thin and uniform glue layer and helps the response of the PZT greatly. One trick of doing this is to have the mirror mounted on a hard flat surface so that the PZT is facing upwards. Meanwhile, setup a moveable plate facing downwards using a micrometer stage at a height slightly above the PZT. The pressure can be applied to the PZT as one moves the plate down and presses the PZT surface. The micrometer stage allows fine control of the pressure. The frequency response of our cavity mirror glued with PZT is measured to be 20 kHz (Section 3.4.3), probably limited by the weight of the mirror and the mirror mount.

With the cavity mirrors prepared, we can now start setting up the free space optics in

Figure 3.17 for comb filtering. The biggest challenge for coupling a frequency comb versus a CW laser into an optical cavity is that the cavity length has to be exactly right as it requires $mf_{\text{rep}} = \text{FSR}$. However, the cavity length is hard to optimize when there is nearly no signal until $mf_{\text{rep}} \approx \text{FSR}$. Therefore, for our convenience, it is better to use a CW source at first to see cavity resonance regardless of the cavity length. Once the alignment for a CW laser is optimized, one can switch to the comb and optimize the cavity length.

With a collimated CW light coupled into free space, one can start positioning the steering mirrors M1 and M2. The goal is to have a straight beam (in 3D space) after M2. This can be done by setting up two irises along the line with equal height, and adjusting the tilting knobs on M1 and M2 such that the beam goes through both irises simultaneously. Then one can install the lenses (FL1 to FL3) one by one without altering the beam path (we will skip the waveplate and PBS for now). FL3 is mounted on a translation stage, allowing fine control along the beam path. Now it is time to mount the first cavity mirror (CM1). To achieve a better cavity stability, we built an aluminium block stage for mounting the two cavity mirrors, as shown in Figure 3.18. The tilting angle for the first cavity mirror is optimized such that the laser beam is perfectly retro-reflected back to the fiber circulator, resulting in a maximum signal from the large-area photodetector (LAPD#1 in Figure 3.17). For aligning the second cavity mirror (CM2), it is best to apply a voltage scan to the PZT for a cavity length modulation larger than $\lambda/2$ so that at least one entire FSR will be observed in the transmission. The reason for this modulation is to make sure that the cavity is constantly on resonance with the laser beam during the scan. Without the modulation, the cavity may not be on resonance with the laser during the alignment, and thus no light will enter the cavity at all. With the second cavity mirror mounted on a translation stage roughly parallel to the first mirror, it should be possible to see faint higher order cavity modes exiting from the cavity using an IR card. Fine tuning the angle of the second mirror should give a bright circular spot at the cavity output, which is the desired fundamental mode (TEM_{00}) (Figure 3.12). At this point, we can place another large-area photodetector after CM2 (not

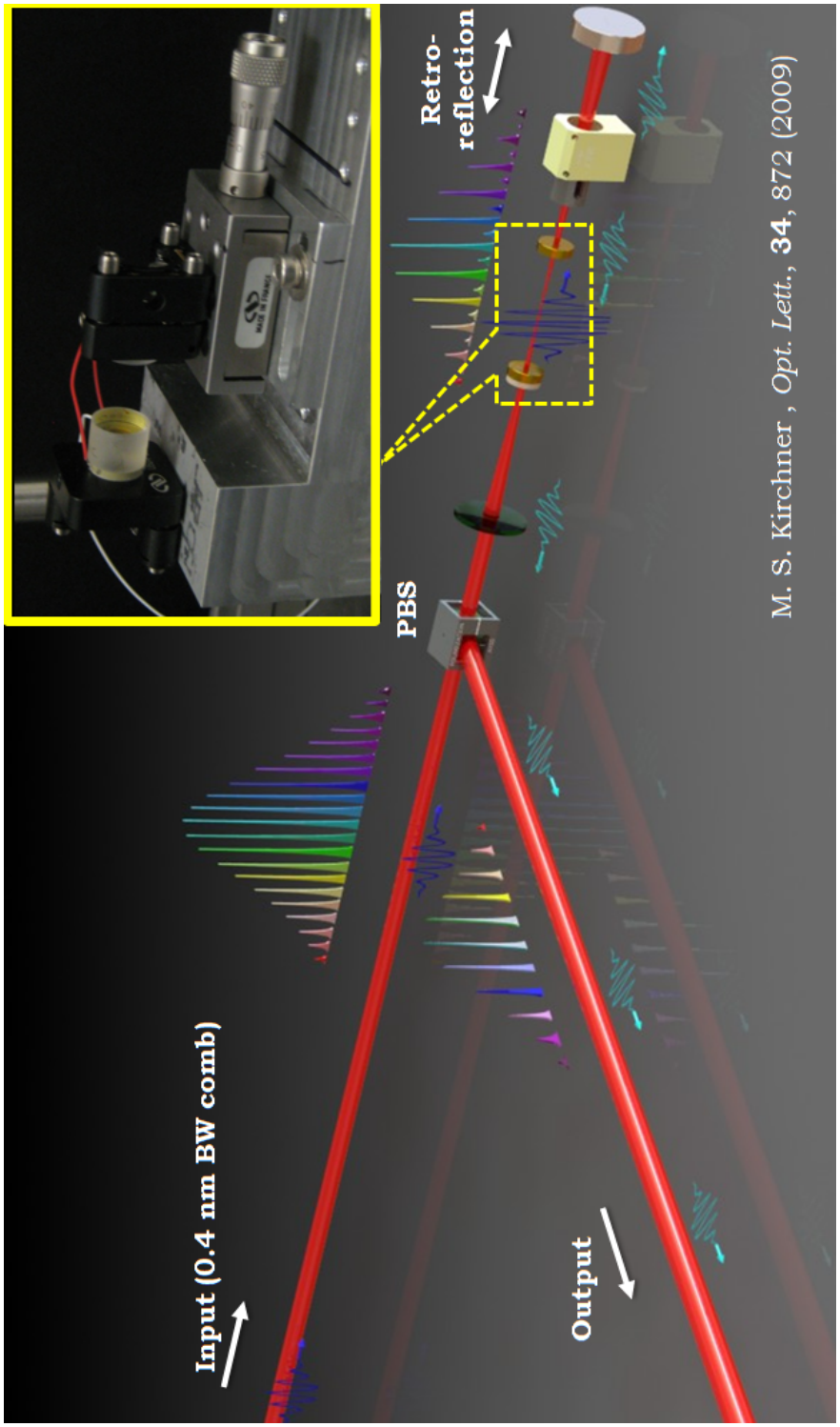

Figure 3.18: *SolidWorks image for a double-pass Fabry-Perot filtering cavity showing the comb filtering mechanism in both time and frequency domain. Inset: actual cavity mirror setup in the lab.*

shown in Figure 3.17), and should be able to see cavity transmission peaks as we scan the cavity length. Figure 3.19 (a) shows a non-optimized cavity transmission signal with a few high order modes existing in the picture. By further fine adjusting the tilting angle of both cavity mirrors and position of FL3 for an optimized mode-matching, the fundamental transmission peaks can be maximized while the high order peaks are minimized, as shown in Figure 3.19 (b).

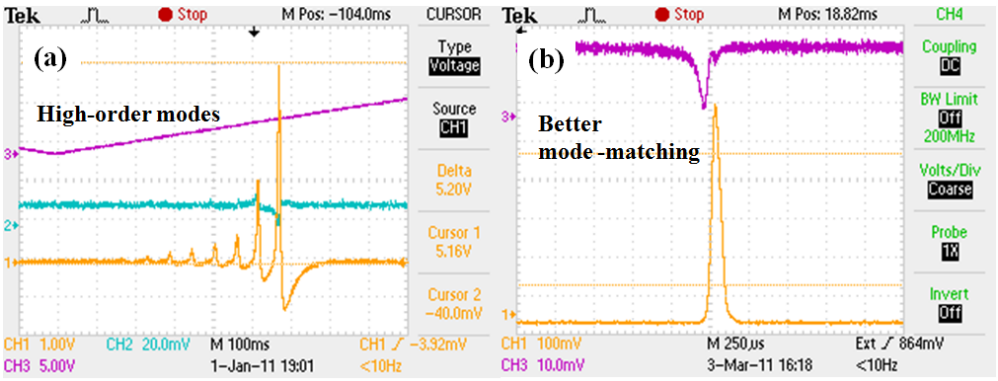

Figure 3.19: *Optimization of coupling a CW laser into the Fabry-Perot cavity. (a) Cavity transmission for a non-optimized coupling scheme with prominent high order modes and a reduced fundamental mode signal due to poor alignment or mode-matching. (b) Cavity transmission for an optimized coupling scheme with a maximum fundamental mode signal.*

With the first-pass beam well aligned, it is time to align for the second-pass beam. We can now position the polarization beam splitter (PBS) before FL3 in the beam path and make sure it is perfectly aligned. An obvious sign of non-optimized positioning is the appearance of extra scattered light exiting the PBS at an angle, which can be easily observed with an IR card. With the Faraday rotator and polarizer installed for a maximum transmission signal on the large-area photodetector located after the cavity, the last step is to place the retro-reflector. The retro-reflector can be mounted on a translation stage. Now one should be expected to see light out from the output port of the PBS while fine adjusting the mirror tilting knobs. The output power can be further maximized by fine tuning the position of the retro-reflector for better mode-matching. It is best to lock the cavity to the

CW laser such that the cavity is always on resonance with the laser while one is doing the second-pass alignment. The locking techniques will be discussed in the following section.

Using the CW laser as a guide, one can optimize the alignment of the laser beam to the cavity. It is now a good time to switch the laser source to a frequency comb. It is not surprising that if one does not see resonances with a comb source at first, that is because the cavity length is not exactly right. With a well-aligned cavity setup, it is straightforward to fine adjust the cavity length by moving the micrometer stage for the cavity mirror until one sees maximized resonances at the cavity output. In this case, the condition $mf_{\text{rep}} = \text{FSR}$ is satisfied.

3.4.2 Cavity Stabilization: Pound-Drever-Hall locking

For proper comb filtering, the comb teeth are required to match up with the cavity transmission modes (TEM_{00}) in the first place. Therefore, stabilization of the FP cavity to the laser source becomes necessary. A popular laser-locking method is the Pound-Drever-Hall (PDH) locking technique based on fast modulation, very similar to the frequency modulation spectroscopy described in Section 2.6. It was invented in 1983 by Ron Drever, based on similar microwave techniques by R. V. Pound, and further implemented in laser's field by Jan Hall. Using this technique, the laser can either be locked to an ultra-stable cavity [107], which is the most common way this technique is being used, or vice versa, an optical cavity can be locked to a laser, which has been utilized in our work for comb filtering purposes (discussed in Section 2.6). In addition to all the benefits of FM spectroscopy from fast modulation, one important feature about PDH locking worth mentioning here is that it is a reflection technique, which means that the error signal is generated based on the reflected RF sidebands from the optical cavity. Therefore, the response of the error signal is not limited by the cavity storage time (a counter example would be side locking, which uses cavity transmission as the source to generate the error signal). The limiting factor for the response would be the resonant frequency of the transducers in the system, i.e. the

piezoelectric transducer (PZT) that changes the laser frequency. Additionally, because the sidebands are not transmitted by the optical cavity, the transmitted field is unmodulated and has very low noise. Similar to FM spectroscopy, PDH locking also suffers from RAM, which gives an offset in the error signal, or sometimes asymmetries on the error signal.

As an initial test, we will first show how to lock the cavity to a CW laser, and then move on to the comb. The locking technique we use is called the Pound-Drever-Hall (PDH) locking.

Setup for PDH Locking

As we discussed in the Introduction Chapter (Section 2.5), PDH locking is a type of fast frequency modulation technique based on the reflection signal from the cavity. It takes advantage of an optical cavity property that all light is reflected off the cavity unless the laser frequency is on resonance with the cavity. While the reflection intensity is symmetric about the resonance frequency, the derivative of the reflection intensity is antisymmetric across the resonance. By modulating the laser frequency, an antisymmetric error signal can be produced and indicates which side of resonance the laser is on, and forces the following servo to adjust accordingly.

Figure 3.20 shows the schematic setup for PDH locking. A CW laser passes through an electro-optic modulator (EOM) and experiences phase modulation, which essentially adds two sidebands with opposite phase to the laser carrier frequency. The modulation frequency (f_{mod} = 22 MHz in our case) is chosen to be larger than the laser linewidth. The light then goes into the circulator and passes through the cavity. The reflected light goes back into the circulator, exits from port 3, and is detected by a fast photodetector. Mixing the photodetector signal with the original modulation signal that drives the EOM produces the error signal. After passing a 2 MHz low pass filter (LPF), the error signal is fed into a servo amplifier to adjust the cavity length by driving the PZT on the cavity mirror, thereby locking the cavity resonance frequency to the CW laser frequency. The top curves in figure 3.21

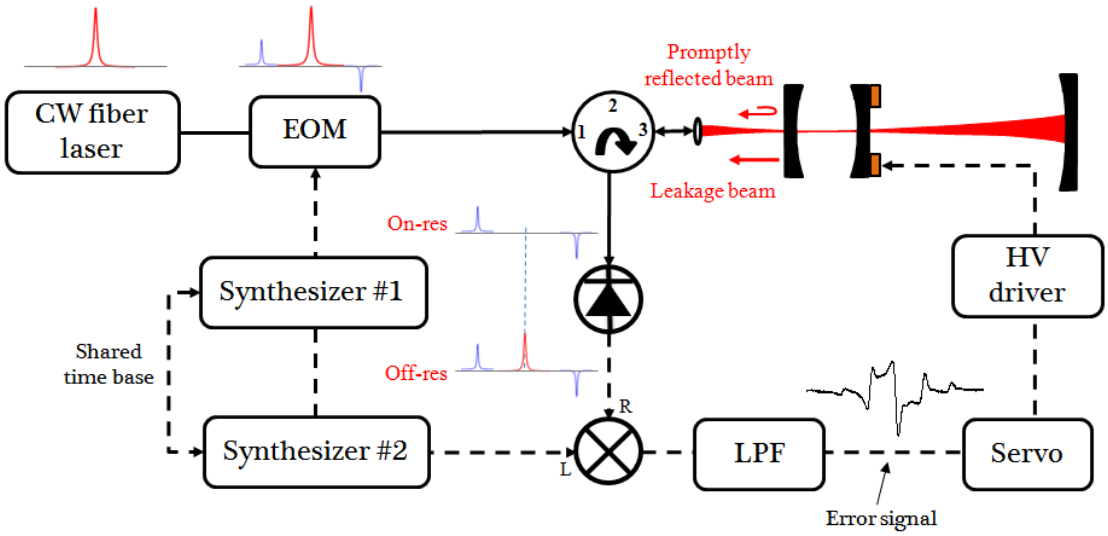

Figure 3.20: *Schematic diagram for Pound-Drever-Hall locking. EOM: electric-optic modulator, LPF: low pass filter, HV driver: high voltage driver.*

show the produced PDH error signal from both a CW laser and a comb, respectively, as we scan the cavity length. The bottom curves show the resonance peaks when the cavity is on resonance with the CW laser/comb tooth carrier and the two sidebands. The CW error signal has a SNR of over 100, while the comb error signal SNR is limited to less than 20. The degradation of the SNR is mainly due to the reduced optical power per individual comb tooth.

Understanding the PDH Error Signal

To understand the PDH error signal, we will look at the following two cases: when the laser is (1) on resonance, and (2) off (but close to the) resonance with the cavity. Two terms are defined based on Ref. [52]: prompt reflected beam and leaked beam. The *prompt reflected beam* refers to the beam reflected off the first cavity mirror because it is not on resonant with the cavity. The *leaked beam* is a small portion of the intra-cavity standing waves that leaks through the first mirror, and is always on cavity resonance. The signal that is incident on the photodetector is the beating between these two types of beams. In the first case, when

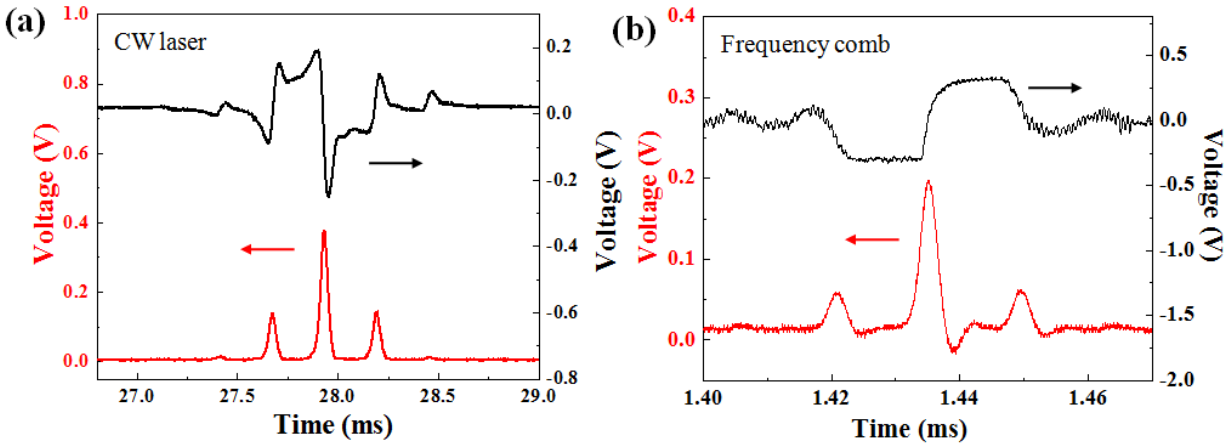

Figure 3.21: *Pound-Drever-Hall error signal when locking the Fabry-Perot cavity to (a) a CW fiber laser, and (2) a frequency comb.*

the laser is resonant with the cavity, the laser carrier enters the cavity, but both sidebands are reflected. The photodetector sees the beat signal between two beats: the beat between the leaked carrier and lower reflected sideband, and the beat between the leaked carrier and the upper reflected sideband. Since the two sidebands are out of phase from each other, the two beats cancel each other perfectly, which gives zero for the error signal at the modulation frequency. In the second case, when the cavity is not quite perfectly resonant, the input laser carrier has a frequency slightly shifted from the cavity resonance frequency, and so do the sidebands. All three components will be reflected because none of them are on resonance with the cavity. And all of them are at the same frequency as the input. But the carrier frequency experiences a small phase shift. The leaked light is at cavity resonance. The signal that is incident on the photodetector is mainly the beat between two beats: leaked carrier beat with the lower sideband of reflected light, and leaked carrier beat with the upper sideband of the reflected light. (There is also beating from the leaked carrier, which is on resonance, and with the reflected carrier, which is slightly off resonance. But the resulting signal is at a very low frequency. Since we will demodulate the signal at the modulation frequency, this low frequency does not contribute to the final error signal.)

Initial Locking

In principle, the filtering cavity can be stabilized to any comb tooth. However, for later performing the saturated absorption, we need to choose a particular comb tooth that is as close to the P(23) line as possible due to limited scan range for single tooth locking. To help choose the right comb tooth to lock, we first stabilize a CW diode laser (Santec TSL-210) to the P(23) transition as a reference. Then we optically heterodyne beat the filtering cavity output with this reference. As we scan the cavity length, the cavity can be resonant with a number of comb teeth. When the cavity is in resonant with the right tooth, the resulting RF beatnote between the comb and CW reference is close to DC frequency.

Initial locking of the cavity to the laser is achieved using the home-made servo discussed in Section 2.7.3. With an appropriate servo design, the steps for acquiring a lock should be straightforward, and are described as follows: The first step for an initial lock is to optimize the error signal. The error signal should be centered at zero voltage. Any voltage offset can be compensated by adjusting the servo "input offset". The SNR can be maximized by adjusting the relative phase between the two synthesizers (Figure 3.20). The second step is to check polarity. We manually scan the PZT voltage until the cavity is nearly resonant with the laser, in which case the cavity transmission is close to the maximum. If the transmission signal suddenly drops as we turn up the proportional gain, that means we have the wrong polarity sign. This can be corrected either by switching the "polarity switch" on the servo box, or changing the demodulation phase by 180°. The third step is to try to lock. With the proportional gain slightly above zero, one can scan the cavity until it is close to resonance, and turn on the integrator switch. If the transmission signal increases to and remains at maximum after the integrator switch is on, that is a good indication of a lock. The fourth step is to optimize the proportional gain. Now one can increase the proportional gain slowly until the system starts to oscillate, in which case the error signal becomes noisier. This indicates the gain is too much. An optimum proportional gain should be slightly below this oscillation gain. An optimized locking setting should give a maximum cavity transmission,

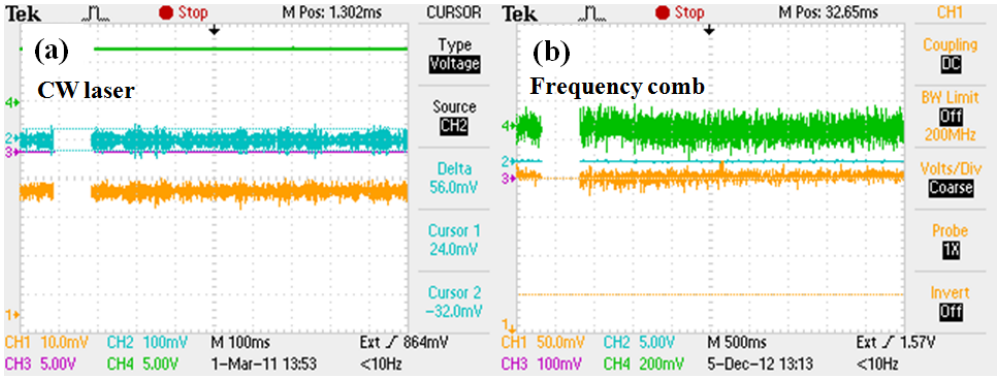

Figure 3.22: *Locking the Fabry-Perot cavity to (a) a CW fiber laser, and (b) a frequency comb. Cavity transmission is maximized when it is locked.*

and minimum noise on the error signal. Figure 3.22 shows the transmission and error signal for both CW laser and comb locking.

3.4.3 Cavity Characterization

Two different Fabry-Perot cavities have been built for the purpose of filtering a narrow bandwidth frequency comb. One is a nearly confocal cavity, with the mirror separation L slightly larger than the mirror ROC. The other is a nearly plano cavity, with the mirror ROC much larger compared with the cavity length. The cavity parameters for both cavities are given in Table 3.1. The following paragraphs show a few characteristics of these two cavities.

PZT Response

Once the ring PZT is glued to the cavity mirror, a straightforward way to measure the PZT response is to lock the cavity to the laser source, and to look at the cavity transmission signal on a Fast Fourier Transform (FFT) spectrum analyzer. As one turns up the proportional gain until the system oscillates, a resonance peak should appear on the FFT spectrum analyzer, which is the PZT resonance frequency.

Item	Spherical cavity	Plano cavity
Configuration	Double-pass	Single-pass
FSR	1.9 GHz	9.4 GHz
Cavity Length	7.9 cm	1.6 cm
Selection Ratio (FSR/f_{rep})	21	105
Mirror Reflectivity	$99\% \pm 0.5\%$	$99\% \pm 0.5\%$
Coating Central Wavelength	1570 nm	1550 nm
Mirror ROC	7.5 cm	50 cm
Mirror Diameter	0.5 inch	0.5 inch
Mirror Surface Figure	$\lambda/10$ at 633 nm	$\lambda/10$ at 633 nm
Intracavity Beam Waist	136 μm	60 μm
Telescope Lenes	50 and 15.28 mm	200 and 60 mm
Focusing Lens Before Cavity	150 mm	200 mm

Table 3.1: *Fabry-Perot filtering cavity parameters for a (a) spherical cavity, and (b) plano cavity.*

If one cannot lock the cavity, an alternative way to measure the PZT response is to apply a modulation voltage to the PZT, and compare the relative phase difference between the cavity transmission and the driving signal. The phase shift increases as one increases the modulation frequency due to the PZT response. Before applying the modulation, it is better to park the laser near the bottom of a transmission peak, as shown in Figure 3.23 (a), where the slope is less steep so that the voltage modulation over that small region will not cause large change in power transmission. Figure 3.23 (b)-(d) shows the increasing phase shift as we increase the modulation frequency. From this measurement, the PZT response is about 20 kHz when the relative phase shift reaches 90°.

Cavity FSR

When the cavity is locked to the comb, the cavity FSR can be easily measured by looking at the cavity transmission signal on an RF spectrum analyzer, as displayed in Figure 3.24 (a). The filtered repetition rate signature for the spherical cavity is at 1.94 GHz. The repetition rate peaks below 1.94 GHz are from the suppressed comb teeth. The fast photodetector

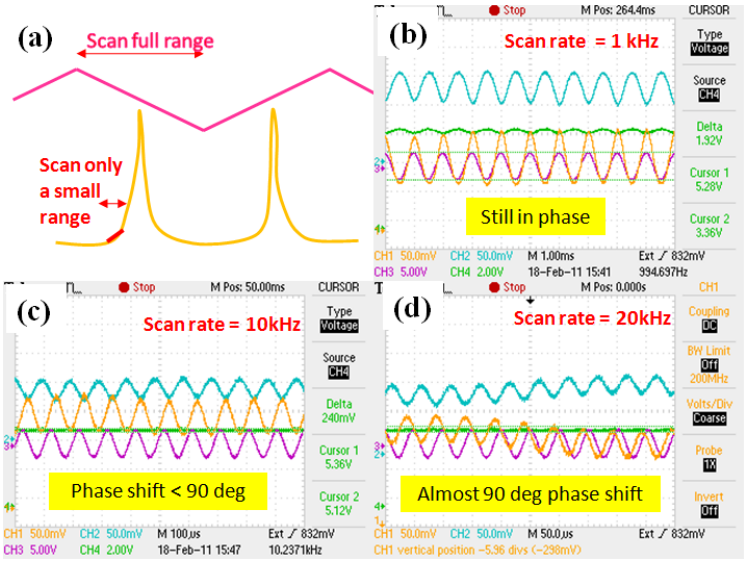

Figure 3.23: *PZT response measurement by comparing the relative phase shift between the cavity transmission signal (yellow) and the driving voltage (pink).*

used in this measurement has a limited bandwidth of 1 GHz (New Focus, 1611), causing the roll off in the peak power beyond 1 GHz.

To measure the FSR of the plano cavity, this method would not work because the FSR is above the maximum frequency at which the RF spectrum analyzer (Model number: 8561B by Hewlett Packard) can respond, which is about 6.5 GHz. Fortunately, the FSR is slightly above the spectral resolution of our optical spectrum analyzer ((Model number: AQ-6315E, by ANDO). The red oscillating curve shown in Figure 3.24 (b) represents the filtered comb measured by the OSA, resolving each individual comb tooth. For comparison, the spectrum of a 1 kHz linewidth CW fiber laser (blue curve) is also plotted in Figure 3.24 (b), representing the spectral resolution of the OSA, which is about 0.06 nm. The separation between adjacent teeth is 0.074 nm, corresponding to a FSR of 9.4 GHz.

A more precise FSR measurement can be done utilizing the PDH method [108, 109] resulting in sub-Hz level resolution. It requires a CW reference laser with a linewidth narrower than the cavity resonance.

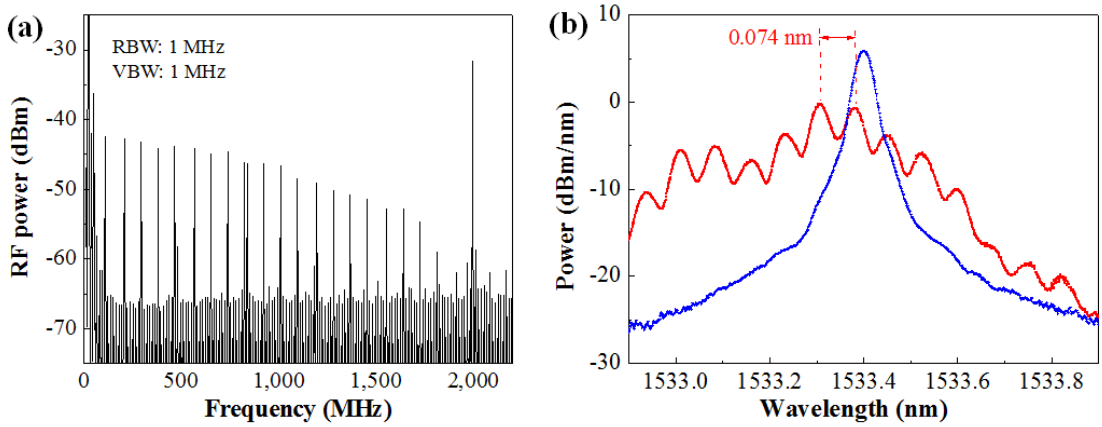

Figure 3.24: *Free spectral range (FSR) measurement for two filtering cavities. (a) The RF spectrum of a double-pass spherical cavity transmission signal indicates a FSR of 1.94 GHz. (b) The optical spectrum of a single-pass plano cavity transmission signal (red ripples) indicates a FSR of 9.4 GHz. The optical spectrum of a narrow linewidth CW laser (blue) is plotted to represent the spectral resolution of the spectrum analyzer.*

Cavity Finesse

The cavity finesse is measured by comparing the cavity FSR to the linewidth of the cavity resonance, based on Eqn 3.15. Direct measurement based on the time-domain oscilloscope information may lead to large discrepancies. That is, we measure the resonance linewidth in time, and compare this number to the time separation of two successive cavity transmission peaks. The discrepancy comes from the fact that the PZT does not have a linear response to the applied voltage. So the voltage to frequency calibration would not be linear.

There are two other ways to measure the resonance linewidth in a more precise manner. The first method involves the phase modulation by an electro-optic modulator (EOM). One can adjust the modulation frequency to a proper value such that the spacing between the carrier and one sideband is equal to the cavity resonance linewidth (in time domain). Then the modulation frequency would correspond to the resonance linewidth. Since the cavity FSR can be directly read from the RF spectrum analyzer, it is straightforward to calculate the finesse. The finesse for our 1.9 GHz cavity is about 250. Given a mirror reflectivity of $99\% \pm 0.5\%$, the calculated finesse should be between 209 and 626.

The other way to measure the cavity resonance linewidth requires a little more effort. One can beat the filtered comb against a narrow linewidth (much narrower than the cavity resonance linewidth) CW laser. The linewidth of the resulting RF beatnote can be directly measured on an RF spectrum analyzer. Assuming the CW laser linewidth is negligible compared to the cavity resonance, the beatnote linewidth presents the cavity resonance linewidth.

Power Transmission

For a CW laser source in a single-pass FP cavity, the maximum power transmission achieved with the above mirrors is about 42%. The power loss is mainly due to the absorption or scattering caused by the cavity mirror (as discussed in Section 3.3.2), which is about 0.1% per bounce. Another factor that could contribute to the loss is mode-matching.

For comb filtering, the power loss is dependent on the selection ratio $m = \mathrm{FSR}/f_{\mathrm{rep}}$. A high selection ratio means a smaller fraction of power (one tooth out of m teeth) is transmitted from the cavity. Since m equals 21 and 105 for the 1.9 GHz double-pass and 9.4 GHz single-pass cavity, the total power transmission measured in the experiment is about 0.7% and 0.4%, respectively.

Suppression Ratio

When we beat a CW laser against a filtered comb, two types of beatnotes are obtained: one is between the CW laser and a filtered comb tooth, the other is between the CW laser and a suppressed tooth. The difference in the SNR of these two beatnotes gives the cavity suppression ratio, shown in Figure 3.25. The 1.9 GHz double-pass FP cavity has a suppression ratio of 30 dB, while the 9.4 GHz single-pass cavity is 22 dB.

Based on Eqn 3.23, the 1.9 GHz cavity in a single-pass configuration should give a calculated suppression ratio between 25-29 dB (51-58 dB for a double-pass cavity), given a mirror reflectivity of $99\% \pm 0.5\%$. For the 9.4 GHz single-pass cavity, the calculated values

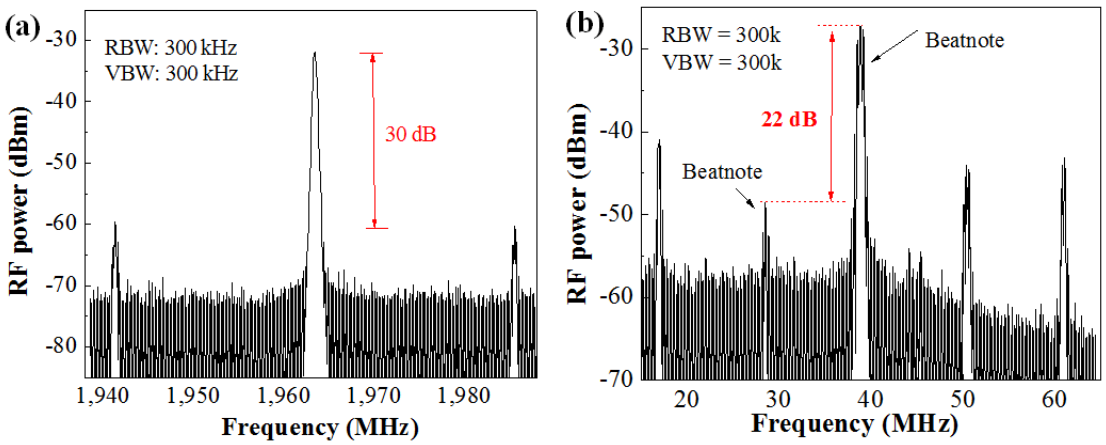

Figure 3.25: *Suppression ratio for (a) a single-pass spherical Fabry-Perot cavity, and (b) a single-pass plano Fabry-Perot cavity. Suppression ratio is measured by the difference in SNR between two beatnotes: a CW laser beating with filtered and suppressed comb teeth.*

are 15-22 dB, which is close to what we obtained in the experiment.

Although we started with a double-pass 1.9 GHz filtering cavity with higher suppression ratio, we had to modify it to a 9.4 GHz cavity later in order to have single comb tooth output after the following 7 GHz fiber Bragg grating. We had to make it single pass for higher power transmission. Fortunately, the suppression ratio we achieved is sufficient for our purpose, i.e. injection locking the DFB laser.

Chapter 4

Single tooth Saturated Absorption Spectroscopy

In order to stabilize a single comb tooth via saturated absorption spectroscopy (SAS), the optical power of the comb tooth has to be comparable to the saturation power, which is 23 mW measured in our hollow-core fiber reference setup [40]. The calculated power per tooth at 1532.8 nm directly from the NPR fiber ring oscillator is about 20 nW. Therefore, a power amplification of a factor of 10^6 is required. This is a great challenge because significant comb amplification can introduce devastating amplified spontaneous emission noise, leading to the degradation of comb SNR.

In this chapter, we start off by briefly reviewing a few current comb amplification methods. Then we will focus on optical amplification through erbium-doped fiber amplifiers (EDFAs). The power amplification stages can be divided into two parts: before and after the filtering cavity, shown in Figure 4.1. Section 4.3 will talk about comb amplification before the filtering cavity. Our initial design involving a short-pulse EDFA was not successful. It amplifies the comb power at our wavelength of interest, but destroys the comb SNR at the same time. This problem is eventually solved by making a small gain CW EDFA instead. Section 4.4 and 4.5 presents two comb amplification methods after the filtering

cavity: distributed-feedback (DFB) laser injection locking and single tooth amplification directly using a CW EDFA. We were able to observe a sub-Doppler error signal using both methods. But the injection locking technique gives a much better SNR.

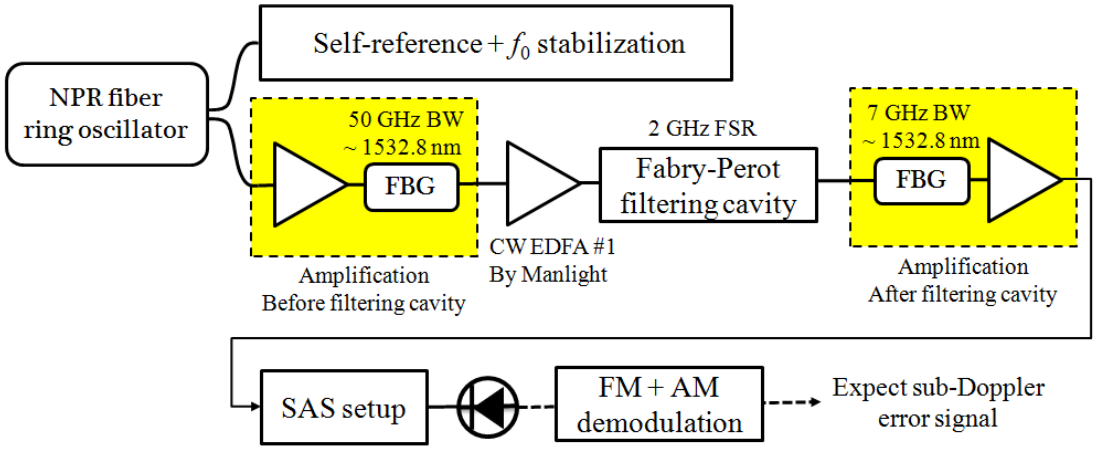

Figure 4.1: *Overview schematic setup for single tooth saturated absorption spectroscopy.*

4.1 Review of comb amplification

Comb amplification has been of great interest in the frequency metrology community. However, it is challenging to optically amplify frequency combs with high SNR. This section reviews a few of the current methods for comb amplification. Each method has its own pros and cons. For our purpose, we only need to amplify a single comb tooth. Our choice was to injection lock a diode laser with a single comb tooth to achieve a high SNR performance, discussed in the last sub-section.

4.1.1 Erbium-doped Fiber Amplifier (EDFA) and Semiconductor optical amplifier (SOA)

Both *Erbium-doped fiber amplifiers* (EDFAs) and *Semiconductor optical amplifiers* (SOAs) [110] provide optical gain based on different but comparable interactions of light with matter.

In erbium-doped fiber amplifiers, the gain medium is the *erbium doped fibers* (EDFs), a conventional silica fiber doped with rare-Earth element erbium ion in the core. When an EDF is pumped by light at certain wavelengths, electrons can be excited from the ground state to an intermediate state, then decay back to the ground state by emitting photons within the 1525-1565 nm band. Meanwhile, if a light signal passing through the EDF is within the 1525-1565 nm band, it will stimulate this decay process, resulting in signal amplification. This is the so-called *stimulated emission*.

In semiconductor devices, the energy levels of the erbium ion are replaced with the energy bands of the semiconductor crystal, but other than that the gain mechanism is similar. The semiconductor is brought into an excited state by pumping it electrically, populating the bands with electrons and holes. An optical signal propagating through the device gives rise to carrier recombination, and the associated stimulated emission amplifies the signal.

Both types of amplifiers are used for broadband astro-comb amplification [91, 92]. Ref. [111] uses a tapered semiconductor amplifier to amplify a fs optical frequency comb ($\sim$ 780 nm) with a gain of more than 17 dB (12 dB) for 1 mW (20 mW) average input power. However, there are drawbacks for both amplifier designs.

One major disadvantage for an EDFA is the so-called *Amplified Spontaneous Emission* (ASE) noise. Excited electrons can fall back to the ground state without any trigger, resulting in photons being emitted in random phase and directions (with respect to the signal photons). These random photons become a source of optical noise and are then amplified by the remaining erbium doped fiber. This ASE noise degrades the SNR of the optical signal that we want to amplify. Since the decaying erbium ions can emit photons over a span of 1525-1565 nm, the ASE noise will also be distributed over this spectrum. A

proper EDFA design should keep the ASE noise to a minimum.

SOAs have advantages of being commercially available, and inexpensive. However, they have issues like pulse distortion and spectral broadening due to gain dynamics and self-phase modulation (SPM) [103, 112, 113].

4.1.2 Single Tooth Amplification via Stimulated Brillouin Scattering (SBS)

Stimulated Brillouin Scattering (SBS) [114] is an nonlinear effect that can occur when a sing-mode fiber (SMF) is pumped by a light beam above a certain power threshold. This causes density-fluctuations in the fiber medium, and results in a modulated refractive index induced by the strong pump. The scattering of pump light through Bragg diffraction, also called *Stokes waves*, propagates mainly in the opposite direction of the pump inside the fiber. The backscattered Stokes light interferes with the pump light and generates an acoustic wave through the effect of electrostriction [115]. The frequency of the Stokes light is Brilliouin shifted by the frequency of the acoustic wave, usually on the order of 10-20 GHz for SMF. In other words, an incident photon is converted into a backscattered photon with most of the power of the incident photon, and a phonon. Therefore, if a weak signal at a suitable optical frequency counter-propagates with respect to the pump, it can be strongly amplified.

This effect is suitable for single comb tooth amplification for the following reasons. First, due to the phase matching between the pump, Stokes wave, and acoustic wave, amplification only occurs for a well-defined Brillouin frequency shift between the pump and Stokes field, which is given by the refractive index and acoustic velocity in the fiber. Second, the Brillouin gain bandwidth is determined by the lifetime of the involved phonons. For standard telecom fibers, this number is of the order of 10 MHz at 1550 nm. The narrow gain bandwidth allows the selection of an individual comb tooth from fiber lasers with low repetition rate down to tens of MHz. Third, the requirement on the pump, in terms of pump power, frequency stability and accuracy is not very high.

Ref. [116] used this technique to achieve a high SNR single comb tooth amplification from a 56 MHz fiber laser. A narrow bandwidth spectrum from the comb directed into a 12 km long SMF with linear polarization, serves as the probe. An orthogonally polarized 30 mW pump light counter-propagating inside the fiber is frequency shifted by 10 GHz from the probe. This results in a 34 dB power amplification for a single comb tooth. The RF beatnote between the amplified comb line and the original comb has a SNR of more than 40 dB with 10 Hz RBW.

There are two drawbacks for this technique. One is the temperature-dependent long term stability of the sidemode suppression, which is how much the unamplified comb teeth are suppressed with respect to the amplified single comb tooth. The other is that spontaneous Brillouin scattering imposes a pedestal at the base of the amplified tooth, which reduces the comb SNR.

4.1.3 Injection Locking Diode Laser

The interest in injecting locking has been generated by the desire to produce a laser which emits high power and is also spectrally pure at the same time. The concept of injection locking involves two lasers at nearly identical wavelengths: a master laser, and a slave laser. The master laser operates at low power but produces a single-mode beam. The slave laser has high optical power but is spectrally noisy. In this technique, the master laser is injected into the resonant cavity of the slave laser. The term "injection locking" refers to the condition in which the intensity injected into the resonant cavity is sufficient to completely quench all that cavity's "normal" oscillation modes, as the result of gain saturation. The slave laser is then "forced" to lase at the seeding frequency, producing a high power single-mode beam.

In the case of comb amplification, a narrow band frequency comb, serving as the master laser, can be injected into a diode laser. By adjusting the currents and temperatures of the diode laser, the slave cavity is made resonant with the master optical field, which is then amplified since there is gain available.

A key parameter for this injection locking is the locking bandwidth. A narrow locking bandwidth is often preferred because it allows for amplification of an individual comb tooth from a low repetition rate laser. Large locking bandwidth will result in multiple comb teeth amplification at the same time, which leads to unstable injection locking. According to Ref. [117], the upper limit of locking bandwidth is determined by a few parameters: (1) the free spectral range (FSR) of the diode laser, (2) the injection power, and (3) the injection coupling efficiency. In practice, the locking range also depends on the gain profile of the diode laser.

Table 4.1 summaries some of the works using this injection locking technique for comb amplification. High gain amplification with low noise has been demonstrated.

Ref	Slave laser	Wavelength	Comb rep rate	Input power	Gain	Year
[118]	Fabry-Perot laser diode	794.7nm	100.5 MHz	4 mW (600 nW / tooth)	50 dB	2006
[119]	DBR	852 nm	1 GHz	10 μW (16 nW / tooth)	60 dB	2006
[120]	DFB	1542.72 nm	250 MHz	380 μW (1.9 μW / tooth)	42 dB	2008
[121]	DBR	852.3 nm	1 GHz	200 μW (300 nW / tooth)	52 dB	2008
[122]	DFB	1542.38 nm	1.5 GHz	125 μW (3.75 μW / tooth)	24 dB	2010
[123]	External cavity laser diode	1520-1590 nm	25 GHz	100 μW (2 μW / tooth)	31 dB	2010
[124]	DFB	1529 nm	1 GHz	130 μW (3.9 μW / tooth)	24 dB	2011
[125]	Microlens -coupled DL	633 nm	250-500 MHz	1.5 μW CW	39 dB	2005

Table 4.1: *List of references using injection locking diode laser for comb amplification. DBR: distributed-Bragg-reflector, DFB: distributed-feedback laser, DL: diode laser.*

4.2 Introduction to EDFA Design

The performance of an erbium-doped fiber amplifier (EDFA) depends on a few factors: (1) the Er^{3+} doping concentration, or the selection of the gain fiber, (2) the pump wavelength used, and (3) the pumping configuration.

Given a finite pump power and certain EDF length, high doping is necessary for a high gain. If the doping level is too low, the ground state may become depleted if the number of available ions is fewer than the pump photons. However, if the doping is too high, it causes additional losses due to energy transfer upconversion between ions, which significantly reduces the efficiency of the amplifier [126, 127].

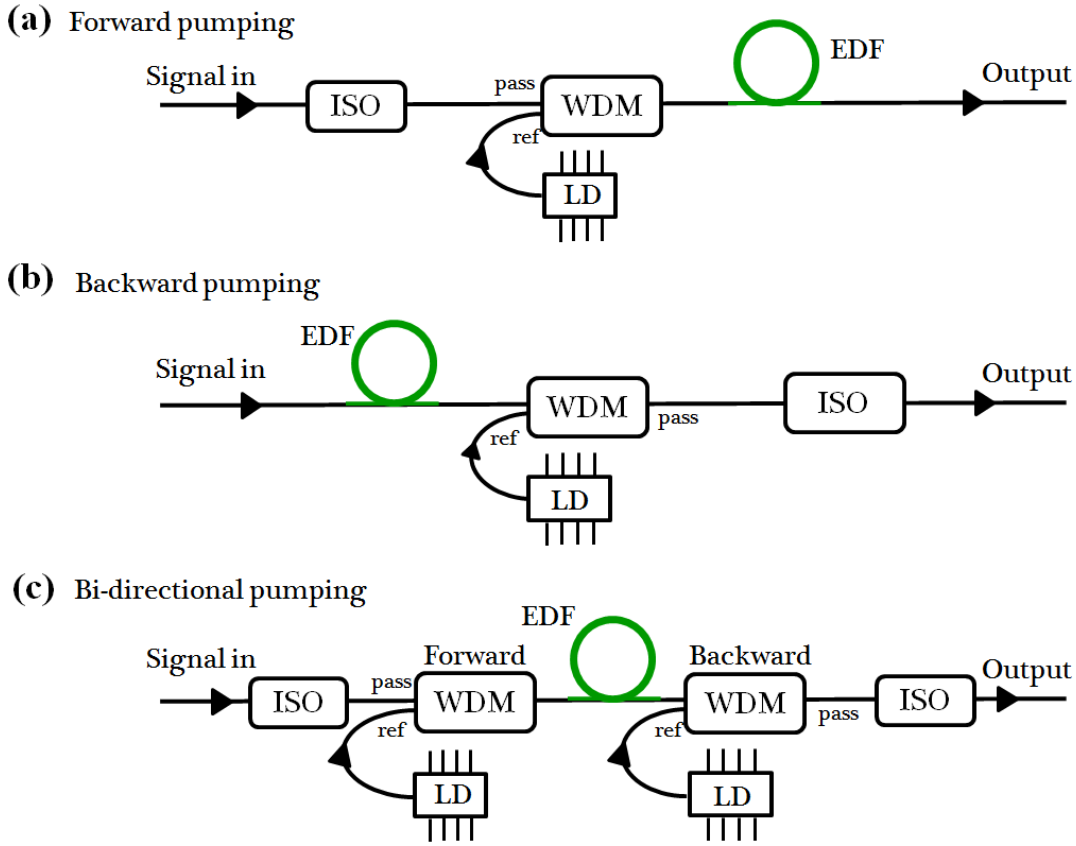

Figure 4.2: *Three pumping configurations for erbium-doped fiber amplifiers.*

For selecting pump wavelength, the two commonly used pump wavelengths are 980 nm

and 1480 nm. A pump wavelength of 980 nm provides high population inversion, leading to a high gain with low noise [128]. A 1480-nm pump wavelength will provide a better power conversion efficiency, but with more ASE noise.

There exist three types of pumping configurations, shown in Figure 4.2. In all three schemes, a length of EDF is fusion spliced to other components in the figure. The optical pump is combined with the optical signal into the EDF with a *wavelength-division-multiplexer* (WDM). An optical isolator is used to prevent reflected light from other portions of the optical system from entering the amplifier. The three pumping configurations are named *forward*, *backward* and *bi-directional* pumping, depending on the pumping direction with respect to the input signal. A forward-pump scheme will ensure a high population inversion at the input of the EDFA, resulting in a high gain and low ASE noise performance [129]. Whereas, a backward-pumped scheme has high output power but also high ASE noise. A bi-directional scheme has the merits of both, providing an optimized version but at the cost of complexity.

4.3 Two Home-made Erbium-doped Fiber Preamps

Due to low optical power at our wavelength of interest ($\sim$ 1532.8 nm) directly from the NPR fiber ring oscillator, it is necessary to build a pre-amplifier to have sufficient seeding power for the following commercial CW EDFA (Figure 4.1) before the filtering cavity. Our initial idea was to build a short-pulse amplifier, which could broaden the oscillator output spectrum until we have enough optical power at the wavelength of interest. However, it was proved later that this design of this amplifier introduces significant ASE noise. An alternative way is to design a small-signal CW EDFA, which preserves the comb SNR much better than the short-pulse EDFA.

4.3.1 Short-pulse Amplifier Design

There are three steps for making this amplifier. First is to optimize the length of gain fiber for a maximum average output power. Then we need to minimize the pulse duration for maximum peak power. Last, if necessary, we can add a piece of highly nonlinear fiber to further broaden the optical spectrum to the wavelength of interest.

The second step is achieved through the *solitonic effect*. There are two different kinds of fiber used in this pre-amplifier: the EDF with a positive dispersion, and the standard single-mode fiber (SMF) with a negative dispersion. For pulses propagating inside fibers with opposite dispersion signs, the temporal broadening due to group velocity dispersion (GVD) could be balanced by the spectral broadening due to self-phase modulation (SPM) if a proper length of each fiber is used. In this case, the pulse duration remains unchanged after travelling certain lengths inside the fiber. This is the formation for the so-called *optical soliton*. Practically, this can be done by adding (or subtracting) the right amount of SMF length (for a given length of EDF).

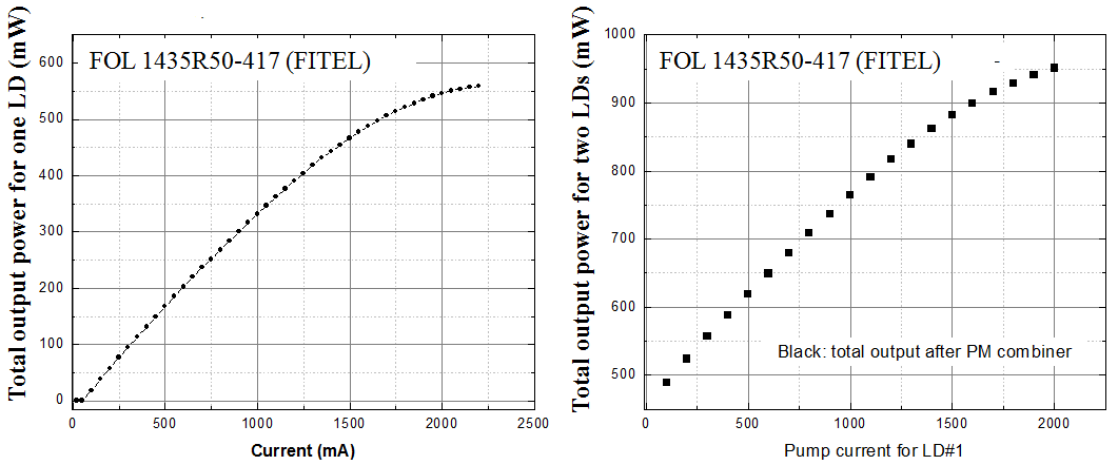

Figure 4.3: *Measured output power for the two pump diodes used in the short-pulse amplifier.*

The EDF fiber we used (Liekki Er110-4/125) has an absorption coefficient of 110 dB/m at 1530 nm. The length of this EDF is roughly determined through the following *small*

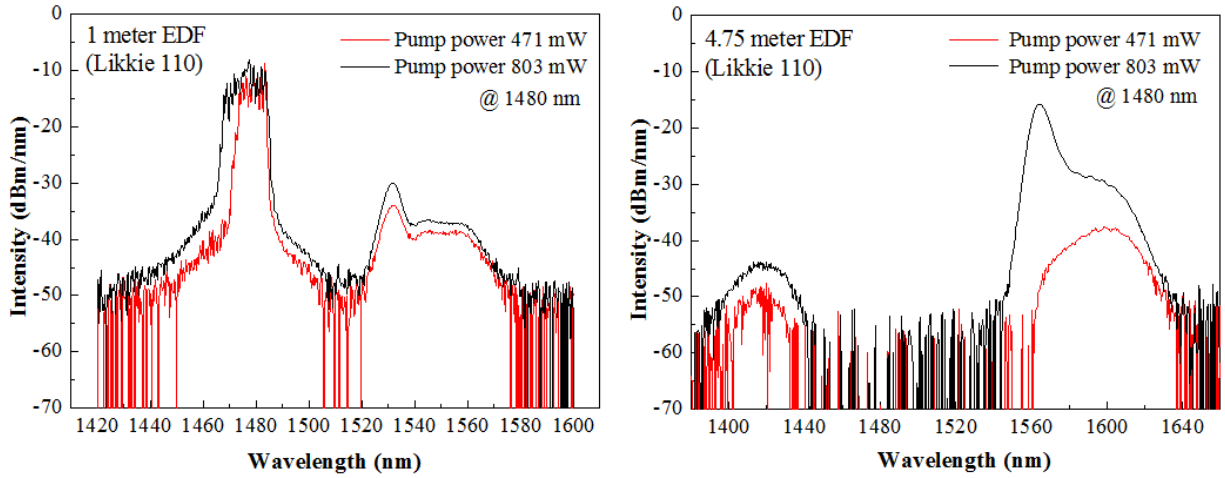

Figure 4.4: *Choosing EDF length: small signal gain measurement for a 1 meter (left) and 4.75 meter (right) EDF (Lekkie) in a forward pumping configuration. Input signal: CW laser at 1532.7 nm with a peak power of -38 dBm/nm (left) and -48 dBm/nm (right), respectively.*

signal gain measurement. We first tried with a forward pumping configuration. Figure 4.3 shows the measured pump power for the pump diodes used in this measurement, with the left figure being the individual diode output, and the right figure being total output of two diodes including the beam combiner loss.

Figure 4.4 shows the optical spectrum from the EDF output when seeded with 0.1 μm (or below) CW light at 1532.8 nm. By comparing the input and output peak intensities at the signal wavelength, a one meter EDF gives a small signal gain of 8 dB for 803 mW pump power at 1480 nm. Whereas, a 4.75 meter EDF gives 33 dB gain for the same pump power. Therefore, we chose to start with a 4 meter piece of EDF.

When we seeded the EDF with a comb, the length of EDF was further optimized by cutting small increments and measuring the power and spectrum each time. Because of technical problems, the NPR laser was not fully functional at the time that the short-pulse amplifier was being made. Therefore, the laser we used to seed this amplifier is a carbon nanotube fiber ring laser, shown in Figure 4.5. A 35 cm EDF (OFS 150) is pumped by a 980 nm diode with a maximum power of 300 mW. The repetition rate of the laser is about

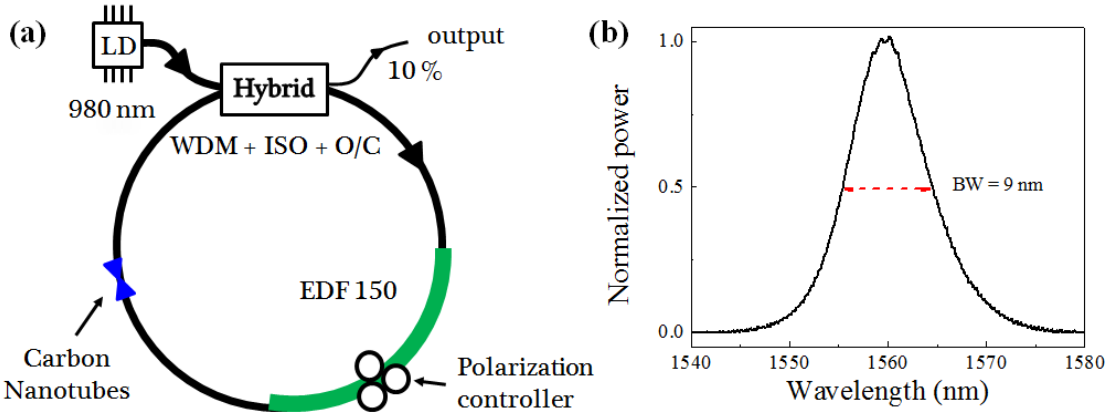

Figure 4.5: *Schematic layout of a carbon nanotube fiber ring laser.*

98.7 MHz. The output spectrum is centered at 1560.3 nm, with a bandwidth of 9.8 nm when the pump current is about 95 mA, giving an average output power of 0.19 mW.

Figure 4.6 shows the amplifier output power and optical spectrum when we did the cut-back measurements. The spectrum intensity is plotted in linear scale. We can see that as we cut back the EDF, the total output power increases and the center of the spectrum tends to shift to shorter wavelengths, which is what we desired.

However, as we keep cutting down the EDF, the maximum output power obtained was always below 20 mW, and the light intensity at 1532.8 nm was not sufficient for our need. We suspected that this low output power might be due to the forward pumping scheme. Therefore, we changed our setup into a backward pumping configuration, which resulted in an immediately high output power of more than 100 mW when seeded with the carbon nanotube comb.

Another concern when optimizing EDF length is the pump absorption. For best amplifier performance, the length of EDF should be chosen such that one can still see some pump residue at the amplifier output. A rule of thumb is to have the residual pump light 10-15 dB below the amplified light.

Considering all these factors, namely, the output power, maximum gain at our wavelength of interest, and pump absorption, the EDF length was re-optimized to be 3.07 meters

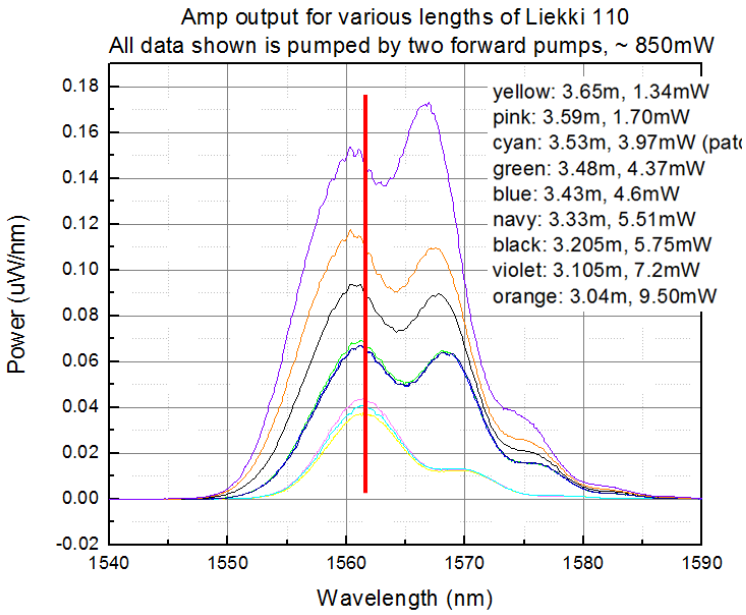

Figure 4.6: *Optimization of EDF length for a forward pumping configuration: Amplifier output spectrum with different EDF lengths in a forward pumping configuration. Input signal: carbon nanotube laser output (Figure 4.3), with average power of 0.19 mW.*

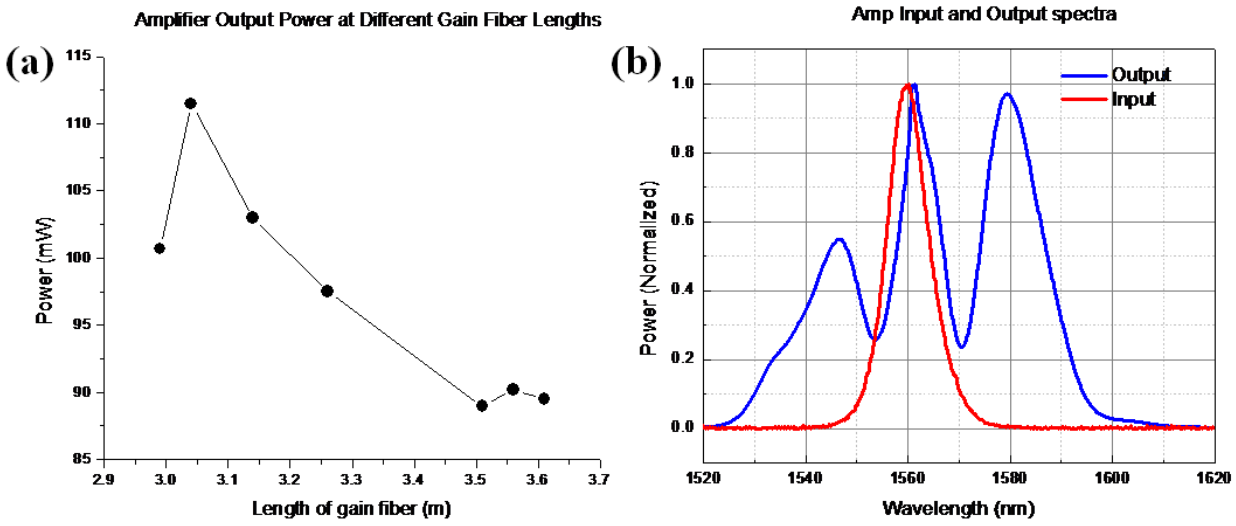

Figure 4.7: *Optimization of EDF length for backward pumping configuration. (a) Output power as a function of EDF length. (b) Normalized spectrum of amplifier input and output.*

for a backward pumping configuration. Figure 4.7 (a) shows the total average output power (with a pump power of 950 mW at 1480 nm) as a function of EDF length. A 3 meter EDF gave an output power of more than 100 mW. Figure 4.7 (b) shows the normalized spectrum for the amplifier input and output for comparison. The output spectrum is sensitive to polarization. By adding two polarization controllers (Figure 4.8), the gain at 1532.8 nm can be maximized to be 20 dB, which is sufficient for feeding the following CW EDFA (Figure 4.1).

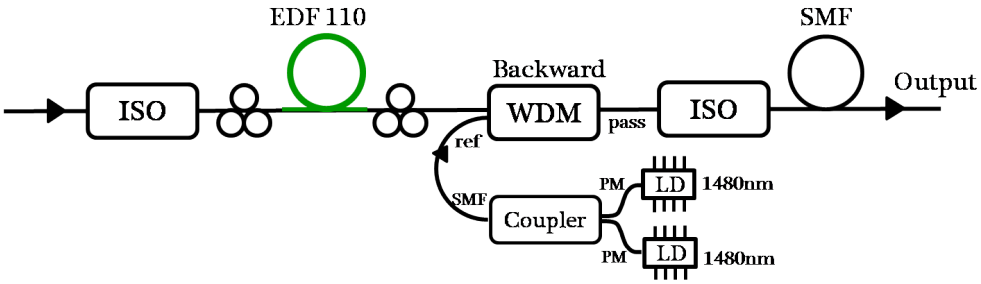

Figure 4.8: *Schematic setup of the home-made short-pulse amplifier.*

The next step is to optimize the length of SMF for pulse compression. This is again done by cutting back SMF fibers after the EDF until a minimum pulse duration is reached. The minimum pulse duration is expected to be below 100 fs, estimated from the spectral bandwidth of the amplifier output.

To measure the pulse duration, we measured the intensity autocorrelation (AC) trace of the output pulses [130]. The idea is to use the short pulse under test to measure itself. It involves splitting the pulse into two, variably delaying one with respect to the other, and spatially overlapping the two pulses in a second-harmonic-generation (SHG) crystal. The heart of this technique relies on the fact that the nonlinear processes (e.g. SHG), which are typically on a time scale of $\sim$ 1 fs, are faster than the pulse duration ($\sim$ 100 fs).

Figure 4.9 shows the autocorrelation trace of amplifier output pulses as we gradually cut back the SMF after the EDF. The black curve gives the minimum AC trace of 111 fs, corresponding to a pulse duration of 76 fs. The schematic setup of this short-pulse amplifier is shown in Figure 4.8. We have 87.5 cm SMF (including the isolator) before the EDF fiber,

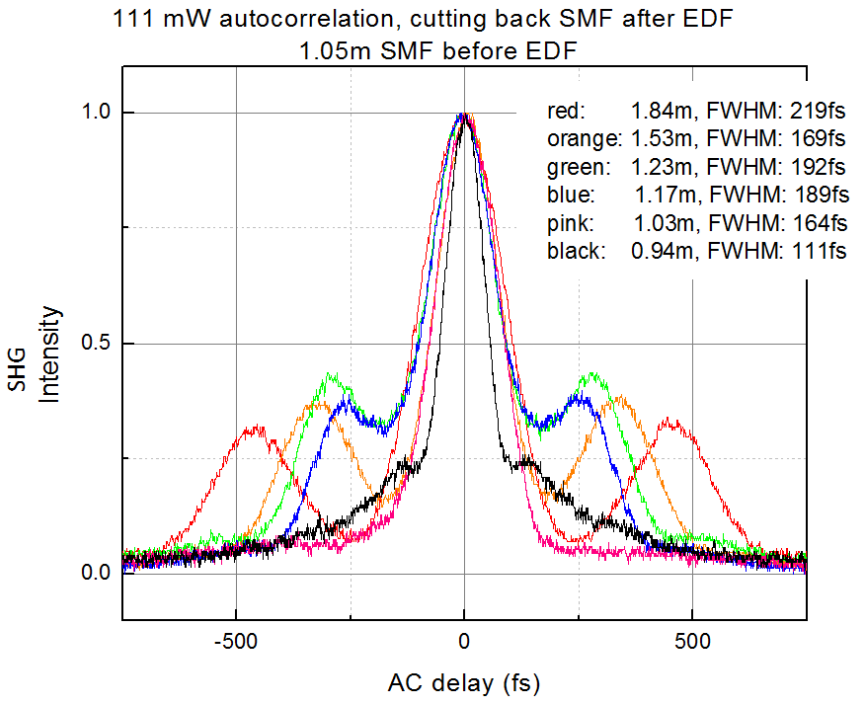

Figure 4.9: *Optimization of pulse duration. Autocorrelation trace of amplifier output pulses as we cut back SMF after EDF. Black curve shows the minimum AC trace of 111 fs.*

3.07 meter of EDF 110, and 94 cm SMF after the EDF.

To test this short-pulse EDFA, we conducted an optical heterodyne measurement between the comb light and a CW fiber laser (with linewidth of $\sim$ 1 kHz), stabilized to the acetylene P(13) transition at 1532.83 nm, illustrated in Figure 4.10. We compare the RF beatnote in two cases: using the comb (1) directly from the NPR laser oscillator, and (2) after being amplified by the short-pulse EDFA, as shown in Figure 4.10 (a) and (b), respectively. The resulting CW/comb beat SNR is 22 dB (with 1 MHz RBW) for the un-amplified comb and 8 dB for the amplified comb.

It is possible that the comb SNR was degraded during the amplification process because the highly backward pumped EDFA introduces significant amounts of ASE noise. However, there exists another possibility. Studies have shown that the InGaAs photodiode used for optical heterodyne measurements could be saturated due to high peak power of short pulses,

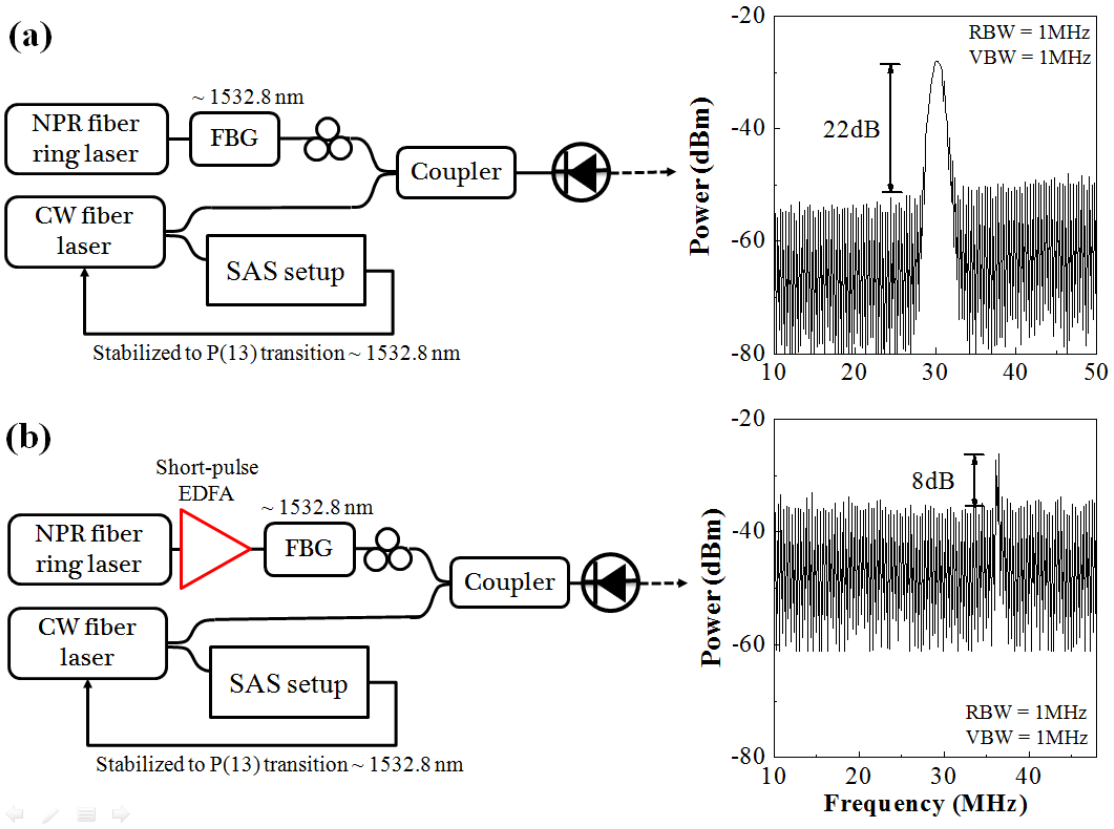

Figure 4.10: *Heterodyne beatnote between an acetylene-stabilized CW reference and (a) the oscillator comb, (b) the amplified comb using the short-pulse EDFA.*

which degrades the temporal response of the resulting electrical pulses in the photodetector, and leads to the degradation of the electrical SNR [131]. This can be easily tested by gradually decreasing the comb power, to see if the resulting RF beatnote SNR improves or not. The following section will talk about this photodetector saturation test.

4.3.2 Photodetector Saturation Test

In this section, I will present the two measurements we did to test if the photodetector was saturated during our heterodyne beat measurement discussed above. These two measurements follow the same experimental setup shown in Figure 4.10. One is to use a comb amplified by the short-pulse EDFA, the other is to use the NPR comb directly from the

oscillator. In both cases, the comb power was controlled by variable attenuation, while the CW fiber laser power was kept the same for all beat measurements.

Figure 4.11 shows the resulting CW/comb beatnote SNR for the amplified comb as a function of comb average power. We can see that the maximum SNR at 1 MHz RBW is less than 5 dB when the comb power is 10-20 μW. A higher (30 μW) or lower (1 μW) comb power results in a decrease in the beatnote SNR. Therefore, we can conclude that the photodetector was not saturated for the result shown in Figure 4.10(b).

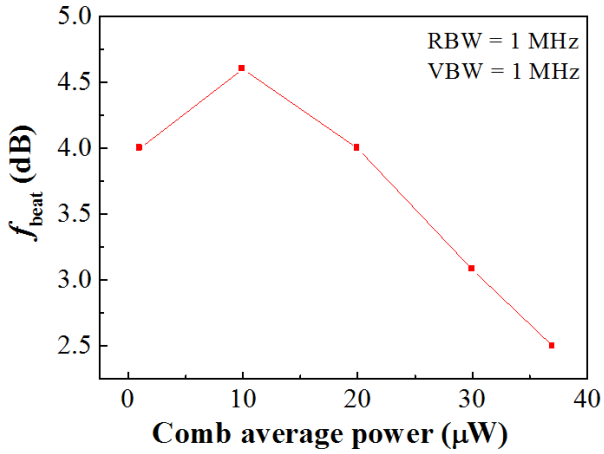

Figure 4.11: *The SNR of the heterodyne beatnote between an acetylene-stabilized CW reference and an amplified comb using the short-pulse EDFA as a function of comb average power. The CW laser power is held constant.*

The test we did for the oscillator comb was similar but more complicated. We took the same measurement in different cases, when the pulse duration was either stretched to 1.35 ps by adding long pieces of SMF, or compressed back to $\sim$ 100 fs by adding another piece of vascade fiber (Corning S1000) that has an opposite dispersion sign with respect to SMF. A schematic setup for the measurement is shown in Figure 4.12. The five cases represents five different pulse durations (ranging from ps to $\sim$ 100 fs) with similar comb average power. In each of the five cases, beatnote SNR was measured at various comb powers.

In order to have a larger comb power range for the test, we chose to perform the heterodyne beat at 1560 nm (instead of 1532.8 nm), which had the most optical power within the

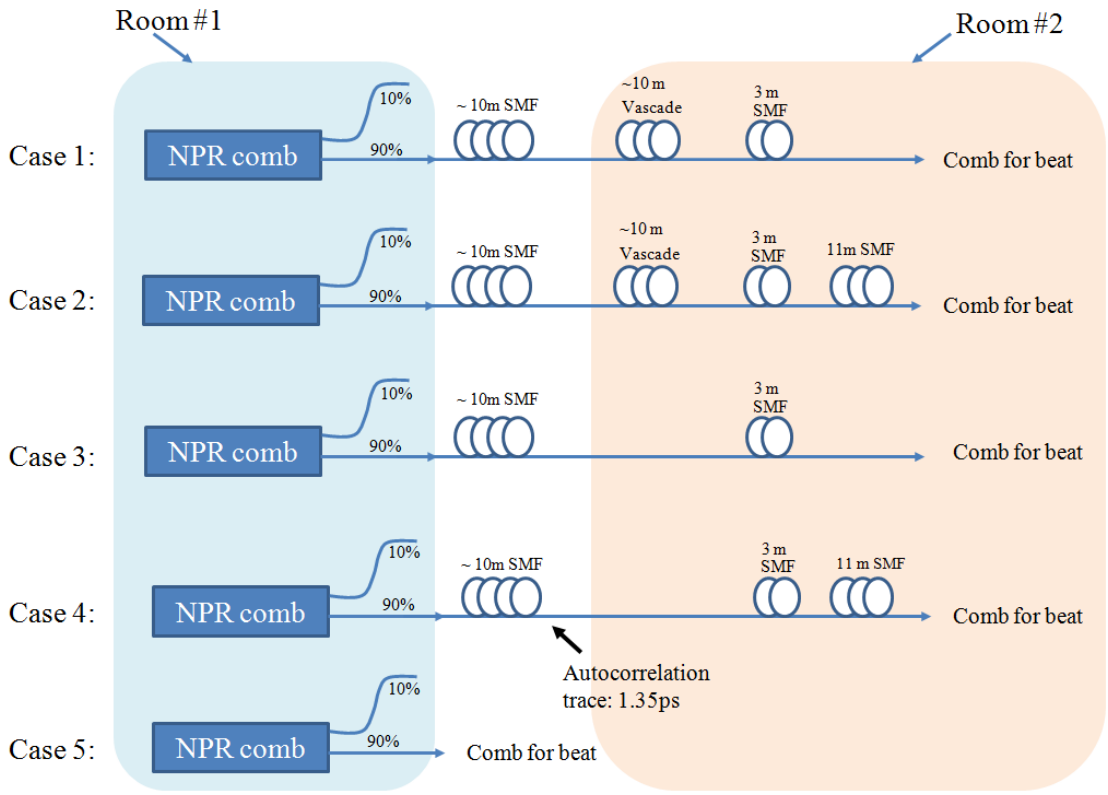

Figure 4.12: *Experimental setup for photodetector saturation test.*

comb spectrum (Figure 3.3). A 50 GHz FBG (at 1560 nm) was used after the oscillator output for the beatnote. The CW laser we used was a diode laser (Santec TS-210). Figure 4.13 shows the SNR of these beanote measurements in both log (left) and linear (right) scales as a function of the comb average power. Two different photodetectors (PD) were used in the measurement with different saturation power thresholds: a 125 MHz and 1 GHz PD, shown in the top and bottom plots, respectively. Detailed specifications of both detectors are given in Table 4.2.

The results in Figure 4.13 indicate a general trend for all measurements: the SNR of the beatnote increases with the comb power, for all the pulse duration cases we investigated. The data for both detectors are consistent with each other. At 1532.8 nm, the comb average power from the oscillator is below 2 μW within 100 GHz bandwidth, in which power range

	125 MHz PD	1 GHz PD
Model number	New Focus, 1811	New Focus, 1611
Material	InGaAs/PIN	InGaAs/PIN
Photodiode size	100 μ diameter	100 μ diameter
Rise Time	3 ns	400 ps
Output impedance	50 ohm	50 ohm
Min NEP	2.5 pW/rtHz	2.5 pW/rtHz
CW saturation power	120 μW@950nm	10 mW
Max pulse power	5 mW	N/A
Responsitivity	1 A/W @ 1500nm	1 A/W @ 1500nm

Table 4.2: *Comparison of specifications for the two photodetectors used in the saturation test. NEP: noise equivalent power.*

the SNR increases almost linearly with the comb average power. This indicates that for the previous beatnote measurements shown in Figure 4.10(a), the SNR is limited not by the photodetector saturation, but rather by the low comb power from the oscillator.

To summarize, if we look back at the results shown in 4.10, we now can say that both beatnote signals are not limited by the photodetector saturation, and should reflect the true SNR from the optical signal, based on the above photodetector saturation tests. This indicates that although we have enough optical power generated from the short-pulse EDFA at the wavelength of interest, a lot of ASE noise is introduced during the amplification process, probably due to fiber nonlinearities [93].

Therefore, we started to look for another method to build a low noise amplifier, which is what I will talk about in the next section. Later, I will show that using the following small gain CW amplifier, the comb SNR is well preserved. We were also able to observe the desired sub-Doppler error signal from an amplified comb tooth. In Section 4.3.4, I will discuss more details of noise analysis for comb amplification by comparing the performances of these two home-made EDFAs.

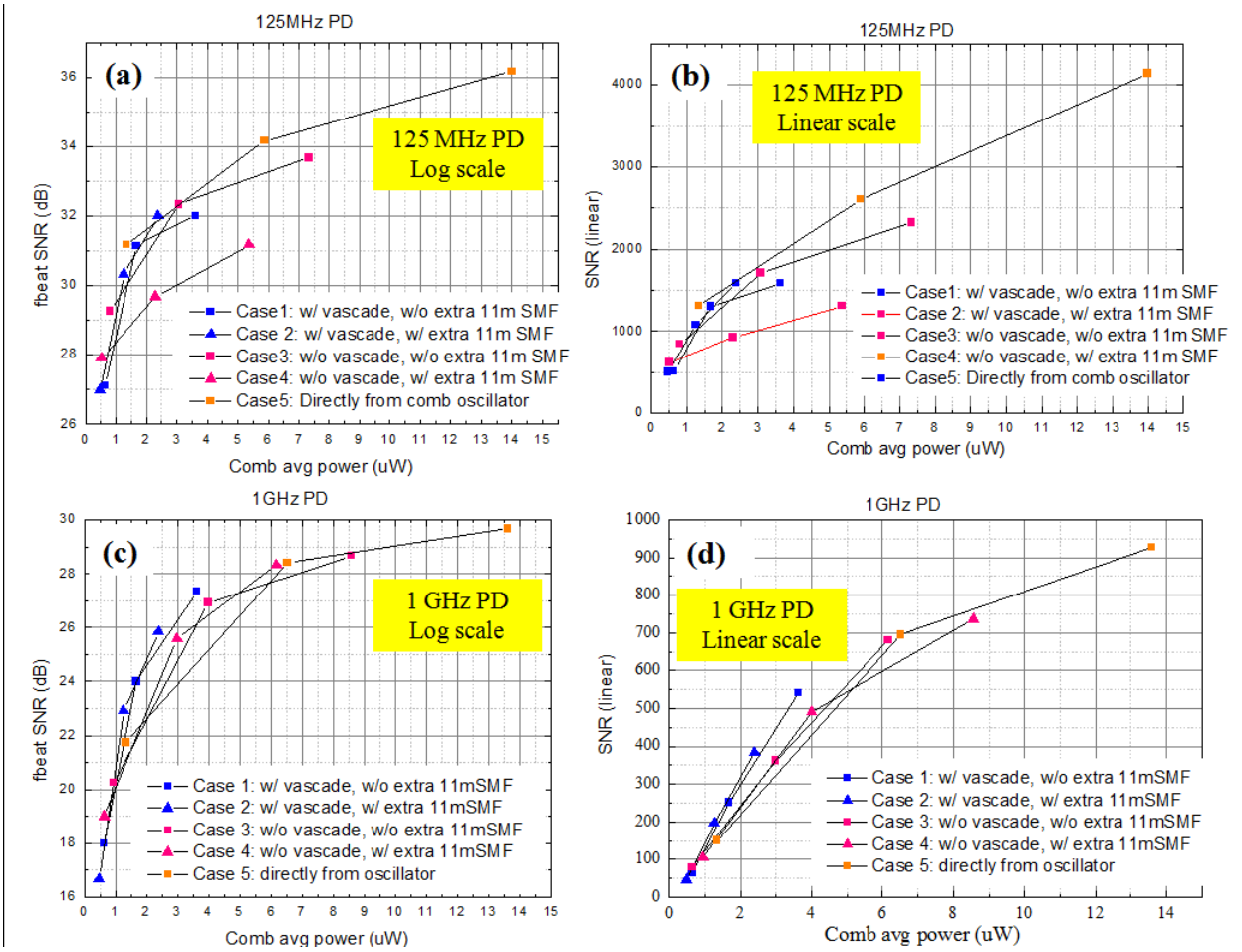

Figure 4.13: *The SNR of heterodyne beatnote between an acetylene-stabilized CW reference and comb directly from oscillator as a function of comb average power, using two different photodetectors (Table 4.2): (1) the 125 MHz PD, plot in (a) log, and (b) linear scale, and (2) the 1 GHz PD, plot in (c) log, and (d) linear scale.*

4.3.3 Small Gain CW Amplifier Design

The motivation for this amplifier design is from the early efforts made for telecom industry in the 1990s [132–136]. These studies are focused on how to design high gain EDFAs with low noise figure to compensate the loss of a CW signal during long distance transmission in fiber. Studies have shown that: (1) a narrow optical bandwidth of the signal is the key to a high SNR amplification [132], and also (2) the forward pumping scheme results in high gain and low noise amplification process when the backward-travelling ASE is suppressed

with an integrated isolator [135]. Therefore, we decided to build a low noise small gain CW amplifier, seeded with a narrow bandwidth comb around the wavelength of interest.

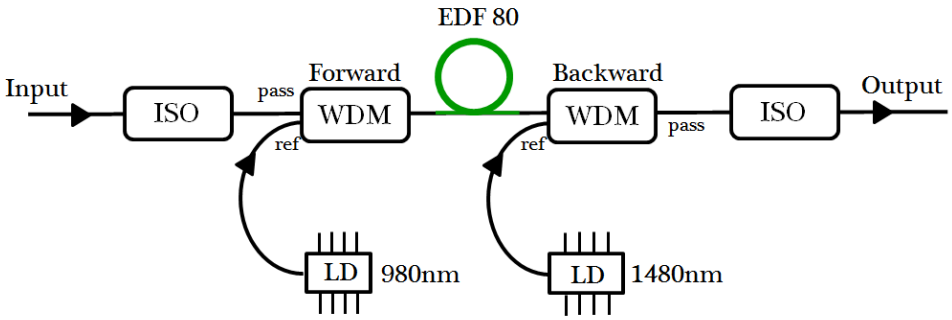

Figure 4.14: *Schematic setup of the home-made small gain CW amplifier.*

Sufficient gain could possibly be achieved by building multiple similar amplification stages without introducing much ASE noise.

The small gain CW EDFA was initially built by a previous graduate student in our group, May Ebbeni [137], and it has the codirectional pumping configuration shown in Figure 4.14. The length of the gain fiber (EDF 80) was re-optimized to be 107 cm for our purpose. The SMF length before and after the Erbium fiber are $\sim$ 4m and $\sim$ 4.2m, respectively.

Figure 4.15 shows the measured output power for both pump diodes of this EDFA. During our experiment for comb amplification, this amplifier is mainly forward pumped at 980 nm with a pumping power of 220 mW, and slightly backward pumped at 1480 nm (below 40 mW) to increase the output power so that it is enough to seed the following CW EDFA before the filtering cavity (Figure 4.1). With this pumping power, the EDFA has a small signal gain of 38 dB at 1532.83 nm when seeded with 1 μW CW light, and a large signal gain of 14 dB with 1 mW CW seed.

Similar heterodyne beat measurements were performed between the CW reference and the amplified comb (using this small gain CW EDFA). Results in Figure 4.16 show a beatnote SNR of 21 dB at 1 MHz RBW, almost the same as that from an un-amplified comb shown in Figure 4.10 (a) , which is about 22 dB.

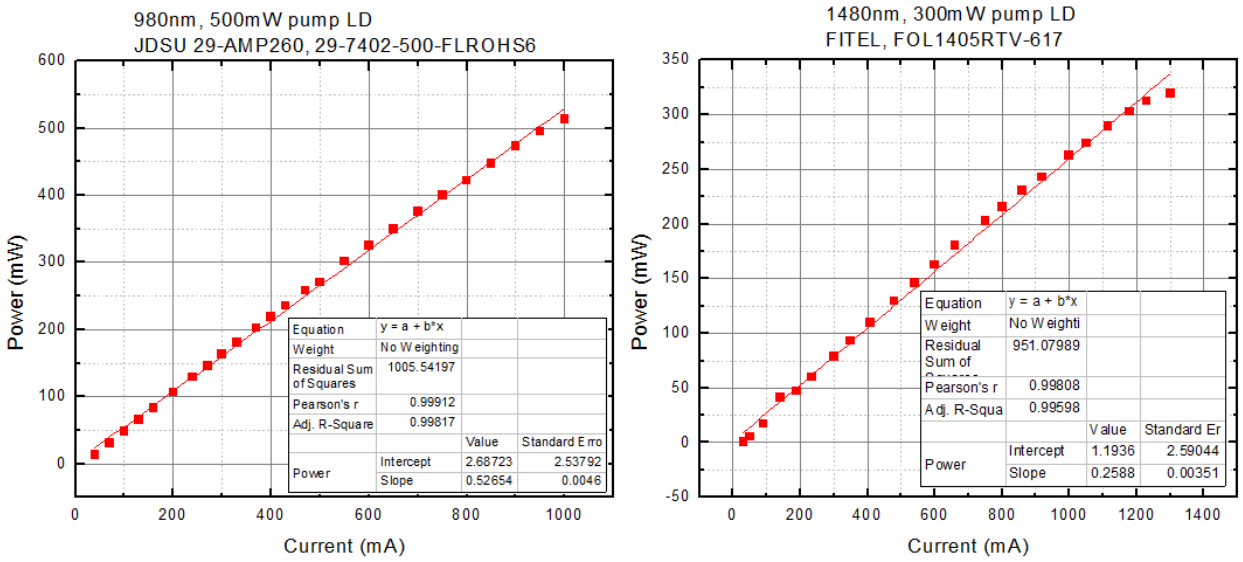

Figure 4.15: *Measured output power for the two pump diodes used in the small gain CW amplifier.*

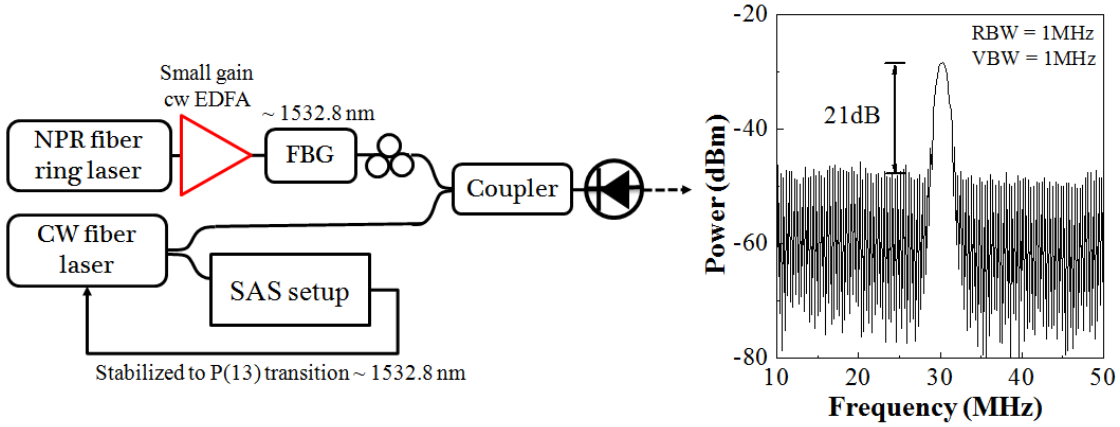

Figure 4.16: *Preserved comb SNR using small gain CW EDFA (as compared to Figure 4.10(a)). Heterodyne beatnote between an acetylene-stabilized CW reference and amplified comb.*

4.3.4 Comparison of Performance

In this section, we compare the performance of the two home-made fiber amplifiers: the short-pulse EDFA and the small gain CW EDFA. We will first look at the output spectrum from both EDFAs when seeded with the NPR comb, then we will compare the RF spectrum

when we beat the amplified comb with a CW source.

Figure 4.17 shows the comparison of three spectra: (1) the NPR oscillator comb (green), which also serves as the input for the short-pulse EDFA, (2) short-pulse EDFA output (blue), and (3) small gain CW EDFA output (red) when seeded with a filtered NPR comb at wavelength of 1532.8 nm with an optical bandwidth of 100 GHz. For comparison purpose, the intensity for all curves are offset by different amount to be shown in one plot.

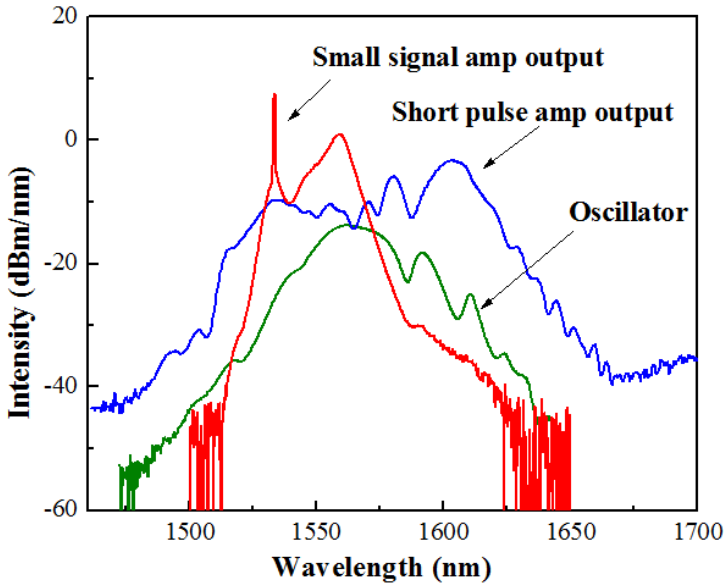

Figure 4.17: *Optical spectrum of (1) the NPR oscillator comb (green), (2) short-pulse EDFA output (blue), and (3) small gain CW EDFA output (red). The intensity for all curves are offset by different amounts for comparison.*

To investigate how the two EDFAs behave in terms of noise and signal amplification, we measured the electronic noise floor and the SNR of the CW/comb beat in three scenarios, shown in Figure 4.18. The CW fiber laser power was kept the same for all beat measurements, while the comb power was controlled by variable attenuation. The noise floor behaves like technical noise on the amplified comb. Figure 4.18 indicates that the small signal EDFA produces an amplified comb with a lower noise floor by a factor of ten and more than 15 dB higher SNR as compared to the short pulse EDFA. The degradation in SNR from the short pulse amplifier may be due to the fiber nonlinearities [93].

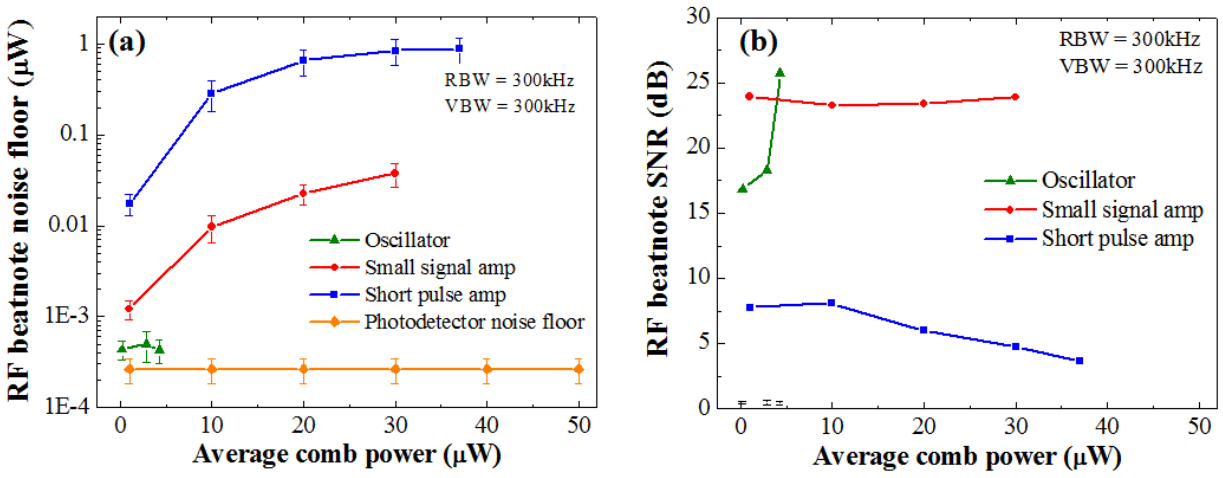

Figure 4.18: *(a) The electrical noise floor, and (b) SNR of RF beatnote (between comb and CW reference at 1532.8 nm) measured by RF spectrum analyzer as a function of comb power.*

4.4 Single Tooth Amplification by Injection locking DFB laser

The distributed-feedback (DFB) laser we used is a customized product from FITEL. It is a 14-pin butterfly package with integrated thermoelectric cooler, and photodiode, allowing for precise control over the pump current, which adjusts the output power, and the diode temperature, which fine tunes the lasing wavelength. Since we are going to inject light into the laser diode, this DFB laser is designed not to have the isolator that is built in regular DFB lasers. This results in a broad laser linewidth, which could be over 10 MHz. For DFB lasers, the outside reflection makes the linewidth broader, which is the reason why an optical isolator is usually integrated into the laser package for a narrow linewidth.

A safe injection optical signal to the DFB laser is related to the specified output power and wavelength of the laser. It is suggested by the manufacturer that: (1) 1.5-2.5 times higher power injection (i.e. 60-100mW injection power for our 40 mW output DFB laser) would be "red zone" for the damage, and (2) injection of shorter wavelength light than

DFB wavelength causes more damage. In our case, we seed the DFB laser with a frequency comb (pulsed laser) with an optical bandwidth of 7 GHz, so a 60 mW maximum peak power corresponds to an average power of 7.54 mW for a 2 GHz comb, and 35 mW for a 9.2 GHz comb. Our seeding powers are well below these threshold values.

We initially seeded in the DFB laser with multiple comb teeth, and discovered that this could cause mode competition between the seeds, which gave us an unstable sub-Doppler error signal. In order to seed the DFB laser with a single comb tooth, we had to re-build a 9.2 GHz Fabry-Perot filtering cavity. A stable sub-Doppler error signal was then obtained.

4.4.1 Threshold Test with a CW Seed

Before we tried the comb injection locking, we needed to know the minimum optical power required for a stable injection locking. Therefore, we did the following test, shown in Figure 4.19. Two CW fiber lasers are used in the test, with nearly identical wavelengths. One is acetylene-stabilized to the P(13) transition at 1532.8 nm with an accuracy of 20 kHz. The other is tunable by $\sim$ 10 GHz over the same wavelength. The DFB laser is seeded with the wavelength-tunable CW laser through a 3-port fiber circulator. The seeding optical power can be controlled with a variable attenuator. Here we have two RF beatnotes: $f_{\text{beat},1}$ and $f_{\text{beat},2}$, which are the beatnotes between the acetylene-stabilized CW fiber laser and (1) the CW seed, and (2) the injection-locked laser output, respectively. For perfect injection locking, $f_{\text{beat},2}$ must be stable as we observe on the RF spectrum analyzer, and also has identical frequency values as $f_{\text{beat},1}$.

Figure 4.20 (a) shows the RF spectrum of $f_{\text{beat},1}$. It has $\sim$ 70 dB SNR with 100 kHz RBW. Figure 4.20 (b-d) shows the RF spectrum of $f_{\text{beat},2}$ at various CW seeding power from 186 μW down to 1 μW. The beanote SNR is clearly degraded from almost 70 dB to 40 dB. On the RF spectrum analyzer, background noise for $f_{\text{beat},2}$ increases occasionally when the seeding power is below 10μW. However, even with 1 μW seeding power, $f_{\text{beat},2}$ follows $f_{\text{beat},1}$ very well, as we can see in Figure 4.20 (e). It plots the difference between the two

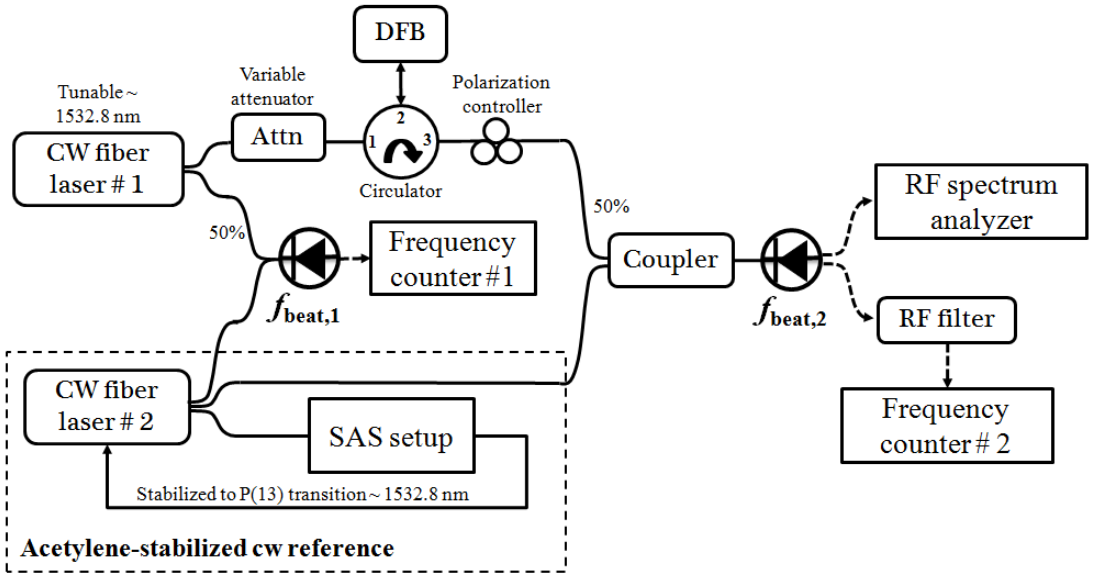

Figure 4.19: *Schematic setup for testing the CW seeding power threshold for DFB laser injection locking.*

beanotes as a function of time. The fact that the short term uncertainty is within +/- 400 Hz indicates a stable injection lock.

Knowing the minimum threshold power for a stable injection lock is about 10 μW, we tried to seed the DFB laser with a comb. With a 7 GHz fiber bragg grating (FBG) after the 2 GHz filtering cavity, the DFB seed includes three major comb teeth, and 42 suppressed teeth (due to the filtering cavity) with a suppression ratio of 35 dB. We expected that the DFB laser can be injection locked to any one of the three main teeth. After a simple calculation, we can estimate that with a total average seeding power of $\sim$ 50 μW, we have 16.6 μW for each of the three major teeth, and 5.3 nW for each of the suppressed teeth. The 10 μW injection locking threshold ensures that the DFB laser can be locked to any of the three major comb teeth but not the suppressed comb teeth.

However, our initial trials of the single tooth saturation experiment were not very successful. The sub-Doppler error signal could only be observed momentarily. It seemed like sometimes the DFB laser is locked to the desired injected comb tooth, but sometimes not.

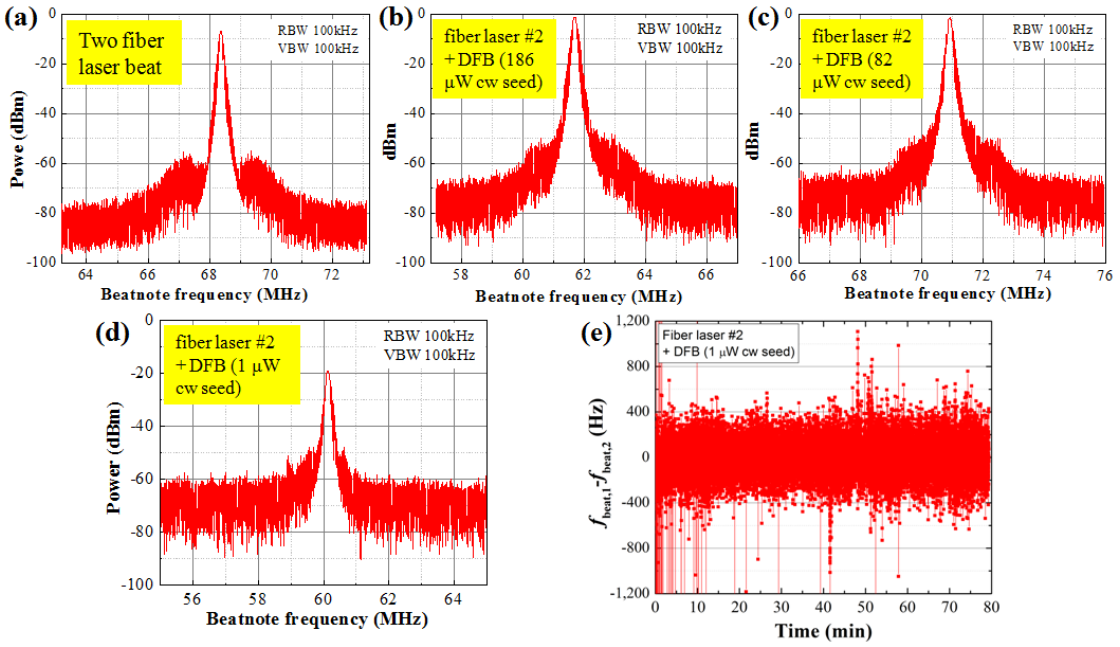

Figure 4.20: *(a) RF beanote between two CW fiber lasers at 1532.8 nm. (b-d) RF beanote between an acetylene-stabilized CW laser and injection locked DFB laser, with CW seeding power of 186 μW, 82 μW, and 1 μW, respectively. (e)Test of how well the DFB is injection locked to the seed. Y axis: $f_{beat,1}$-$f_{beat,2}$ in Figure 4.19*

This leads us to think that maybe there exists mode competition for the injection locking because we are seeding multiple comb teeth into the DFB laser simultaneously. The test measurement we did next confirmed our thought.

4.4.2 Mode Competition Test with Two CW Seeds

In order to find out if the unstable sub-Doppler error signal is due to mode competition between multiple comb teeth for the DFB laser injection locking, we did a simple test, shown in Figure 4.21: we injected two CW lasers into the DFB laser to mimic the case of two comb teeth seeding into the DFB laser at the same time. As we changed the two seeding lasers in terms of frequency spacing and relative optical power, we could see from the RF spectrum analyzer how these changes influence the RF beatnote, which represents the injection locking signal.

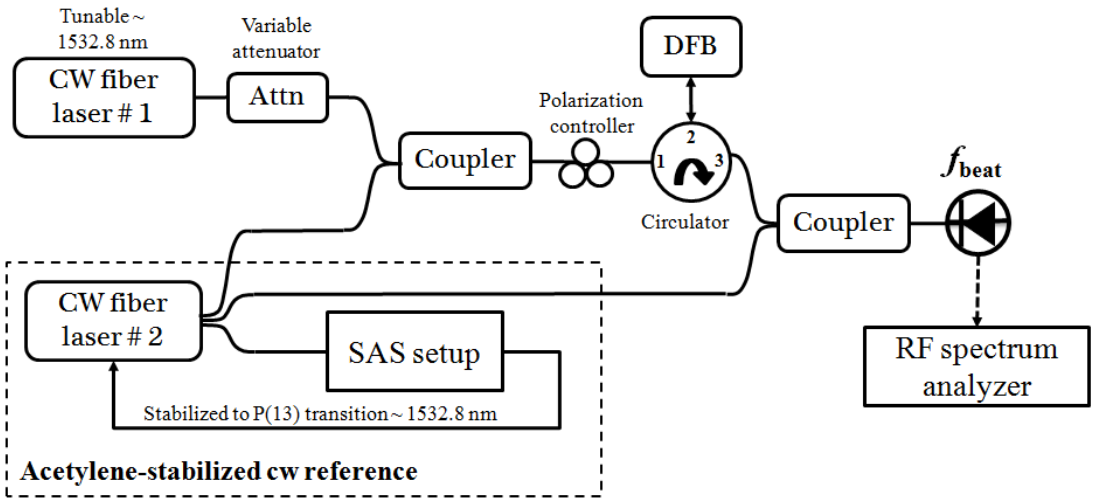

Figure 4.21: *Mode competition test. Schematic setup for seeding the DFB laser with two CW lasers separated by 2 GHz in frequency.*

We started with equal power of 140 μW for both CW lasers, which are tuned to be 0 to 2 GHz apart from each other in a step of 500 MHz. An unstable beatnote was observed on the spectrum analyzer all the time. The peak of the beatnote moved up and down by more than 30 dB, which we thought was caused by strong mode competition between the two CW seeds. This thought was confirmed by the fact that if we disconnected one of the seeds, the beatnote movement stopped immediately.

Then we began to reduce one of the two μW CW seeds to 50 nW by the variable attenuator (while the other CW seed remained at 140 μW). This was a mimic of the case when there was one major tooth and another suppressed tooth with 35 dB suppression ratio. The beatnote was very stable with a high SNR of more than 65 dB with 1 MHz RBW, as we tuned the frequency spacing from 2 GHz to below 100 MHz. This indicates that with a 35 dB suppression ratio of the filtering cavity, the suppressed comb teeth would not affect the injection locking.

Next we wanted to measure what was the minimum required suppression ratio for a stable injection lock, so we started to gradually increase the 50 nW CW seeding power until

we saw an unstable beanote. For a suppression ratio of 11 dB, the peak of the beatnote started to move up and down by 4 dB. The measured minimum suppression ratio threshold was about 21 dB for a stable beatnote.

4.4.3 Producing Error Signal

So far, we have confirmed that the unstable sub-Doppler error signal is due to the mode competition between multiple comb teeth to the DFB laser. This tells us that only one comb tooth can be injected into the DFB laser for a stable locking. The minimum bandwidth of the FBGs we found available at that time was 7 GHz at the wavelength of interest (1532.8 nm). This means that we need to have a comb with repetition rate higher than 7 GHz out

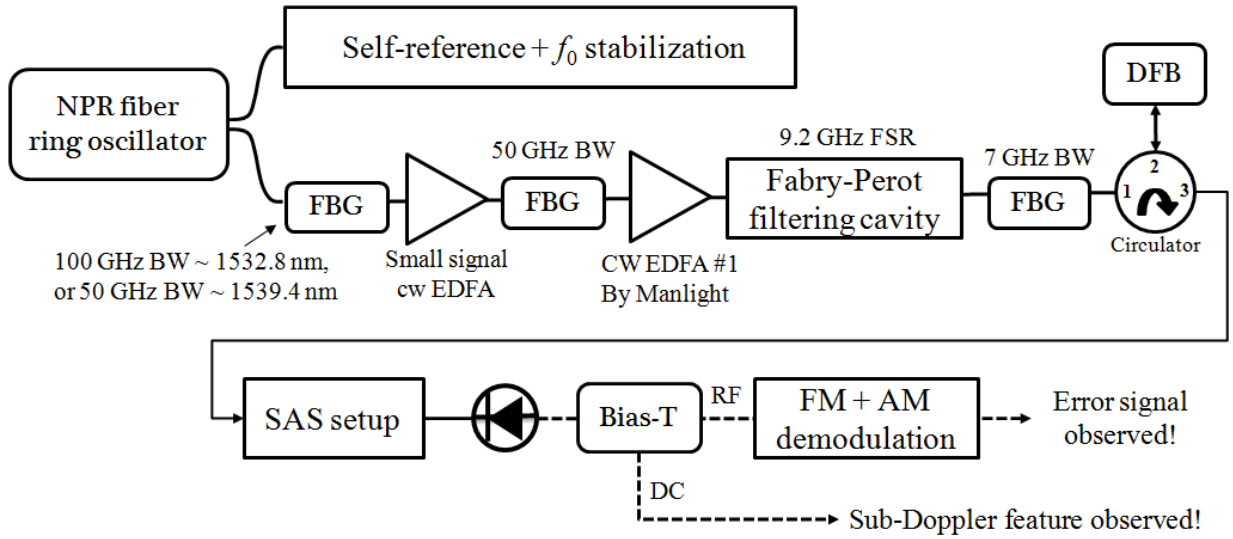

Figure 4.22: *Schematic setup for single tooth saturated absorption spectroscopy producing a stable sub-Doppler error signal for amplified single comb tooth.*

from the filtering cavity. Therefore, we re-built a plano Fabry-Perot filtering cavity with a free spectral range (FSR) of 9.2 GHz (see Section 3.4.3 for details). The final optical power seeded into the DFB laser became $\sim$ 25 μW, including only one major tooth and 79 suppressed teeth 25 dB below the major teeth. Based on the above measurement, this

power level is sufficient for a stable injection locking without interruption by the suppressed teeth.

With the configuration shown in Figure 4.22, as we scan the comb repetition rate frequency by scanning the driving voltage to the PZT inside the ring oscillator, we are able to scan a single comb tooth over an acetylene transition. Both a stable sub-Doppler feature, as well as the error signal were successfully produced for the first time from an amplified comb tooth at 1532.8 nm, shown in Figure 4.23 (a) and (b), respectively. The sub-Doppler feature in Figure 4.23 (a) is obtained when the repetition rate is scanned by $\sim$ 40 Hz, limited by the scan range of the driver, the target comb line near 1532.8 nm can be moved by $\sim$ 88MHz across the P(13) overtone transition, which gives only part of the Doppler-broadened feature, as compared to the complete feature shown in Figure 2.2 (a) using a CW fiber laser as the source. In both cases, the sub-Doppler features have comparable linewidth.

Considering that the CW fiber laser reference developed in our lab is stabilized to the P(13) line at 1532.8 nm, in order to measure comb stability using this CW reference, we need to stabilize a comb line to a different wavelength, in other words, to a different overtone transition line of acetylene. The choice of a different line is a balance for the following two factors: (1) the erbium-fiber gain spectrum prefers higher wavelengths (close to 1560 nm) for low noise amplification. (2) the $\nu_1+\nu_3$ overtone transition covers spectrum only up to 1545 nm (Figure 1.8), higher wavelengths than 1533 nm gives lines with weaker absorption strength, which requires higher pressure loaded inside the hollow-core fiber for the same fractional absorption. This leads to a higher pressure broadening of the sub-Doppler signal. Our final choice of the new transition is the P(23) line at $\sim$ 1539.4 nm.

The two sub-Doppler signals generated at 1532.8 nm and 1539.4 nm are shown in Figure 4.23 (b) and (c). Both error signals have a width of $\sim$ 17 MHz, and high signal-to-noise ratio (SNR) of $\sim$ 150 within a 4 kHz RF bandwidth, comparable to that from a CW fiber laser (Figure 2.12 (b)). The optimum parameters for both DFB lasers producing these sub-Doppler signals are listed in Table 4.3.

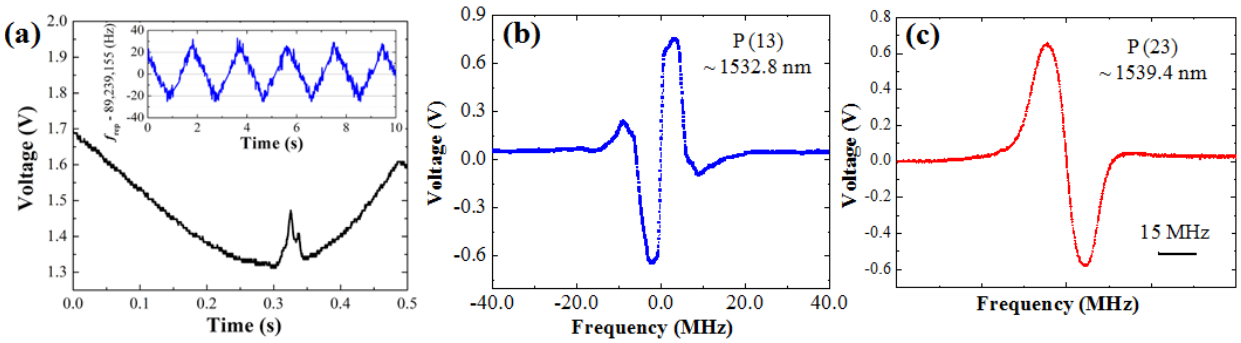

Figure 4.23: *Sub-Doppler error signals for amplified single comb tooth at two wavelengths: (a) 1532.8 nm, and (b) 1539.4 nm.*

Item	DFB laser #1	DFB laser #2
Output fiber type	PM	PM
Maximum output power	40 mW	40 mW
Peak emission wavelength	1532.636 nm	1539.323 nm
Optimum pump current	240 mA	172 mA
Optimum temp	30.15°C	32.92°C
Temp tuning	0.01 nm/1°C	0.01 nm/1°C
DFB seed (single tooth)	25 μW	50 μW

Table 4.3: *Optimized parameters for two DFB lasers used for injection.*

4.5 Single Tooth Amplification Directly by EDFA

So far, we have successfully generated sub-Doppler error signals by injection locking the DFB laser to a single comb tooth. However, one has to purchase the DFB laser diode at a specific wavelength in the first place in order to use this technique. For more wavelength flexibility, we tried to replace the DFB laser by a commercial EDFA (Model number: HWT-EDFA-B-PM-C27X, by Manlight) to directly amplify a comb tooth in the last amplification stage. In order to have enough optical seeding power to the EDFA, we had to modify the comb amplification setup slightly. Figure 4.24 shows the setup after the modification. The 50 GHz FBG before comb filtering was replaced by a 7 GHz FBG to reduce the comb bandwidth being amplified. Given a fixed 300 mW total average output power, the power per each comb tooth was increased. This essentially produces about 100 μW out from the

7 GHz FBG after comb filtering, which is enough to run the EDFA. The sub-Dopper error signal generated in this case is shown in Figure 4.24, with a SNR of about 4.

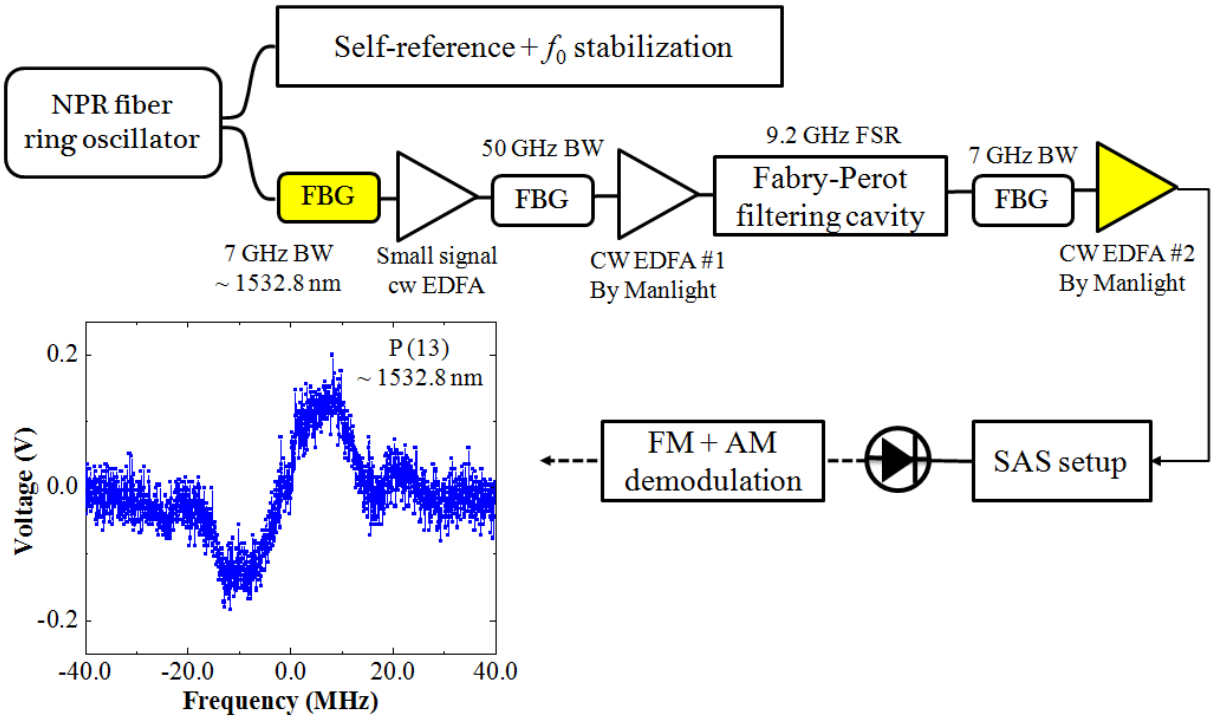

Figure 4.24: *Single tooth amplification directly by CW EDFA (instead of DFB injection locking).*

A few factors account for the degradation of SNR. First, by using a 7 GHz FBG instead of 50 GHz, the seeding power for EDFA I is reduced from - 2 dBm to - 8 dBm, which is close to the minimum input power required (- 10 dBm). Also, 1532 nm is not a preferred wavelength by erbium-doped fiber amplifiers, due to the fact that it is on the edge of the erbium gain spectrum. Because of these two factors, significant ASE noise can be produced from this amplification process before comb filtering. Second, the light out from the 7 GHz FBG after the comb filtering is not a pure single comb tooth. It spectrally includes an isolated comb tooth plus a number of suppressed comb teeth with peak power 25 dB below the major filtered tooth. In the case of injection locking, only the major tooth can be recognized and locked, while other suppressed teeth are ignored in that their optical power

are below the threshold for injection locking. However, studies have shown that both the major teeth and suppressed teeth experience uneven power amplification in an EDFA [93]. This results in significant SNR degradation for the single tooth useful for our experiment.

Chapter 5

Frequency reference characterization

In the previous chapter, we discussed the stabilization of a 89 MHz fiber-based frequency comb by locking two comb parameters: a single optical comb tooth at 1539.4 nm to an acetylene overtone transition, and the carrier-envelope offset frequency to an RF synthesizer which is referenced to a GPS-disciplined Rb oscillator. In this chapter, we characterize the comb stability by comparing the comb with a CW fiber laser reference. In Section 5.1, we first look theoretically at how the comb stability is limited by the references being used in the system. This can be done by mathematically interpreting the fractional instability of any comb tooth in terms of the fractional stability of the RF and/or optical references used for stabilizing the comb. Then in Section 5.2, we will show our experimental stability results by comparing the comb to a CW fiber laser reference at 1532.8 nm, $\sim$ 7 nm away from the stabilized comb tooth. Our result shows that the comb has short term stability over an order of magnitude better than the Rb oscillator at 100 ms gate time. In Section 5.3, we present a few tests about investigating possible frequency shifts induced by the various erbium-doped fiber amplifiers (EDFAs) used in our system. Our results show that at 1532.8 nm, there is no frequency shift of more than 20 kHz for comb amplification. This 20 kHz error bar is mainly due to the low comb SNR during the heterodyne beat measurement.

5.1 Calculation of Comb Instability

Comb stabilization requires the stabilization of two locking points. The conventional way to stabilize a comb is to lock both f_0 and f_{rep} to RF references. In this work, we lock f_0 to an RF reference, and f_{rep} is stabilized by locking a single comb tooth to an optical reference. There are also other possible locking schemes, such as (1) locking f_{rep} to a RF reference, and a single comb tooth to an optical reference, and (2) locking two optical comb teeth to two separate optical references. In this section, we evaluate the comb stability for all these four possible approaches.

Based on comb's equation, the frequency of any optical comb tooth can be expressed as

$$\nu_n = n \times f_{\text{rep}} + f_0 \tag{5.1}$$

Here, n is the mode number of the comb tooth, f_{rep} and f_0 are the repetition rate and carrier-envelope offset frequency of the comb, respectively. Assuming we are investigating the stability for the m th comb tooth, rewriting Eqn 5.1, we have

$$\nu_m = m \times f_{\text{rep}} + f_0 \tag{5.2}$$

If we stabilize a single tooth to an optical reference, the stabilized comb tooth frequency can be written as

$$\nu_{\text{ref}} = n_{\text{ref}} \times f_{\text{rep}} + f_0 \tag{5.3}$$

5.1.1 Scheme 1: f_0 and f_{rep} Locked to RF reference

In the first approach stabilizing the comb, both the carrier-envelope offset frequency f_0 and the repetition rate frequency f_{rep} are locked to an RF reference. The fractional uncertainty

of the m^{th} comb tooth under test can be expressed as

$$\sigma_{\nu_m} = \frac{\delta\nu_m}{\nu_m} = \frac{m\delta f_{\text{rep}} + \delta f_0}{\nu_m} = m \times \frac{\delta f_{\text{rep}}}{\nu_m} + \frac{\delta f_0}{\nu_m} \tag{5.4}$$

From Eqn 5.4, we can see that the microwave instability of f_{rep} is transferred to the optical regime via the comb equation due to large m number. The larger term in Eqn 5.4 will determine the overall stability.

In our case, m is on the order of 10^6, f_{rep} is about 90 MHz, f_0 is 30 MHz, one third of f_{rep}. Thus, f_0 is negligible compared to $m \times f_{\text{rep}}$ in the denominator. Eqn 5.4 can be written as

$$\begin{aligned} \sigma_{\nu_m} = \frac{m\delta f_{\text{rep}} + \delta f_0}{m \times f_{\text{rep}} + f_0} &\approx \frac{\delta f_{\text{rep}}}{f_{\text{rep}}} + \frac{1}{m} \times \frac{\delta f_0}{f_{\text{rep}}} \\ &= \frac{\delta f_{\text{rep}}}{f_{\text{rep}}} + \frac{1}{3m} \times \frac{\delta f_0}{f_0} \end{aligned} \tag{5.5}$$

From the GPS spec sheet, the fractional microwave stability of the GPS-disciplined Rb oscillator σ_{GPS} is $2 \times 10^{-11}\ \tau^{-\frac{1}{2}}$. This number sets the upper limit of the uncertainty of f_{rep}, that is

$$\sigma_{\text{GPS}} = 2 \times 10^{-11}\tau^{-\frac{1}{2}} \sim \frac{\delta f_{\text{rep}}}{f_{\text{rep}}} \tag{5.6}$$

Since f_0 is on the order of a few Hz, the second term in Eqn 5.5 is on the order of 10^{-13}, two orders of magnitude smaller than the first term. Therefore, the stability of an RF referenced fiber comb, in this case, is mostly limited by the f_{rep} stability.

5.1.2 Scheme 2: f_0 to RF, Single Tooth to Optical Reference

In the second scenario for comb stabilization, f_0 is locked to an RF reference, while a single optical comb tooth ν_n is locked to an optical reference ν_{ref}, and again we look at the stability

for the m th comb tooth. From the comb's equation, we have

$$\nu_m = m \times f_{\text{rep}} + f_0, \text{ and} \tag{5.7}$$

$$\nu_{ref} = n_{\text{ref}} \times f_{\text{rep}} + f_0 \tag{5.8}$$

We can deduce the frequency of the m th tooth from the above two equations by cancelling f_{rep}

$$\nu_m = \frac{(n_{\text{ref}} - m) \times f_0 + m \times \nu_{\text{ref}}}{n_{\text{ref}}} = (1 - \frac{m}{n_{\text{ref}}})f_0 + \frac{m}{n_{\text{ref}}}\nu_{\text{ref}} \tag{5.9}$$

Therefore, the fractional instability of ν_m is

$$\begin{aligned} \sigma_{\nu_m} = \frac{\delta\nu_m}{\nu_m} &= \frac{(1 - \frac{m}{n_{\text{ref}}})\delta f_0 + \frac{m}{n_{\text{ref}}}\delta\nu_{\text{ref}}}{\nu_m} \\ &= (1 - \frac{m}{n_{\text{ref}}}) \times \frac{\delta f_0}{\nu_m} + \frac{m}{n_{\text{ref}}} \times \frac{\delta\nu_{\text{ref}}}{\nu_m} \\ &= (1 - \frac{m}{n_{\text{ref}}})\frac{f_0}{\nu_m} \times \frac{\delta f_0}{f_0} + \frac{m}{n_{\text{ref}}}\frac{\nu_{\text{ref}}}{\nu_m} \times \frac{\delta\nu_{\text{ref}}}{\nu_{\text{ref}}} \\ \equiv \sigma_{m1} + \sigma_{m2} \end{aligned} \tag{5.10}$$

Eqn 5.10 shows that the stability of the mth comb tooth is the sum of two terms: one is from the uncertainty of f_0 locking ($\delta f_0/f_0$), the other is from the single tooth locking ($\delta\nu_{\text{ref}}/\nu_{\text{ref}}$), denoted by σ_{m1} and σ_{m2}, respectively.

If we plot σ_{m1}, σ_{m2} and the sum of both as a function of the wavelength under test λ_m, we should be able to tell which term dominates the comb stability around the stabilized comb tooth ($\sim$ 1539.4 nm). Figure 5.1 shows this result particularly for our NPR comb. We can see that the comb instability σ_m follows σ_{m2} if the uncertainty of single tooth locking ($\sigma_{\text{ref}} = \delta\nu_{\text{ref}}/\nu_{\text{ref}}$) is on the order of 10^{-12} or 10^{-13} (blue and black curves). In other words, the uncertainty of comb teeth within 400 nm of the stabilized comb tooth is dominated by the single tooth locking. In this locking scenario, the uncertainty of the optical tooth locking (σ_{ref}) needs to be at least on the order of 10^{-14} (red curve) to be less dominant and

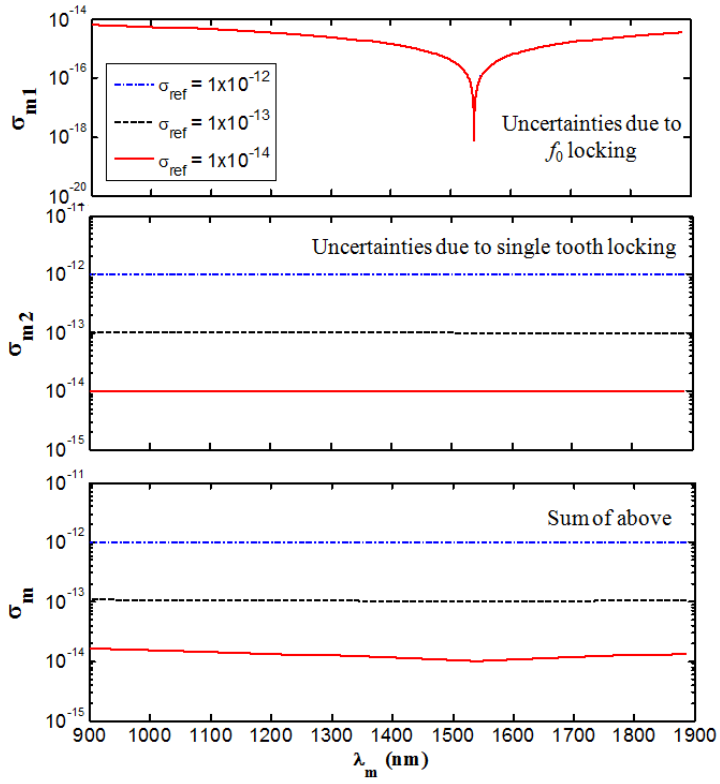

Figure 5.1: *Scenario # 2: f_0 and single tooth locking. The fractional stabilities of the m^{th} comb tooth at 1 s gate time are calculated assuming different frequency uncertainties for single tooth locking, represented by blue, black and red curves.*

comparable to the instability induced by f_0 locking.

5.1.3 Scheme 3: f_{rep} to RF, Single Tooth to Optical Reference

The third comb stabilization scenario involves f_{rep} locked to an RF reference and one comb tooth locked to an optical reference. We can rewrite the frequency of the m^{th} comb tooth in terms of f_{rep} and ν_{ref}. Subtracting Eqn 5.8 from Eqn 5.7 gives

$$\nu_m = (m - n_{\mathrm{ref}})f_{\mathrm{rep}} + \nu_{\mathrm{ref}} \tag{5.11}$$

Therefore, we have

$$\begin{aligned}\sigma_{\nu_m} = \frac{\delta\nu_m}{\nu_m} &= \frac{(m - n_{ref})\delta f_{\text{rep}} + \delta\nu_{\text{ref}}}{\nu_m} \\ &= (m - n_{\text{ref}}) \times \frac{\delta f_{\text{rep}}}{\nu_m} + \frac{\delta\nu_{\text{ref}}}{\nu_m} \\ &= (m - n_{\text{ref}})\frac{f_{\text{rep}}}{\nu_m} \times \frac{\delta f_{\text{rep}}}{f_{\text{rep}}} + \frac{\nu_{\text{ref}}}{\nu_m} \times \frac{\delta\nu_{\text{ref}}}{\nu_{\text{ref}}} \\ \equiv \sigma_{m1} + \sigma_{m2}\end{aligned} \tag{5.12}$$

where σ_{m1} and σ_{m2} denote the first and second term in Eqn 5.12, respectively.

In this comb locking scenario, the uncertainties of f_{rep} can be multiplied to the optical frequency domain. However, if the stability of the RF reference is high enough, the multiplied RF instability contribution may still be below the instability contribution from the optical reference, that is, $\sigma_{m1} < \sigma_{m2}$. Assuming the fractional uncertainty of our optical tooth locking (σ_{ref}) is on the order of 10^{-12} at 1 s gate time, we would like to investigate how well our RF reference (for f_{rep} locking) needs to be locked in order to satisfy this condition ($\sigma_{m1} < \sigma_{m2}$).

Figure 5.2 shows σ_{m1}, σ_{m2} and the sum of both terms as a function of wavelength. The stabilized single tooth is again at $\sim$ 1539.4 nm. For our NPR comb, we look at three cases in which the uncertainty of the RF reference ($\sigma_{\text{rep}} = \delta f_{\text{rep}}/f_{\text{rep}}$) is on the order of 10^{-11}, 10^{-12} and 10^{-14}, representing the performance of a Rb oscillator, hydrogen maser, and a Caesium clock at 1 s gate time, respectively. The uncertainty for single tooth locking ($\sigma_{\text{ref}} = \delta\nu_{\text{ref}}/\nu_{\text{ref}}$) is assumed to be 10^{-12} for all three cases.

In our lab, we have a GPS-disciplined Rb oscillator (GPS-Rb) as the RF reference. If we stabilize f_{ref} to the GPS-Rb, the multiplied RF instability σ_{m1} will surpass the instability induced by optical comb tooth locking σ_{m2}, and thus the overall comb stability σ_m will be dominated by f_{rep} locking, as shown in the blue curves in Figure 5.2. If we were to use a hydrogen maser (10^{-12}) as the RF reference, represented by the red curves, these two contributions (σ_{m1} and σ_{m2}) will be comparable. If an even better RF reference with

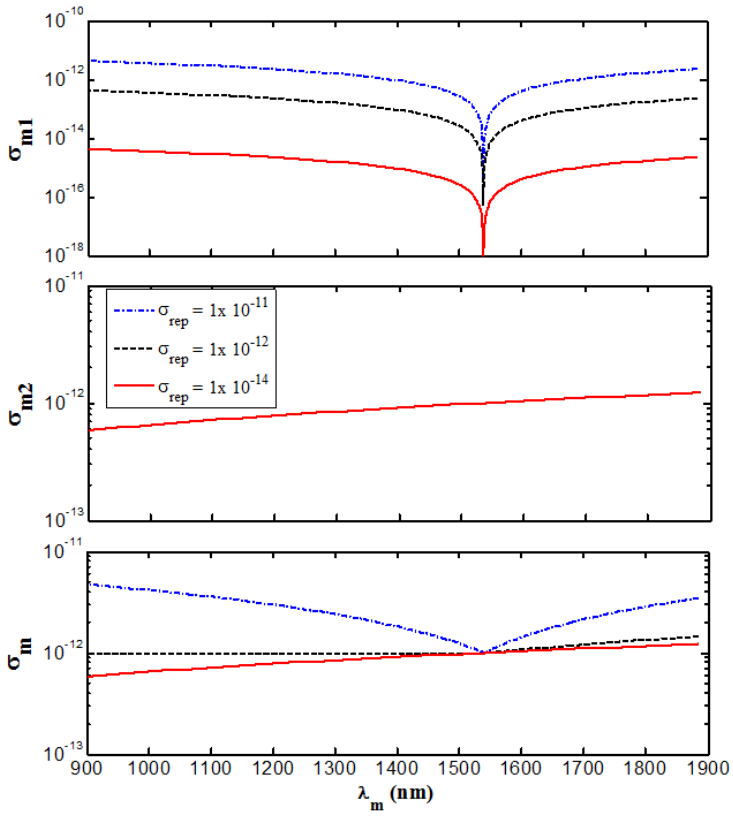

Figure 5.2: *Scenario # 3: f_{rep} and single tooth locking. The fractional instability of the m^{th} comb tooth at 1 s gate time calculated assuming different frequency uncertainties for f_{rep} locking, represented by blue, black and red curves.*

uncertainty of 10^{-14} was used in our setup, the comb stability (σ_m) would then be limited by the single tooth locking (σ_{m2}), indicated by the red curves in Figure 5.2.

5.1.4 Scheme 4: Two Teeth Locked to Optical References

In the fourth locking scenario, the comb is stabilized by locking two optical comb teeth $\nu_{\mathrm{ref},1}$ and $\nu_{\mathrm{ref},2}$ to two different optical references. Based on comb's equation, we have

$$\nu_{\mathrm{ref},1} = n_{\mathrm{ref},1} \times f_{\mathrm{rep}} + f_0 \tag{5.13}$$

$$\nu_{\mathrm{ref},2} = n_{\mathrm{ref},2} \times f_{\mathrm{rep}} + f_0 \tag{5.14}$$

Subtract Eqn 5.14 from Eqn 5.13 gives

$$f_{\text{rep}} = \frac{\nu_{\text{ref},1} - \nu_{\text{ref},2}}{n_{\text{ref},1} - n_{\text{ref},2}} \tag{5.15}$$

Eqn 5.13 and 5.14 gives

$$f_0 = \frac{n_{\text{ref},2}\nu_{\text{ref},1} - n_{\text{ref},1}\nu_{ref,2}}{n_{\text{ref},2} - n_{\text{ref},1}} \tag{5.16}$$

Plugging Eqn 5.15and 5.16 back into Eqn 5.2,

$$\begin{aligned} \nu_m =& m \times \frac{\nu_{\text{ref},1} - \nu_{\text{ref},2}}{n_{\text{ref},1} - n_{\text{ref},2}} + \frac{n_{\text{ref},1}\nu_{\text{ref},2} - n_{\text{ref},2}\nu_{\text{ref},1}}{n_{\text{ref},1} - n_{\text{ref},2}} \\ =& \frac{(m - n_{\text{ref},2})\nu_{\text{ref},1} - (m - n_{\text{ref},1})\nu_{\text{ref},2}}{n_{\text{ref},1} - n_{\text{ref},2}} \end{aligned} \tag{5.17}$$

Thus, we have the fractional stability of ν_m

$$\begin{aligned} \sigma_{\nu_m} = \frac{\delta\nu_m}{\nu_m} &= \frac{m - n_{\text{ref},2}}{n_{\text{ref},1} - n_{\text{ref},2}} \times \frac{\delta\nu_{\text{ref},1}}{\nu_m} - \frac{m - n_{\text{ref},1}}{n_{\text{ref},1} - n_{\text{ref},2}} \times \frac{\delta\nu_{\text{ref},2}}{\nu_m} \\ &= \frac{m - n_{\text{ref},2}}{n_{\text{ref},1} - n_{\text{ref},2}} \times \frac{\nu_{\text{ref},1}}{\nu_m} \times \frac{\delta\nu_{\text{ref},1}}{\nu_{\text{ref},1}} + \frac{n_{\text{ref},1} - m}{n_{\text{ref},1} - n_{\text{ref},2}} \times \frac{\nu_{\text{ref},2}}{\nu_m} \times \frac{\delta\nu_{\text{ref},2}}{\nu_{\text{ref},2}} \\ &\equiv \sigma_{m1} + \sigma_{m2} \end{aligned} \tag{5.18}$$

For simplicity, we assume both comb teeth are stabilized independently from each other and have comparable fractional stabilities both on the order of 10^{-12} at 1 s gate time. In this case, we would like to study how the wavelength separation of two stabilized comb teeth, denoted by $d = \lambda_{\text{ref},1} - \lambda_{\text{ref},2}$, influences the NPR comb stability. Here we assume $\lambda_{\text{ref},1}$ is $\sim$ 1539.4 nm, and vary $\lambda_{\text{ref},2}$. The top two plots in Figure 5.3 show the instability contributions from the stabilization of both comb teeth. We can see that the comb stability, that is the sum of both contributions shown in the bottom plot, can be greatly enhanced by increasing the separation between the two stabilized teeth d. The shorter the separation d is, the faster the comb stability degrades as we look at comb teeth further away from the stabilized teeth. For example, if the two locked teeth are separated by only 3 nm, represented by the blue

curve in the bottom plot, within 100 nm of the locked tooth at 1539.4 nm, that is $\lambda \sim 1440$ nm, the stability σ_m already degrades by two orders of magnitude. In contrast, if $d = 300$ nm, shown by the red curve in the same plot, the degradation is less than a factor of two even for comb teeth at 900 nm, that is almost 340 nm away from one of the locked teeth at 1239.4 nm.

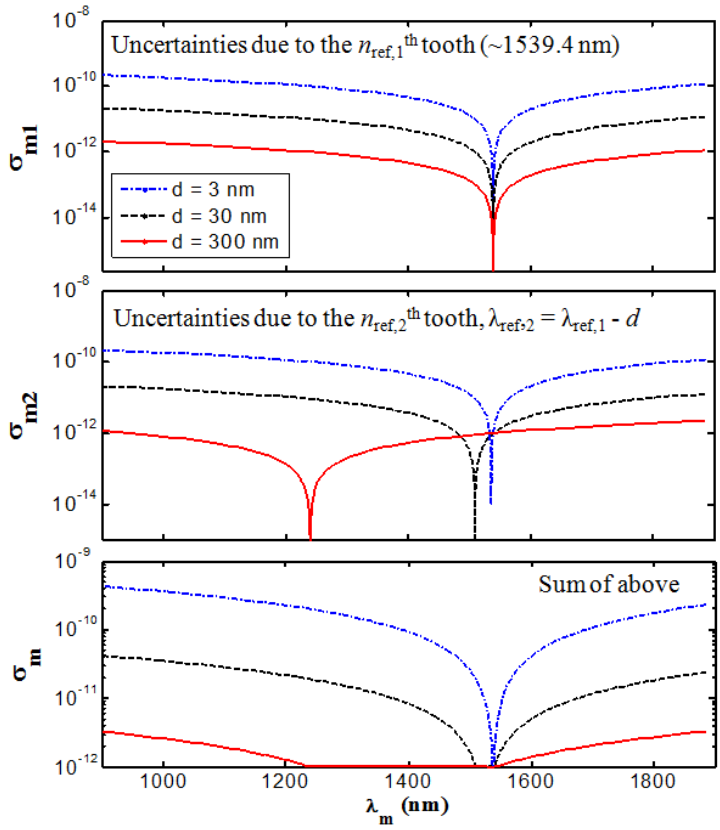

Figure 5.3: *Scenario # 4: Two optical comb teeth locking. The fractional stability of the m th comb tooth at 1 s gate time are calculated at different separation wavelengths ($d = \lambda_{ref,1} - \lambda_{ref,2}$) between the two stabilized teeth, represented by blue, black and red curves. $\lambda_{ref,1} = 1539.4$ nm.*

Therefore, for the two comb teeth locking scenario, the wavelength separation between the two stabilized teeth should be more than 100 nm to achieve a comb stability that does not degrade too fast. However, common gases for referencing the wavelengths near telecom wavelengths usually have limited absorption bandwidth of only 30 - 50 nm [138].

This means that we need to choose two different gases (one could be acetylene) that have absorption bands separated by over 100 nm for comb teeth stabilization. Considering the various factors, such as absorption strengths and pressure broadening coefficients, which significantly influence the saturated absorption error signal, this two comb teeth locking approach can be a challenging task for practical implementation.

5.2 Reference Characterization

Direct measurement of an optical frequency (THz), i.e. using a frequency counter, is not possible because the response of electronics is limited to the ns (or GHz) level. Indirect measurement can be done through a heterodyne comparison with another optical reference. This so-called *optical heterodyne measurement* involves two optical frequencies incident on a fast photodetector, resulting in a RF signal, which is the difference between the two optical frequencies. The RF beatnote signal can be easily measured by a frequency counter. The stability of the optical frequency under test can then be deduced from the RF beat signal.

To characterize a reference, we look at both the *stability* and *accuracy* of the measured optical frequency. For a portable reference, short term stability (averaging time less than one second) is more important than the long term stability. Our results show that the optically referenced comb has short term stability over an order of magnitude better than the GPS-Rb oscillator, which serves as the RF reference for all the synthesizers and frequency counters. For long averaging times, our beatnote data show a slow drift of hundreds of kHz over tens of hours. The second subsection will be mainly focused on efforts to diagnose the source(s) of this slow drift.

5.2.1 Stability

To investigate the comb stability, an optical heterodyne beat measurement can be done by comparing the comb with a stable CW source. Ideally, we would like to study the comb

stability at a number of wavelengths, and investigate how it degrades as the wavelength of interest goes further away from the stabilized comb tooth. However, this requires multiple narrow-linewidth CW references at different wavelengths. In our lab, we only have one available CW fiber laser source around 1532.83 nm. Therefore, the comb stability at 1532.83 nm is measured, that is 7 nm away from the stabilized single tooth.

Figure 5.4(a) illustrates the measurement between the stabilized comb and the CW reference. There are four servo loops involved in the system: (1) f_0 is locked to GPS-Rb oscillator using a PPC box, (2) the Fabry-Perot filtering cavity is locked to the comb using a home-made servo, (3) a single comb tooth is locked to the P(23) overtone transition of $^{12}C_2H_2$ using a PPC box, and (4) a CW fiber laser is locked to the P(13) overtone transition of $^{12}C_2H_2$ using a PPC box.

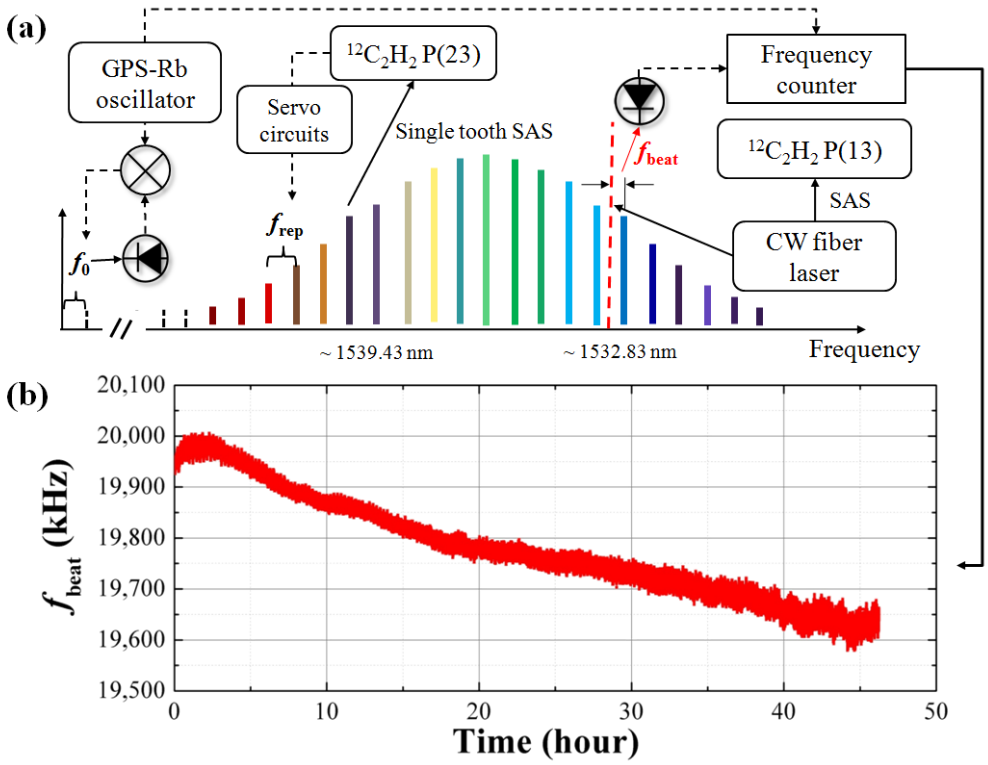

Figure 5.4: *Optical heterodyne beatnote measurement between the an optically referenced comb and a CW fiber laser reference.*

Here, we will say a few more words about the CW reference setup. It is a CW fiber laser referenced to an acetylene overtone transition using the same saturated absorption technique. The SAS setup is nearly identical to the one used for single tooth locking (Figure 2.2. The only difference is the hollow-core fiber being used, described in detail in Section 2.3, with an SEM image shown in Figure 2.4 right.

The resulting RF beatnote between the comb and the CW reference is shown in Figure 5.4 (b), with a gate time of 100 ms. Although the beatnote did show a slow drift at large time scales, it was quite remarkable that the entire system remained locked for 46 hours without much degradation in the short term stability.

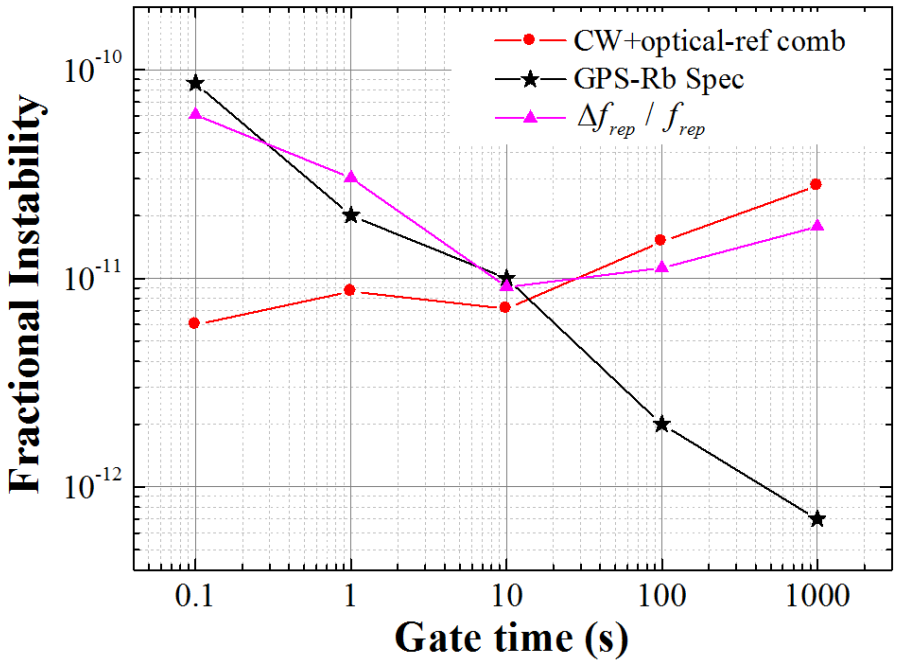

Figure 5.5: *Fractional instability of the optically-referenced comb at 1532.8 nm compared to a CW fiber laser reference.*

If we deduce the stability of this optical tooth based on this RF beat, we could plot the fractional instability of this optical comb tooth. The red dots in Figure 5.5 show the deduced instability from the first three hours of the 46-hour measurement. It has a short time fractional instability of 6×10^{-12} at 100 ms gate time, which is over an order of

magnitude better than the GPS-disciplined Rb oscillator, shown in black stars [139].

If we plot the fractional instability of f_{rep} from the same measurement, shown in the pink triangles, we find it is limited by the GPS-Rb at short time scales. This is because all frequency counters are referenced to GPS-Rb. To measure the real f_{rep} stability at short time scales, we would have to have an RF reference better than GPS (e.g. hydrogen maser).

However, it is important to keep in mind that when conducting a single heterodyne experiment, the Allan deviation calculated from the measurement is merely the upper limit for the instability from both references. In order to know if this result is limited by the comb or the CW reference, we need to know the short term stability for the CW reference.

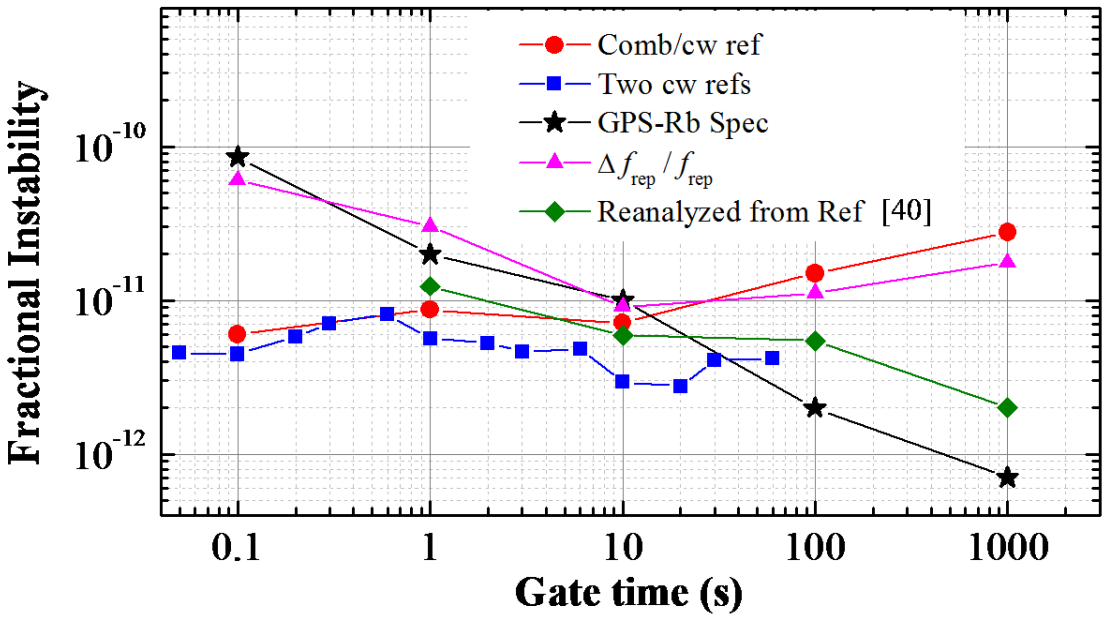

Figure 5.6: *Comparison of the fractional instability between the optically referenced comb stability measurement and the CW fiber reference extrapolated from (1) two identical CW reference beating [38], and (2) heterodyne beat between the CW reference and a carbon nanotube fiber laser frequency comb (data reanalyzed from Ref. [140]).*

The stability of the CW reference used for comparison was extrapolated from two previous measurements. One is the heterodyne beating of two identical CW fiber references in our lab [38], shown in blue squares in Figure 5.6. They are two fiber lasers stabilized

independently to two separate acetylene-filled hollow-core fibers using the same SAS technique. Therefore, the blue squares data shows the relative instability between the two CW references, which is independent of the GPS limit. The other is the beat between one CW fiber reference and a carbon nanotube fiber laser-based frequency comb referenced to the GPS-Rb oscillator, originally published in [140]. The original data set has been reanalyzed to correct an error and shows improved stability at 1000 s (green diamonds). Because the stability of the optically referenced comb is comparable to that of the CW reference at short time scales, the stability of our optical reference at 1539.43 nm has been transferred to the measured tooth at 1532.83 nm, without much degradation over ~ 7 nm.

For comparison, the frequency comb of Hu *et al.* [141] is referenced to a Rb vapor cell by stabilizing a single tooth to the two-photon transition at 778 nm and f_{rep} to an electromagnetically induced transparency resonance at 3 GHz; the microwave reference limits the optical fractional instability to be about 10^{-10} at 1 s, and 10^{-11} at 1000 s. Stability similar to that of Figure 5.5 is achieved in the direct comb spectroscopy demonstrated by Heinecke *et al.* [43] based on an optically-referenced 10 GHz Ti:sapphire comb. There, a single tooth is stabilized to a Rb transition using sub-Doppler spectroscopy while the comb repetition rate is locked to a H maser. The stability of a comb tooth 20 nm away from the Rb resonance is measured to be 7×10^{-12} at 1 s gate time.

Although the optically referenced comb data (red dots) shows great improvement in short term stability over the GPS/Rb oscillator, the beatnote shows a slow drift at a time scale of a few hours, which correlates with drift in the repetition rate. This slow drift is independent of leakage of vacuum chambers, temperature or humidity, and is likely due to offsets in the locking electronics. We believe with improved servo electronics, the system is expected to have comparable long-term stability as the single CW reference data (green diamonds) in Figure 5.6.

5.2.2 Understanding the Long-Term Drift

For the above beatnote measurements, our data shows a slow drift (Figure 5.4) on a time scale of a few hours. This is probably due to the single comb tooth locking because similar drifting behaviour was also observed in the repetition rate signal, shown in Figure 5.7. We do not fully understand exactly what causes the lock point to drift. In this section, we will present a few tests that have been done in order to diagnose the source(s) of the long time drift.

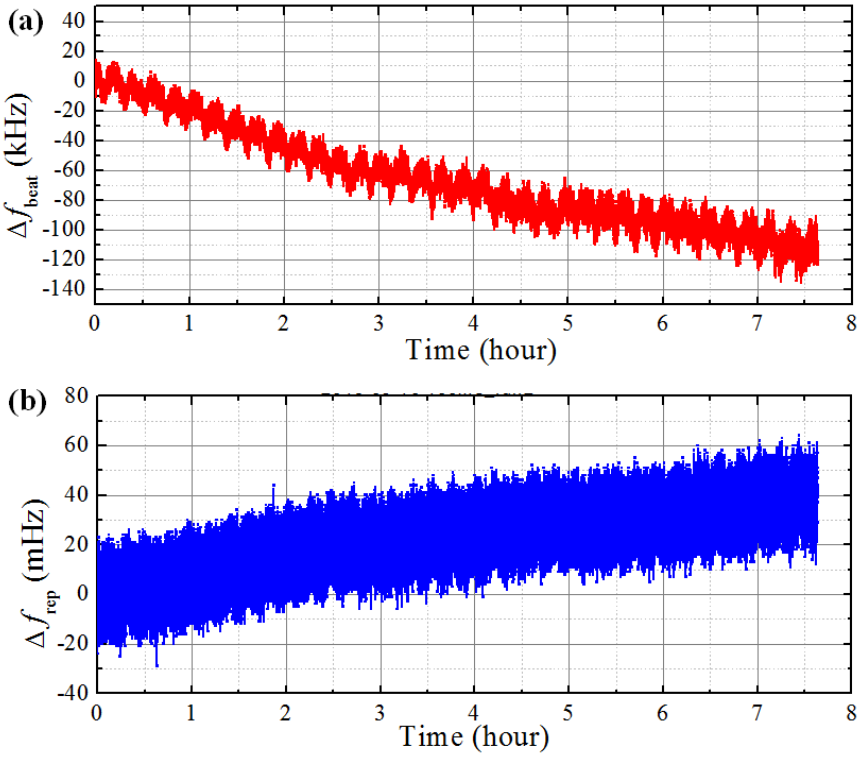

Figure 5.7: *Heterodyne beat between an optically referenced comb and a CW reference at 1532.8 nm. The RF beatnote shows a long term drift, associated with a repetition rate drift. (a) RF beanote data offset by 23 MHz. (b) Resulting repetition rate from the optically referenced comb, offset by 89.4 MHz.*

Slow drift in the beatnote signal has been observed at various rates, ranging from 3-18 kHz/hr (mostly above 10 kHz/hr). Several factors could contribute to this drift: (1) the contamination of the acetylene gas due to a slow vacuum leak broadens the sub-Doppler

feature, and may add some extra offset to the error signal due to the Doppler background variation, which changes the zero lock point. (2) We have observed a beatnote frequency variation associated with the temperature cycle caused by the air conditioner in our lab. A slow drift in the beatnote may be caused by temperature change in the lab. This can be easily tested by monitoring the temperature for a long time, and compared with the beatnote data. (3) The PPC servo box used for single tooth locking has a gain-dependent offset (from a few mV to over a hundred mV). Usually, we can remove this offset by changing

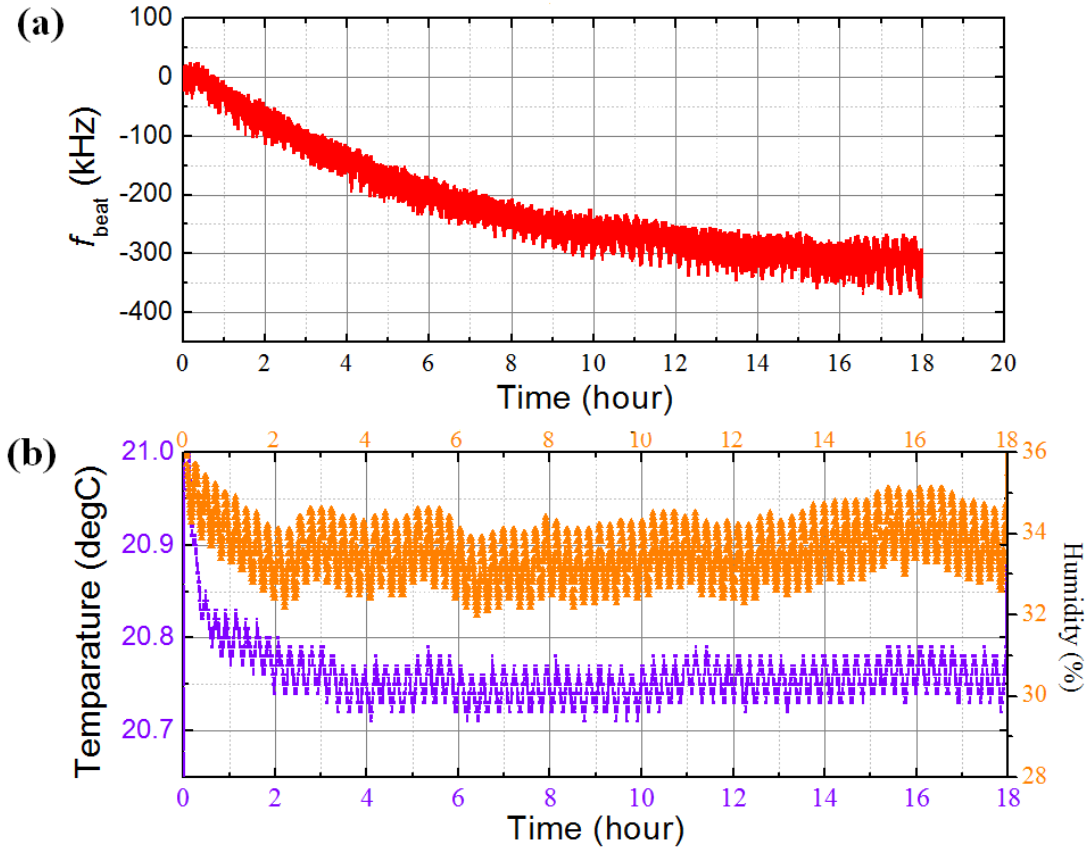

Figure 5.8: *Trying to figure out the drift: (a) Beatnote measurement between optically referenced comb and a CW reference at 1532.8 nm. (b) temperature and humidity in the lab during the measurement.*

the input offset of the servo box before data acquisition starts. However, for a long time (a couple of hours) measurement, the optimum gain for locking the single tooth may change

slightly over time.

To check if the chamber contamination is associated with this drift, we switched two reference setups because the two pairs of vacuum chambers have slightly different leaking rate. A 110 kHz drift was still observed during a 7.5-hour measurement, shown in Figure 5.7.

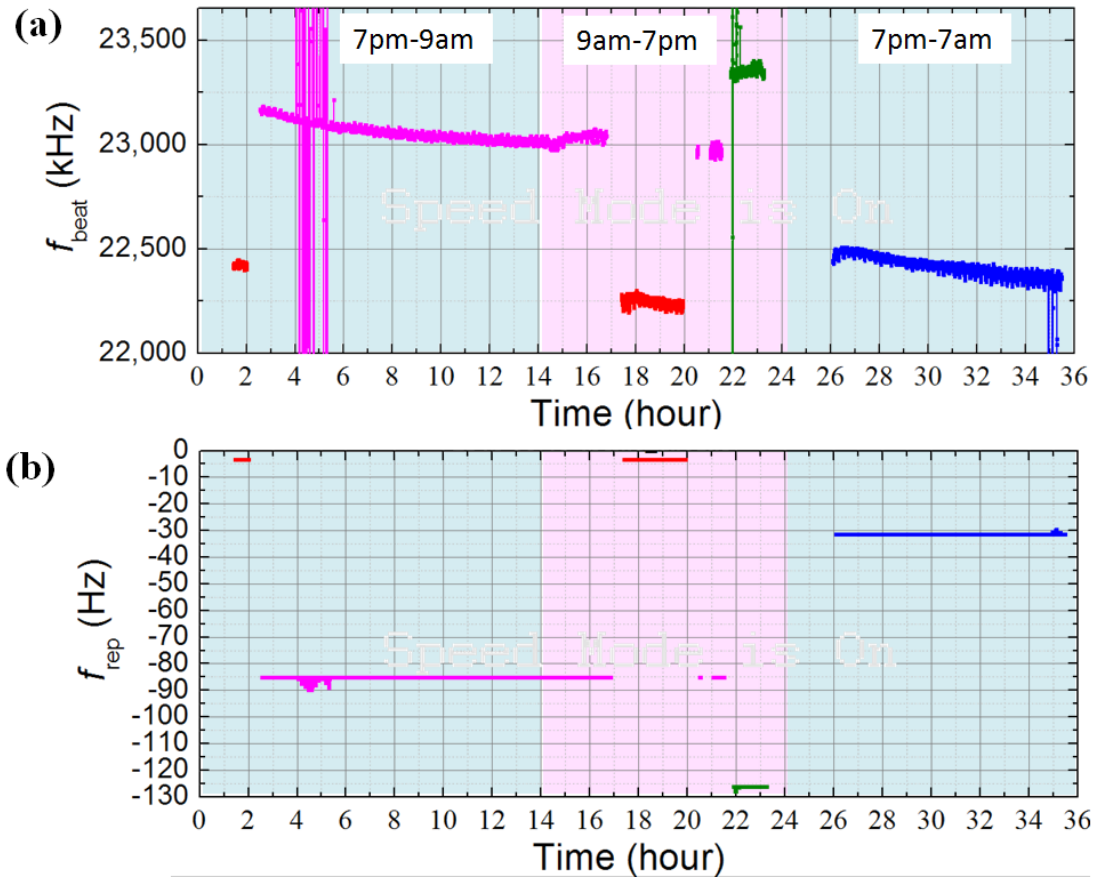

Figure 5.9: *Trying to figure out the drift: (a) Beatnote measurement between the optically referenced comb and a CW reference at 1532.8 nm. Relocking the filtering cavity resulted in locking to different comb teeth, represented in different colors. (b) Resulting repetition rate signal due to the single tooth locking. Discontinuity occurs when a different comb tooth is locked to the acetylene transition.*

For temperature concerns, we made boxes using thermal-isolating materials to isolate the two hollow-core fibers in both reference setups and repeated the measurement. However, similar drift was still observed. A more rigorous measurement was done by recording the

temperature and humidity near the two reference setups while taking the beatnote data. For an 18 hour measurement shown in figure 5.8, the beatnote drifted by 300 kHz (16.7 kHz/hr) while the temperature and humidity remained nearly unchanged in the lab.

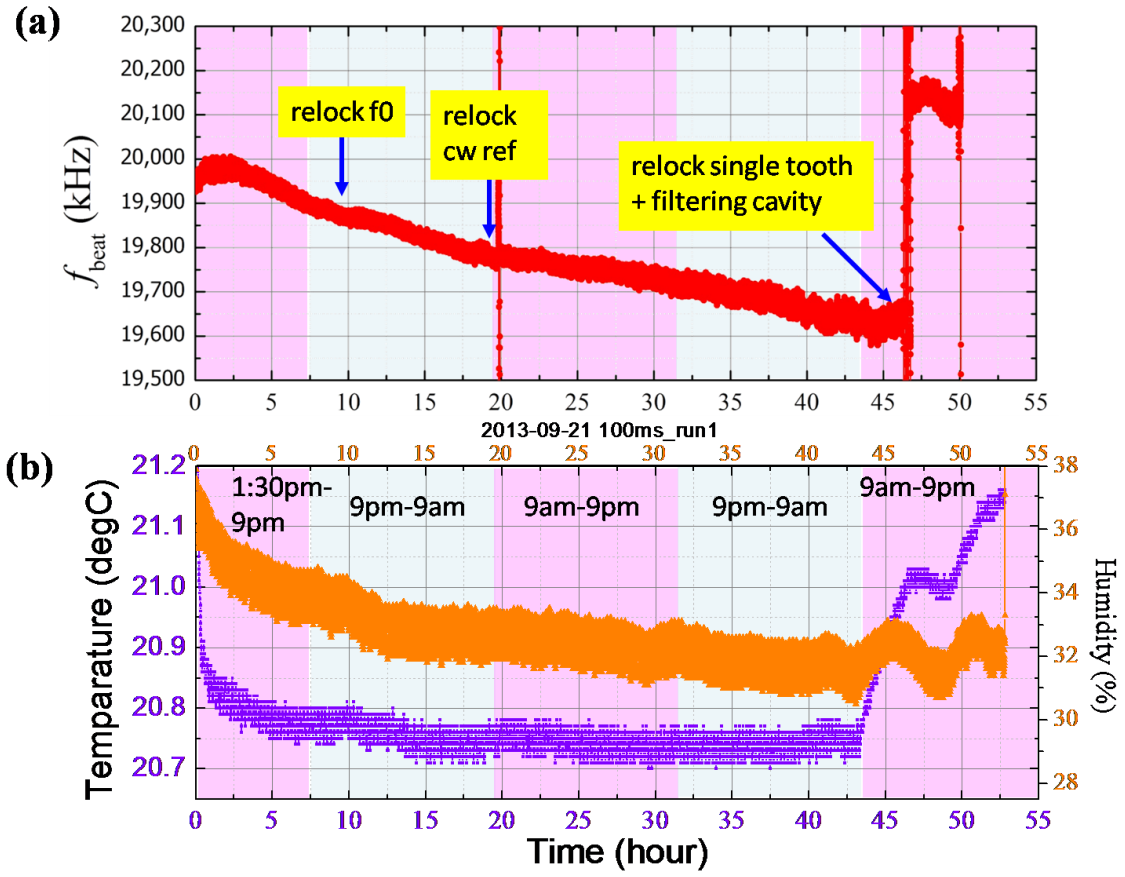

Figure 5.10: *Understanding system drift: (a) Beatnote measurement between optically referenced comb and a CW reference at 1532.8 nm. Several parameters were intentionally re-locked (while keeping other servo loops locked) during the measurement. (b) Temperature and humidity in the lab during the measurement.*

As we took longer measurements, we noticed that the drift tended to reach an "equilibrium" after 15 hours or so. Therefore, we did the following long measurement to see if the beatnote stops drifting after 15 hours, shown in Figure 5.9. However, during this measurement, we had to relock the filtering cavity several times to a different comb tooth (represented by different colors) once the originally stabilized comb tooth moved beyond

the PZT's capture range and fell out of lock. This can be seen in Figure 5.9(b) from the discontinuity of the repetition rate signal, which is due to the fact that different comb teeth were stabilized to the acetylene P(23) overtone transition. We can see from the data that the drift slows down after about 10 hours, and also that the drifting rate varies when a different comb tooth is stabilized.

Finally, we tried to intentionally relock f_0, the filtering cavity, or single tooth, one at a time, and see if any of these actions "reset" the beatnote. The slope of the drift changes slightly, as shown in Figure 5.10.

However, all of the above tests did not solve the drifting problem for us. We believe it is likely due to offsets in the locking electronics. The commercial PPC box was used to stabilize the single comb tooth, which has a gain-dependent offset. With improved servo boxes, the system is expected to have comparable long-term stability to the green diamonds in Figure 5.6. The accuracy of this comb reference is expected to be comparable to the cw reference in Ref. [140] of ±10 kHz.

5.3 Tests for Possible Frequency Shift from EDFAs

There are a few erbium-doped fiber amplifiers (EDFAs) used in the setup, most of which are seeded with a narrow-bandwidth comb. Although the total average power is enough for seeding the EDFAs, the actual optical power per individual comb tooth is rather low (sometimes nW level). In addition, the wavelength we want to amplify is on the edge of the erbium-doped fiber gain spectrum. To study if any possible frequency shift is induced by the power amplification, we did the following test: we split our laser source into two portions, one goes into a particular amplifier under test, the output of the amplifier is then optically heterodyne beated against the other un-amplified portion. Any frequency shift induced by the amplifier will result in a non-zero RF beanote. We use both CW fiber laser and a narrow-bandwidth comb as the laser source, discussed in the following two sub-sections.

The amplifiers under test are: (1) a commercial CW PM EDFA from IPG Photonics (Model number: EAR-0.5K-C-LP-SF-KS), used in the CW reference SAS setup, (2) commercial CW PM EDFA from Manlight (Model number: HWT-EDFA-B-PM-C27X), used before filtering cavity, as well as in the single tooth SAS setup, (3) a home-made CW EDFA with both forward and backward pump, described in Section 4.3.3, used to amplify a narrow bandwidth comb to seed the Manlight EDFA before the filtering cavity.

Specifically, we look at two wavelengths: 1532.8 nm and 1560 nm. The former is the wavelength we would like to amplify in our actual experiment, which is on the edge of the erbium fiber gain spectrum. For comparison, the latter is the gain spectrum central wavelength. A general conclusion from these tests is that: when seeded with a CW laser, no obvious frequency shift is observed for all the EDFAs under test. The error bars are less than tens of Hz. When seeded with a comb, again no frequency shift is observed for 1560 nm, with error bar less than 20 Hz. However, for 1532.8 nm, the error bar is within 20 kHz. The larger error bar is due to the low SNR of the beatnote signal.

5.3.1 EDFAs with Low CW Seeding

Figure 5.11 shows the experimental setup for this test. An AOM is added in the setup for the purpose of creating a non-zero beatnote which is separated from the DC background of the spectrum analyzer. If there is no frequency shift induced, the beatnote should occur at the AOM frequency.

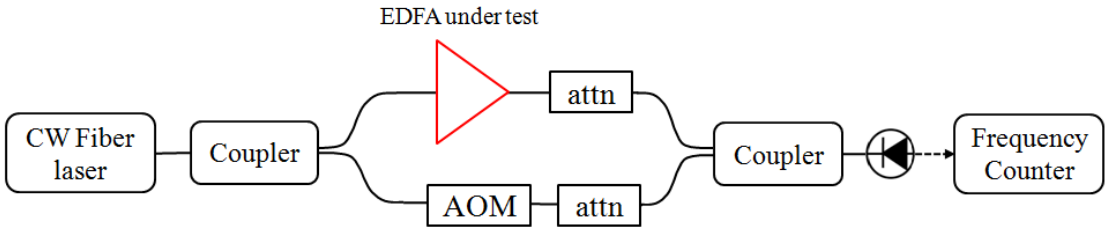

Figure 5.11: *Schematic setup for measuring any frequency shift induced by EDFAs with low CW seeding power.*

Input	Output	Center shift (Hz)	Error bar (Hz)
5.3 mW	100 mW, 50 mW, 20 mW	0	+/- 2 Hz
75 μW	100 mW, 50 mW	0	+/- 2 Hz
26 μW	50 mW, 20 mW	0	+/- 20 Hz
275 nW	50 mW, 20 mW	0	+/- 10 Hz
105 nW	20 mW	0	+/- 40 Hz

Table 5.1: *Frequency shift test for IPG PM EDFA when seeded with CW light at 1532.8 nm.*

Table 5.1 gives a summary of our observations for the IPG EDFA. The input optical power of the CW laser at 1532.8 nm is attenuated from 5.3 mW down to 105 nW. The output power setting varies from 100 mW to 20 mW. All measurements show no shift in the central frequency. However, the error bar does increase for lower CW seeds, but is still within 100 Hz. Figure 5.12 gives a few examples of the beatnote data for an IPG EDFA, with the y-axis being the AOM frequency subtracted from the RF beatnote.

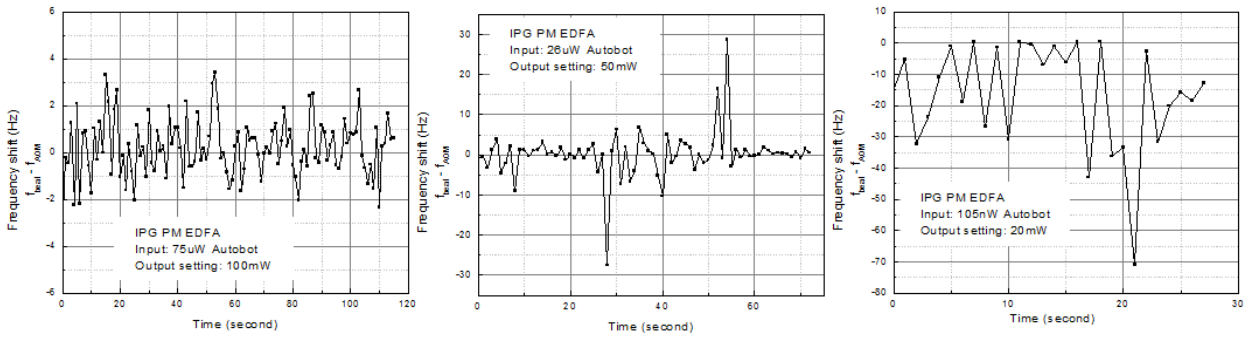

Figure 5.12: *Beatnote between amplified and un-amplified light with CW seed at 1532.8 nm. EDFA under test: IPG PM EDFA.*

The home-made CW EDFA is tested using the same setup shown in Figure 5.11. Instead of varying the output setting, the forward and backward pump currents are varied during the test for different CW seeding powers. The results are summarized in Table 5.2.

Similar tests are done for the Manlight EDFA. No frequency shift within tens of Hz was observed for a CW seeding power greater than or equal to 0.1 mW. For CW seeds less than 0.1 mW, the EDFA shuts off automatically.

Input	Forward pump	Backward Pump	Central shift (Hz)	Error bar (Hz)
225 μW	500-1000 mA	800-900 mA	0	+/- 10 Hz
22.7 μW	500-1000 mA	800-1400 mA	0	+/- 12 Hz
2.27 μW	500-1000 mA	800-1400 mA	0	+/- 12 Hz
206.4 nW	500-1000 mA	800-1400 mA	0	+/- 12 Hz

Table 5.2: *Frequency shift test for home-made CW EDFA when seeded with CW light at 1532.8 nm.*

5.3.2 EDFAs with Low Comb Seeding Power

When seeded with a comb, we only tested the home-made EDFA. The comb we used is directly from the NPR fiber ring oscillator, with a repetition rate of 90 MHz. The setup is similar except that instead of a heterodyne beatnote measurement between two CW lasers, we now beat an amplified comb against the un-amplified comb. Successful heterodyne beatnote measurement requires two pulses to overlap in time. Therefore, we add a tunable delay stage in one of the arms to compensate any time delay, illustrated in Figure 5.13. In order to have sufficient power for dual comb beating, we had to first amplify the comb using a home-made short-pulse EDFA (described in Section 4.3.1) and then use a fiber Bragg grating to filter a narrow spectral bandwidth (50-100 GHz) of the comb around the wavelength of interest.

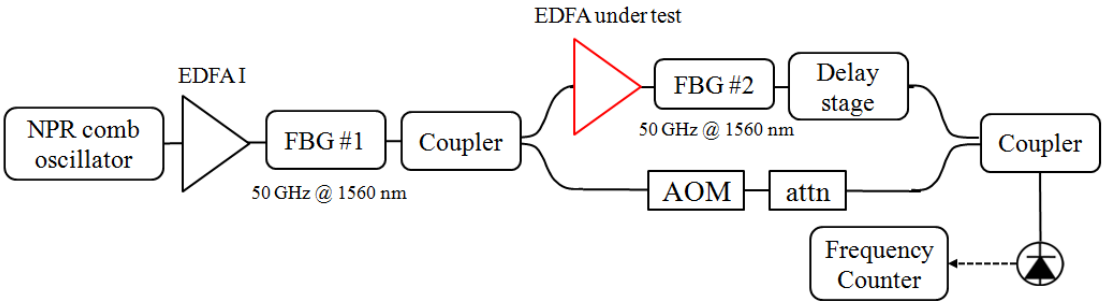

Figure 5.13: *Schematic setup for testing frequency shift induced by EDFAs with low comb seeding power at 1560 nm.*

For a comb seed at 1560 nm, we have sufficient beatnote SNR of more than 30 dB in 1

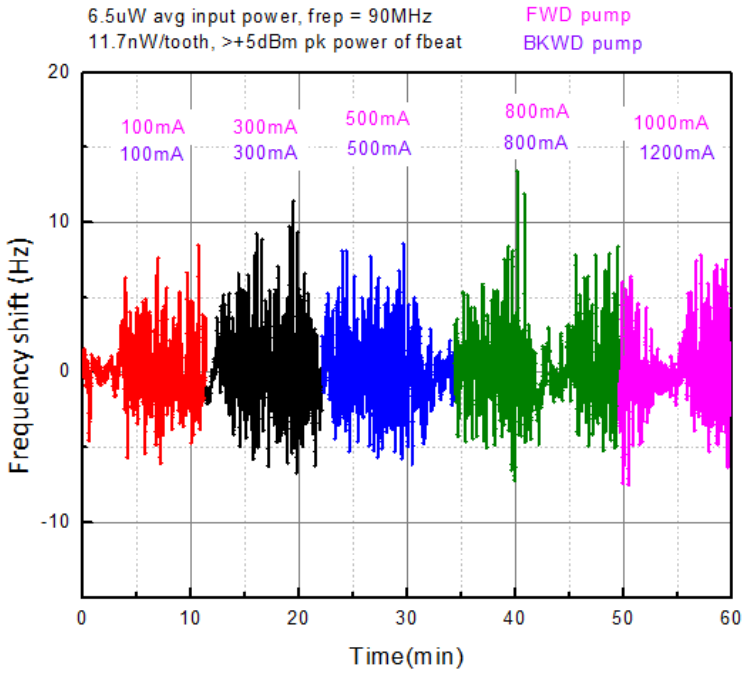

Figure 5.14: *Frequency shift versus time for different pump current settings. EDFA under test: the home-made CW EDFA, seeded with 50 GHz bandwidth comb with an average power of 6.6 μW at 1560 nm.*

MHz resolution bandwidth (RBW). The average seeding power varies from 450 μW down to 6.5 μW, corresponding to 11.7 nW per comb tooth. No frequency shift is observed, with an error bar of +/- 8 Hz. Figure 5.14 gives a plot of frequency shift in Hz versus time for different pump current settings, with an average comb seeding power of 6.6 μW. For a comb seed at 1532 nm, it is a little tricky to conduct the dual comb beatnote measurement because of the low comb power around 1532 nm. For this reason, we cannot use the comb directly from the NPR fiber ring oscillator. Instead, we used the light from the supercontinuum, denoted "SC" in Figure 5.15. Two setup schemes were tried, shown in Figure 5.13, but both failed. In plan (a), no RF repetition rate signatures were observed after the EDFA output, probably because the seeding power was too low for the EDFA under test. Therefore, we tried plan (b), in which the fiber Bragg grating was replaced by a filter WDM to provide more seeding power for the following EDFA. An RF beatnote was observed but with a low

SNR of only 6 dB in 1 MHz RBW. For a proper measurement by the frequency counter, the minimum SNR is about 22 dB.

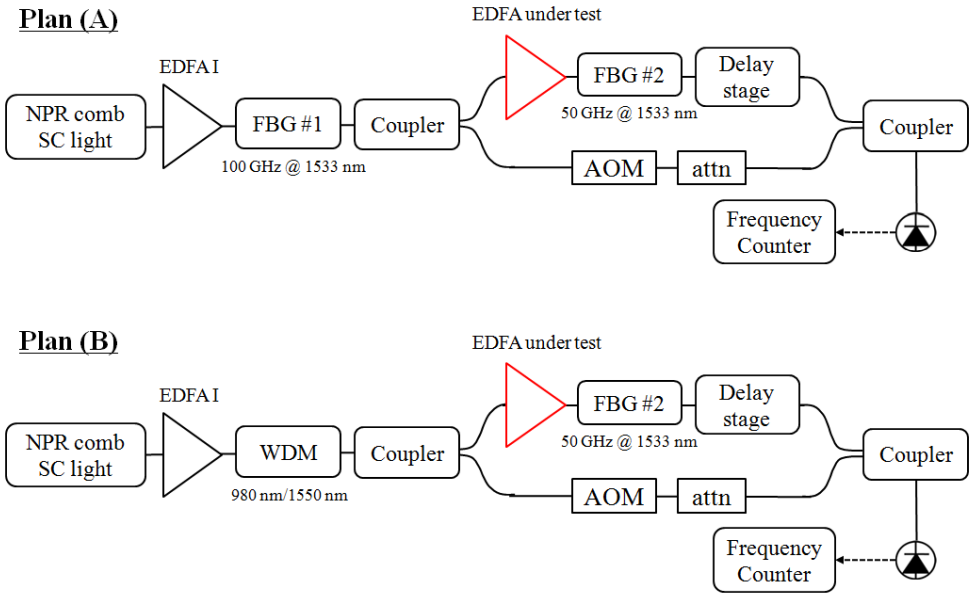

Figure 5.15: *Two proposed setups for testing frequency shift induced by EDFAs with low comb seeding power at 1532.8 nm. Both methods failed because of low comb SNR.*

We finally came up with Plan (c) to do this dual comb heterodyne beatnote measurement at 1532.8 nm, shown in Figure 5.16. Instead of a dual comb beat, we compare the comb with a CW reference. This time we had to make the measurement in three steps: we recorded the beatnote between the un-amplified comb (the supercontinuum) and a CW fiber laser stabilized to an acetylene transition, P(13). Then we repeat the same measurement using an amplified comb. In the end, we compared the two RF beatnotes and see if they are different or not.

This measurement gives the following result, shown in Figure 5.17 (c) and (d). The y-axis is the frequency difference between the two RF beatnotes. If no frequency shift is introduced, the difference signal should be centered at zero Hz. The oscillatory behaviour in (c) and (d) is probably due to the unstable f_0, shown in (a). Different colors represent measurements under various pump current settings. The fact that there is no obvious jump

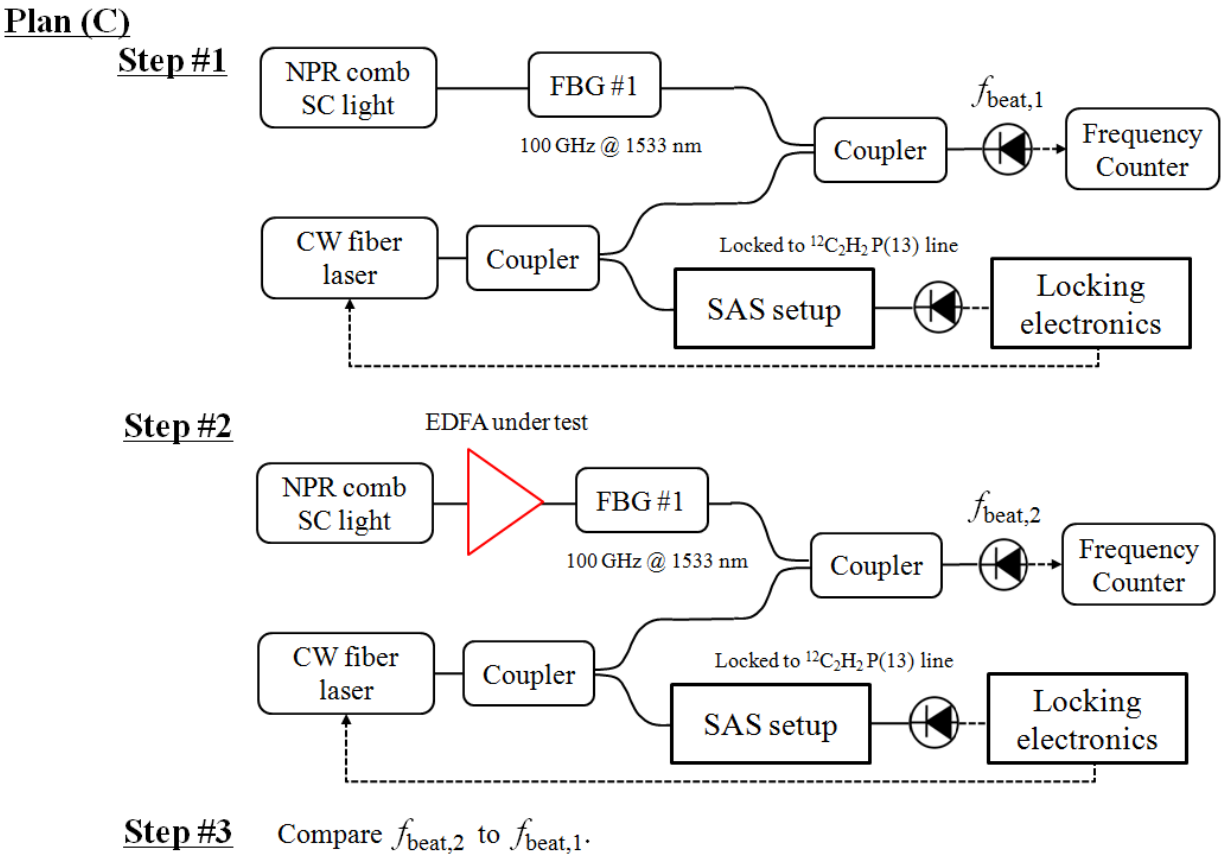

Figure 5.16: *Plan (C): Successful setup for testing frequency shift induced by EDFAs with low comb seeding power at 1532.8 nm.*

between any adjacent colors indicates that no obvious frequency shift was introduced when one changed the pump currents. We also noticed that the beatnote data is consistent with or without any amplification. However, this data still shows a 10 kHz scattering, due to the low beatnote SNR.

Based on the tests done using a low power frequency comb as the seed for EDFAs, no frequency shift is observed for the wavelength 1560 nm, with error bars less than 20 Hz. For wavelength at 1532.8 nm, the error bar increases to 20 kHz, but mainly due to the low SNR of the beatnote signal from low comb powers at this wavelength.

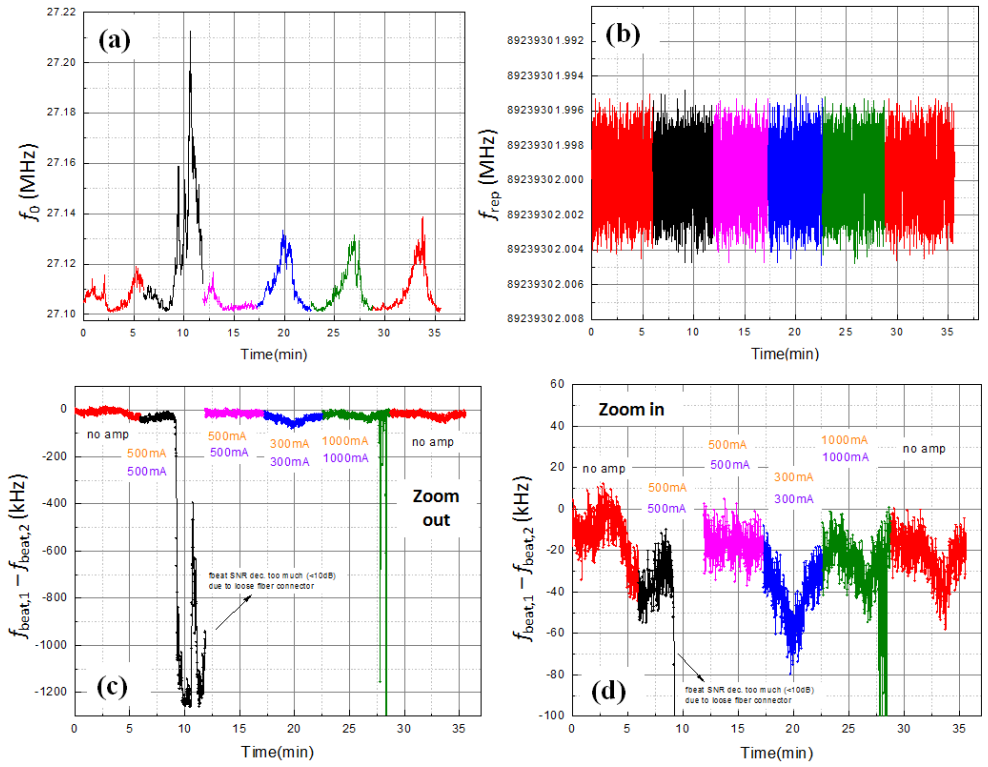

Figure 5.17: *(a) f_0 locking and (b) f_{rep} locking versus time, (c) and (d) are zoom out and zoom in pictures of frequency shift versus time. EDFA under test: the home-made CW EDFA, seeded with supercontinuum comb with an average power of 0.52 mW at 1532.8 nm. The forward and backward pump current settings are in orange and green color, respectively.*

Chapter 6

Prism-based Cr:forsterite frequency comb

This chapter presents the experimental work I did on a free space Cr:forsterite laser frequency comb. The work I'm going to talk here is not quite relevant to my major PhD project on single comb tooth saturated absorption described in previous Chapters 2 - 5. However, it was a great personal experience to work on a free space solid-state laser, and some of the following unpublished results may still be valuable for future research work in the laser community. Therefore, I summarize the work I have done as an independent Chapter.

Self-referenced Cr:forsterite (Cr:f) based combs tend to exhibit wide carrier-envelope offset frequency (f_0) linewidths, which result in broad comb teeth. This can be attributed to significant frequency noise across the combs spectral bandwidth. However, we have observed significant carrier-envelope offset frequency (f_0) linewidth narrowing in our prism-based Cr:f frequency comb from $\sim$ 1.4 MHz down to 100 kHz by changing the prism insertion only, and further down to 23 kHz by inserting a knife edge into the intracavity beam while keeping the same prism insertion.

The Cr:f comb in our lab was setup by a few of our previous group members: Karl Tillman, Rajesh Thapa, Kevin Knabe, and Andrew Jones. Karl and Rajesh observed this

f_0 narrowing effect for the first time and did a lot of initial work on f_0 noise dynamics trying to explain this phenomenon [142]. My contribution to this project is a continuation of their work. In addition, I also made multiple noise measurements in order to explain the f_0 narrowing effect. I found that the previously-developed theoretical expression [143] based on laser relative intensity noise does not explain the observed narrowing of f_0, but indicates that other noise processes may contribute.

6.1 Introduction and Motivation

As discussed in the Introduction (Section 1.2.2), the first and highest performance frequency combs have been based on Ti: Sapphire lasers, and access primarily the visible spectrum out to $\sim$ 1.0 μm. However, many of the above applications benefit from near IR combs extending into the eye-safe, optical telecomunication regions. Cr:forsterite, Cr:YAG, and Erbium-doped fiber lasers are all important sources in that region [144–148].

The linewidths of the carrier-envelope offset frequency (w_{f_0}) become important in many applications, including optical frequency metrology. Wide linewidths lead to broadening of the comb teeth when the comb is self-referenced, and degrade the precision of frequency measurements made with the comb. Narrow linewidths potentially provide better short-term stability, improving the stabilization of f_0, and therefore allowing higher accuracy measurements to be made in shorter time. Nowadays, the f_0 linewidth (w_{f_0}) in Ti: Sapphire laser frequency combs reach the mHz level [41, 149]. Locked fiber-based combs also have f_0 linewidths reduced from a few MHz [150, 151] to subHz [130]. In contrast, to the best of our knowledge, no Cr:forsterite combs described in the literature has ever demonstrated w_{f_0} less than 1 MHz [147, 152].

In this work, we have stabilized a prism-based Cr:forsterite laser frequency comb and examined its w_{f_0}. Surprisingly, we find experimentally that the free-running w_{f_0} can be reduced from $\sim$ 1.4 MHz down to $\sim$ 23 kHz by inserting a knife edge (KE) into the cavity,

while keeping all other laser parameters the same (i.e. pump power, prism insertion, beam alignment). In prism-based cavities, a knife edge or slit is often used to tune the center frequency of a mode-locked laser by introducing wavelength-dependent loss into the cavity [153, 154]. Here, we describe the first system in which the w_{f_0} is observed to narrow by a factor of 60 when a knife edge is introduced in a prism-based Cr:forsterite laser system. Narrowing of w_{f_0} can be induced when varying the prism insertion in the cavity, but the reduction is less dramatic. The cause of this linewidth reduction is discussed later.

Previous investigations [155–158] offer insight into the cause of f_0 fluctuations in Ti: Sapphire frequency combs. In particular, Helbing *et al.* [157] found that fluctuations in intracavity peak power couple to f_0 differently in prismless and prism-based lasers. In their prism-based Ti: Sapphire laser, the major contribution to w_{f_0} is jitter in the intracavity beam pointing stability which gives rise to dispersion fluctuations inside the prism. In contrast, in prismless systems, the change in linear dispersion due to the Kerr effect is dominant. In Ti: Sapphire lasers with and without prisms, Holman *et al.* [156] investigated the dependence of f_0, f_{rep} and the central frequency of the pulse spectrum on intracavity power. They measured how f_0 changed with intracavity intensity ($\Delta f_0/\Delta I$) and found that in order to obtain optimum conditions for f_0 control, the intracavity power must be chosen such that $\Delta f_0/\Delta I$ is non-zero. Furthermore, they concluded that smaller cavity group delay dispersion (GDD) leads to reduced spectral shift induced by power fluctuations. Thus, in prism-based lasers, where GDD is typically minimized, w_{f_0} is minimized but f_0 is very difficult to control by changing the pump power.

Efforts have also been made to understand the origins of frequency jitter on the carrier-envelope offset frequency of fiber-based laser frequency combs [159]. McFerran *et al.* [143] showed that the pump laser's intensity is a significant noise source in their erbium fiber laser frequency comb. The reduction of relative intensity noise (RIN) of the pump results in a narrowing of the free-running f_0 from hundreds of kHz to $\sim$ 60 kHz. They developed a theoretical model incorporating the RIN and response of f_0 to pump power fluctuations,

and the roll-off frequency of the laser gain medium. The model agrees well with their experimental results.

In this chapter, we present the experimental observations of f_0 linewidth (w_{f_0}) narrowing when two aspects of the Cr:forsterite laser are changed: the presence of a KE in the cavity, and the prism insertion. We apply aspects of the model developed by McFerran *et al.* [143] for their Er-doped fiber frequency comb to our Cr:forsterite laser system, and compare the calculated linewidths $w_{f_0}^{\text{calc}}$ to our experimental data $w_{f_0}^{\text{exp}}$. We also compare our observations to the results in the Ti: Sapphire laser system [156] developed by Holman *et al.* The effect of frequency-dependent relative intensity noise (RIN(f)) of both the pump and Cr:forsterite laser on the linewidth of the carrier envelope offset frequency is explored in this work. Application of these explanations and this model to the Cr:forsterite KE narrowing phenomenon leaves some unanswered questions.

6.2 Laser Configuration

In this section, we introduce both the cavity configuration and the scheme for f_0 detection and stabilization. The general cavity layout of the prism-based femtosecond Cr:forsterite laser is shown in Figure 6.1 (a). It is a folded cavity that uses a negatively chirped SF6 prism pair for dispersion compensation. The separation between the two SF6 prisms is 30 cm. The pump beam is focused into the 15 mm long Cr:forsterite crystal (0.2 % doping by weight) by a focusing lens with 10 cm focal length. When pumped by a continous wave Yb-doped fiber laser at 1075 nm with 9.6 W (IPG Photonics), mode locking can be easily initiated by quickly changing the insertion of the prism farther from the end mirror (EM). The mode-locked laser spectrum spans from 1175 nm to 1325 nm, with a typical bandwidth of 38 nm, as shown in Figure 6.1 (b). The average mode-locked lasing power is about 360mW at a repetition frequency of 113 MHz after the 6 % output coupler (OC).

Figure 6.2 shows the self-referencing configuration for f_0 detection and a simplified

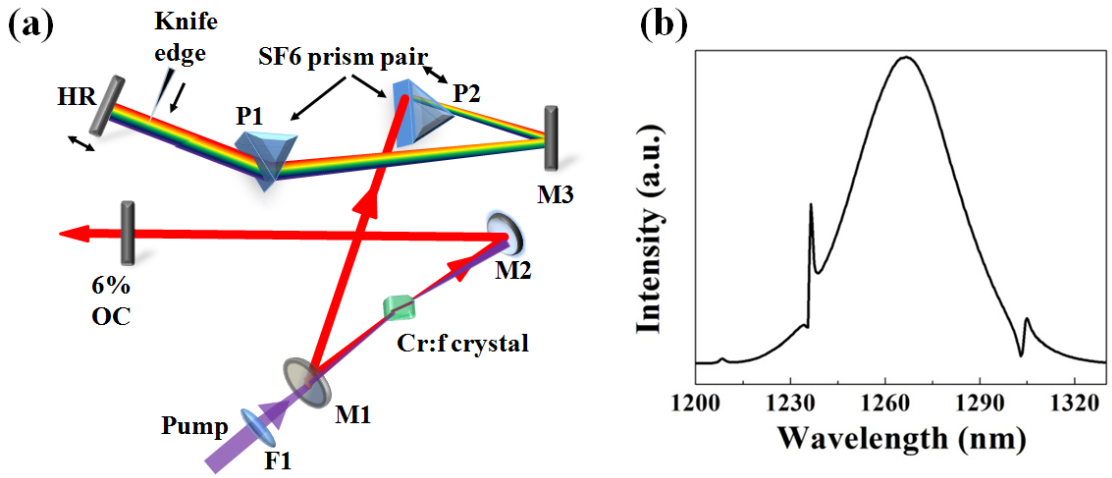

Figure 6.1: *(a) Cavity configuration and (b) mode-lock spectrum for the prism-based Cr:forsterite laser. (F1 = 100 mm focusing lens, M1 and M2 = cavity mirrors, ROC = radius of curvature, M3 = cavity folding mirror, P1 and P2 = SF6 prisms, HR = high reflector, OC = output coupler). The two arrows near the prism and HR indicate the servo controlled elements for both f_{rep} and f_0 stabilization. The arrow near the knife edge shows the direction of knife edge movement.*

schematic of the locking scheme for both f_0 and f_{rep}. The mode-locked Cr:forsterite laser output is launched into a 2 m length of highly nonlinear fiber (HNLF) with a dispersion parameter of D = 1.19 ps/(nm km) at 1550 nm in order to generate a supercontinuum (SC) spectrum spanning from 1010 nm up to 2300 nm. The offset frequency f_0 is obtained by employing the f-to-2f self-referencing technique [160]. The second harmonic generation of the 2060 nm light is produced and combined with the 1030 nm light, which results in the heterodyne beat signal f_0. The signal-to-noise ratio (SNR) of the f_0 beat note is about 42 dB at 100 kHz resolution bandwidth (RBW). For f_0 stabilization in a prism-based laser cavity, a common method is to change the cavity dispersion by swiveling the end mirror [162]. However, this method limits the servo bandwidth, which restricts the accuracy with which f_0 can be locked [163]. An alternate method which allows for a larger bandwidth is to control the pump power. In our experiment, we use a combination of a slow servo controlling prism insertion with a fast AOM servo that controls the pump power for f_0 stabilization.

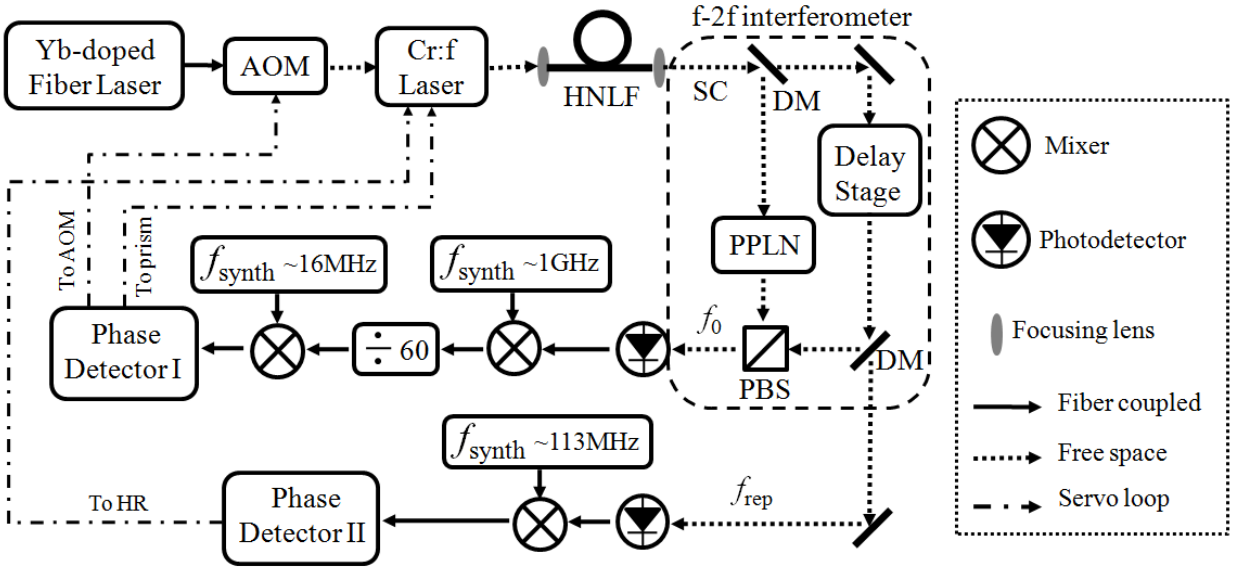

Figure 6.2: *Locking scheme for the phase stabilization of f_0 and f_{rep}. All synthesizers and frequency counters are referenced to a Global Positioning System (GPS)disciplined rubidium (Rb/GPS) oscillator. Refer to [161] for a more detailed description. PBS: polarization beam splitter, SC: supercontinuum, DM: dichroic mirror.*

f_{rep} lock is obtained by creating a feedback loop to the piezoelectric transducer (PZT) on the high reflecting (HR) mirror in order to control the cavity length. Ref. [161] gives a more detailed description of the stabilization scheme for this Cr:forsterite comb.

6.3 Observation of f_0 Linewidth Narrowing

Significant narrowing of f_0 linewidths is observed when we insert the KE into the beam at the Fourier plane of the prism pair within the laser cavity. Figure 6.3 (a) shows the snapshots of f_0 linewidths as the KE is gradually introduced. However, the values given in Fig. 3 represent an average of multiple 3-dB linewidths recorded at different resolution bandwidths (RBWs). The KE starts out from a position that is away from the intracavity laser beam, i.e. 0.125 mm and 1.625 mm in Figure 6.3 (a). $w_{f_0}^{\text{exp}}$ is measured to be $\sim$ 1.2 MHz and 1.5 MHz, respectively. As we move the KE in, it starts to intersect and cut the beam from

the long wavelength section to shorter wavelengths. Meanwhile, $w_{f_0}^{\exp}$ becomes narrower and reaches its minimum of $\sim$ 23 kHz when the KE is at a position of 0.5 mm. When we insert the KE further, f_0 becomes unstable and the linewidth $w_{f_0}^{\exp}$ is wider again (KE = 0.625 mm and 0.750 mm in Figure 6.3 (a)). We experience difficulty in phase stabilizing f_0 at its narrowest linewidth, where f_0 does not respond well to pump power servoing. The possible reasons will be discussed below.

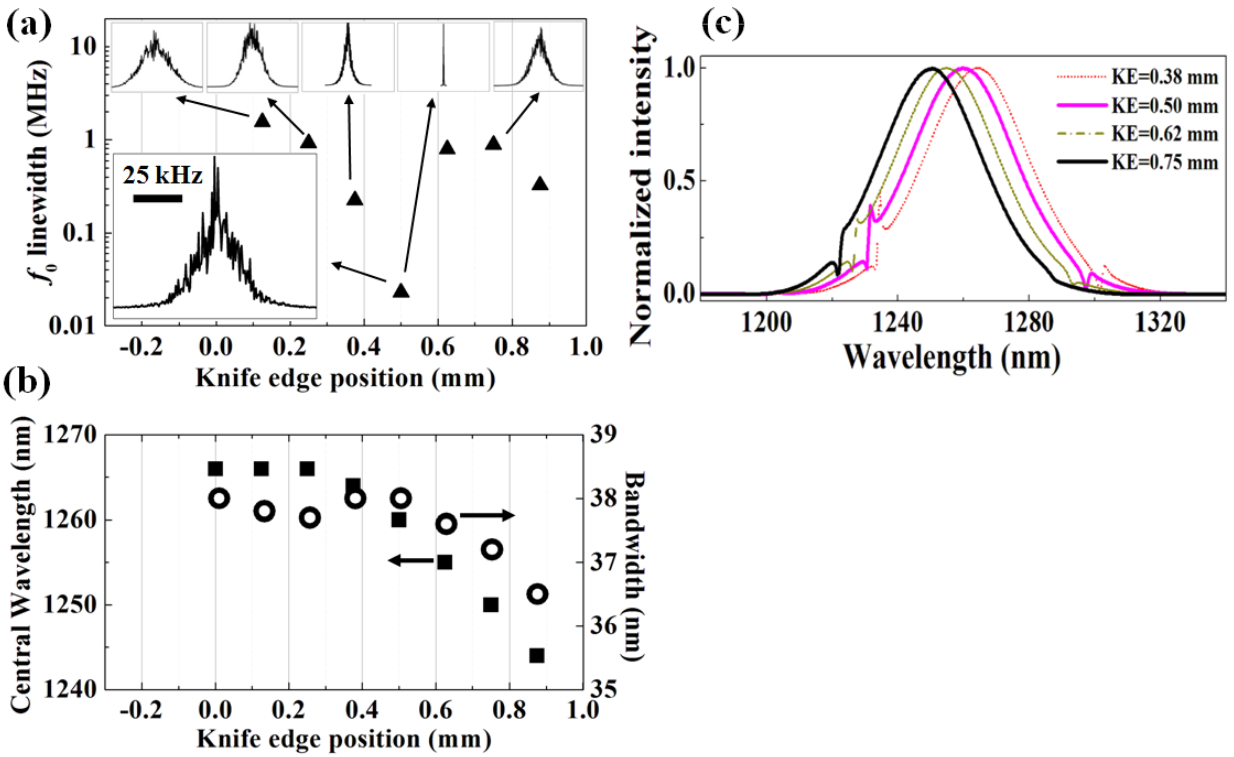

Figure 6.3: *(a) Measured f_0 linewidth on a log scale as a function of relative knife edge position. Insets on top show f_0 linewidths on a linear scale at a span of 4 MHz, with RBWs of 30 kHz, 3 kHz, 1 kHz, 1 kHz, and 30 kHz from left to right. The lower left inset is a zoom-in plot of the narrowest linewidth, span 100 kHz, RBW 1 kHz. Data was taken within 26 hrs. (b) The change in central wavelength (solid square) and bandwidth (open circle) of the Cr:forsterite mode-locked spectrum as a function of knife edge position. (c) Mode-locked optical spectrum of the Cr:forsterite laser when the KE is inserted at four different positions in (a).*

While w_{f_0} changes by orders of magnitude as the KE is inserted, other laser parameters

change very little. Figure 6.3 (b) and (c) indicate the simultaneous narrowing and shifting of the Cr:forsterite laser's optical spectrum when the KE is inserted as shown in Figure 6.3 (a). In our measurements, the overall shift of the central wavelength is about 14 nm, while the modelocked bandwidth of the laser ($\sim$ 45-50 nm) is reduced by only a few nanometers (less than 10 %). We notice that there exists a "turning point", at which both the central wavelength and bandwidth start to change significantly as the KE is inserted. In Figure 6.3 (a), this "turning point" occurs when the KE is at 0.5 mm. This "turning point" changes day-to-day with respect to the KE position due to laser alignment and modelocked behavior (i.e., in some days, the spectrum bandwidth changes from 49 nm to 45 nm as the KE is inserted). However, the narrowest linewidth always occurs near this "turning point". As the KE is introduced further, the f_0 linewidth becomes wider. This "turning point" observation is consistent with the threshold behavior that Holman *et al.* found for their Ti: Sapphire laser system when varying the prism insertion [156]. That is, for a pulse spectrum bandwidth below the "threshold", which is 47 nm for the 100 MHz Ti: Sapphire laser, the f_0 linewidth increases as the spectral bandwidth decreases.

We also observe a similar linewidth reduction (from 1.4 MHz to 150 kHz) merely by changing the prism insertion (without the KE inserted). The prism was inserted 1.128 mm less for the latter case (equivalent to a decrease in net cavity GDD of 205 fs^2 per round trip) and a reduction in $w_{f_0}^{exp}$ is observed. At the same time, the central wavelength of the modelocked spectrum shifts by 0.3 nm, and the bandwidth increases from 43 nm to 48.8 nm. An interesting observation is that the minimum linewidth $w_{f_0}^{exp}$ obtained by optimizing laser alignment and prism insertion is around 100 kHz, which is much larger than the $\sim$ 23 kHz linewidth obtained when the KE is inserted. Also, for a 100 kHz linewidth, f_0 can be phase stabilized easily. Whereas, it is much more difficult to phase stabilize with when the f_0 width is 23 kHz.

6.4 Developed Theory

In order to explain these phenomena, we adopt a theoretical model developed by J. J. McFerran *et al.* [143] for their Erbium-doped fiber laser frequency comb. The model predicts the noise on the carrier envelope offset frequency, which shows up as the width of the f_0 peak when measured with the f-to-2f interferometer. We incorporate this idea into our free-space Cr:forsterite laser frequency comb such that the free-running Δf_0 can be predicted as:

$$w_{f_0}^{\text{calc}} \cong \pi[\int_{f_{\text{min}}}^{f_{\text{max}}} (P_{\text{pump}} \frac{df_0}{dP_{\text{pump}}(f)})^2 \text{RIN}_{\text{Cr:f}}(f) df]^{\frac{1}{2}} \tag{6.1}$$

where P_{pump} is the pump power, $df_0/dP_{\text{pump}}(f)$ is the frequency-dependent frequency response of the f_0 signal to the amplitude modulation of pump power, and $\text{RIN}_{\text{Cr:f}}(f)$ is the relative intensity noise ($\text{RIN}(f)$) of the mode-lock Cr:forsterite laser in dBc/Hz. The quantity inside the integral represents the power spectral density of w_{f_0}, which is described by squaring the frequency response of f_0 to pump power changes and multiplying by the laser RIN. The free-running offset frequency linewidth can be approximated by integrating the power spectral density over all frequencies up to a 3-dB roll-off of the gain medium at ~ 700 kHz [152]. In our calculation, we convert the response of f_0 to pump power changes into the response with respect to the change in the mode-locked laser power ($P_{\text{Cr:f}}$). Therefore, the term $P_{\text{pump}} df_0/dP_{\text{pump}}$ is assumed to be equal to $P_{\text{Cr:f}} df_0/dP_{\text{Cr:f}}$.

6.5 Measurement of Noise Dynamics

To determine if Eqn 6.1 describes the noise processes in the Cr:forsterite laser, we first measure under a variety of conditions both w_{f_0} and the quantities under the integral in Eqn 6.1 ($P_{\text{Cr:f}}$, $df_0/dP_{\text{Cr:f(f)}}$, and $\text{RIN}_{\text{Cr:f}}(f)$), which describe the noise dynamics of f_0. Then we compare the measured and calculated values of w_{f_0}. Because the laser drifts and these measurements take time, we cannot compare $w_{f_0}^{\text{exp}}$ with $w_{f_0}^{\text{calc}}$ for all the KE insertions shown

in Figure 6.3 on a given day. Instead, we compare the w_{f_0} with no insertion and with insertion to minimum linewidth on a variety of days. Figure 6.4 shows the measured w_{f_0}

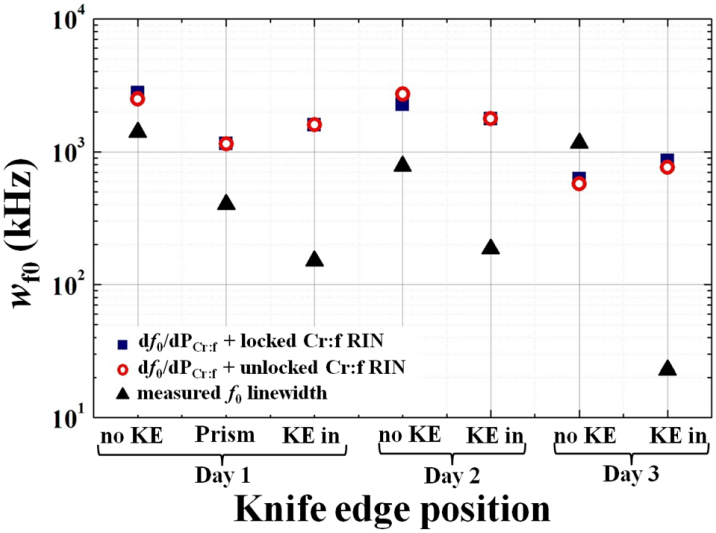

Figure 6.4: *Measured $w_{f_0}^{exp}$ (solid black triangles) on three different days, compared with calculated values $w_{f_0}^{calc}$ using locked (solid blue square) and unlocked (open red circle) Cr:f RIN. "no KE" and "KE in" represent the case of no KE present in the laser cavity and with KE inserted for minimum w_{f_0}, respectively. "Prism" indicates the case of minimum w_{f_0} being obtained by changing the insertion of prism P2 only (no KE present).*

(solid triangles) for three such days. It is an averaged 3-dB linewidth recorded at various RBWs when both f_0 and f_{rep} are phase stabilized (or locked) simultaneously (i.e., f_{rep} = 113 MHz ± 2 mHz and f_0 = 35 MHz ± 1 Hz using 1s gate time), also denoted as $w_{f_0}^{\text{exp}}$ in later paragraphs. Day 3 "no KE" and "KE in" in Figure 6.4 represent data points from Figure 6.3 (a) at KE = 0.125 and KE = 0.5 mm, respectively. For each of these points in Figure 6.4, the noise dynamics of f_0 were also characterized, as described below to facilitate comparison. Before describing that comparison, we first describe the measurement of those quantities.

The quantities that describe the noise dynamics ($P_{\text{Cr:f}}$, $df_0/dP_{\text{Cr:f}}(f)$, and $\text{RIN}_{\text{Cr:f}}(f)$) are measured in the following way. $P_{\text{Cr:f}}$ is determined from the measured average output power at the 6 % output coupler (OC), which is ∼ 300 mW. The frequency-dependent $\text{RIN}_{\text{Cr:f}}(f)$

and $\mathrm{RIN}_{\mathrm{pump}}(f)$ are measured as described in detail in Ref. [152]. Figure 6.5 (a) shows the behaviour of the Cr:forsterite RIN with and without knife edge present in the cavity on the same day, when both f_0 and f_{rep} are phase stabilized. The data labeled "prism" is when no KE is present, and we change the prism insertion for minimum f_0 linewdith. The Yb-doped fiber pump laser RIN is also plotted for comparison. Figure 6.5 (a) shows that the Cr:forsterite RIN is reduced, but not significantly, as we change prism insertion or introduce the KE into the cavity. This is confirmed by comparing the integration of $\mathrm{RIN}(f)$ over all frequencies. The integral is only 24.3 % smaller with KE than that of without KE, while $w_{f_0}^{\mathrm{exp}}$ is reduced almost by a factor of 10. The independence of the RIN on the KE leads us to believe that the RIN is not the main contribution to the change in w_{f_0}. In order to explain the dependence of the measured w_{f_0} on KE position we need to discuss the dependence of f_0 on changes in pump power (df_0/dP).

First we will describe the measurement of $df_0/dP(f)$. The setup for this measurement is shown in Figure 6.6. $df_0/dP_{\mathrm{pump}}(f)$ is measured by step modulating the acousto-optic modulator (AOM), or pump power, and counting the free-running f_0 simultaneously. For modulation frequencies below 300 Hz, we use the same method as described in Ref. [152]. The corresponding change in f_0 due to the modulation ($df_0(f)$) is extracted by Fourier transforming the free-running $f_0(t)$ signal (Figure 6.6 (a) left inset) into the frequency domain, filtering the DC component, and again converting back to the time domain where df_0 can be extracted as a function of time (Figure 6.6 (a) right inset). This is called slow modulation, as depicted in Figure 6.6 (a).

To measure $df_0/dP_{\mathrm{pump}}(f)$ at modulation frequencies above 300 Hz (specifically, from 100 kHz to 2 MHz), the changing f_0 cannot be tracked by frequency counters with sufficient resolution and speed, so a faster modulation technique is employed (Figure 6.6 (b)). In order to minimize the effect of slow drift of the free-running f_0, f_0 is loosely locked with the slow prism servo (bandwidth $<$ 30 kHz) as the fast modulation is applied. The recorded linewidth is an average of multiple 3-dB linewidths recorded at different RBWs. Due to

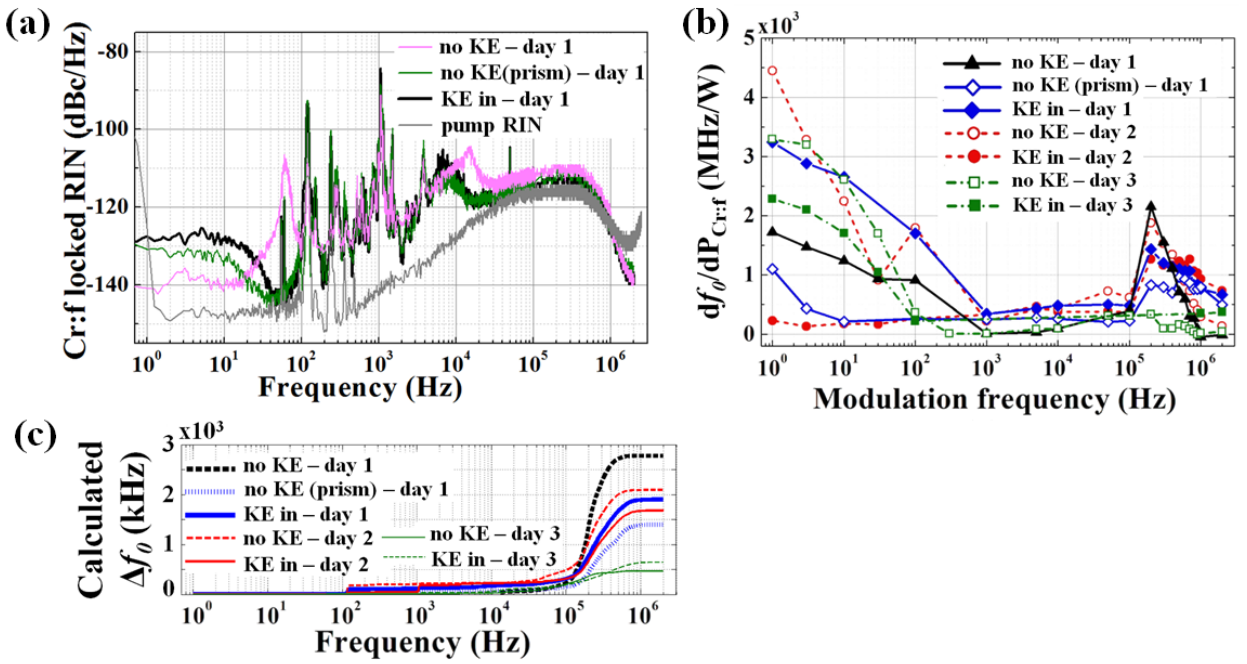

Figure 6.5: *(a) Cr:forsterite RIN(f) measurements taken in three cases when the locked f_0 linewidth is measured to be 150 kHz, 400 kHz and 1.4 MHz, respectively. For comparison, the pump RIN(f) is included. Data beyond 100 Hz are at least 10 dB above the background noise of the photodetector. (b) $df_0/dP_{Cr:f}$ as a function of frequency. (c) The calculated change in f_0 as a function of frequency limit of integration.*

the pump power modulation, it is broadened as compared to $w_{f_0}^{\exp}$, the linewidth measured when both f_0 and f_{rep} are phase stabilized and pump power is not modulated. The difference between these two linewidths gives the change in f_0 (df_0) at a certain modulation frequency. $df_0/dP_{\text{Cr:f}}(f)$ can be obtained by dividing df_0 by the change in Cr:f laser output power induced at a given change in pump power. Figure 6.5 (b) is a comparison of $df_0/dP_{\text{Cr:f}}(f)$ measured on different days with and without KE insertion. Here we are focusing on high modulation frequencies. This is because as we calculate the integral $w_{f_0}^{\text{calc}}$ as a function of the upper frequency limit $f_{\max}$, shown in Figure 6.5 (c), the plot indicates that $w_{f_0}^{\text{calc}}$ is dominated by noise above 200 kHz (The 3-dB roll-off frequency of the gain medium is 700 kHz [152].) For high modulation frequencies, we observe change in the absolute value of $df_0/dP(f)$ from day to day (Figure 6.5 (b)). However, $df_0/dP(f)$ does not vary significantly

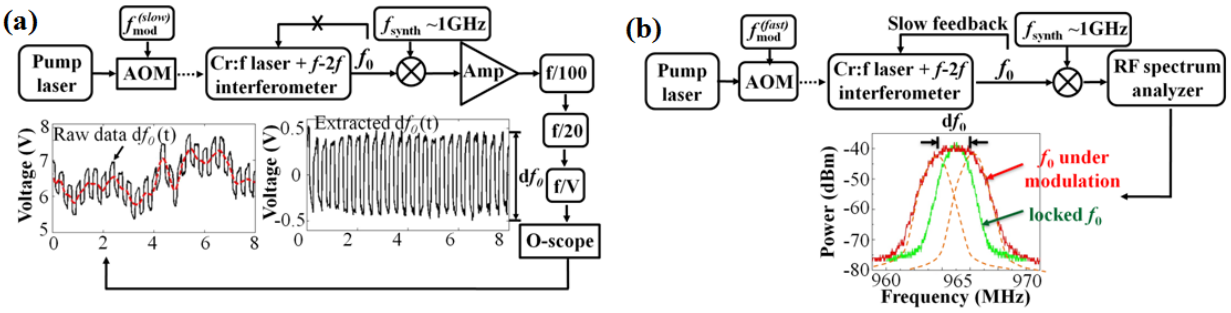

Figure 6.6: *Schematic figure of (a) "slow" and (b) "fast" AOM modulation. (a) The "cross" in the diagram indicates that no f_0 feedback is used (i.e. f_0 is unlocked), under the "slow" modulation scheme. The left inset shows an example of the f_0 trace (f_{mod} = 3 Hz) as a function of time (solid line). The red dashed curve indicates the DC component of the Fourier transformed f_0 trace that was subtracted to create the right inset. The right inset shows an extracted df_0 as a function of time. (b) The inset shows how the f_0 linewidth under 200 kHz modulation (red envelope) is broadened as compared to the locked linewidth (green). The dashed curves are a cartoon illustrating that this broadening is due to the oscillation of f_0 under modulation.*

overall whether the KE is present or not, compared to the order of magnitude narrowing of $w_{f_0}^{\text{exp}}$.

Once the noise dynamics are measured, $w_{f_0}^{\text{calc}}$ can be calculated using Eqn 6.1 and compared directly with $w_{f_0}^{\text{exp}}$. Now we go back to Figure 6.4, and describe the comparison on three different days. For the calculated values, we used the locked and unlocked Cr:forsterite RIN to perform the integral from 0 to 2 MHz. Both calculations give similar $w_{f_0}^{\text{calc}}$, indicating that the effects of cavity noise on f_0 are not significantly reduced by locking f_0 and f_{rep}. Overall, $w_{f_0}^{\text{exp}}$ and $w_{f_0}^{\text{calc}}$ agree within a factor of 3 when the knife edge is not present in the cavity. However, larger discrepancies occur when the KE is inserted for minimum Δf_0. This indicates that there might be other noise mechanisms when the knife edge is inserted that counteract the frequency noise due to the pump. We will try explaining our results in the next section.

6.6 Proposed Explanation

Since the McFerran's model [143] does not fully explain our results, especially for cases when the knife edge (KE) is inserted, in the next three paragraphs we try to understand the effect of the KE and prism on w_{f_0} narrowing qualitatively based on the results in Ti: Sapphire described in Ref. [156].

Ref. [156] found that in Ti: Sapphire lasers, f_0 linewidth (w_{f_0}) is related to the intensity-related spectral shift and group-delay dispersion (GDD). Thus, we calculate the net cavity group-delay dispersion of our Cr:forsterite laser as a function of wavelength, which is shown in Figure 6.7. We consider the material dispersion of both the Cr:forsterite crystal and the

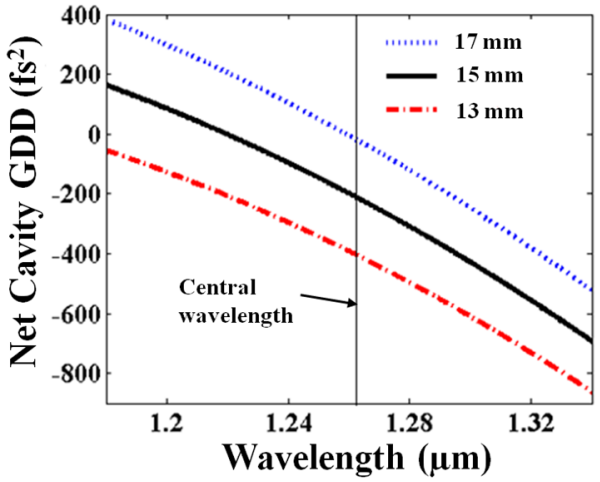

Figure 6.7: *Calculated net cavity GDD as a function of wavelength under three different round trip path lengths inside prisms. The vertical line in the center indicates the central wavelength (1262 nm) of the pulse spectrum when no KE is present.*

prism pair, and angular dispersion due to the separation of the prism pair. The net cavity dispersion is the sum of the three. The details of the calculation are given in Ref. [164]. The parameters used in this calculation are: 30 mm prism separation, overall prism insertion of 15 mm per round trip, 30 mm Cr:forsterite crystal length (round trip), and a beam waist of 1.5 mm. Based on this calculation, we believe that our laser operates in a region where the net cavity GDD is very close to zero. The reduction of w_{f_0} by adjusting KE insertion can

be explained by the change in net cavity GDD. Figure 6.7 shows that the absolute value of the net cavity dispersion decreases as wavelength decreases. Therefore, as the mode-locked spectrum shifts toward shorter wavelengths due to the KE insertion, the magnitude of net cavity dispersion is reduced by a small amount and thereby closer to zero. As a result, according to Ref. [156], the coupling of f_0 to intensity fluctuation decreases, which leads to a reduction in f_0 linewidth. As we insert the KE further after the turning point (when w_{f_0} reaches a minimum), the central wavelength of the pulse spectrum decreases dramatically (Figure 6.3 (b)). This pushes the net cavity GDD much faster in the positive direction and away from the zero point, in which region the laser is unstable. Therefore, f_0 becomes wider and unstable.

Figure 6.7 gives three net cavity GDD curves under different round trip path lengths inside the prism: 17, 15, and 13 mm. Since the laser operates near the zero GDD region, it is very likely that the Cr:forsterite laser operates in both the positive and negative GDD regions depending on the optimization of the prism micrometer on different days. This is important because it explains why the f_0 linewidth is narrowed by reducing the prism insertion. The net cavity GDD of the laser may start off with a small positive value, and decrease as the prism insertion is reduced. Minimization of the cavity group-delay dispersion leads to a reduced influence of pump power on f_0. This has the beneficial effect of reducing w_{f_0} while simultaneously reducing the control one can expect over f_0 using pump power.

In order to explain why it is difficult to stabilize f_0 with pump power when the KE is inserted for narrowest w_{f_0}, we plot df_0/dP as a function of KE position under square-wave pump power modulation, as shown in Figure 6.8. For modulation frequencies of 1 Hz, 3 Hz and 10 Hz, df_0/dP decreases as the KE is inserted. Based on the discussion in Ref. [156], in prism-based laser, df_0/dP decreases as the net cavity GDD decreases. When we insert the KE, the cavity dispersion is decreased due to the spectral shift to shorter wavelengths, so df_0/dP becomes small. Therefore, f_0 does not respond sufficiently to pump power servoing. Another factor that could explain the difficulty in locking is as follows: it is possible that the

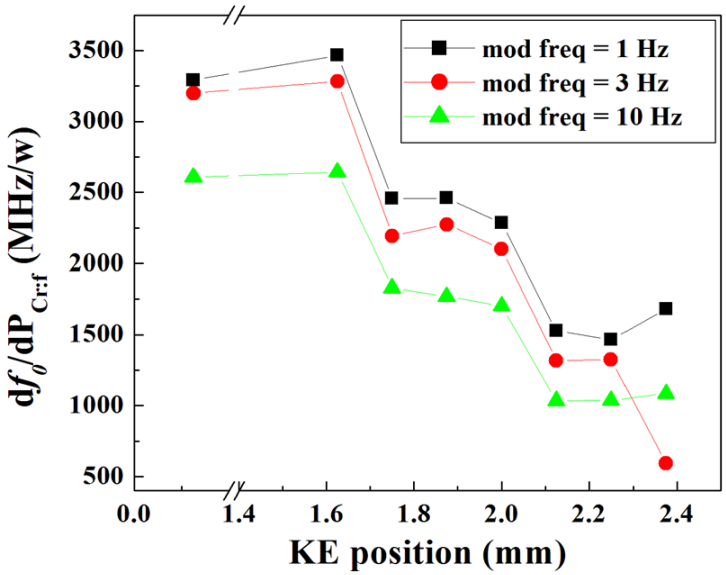

Figure 6.8: *$df_0/dP_{Cr:f}$ as a function of knife edge position under slow pump power modulation.*

way w_{f_0} changes with KE insertion is influenced by the pump power. There exists a small region for minimum w_{f_0} due to large pump power variation. Unfortunately, this region is small, so it is difficult to attain for servoing the pump power for f_0 stabilization.

6.7 Conclusions

Cr:forsterite laser-based frequency combs have historically exhibited wide f_0 beatnote linewidths (w_{f_0}), which limit the comb's usefulness for frequency metrology. The insertion of a knife edge in the Fourier plane of the prism pair dramatically reduces the w_{f_0} and reduces one's ability to control f_0 with pump power. To both narrow and control f_0, it is likely that the technique of tilting the highly reflecting mirror in the Fourier plane commonly used with Ti: Sapphire lasers, in conjunction with the KE, would lead to narrow and phase-stabilized w_{f_0} beats [156].

To better understand the cause of the dramatic narrowing in w_{f_0}, we characterized the response of f_0 to pump power fluctuations, and integrated the relevant product of power

spectral noise density and response to obtain the predicted Δf_0. While this approach has been used to predict w_{f_0} in Er-doped fiber lasers, it did not predict a significant change in the Cr:forsterite lasers w_{f_0}. This may be due to the large fluctuations in pump power that we employed in order to measure df_0/dP, which masks the small df_0/dP over a very small range of powers. The theoretical expression based on laser relative intensity noise does not explain the observed narrowing, but may indicate that other noise processes may contribute to w_{f_0}.

Chapter 7

Conclusions and Outlook

7.1 Conclusions

This thesis work is focused on developing an optically referenced frequency comb based on a low power, low repetition rate erbium-doped fiber laser. The ultimate goal is toward a portable all-fiber frequency reference system.

In the process of building this optically referenced comb, we have successfully demonstrated saturated absorption spectroscopy (SAS) inside an acetylene-filled hollow-core fiber using an amplified comb tooth directly. The major challenge for direct comb spectroscopy for a fiber-based laser frequency comb is significant comb power amplification from nW/tooth to mW/tooth level (by a factor of 10^6) required by performing SAS. This has been achieved by building multiple filtering and amplification stages.

In the first amplification stage, two erbium-doped fiber amplifiers (EDFAs) were developed. Because our wavelength of interest ($\sim$ 1532-1539 nm) is on the edge of the oscillator output spectrum, the first short-pulse amplifier was designed to broaden the oscillator output spectrum. Although we have gained enough optical power from this highly backward pumped EDFA, tremendous amplified spontaneous emission (ASE) noise was also introduced due to the backward pumping scheme, resulting in a degraded comb signal-to-noise

ratio (SNR). We found that the key to a low noise power amplification is to amplify a narrow spectral bandwidth of the comb around our target wavelength by a small gain amplifier. By building multiple "spectral filtering + small gain amplification" stages, a high gain, low noise amplification scheme can be achieved. Moreover, a forward pumping scheme prevents introducing excessive ASE noise. Our second design of a small gain CW EDFA successfully amplifies the comb power by 22 dB (a factor of 158) while preserving the comb SNR.

The isolation of a single comb tooth from the 89 MHz fiber laser is accomplished in two steps. First, a Fabry-Perot (FP) filtering cavity is locked to the comb using the Pound-Drever-Hall (PDH) locking technique, resulting in a repetition rate multiplication from the original 89 MHz to 9.4 GHz, matching the free spectral range (FSR) of the filtering cavity. Second, when the 9.4 GHz comb passes through a spectral filter, the fiber Bragg grating (FBG), which has a 7 GHz bandwidth around our target wavelength, a single comb tooth can be isolated with an optical power of tens of μm.

The last amplification stage is done by seeding the isolated comb tooth into a distributed-feedback (DFB) laser diode such that the DFB laser can be injection locked to the seeding comb tooth. This last step further boosts the single tooth power up to 40 mW, sufficient for SAS. It is critical to have a single comb tooth with optical power above the locking threshold for stable injection locking. Tests done with CW lasers verify that seeding the DFB laser with multiple comb teeth can cause mode competition and lead to an unstable injection locking signal.

Using the amplified comb tooth as the laser source, SAS has been performed inside an acetylene-filled hollow-core kagome fiber. A narrow sub-Doppler feature of 17 MHz was observed, which is comparable to the sub-Doppler linewidth obtained using a CW laser as the source. The comb tooth was stabilized to this sub-Doppler feature by implementing frequency modulation (FM) spectroscopy. This fast frequency modulation technique allows the useful signal to be moved to a high modulation frequency region and later demodulated to DC frequency, in which case the signal is not contaminated by low frequency noise. This

results a high SNR ($\sim$ 150 with 4 kHz bandwidth) of the sub-Doppler error signal, allowing stable locking for tens of hours.

With a single comb tooth stabilized to the P(23) $\nu_1+\nu_3$ overtone transition line of $^{12}C_2H_2$ at $\sim$ 1539.4 nm, while the carrier-envelope offset frequency f_0 is locked to an RF reference (the GPS-disciplined Rb (GPS/Rb) oscillator), the fiber laser frequency comb is fully stabilized. The comb stability is investigated by comparing a CW reference at 1532.8 nm. The results show a short-term stability of 6×10^{-12} at 100 ms gate time, which is superior to that of the GPS/Rb oscillator by over an order of magnitude. At longer time scales, slow drift on the order of kHz/hour was observed. So far, we have not had a concrete conclusion of what effect(s) cause the drift. Based on the tests we have done, this slow drift is independent of temperature, humidity or vacuum leaking. It is possibly caused by the gain-dependent offset in our servo system for the single tooth locking. Further investigations are needed to confirm this possibility.

Compared with long term stability, the short term stability result of our comb is more significant for a portable reference. The fact that it is over an order of magnitude better than the GPS/Rb oscillator indicates that the optically-referenced comb we built can have better stability in practical applications without accessing the GPS signals. With improved portability, this fiber frequency comb system could serve as a portable optical frequency reference for a broad spectral range that covers near infrared telecom wavelengths.

7.2 Outlook

Toward our goal of building an all-fiber portable optical frequency reference, there are a few future directions in terms of improving the portability of the entire system. There are three free space sections in our current setup: 1) the f-2f interferometer for f_0 generation, 2) the Fabry-Perot cavity for comb filtering, and 3) the vacuum-chamber-based SAS setup (Figure 2.2) for single tooth stabilization. One direction for future work involves replacing

these free space setups by fiber-based components, for example, replacing the vacuum-chambers-based setup by an all-fiber photonic microcell reference. Other future directions could be to use alternative comb stabilization schemes, which could make the system simpler, but adds other requirements in order to ensure the reference performance at the same time. In the following paragraphs, I will address these directions in details.

The idea of an all-fiber microcell references is that, instead of installing the gas-filled hollow-core fiber in vacuum chambers, a pair of solid-core single mode fibers (SMF) can be spliced to both ends of the hollow-core fiber, with a low pressure acetylene sealed inside. These fiber cell references have advantages of being alignment free, low cost, light weight, and extremely portable. Stabilizing a fiber comb system to such a fiber cell will provide a portable comb system as a broad spectrum optical reference. The main challenge of making such a fiber cell is the technique for splicing the hollow-core fiber to SMF. First, the splice has to be made within a short time scale (typically less than one minute or shorter) to avoid air contamination during the splicing process, as the sub-Doppler error signal is very sensitive to even small amounts of contamination. Second, angle splicing is preferred (versus normal splicing) to prevent fiber cells suffering from pump reflections off the flat splicing interface. Angle splicing for hollow-core fibers is very difficult because cleaving the hollow-core fiber at an angle tends to damage the hollow-core structure of the fiber and introduce high loss. The current technique is to overpressure the hollow-core fiber with helium gas up to several atmospheres (atms) after loading acetylene, and a quick splice can be made while helium diffuses out from the fiber's open end. After sealing the cell, excessive helium diffuses slowly (up to a few days) through the side of the hollow-core fiber, leaving only acetylene inside. A few fiber cells are made successfully in this way [38], with short-term stability worse than the vacuum-chamber-based system by less than a factor of ten. The worse stability is mostly due to a broader linewidth caused by the fiber core size or air contamination, and a lower SNR of the sub-Doppler error signal. With the development of fiber splicers, it is possible that difficulties such as angle cleave and reduction in splicing

time for hollow-core fibers can be overcome in the near future.

In order to make the reference system simpler and more portable, two other comb stabilization schemes can be utilized to realize an optically referenced comb. One method is to lock f_{rep} to an RF reference while locking a single tooth to an optical transition. The benefit of this locking scheme is that the generation of f_0 becomes unnecessary, which cuts down almost 30 % of the overall system complexity. In our case, this also makes the comb amplification process easier because all the oscillator output (instead of 9.5 % of the total output) can be used for single tooth amplification. Based on the discussion in Section 5.1.3, the disadvantage of this locking scheme is that one has to use an RF reference better than a GPS/Rb oscillator, such as a hydrogen maser in our case, to have an RF uncertainties induced by f_{rep} locking less than the uncertainties caused by the optical reference. This obviously adds to the overall cost of the reference system.

The other promising comb locking scheme is to lock two comb teeth to different optical absorption lines. By integrating two fiber-cells as the optical references, the system can be made simpler, more portable and less expensive without the RF reference. However, this two comb teeth locking approach can be challenging, because based on the calculations in Section 5.1.4, the wavelength separation of these two comb teeth has to be over 100 nm to achieve a comb stability that does not degrade too fast with wavelength. This can be practically difficult since the standard gases for referencing purposes near telecom wavelengths have a limited absorption bandwidth of less than 100 nm [138]. Therefore, a gas other than acetylene needs to be chosen. The uncertainty of referencing a comb tooth to an optical reference largely depends on the sub-Doppler error signal, which is in turn affected by various factors, such as absorption strengths and pressure broadening coefficients. If a suitable absorption line can be found, it would be very promising to have a portable comb reference system with stability performance comparable to the other two locking schemes (f_0 + single tooth, and f_{rep} + single tooth), but with the lowest cost and the least system complexity.

Bibliography

[1] "NIST Time and Frequency from A to Z, url = http://tf.nist.gov/general/glossary.htm,."

[2] J. Ye, H. Schnatz, and L. Hollberg, "Optical frequency combs: from frequency metrology to optical phase control," *Selected Topics in Quantum Electronics, IEEE Journal of*, vol. 9, pp. 1041–1058, July 2003.

[3] D. Kleppner, "A milestone in time keeping," *Science*, vol. 319, no. 5871, pp. 1768–1769, 2008.

[4] P. Gill, H. Margolis, A. Curtis, H. Klein, S. Lea, S. Webster, and P. Whibberley, "Optical atomic clocks for space," *Technical Supporting Document from National Physical Laboratory (NPL)*, pp. 26–56, Aug 2008.

[5] S. A. Diddams, "Invited paper: The evolving optical frequency comb," *J. Opt. Soc. Am. B*, vol. 27, pp. B51–B62, Nov 2010.

[6] J. Tuominen, T. Ritari, H. Ludvigsen, and J. C. Petersen, "Gas filled photonic bandgap fibers as wavelength references," *Optics Communications*, vol. 255, no. 4?6, pp. 272–277, 2005.

[7] W. C. Swann and S. L. Gilbert, "Pressure-induced shift and broadening of 1510-1540 nm acetylene wavelength calibration lines," *J. Opt. Soc. Am. B*, vol. 17, pp. 1263–1270, Jul 2000.

[8] K. Knabe, "Using saturated absorption spectroscopy on acetylene-filled hollow-core fibers for absolute frequency measurements," *PhD thesis*, 2010.

[9] T. Hänsch and B. Couillaud, "Laser frequency stabilization by polarization spectroscopy of a reflecting reference cavity," *Optics Communications*, vol. 35, pp. 441–444, Dec 1980.

[10] C. Pearman, C. Adams, S. Cox, P. Griffin, D. Smith, and I. Hughes, "Polarization spectroscopy of a closed atomic transition: applications to laser frequency locking," *Journal of Physics B: Atomic, Molecular and Optical Physics*, vol. 35, no. 24, p. 5141, 2002.

[11] J. Hall, M. Taubman, and J. Ye, *Handbook of Optics, Book Chapter 27: Laser Stabilization*, vol. II.

[12] "Operating manual for newport LB1005 high-speed servo controller, http://assets.newport.com/webdocuments-en/images/lb1005operatingmanualp2102297reva.pdf."

[13] M. Shirasaki, "Large angular dispersion by a virtually imaged phased array and its application to a wavelength demultiplexer," *Opt. Lett.*, vol. 21, pp. 366–368, Mar 1996.

[14] M. A. Lombardi, "Book Chapter 17: Fundamentals of time and frequency," *CRC Press LLC*, 2002.

[15] E. Peik, "Fundamental constants and units and the search for temporal variations," *Nuclear Physics B (Proc. Suppl.)*, vol. 203-204, pp. 18–32, 2010.

[16] N. Leefer, C. T. M. Weber, A. Cingöz, J. R. Torgerson, and D. Budker, "New limits on variation of the fine-structure constant using atomic dysprosium," *Phys. Rev. Lett.*, vol. 111, p. 060801, Aug 2013.

[17] J. C. Berengut and V. V. Flambaum, "Manifestations of a spatial variation of fundamental constants in atomic clocks, oklo, meteorites, and cosmological phenomena," *Europhys. Lett.*, vol. 97, p. 20006, Jan 2012.

[18] T. Steinmetz, T. Wilken, C. Araujo-Hauck, R. Holzwarth, T. W. Hnsch, L. Pasquini, A. Manescau, S. D'Odorico, M. T. Murphy, T. Kentischer, W. Schmidt, and T. Udem, "Laser frequency combs for astronomical observations," vol. 321, no. 5894, pp. 1335–1337, 2008.

[19] "Official u.s. government information about the global positioning system (GPS) and related topics."

[20] J. R. Vig, "Military applications of high accuracy frequency standards and clocks," *IEEE Transactions on Ultrasonics, Ferroeleci'rics, and Frequency Control*, vol. 40, pp. 522–527, 1993.

[21] W. Lewandowski and C. Thomas, "GPS time transfer," *Proceedings of the IEEE*, vol. 79, pp. 991–1000, Jul 1991.

[22] J. Rutman and F. Walls, "Characterization of frequency stability in precision frequency sources," *Proceedings of the IEEE*, vol. 79, pp. 952–960, Jul 1991.

[23] J. L. Hall and J. Ye, "Laser frequency stabilization, standards, measurement, and applications," 2001.

[24] V. Chebotayev, V. Goldort, V. Klementyev, M. Nikitin, B. Timchenko, and V. Zakharyash, "Development of an optical time scale," *Applied Physics B*, vol. 29, no. 1, pp. 63–65, 1982.

[25] C. O. Weiss, G. Kramer, B. Lipphardt, and E. Garcia, "Frequency measurement of a CH_4 hyperfine line at 88 Thz/"optical clock"," *Quantum Electronics, IEEE Journal of*, vol. 24, pp. 1970–1972, Oct 1988.

[26] H. Schnatz, B. Lipphardt, J. Helmcke, F. Riehle, and G. Zinner, "First phase-coherent frequency measurement of visible radiation," *Phys. Rev. Lett.*, vol. 76, pp. 18–21, Jan 1996.

[27] J. E. Bernard, A. A. Madej, L. Marmet, B. G. Whitford, K. J. Siemsen, and S. Cundy, "Cs-based frequency measurement of a single, trapped ion transition in the visible region of the spectrum," *Phys. Rev. Lett.*, vol. 82, pp. 3228–3231, Apr 1999.

[28] P. Maddaloni, P. Cancio, and P. D. Natale, "Optical comb generators for laser frequency measurement," *Measurement Science and Technology*, vol. 20, no. 5, p. 052001, 2009.

[29] D. J. Jones, S. A. Diddams, J. K. Ranka, A. Stentz, R. S. Windeler, J. L. Hall, and S. T. Cundiff, "Carrier-envelope phase control of femtosecond mode-locked lasers and direct optical frequency synthesis," *Science*, vol. 288, no. 5466, pp. 635–639, 2000.

[30] M. Bellini and T. W. Hänsch, "Phase-locked white-light continuum pulses: toward a universal optical frequency-comb synthesizer," *Opt. Lett.*, vol. 25, pp. 1049–1051, Jul 2000.

[31] J. Rauschenberger, T. Fortier, D. Jones, J. Ye, and S. Cundiff, "Control of the frequency comb from a modelocked erbium-doped fiber laser," *Opt. Express*, vol. 10, pp. 1404–1410, Dec 2002.

[32] T. Udem and F. Riehle, "Frequency combs applications and optical frequency standards," *RIVISTA DEL NUOVO CIMENTO*, vol. 30, no. 12, pp. 563–606, 2007.

[33] T. E. Parker, "Long-term comparison of caesium fountain primary frequency standards," *Metrologia*, vol. 47, no. 1, p. 1, 2010.

[34] K. Watabe, H. Inaba, K. Okumura, F.-L. Hong, J. Hartnett, C. Locke, G. Santarelli, S. Yanagimachi, K. Minoshima, T. Ikegami, A. Onae, S. Ohshima, and M. Matsumoto, "Optical frequency synthesis from a cryogenic sapphire oscillator using a fiber-based frequency comb," *Instrumentation and Measurement, IEEE Transactions on*, vol. 56, pp. 632–636, April 2007.

[35] C. W. Chou, D. B. Hume, J. C. J. Koelemeij, D. J. Wineland, and T. Rosenband, "Frequency comparison of two high-accuracy Al^+ optical clocks," *Phys. Rev. Lett.*, vol. 104, p. 070802, Feb 2010.

[36] W. Zhang, M. J. Martin, C. Benko, J. L. Hall, J. Ye, C. Hagemann, T. Legero, U. Sterr, F. Riehle, G. D. Cole, and M. Aspelmeyer, "Reduction of residual amplitude modulation to 1×10^{-6} for frequency modulation and laser stabilization," *Opt. Lett.*, vol. 39, pp. 1980–1983, Apr 2014.

[37] "NEOARK Corporation, Acetylene Stabilized Diode Laser, http://www.neoark.co.jp/english/, url = ,."

[38] C. Wang, N. V. Wheeler, C. Fourcade-Dutin, M. Grogan, T. D. Bradley, B. R. Washburn, F. Benabid, and K. L. Corwin, "Acetylene frequency references in gas-filled hollow optical fiber and photonic microcells," *Appl. Opt.*, vol. 52, pp. 5430–5439, Aug 2013.

[39] S. Chang, A. Mann, and A. Luiten, "Improved cryogenic sapphire oscillator with exceptionally high frequency stability," *Electronics Letters*, vol. 36, pp. 480–481, Mar 2000.

[40] K. Knabe, S. Wu, J. Lim, K. A. Tillman, P. S. Light, F. Couny, N. Wheeler, R. Thapa, A. M. Jones, J. W. Nicholson, B. R. Washburn, F. Benabid, and K. L. Corwin, "10 kHz accuracy of an optical frequency reference based on $^{12}C_2H_2$-filled large-core kagome photonic crystal fibers," *Opt. Express*, vol. 17, pp. 16017–16026, Aug 2009.

[41] A. Bartels, C. W. Oates, L. Hollberg, and S. A. Diddams, "Stabilization of femtosecond laser frequency combs with subhertz residual linewidths," *Opt. Lett.*, vol. 29, pp. 1081–1083, May 2004.

[42] L.-S. Ma, Z. Bi, A. Bartels, K. Kim, L. Robertsson, M. Zucco, R. Windeler, G. Wilpers, C. Oates, L. Hollberg, and S. Diddams, "Frequency uncertainty for optically referenced

femtosecond laser frequency combs," *Quantum Electronics, IEEE Journal of*, vol. 43, pp. 139–146, Feb 2007.

[43] D. C. Heinecke, A. Bartels, T. M. Fortier, D. A. Braje, L. Hollberg, and S. A. Diddams, "Optical frequency stabilization of a 10 Ghz Ti:sapphire frequency comb by saturated absorption spectroscopy in ^{87}rubidium," *Phys. Rev. A*, vol. 80, p. 053806, Nov 2009.

[44] W. C. Swann, J. J. McFerran, I. Coddington, N. R. Newbury, I. Hartl, M. E. Fermann, P. S. Westbrook, J. W. Nicholson, K. S. Feder, C. Langrock, and M. M. Fejer, "Fiber-laser frequency combs with subhertz relative linewidths," *Opt. Lett.*, vol. 31, pp. 3046–3048, Oct 2006.

[45] I. Coddington, W. C. Swann, and N. R. Newbury, "Coherent multiheterodyne spectroscopy using stabilized optical frequency combs," *Phys. Rev. Lett.*, vol. 100, p. 013902, Jan 2008.

[46] Y. Nakajima, H. Inaba, K. Hosaka, K. Minoshima, A. Onae, M. Yasuda, T. Kohno, S. Kawato, T. Kobayashi, T. Katsuyama, and F.-L. Hong, "A multi-branch, fiber-based frequency comb with millihertz-level relative linewidths using an intra-cavity electro-optic modulator," *Opt. Express*, vol. 18, pp. 1667–1676, Jan 2010.

[47] D. Nicolodi, B. Argence, W. Zhang, R. L. Targat, G. Santarelli, and Y. L. Coq, "Spectral purity transfer between optical wavelengths at the 10^{18} level," *Nature Photonics*, vol. 8, pp. 219–223, Jan 2014.

[48] Y. Kim, S. Kim, Y. J. Kim, H. Hussein, and S. W. Kim, "Er-doped fiber frequency comb with mHz relative linewidth," *Opt. Express*, vol. 17, pp. 11972–11977, Jul 2009.

[49] J. Alnis, A. Matveev, N. Kolachevsky, T. Wilken, T. Udem, and T. W. Haensch, "Sub-Hz line width diode lasers by stabilization to vibrationally and thermally compensated ULE Fabry-Perot cavities," *Phys. Rev. A*, vol. 77, p. 053809, Jan 2008.

[50] S. Hirata, T. Akatsuka, Y. Ohtake, and A. Morinaga, "Sub-hertz-linewidth diode laser stabilized to an ultralow-drift high-finesse optical cavity," *Applied Physics Express*, vol. 7, no. 2, p. 022705, 2014.

[51] J. Lim, Kevin, K. A. Tillman, W. Neely, Y. Wang, R. Amezcua-Correa, F. Couny, P. S. Light, F. Benabid, J. C. Knight, K. L. Corwin, J. W. Nicholson, and B. R. Washburn, "A phase-stabilized carbon nanotube fiber laser frequency comb," *Opt. Express*, vol. 17, pp. 14115–14120, Aug 2009.

[52] M. S. Kirchner, D. A. Braje, T. M. Fortier, A. M. Weiner, L. Hollberg, and S. A. Diddams, "Generation of 20 Ghz, sub-40 fs pulses at 960 nm via repetition-rate multiplication," *Opt. Lett.*, vol. 34, pp. 872–874, Apr 2009.

[53] S. L. Gilbert and W. C. Swann, "Acetylene $^{12}C_2H_2$ absorption reference for 1510 nm to 1540 nm wavelength calibration?SRM 2517a," *National Institute of Standards and Technology Special Publication 260-133*, pp. 1–29, Feb 2001.

[54] S. L. Gilbert and W. C. Swann, "Carbon monoxide absorption references for 1560 nm to 1630 nm wavelength calibration srm 2514 ($^{12}C^{16}O$) and srm 2515 ($^{13}C^{16}O$)," *National Institute of Standards and Technology Special Publication 260-146*, pp. 1–40, Oct 2002.

[55] S. L. Gilbert, W. C. Swann, and C.-M. Wang, "Hydrogen cyanide $H^{13}C^{14}N$ absorption reference for 1530-1560 nm wavelength calibration - SRM 2519," *National Institute of Standards and Technology Special Publication 260-137*, pp. 1–27, Sep 1998.

[56] L. Lundsbergnielsen, F. Hegelund, and F. Nicolaisen, "Analysis of the high-resolution spectrum of ammonia ($^{14}NH_3$) in the near-infrared region, 6400-6900 cm^{-1}," *Journal of Molecular Spectroscopy*, vol. 162, no. 1, pp. 230 – 245, 1993.

[57] J. G. Moorhead, "The near infrared absorption spectrum of methane," *Phys. Rev.*, vol. 39, pp. 83–88, Jan 1932.

[58] V. Weldon, J. O'Gorman, P. Phelan, J. Hegarty, and T. Tanbun-Ek, "H^2S and CO_2 gas sensing using DFB laser diodes emitting at 1.57 μm," *Sensors and Actuators B: Chemical*, vol. 29, pp. 101 – 107, 1995. Proceedings of the 2nd European Conference on Optical Chemical Sensors and Biosensors.

[59] C. S. Edwards, G. P. Barwood, H. S. Margolis, P. Gill, and W. R. C. Rowley, "High precision frequency measurements of the $\nu_1+\nu_3$ combination band of $^{12}C_2H_2$ in the 1.5 μm region," *J. Mol. Spectrosc.*, vol. 234, pp. 143–148, 2005.

[60] A. A. Madej, A. J. Alcock, A. Czajkowski, J. E. Bernard, and S. Chepurov, "Accurate absolute reference frequencies from 1511 to 1545 nm of the $\nu_1+\nu_3$ band of $^{12}C_2H_2$ determined with laser frequency comb interval measurements," *J. Opt. Soc. Am. B*, vol. 23, pp. 2200–2208, Oct 2006.

[61] W. K. L. H. S. Moon and H. S. Suh, "Absolute-frequency measurement of an acetylene-stabilized laser locked to the P(16) transition of $^{13}C_2H_2$ using an opticalfrequency comb," *IEEE Transactions on Instrumentation and Measurement*, vol. 56, pp. 509–512, Oct 2007.

[62] W. Demtröder, *Laser Spectroscopy: Basic Concepts and Instrumentation*. Advanced texts in physics, Springer, 2003.

[63] A. Szöke and A. Javan, "Effects of collisions on saturation behavior of the 1.15 μm transition of Ne studied with He-Ne laser," *Phys. Rev.*, vol. 145, pp. 137–147, May 1966.

[64] R. L. Barger and J. L. Hall, "Pressure shift and broadening of methane line at 3.39 μm studied by laser-saturated molecular absorption," *Phys. Rev. Lett.*, vol. 22, pp. 4–8, Jan 1969.

[65] T. Hänsch and P. Toschek, "On pressure broadening in a He-Ne laser," *IEEE Journal of Quantum Electronics*, vol. 5, pp. 61–67, Feb 1969.

[66] T. W. Hänsch, I. S. Shahin, and A. L. Schawlow, "High-resolution saturation spectroscopy of the sodium D lines with a pulsed tunable dye laser," *Phys. Rev. Lett.*, vol. 27, pp. 707–710, Sep 1971.

[67] "NEOS technologies, an introduction to acousto-optic modulators and deflectors, http://www.neostech.com/pdfs."

[68] S. M. Barger, R. L. and J. Hall, "Frequency stabilization of a cw dye laser," *Applied Physics Letters*, vol. 22, no. 11, pp. 573–575, 1973.

[69] M. S. Taubman and J. L. Hall, "Cancellation of laser dither modulation from optical frequency standards," *Opt. Lett.*, vol. 25, pp. 311–313, Mar 2000.

[70] G. Bjorklund, M. Levenson, and C. Ortiz, "Frequency Modulation (FM) spectroscopy theory of lineshapes and signal-to-noise analysis," *Appl. Phys. B*, vol. 32, pp. 145–152, Jul 1983.

[71] J. A. Silver, "Frequency-modulation spectroscopy for trace species detection: theory and comparison among experimental methods," *Appl. Opt.*, vol. 31, pp. 707–717, Feb 1992.

[72] M. Gehrtz, G. C. Bjorklund, and E. A. Whittaker, "Quantum-limited laser frequency-modulation spectroscopy," *J. Opt. Soc. Am. B*, vol. 2, pp. 1510–1526, Sep 1985.

[73] H. Bode, *Network analysis and feedback amplifier design.* R. E. Krieger Pub. Co., 1959.

[74] D. R. Hjelme, S. Neegård, and E. Vartdal, "Optical interference fringe reduction in frequency-modulation spectroscopy experiments," *Opt. Lett.*, vol. 20, pp. 1731–1733, Aug 1995.

[75] G. R. Janik, C. B. Carlisle, and T. F. Gallagher, "Two-tone frequency-modulation spectroscopy," *J. Opt. Soc. Am. B*, vol. 3, pp. 1070–1074, Aug 1986.

[76] "NewFocus Application Note 7: FM spectroscopy with Tunable Diode Lasers, http://www.newport.com."

[77] G. C. Bjorklund, "Frequency-Modulation spectroscopy: a new method for measuring weak absorptions and dispersions," *Opt. Lett.*, vol. 5, pp. 15–17, Jan 1980.

[78] K.-E. Peiponen and J. J. Saarinen, "Generalized Kramers-Kronig relations in nonlinear optical- and Thz-spectroscopy," *Reports on Progress in Physics*, vol. 72, no. 5, p. 056401, 2009.

[79] D. Hutchings, M. Sheik-Bahae, D. Hagan, and E. V. Stryland, "Tutorial review: Kramers-Kronig relations in nonlinear optics," *Applied Physics B: Lasers and Optics*, vol. 24, pp. 1–30, Aug 1992.

[80] R. W. Fox, C. W. Oates, and L. W. Hollberg, *Stabilizing Diode Lasers to High-finesse Cavities*.

[81] G. Franklin, J. Powell, and A. Emami-Naeini, *Feedback control of dynamic systems*. No. v. 10, Pearson, 2010.

[82] "PID controllers, chapter 8, by caltech, avaialable online."

[83] W. Jung, ed., *Op Amp Applications Handbook*. Elsevier, 2005.

[84] J. Bechhoefer, "Feedback for physicists: A tutorial essay on control," *Rev. Mod. Phys.*, vol. 77, pp. 783–836, Aug 2005.

[85] K. Dutton, S. Thompson, and B. Barraclough, *The art of control engineering*. Pearson Education, Addison Wesley, 1997.

[86] G. Goodwin, S. Graebe, and M. Salgado, *Control system design*. Prentice Hall, 2001.

[87] J. J. McFerran, L. Nenadovic, W. C. Swann, J. B. Schlager, and N. R. Newbury, "A passively mode-locked fiber laser at 1.54 μm with a fundamental repetition frequency reaching 2 Ghz," *Opt. Express*, vol. 15, pp. 13155–13166, Oct 2007.

[88] S. Yamashita, Y. Inoue, K. Hsu, T. Kotake, H. Yaguchi, D. Tanaka, M. Jablonski, and S. Set, "5 Ghz pulsed fiber Fabry-Pérot laser mode-locked using carbon nanotubes," *Photonics Technology Letters, IEEE*, vol. 17, pp. 750–752, April 2005.

[89] S. Yamashita, T. Yoshida, S. Y. Set, P. Polynkin, and N. Peyghambarian, "Passively mode-locked short-cavity 10 Ghz Rr:Yy-codoped phosphate-fiber laser using carbon nanotubes," 2007.

[90] D. Chao, M. Sander, G. Chang, J. Morse, J. Cox, G. Petrich, L. Kolodziejski, F. Kaertner, and E. Ippen, "Self-referenced erbium fiber laser frequency comb at a Ghz repetition rate," in *Optical Fiber Communication Conference*, p. OW1C.2, Optical Society of America, 2012.

[91] F. Quinlan, G. Ycas, S. Osterman, and S. Diddams, "A 12.5 ghz-spaced optical frequency comb spanning $>$ 400 nm for near-infrared astronomical spectrograph calibration," *Review of Scientific Instruments*, vol. 81, pp. 063105–063105–9, Jun 2010.

[92] G. G. Ycas, F. Quinlan, S. A. Diddams, S. Osterman, S. Mahadevan, S. Redman, R. Terrien, L. Ramsey, C. F. Bender, B. Botzer, and S. Sigurdsson, "Demonstration of on-sky calibration of astronomical spectra using a 25 Ghz near-ir laser frequency comb," *Opt. Express*, vol. 20, pp. 6631–6643, Mar 2012.

[93] G. Chang, C.-H. Li, D. F. Phillips, R. L. Walsworth, and F. X. Kärtner, "Toward a broadband astro-comb: effects of nonlinear spectral broadening in optical fibers," *Opt. Express*, vol. 18, pp. 12736–12747, Jun 2010.

[94] C.-H. Li, G. Chang, A. G. Glenday, N. Langellier, A. Zibrov, D. F. Phillips, F. X. Kärtner, A. Szentgyorgyi, and R. L. Walsworth, "Conjugate Fabry-Pérot cavity pair for improved astro-comb accuracy," *Opt. Lett.*, vol. 37, pp. 3090–3092, Aug 2012.

[95] M. Akbulut, J. Davila-Rodriguez, I. Ozdur, F. Quinlan, S. Ozharar, N. Hoghooghi, and P. Delfyett, "Measurement of carrier envelope offset frequency for a 10 Ghz etalon-stabilized semiconductor optical frequency comb," *Opt. Express*, vol. 19, pp. 16851–16865, Aug 2011.

[96] D. Mandridis, C. Williams, I. Ozdur, and P. J. Delfyett, "Low noise chirped pulse mode-locked laser using an intra-cavity Fabry-Pérot etalon," *Opt. Express*, vol. 19, pp. 8994–8999, May 2011.

[97] T. J. Kippenberg, R. Holzwarth, and S. A. Diddams, "Microresonator-based optical frequency combs," *Science*, vol. 332, no. 6029, pp. 555–559, 2011.

[98] M. E. "Höckel David and B. Oliver", "Note: An ultranarrow bandpass filter system for single-photon experiments in quantum optics," *Review of Scientific Instruments*, vol. 81, no. 2, p. 026108, 2010.

[99] C. Roychoudhuri and M. Hercher, "Stable multipass Fabry-Pérot interferometer: design and analysis," *Appl. Opt.*, vol. 16, pp. 2514–2520, Sep 1977.

[100] P. Palittapongarnpim, A. MacRae, and A. I. Lvovsky, "Note: A monolithic filter cavity for experiments in quantum optics," *Review of Scientific Instruments*, vol. 83, no. 6, p. 066101, 2012.

[101] G. D. Cole, W. Zhang, M. J. Martin, J. Ye, and M. Aspelmeyer, "Tenfold reduction of brownian noise in high-reflectivity optical coatings," *Nature Photonics*, vol. 7, pp. 644–650, Jul 2013.

[102] D. Hunger, T. Steinmetz, Y. Colombe, C. Deutsch, T. W. Hänsch, and J. Reichel, "Fiber Fabry-Pérot cavity with high finesse," *New J. Phys.*, May.

[103] G. Agrawal and N. Olsson, "Self-phase modulation and spectral broadening of optical pulses in semiconductor laser amplifiers," *Quantum Electronics, IEEE Journal of*, vol. 25, pp. 2297–2306, Nov 1989.

[104] "Laser resonator stability, http://en.wikipedia.org/," Nov 2007.

[105] "Laguerre-gaussian, http://commons.wikimedia.org/wiki/file:laguerre-gaussian.png," Jul 2007.

[106] T. Steinmetz, T. Wilken, C. Araujo-Hauck, R. Holzwarth, T. Hänsch, and T. Udem, "Fabry-Pérot filter cavities for wide-spaced frequency combs with large spectral bandwidth," *Applied Physics B*, vol. 96, no. 2-3, pp. 251–256, 2009.

[107] T. M. Fortier, M. S. Kirchner, F. Quinlan, J. Taylor, J. C. Bergquist, T. Rosenband, N. Lemke, A. Ludlow, Y. Jiang, C. W. Oates, and S. A. Diddams, "Generation of ultrastable microwaves via optical frequency division," *Nature Photonics*, vol. 5, pp. 425–429, Apr 2011.

[108] F. Q. S. Gee, S. Ozharar and P. J. Delfyett, "High-precision measurement of free spectral range of etalon," *Electron. Lett.*, vol. 42, pp. 715–716, June 2006.

[109] D. Mandridis, I. Ozdur, M. Bagnell, and P. J. Delfyett, "Free spectral range measurement of a fiberized Fabry-Pérot etalon with sub-hz accuracy," *Opt. Express*, vol. 18, pp. 11264–11269, May 2010.

[110] D. R. Zimmerman and L. H. Spiekman, "Amplifiers for the masses:EDFA, EDWA, and SOA Amplets for metro and access applications," *J. Lightwave Technol.*, vol. 22, p. 63, Jan 2004.

[111] F. C. Cruz, M. C. Stowe, and J. Ye, "Tapered semiconductor amplifiers for optical frequency combs in the near infrared," *Opt. Lett.*, vol. 31, pp. 1337–1339, May 2006.

[112] P. P. Baveja, D. N. Maywar, A. M. Kaplan, and G. P. Agrawal, "Spectral broadening in ultrafast semiconductor optical amplifiers induced by gain dynamics and self-phase modulation," *Opt. Lett.*, vol. 35, pp. 294–296, Feb 2010.

[113] N. A. Olsson and G. P. Agrawal, "Spectral shift and distortion due to self-phase modulation of picosecond pulses in 1.5 μm optical amplifiers," *Appl. Phys. Lett*, vol. 55, pp. 13–15, July 1989.

[114] S. P. Singh, R. Gangwar, and N. Singh, "Nonlinear scattering effects in optical fibers," *Progress In Electromagnetics Research*, vol. 74, pp. 379–405, 2007.

[115] R. W. Boyd, *Nonlinear Optics*. San Diego, CA: Academic Press.

[116] F. Rohde, E. Benkler, and H. R. Telle, "High contrast, low noise selection and amplification of an individual optical frequency comb line," *Opt. Lett.*, vol. 38, pp. 103–105, Jan 2013.

[117] M. Vainio, M. Merimaa, and K. Nyholm, "Optical amplifier for femtosecond frequency comb measurements near 633 nm," *Applied Physics B*, vol. 81, no. 8, pp. 1053–1057, 2005.

[118] H. S. Moon, E. B. Kim, S. E. Park, and C. Y. Park, "Selection and amplification of modes of an optical frequency comb using a femtosecond laser injection-locking technique," *Applied Physics Letters*, vol. 89, no. 18, p. 181110, 2006.

[119] S. E. Park, E. B. Kim, Y.-H. Park, D. S. Yee, T. Y. Kwon, C. Y. Park, H. S. Moon, and T. H. Yoon, "Sweep optical frequency synthesizer with a distributed-bragg-reflector laser injection locked by a single component of an optical frequency comb," *Opt. Lett.*, vol. 31, pp. 3594–3596, Dec 2006.

[120] H. Y. Ryu, S. H. Lee, W. K. Lee, H. S. Moon, and H. S. Suh, "Absolute frequency measurement of an acetylene stabilized laser using a selected single mode from a femtosecond fiber laser comb," *Opt. Express*, vol. 16, pp. 2867–2873, Mar 2008.

[121] E. B. Kim, W. K. Lee, C. Y. Park, D. H. Yu, S. K. Lee, and S. E. Park, "Direct comparison of optical frequency combs using a comb-injection-locktechnique," *Opt. Express*, vol. 16, pp. 10721–10727, Jul 2008.

[122] H. Y. Ryu, S. H. Lee, E. B. Kim, H.-S. Suh, and H. S. Moon, "A discretely tunable multifrequency source injection locked to a spectral-mode-filtered fiber laser comb," *Applied Physics Letters*, vol. 97, pp. 141107–141107–3, Oct 2010.

[123] H. Y. Ryu, S. H. Lee, and H. S. Suh, "Widely tunable external cavity laser diode injection locked to an optical frequency comb," *Photonics Technology Letters, IEEE*, vol. 22, pp. 1066–1068, July 2010.

[124] H. S. Moon, H. Y. Ryu, S. H. Lee, and H. S. Suh, "Precision spectroscopy of Rb atoms using single comb-line selected from fiber optical frequency comb," *Opt. Express*, vol. 19, pp. 15855–15863, Aug 2011.

[125] M. Vainio, M. Merimaa, and K. Nyholm, "Optical amplifier for femtosecond frequency comb measurements near 633 nm," *Applied Physics B*, vol. 81, no. 8, pp. 1053–1057, 2005.

[126] V. Chernyak and L. Qian, "Modeling high-concentration L-band EDFA at high optical powers based on inversion function," *Selected Topics in Quantum Electronics, IEEE Journal of*, vol. 8, pp. 569–574, 2002.

[127] P. Myslinski, C. Szubert, A. Bruce, D. DiGiovanni, and B. Palsdottir, "Performance of high-concentration erbium-doped fiber amplifiers," *Photonics Technology Letters, IEEE*, vol. 11, pp. 973–975, Aug 1999.

[128] S. Selvakennedy, M. Mahdi, P. Poopalan, and H. Ahmad, "Pump wavelength's influence in erbium-doped fibre amplifier performance," in *Semiconductor Electronics, 1998. Proceedings. ICSE '98. 1998 IEEE International Conference on*, pp. 124–128, 1998.

[129] G. Keiser, *Optical Fiber Communications*. McGraw-Hill Higher Education, 2000.

[130] "Swamp optics tutorial, http://swampoptics.com/pdfs."

[131] S. A. Diddams, M. Kirchner, T. Fortier, D. Braje, A. M. Weiner, and L. Hollberg, "Improved signal-to-noise ratio of 10 Ghz microwave signals generated with a mode-filtered femtosecond laser frequency comb," *Opt. Express*, vol. 17, pp. 3331–3340, Mar 2009.

[132] R. Steele, G. Walker, and N. Walker, "Sensitivity of optically preamplified receivers with optical filtering," *Photonics Technology Letters, IEEE*, vol. 3, pp. 545–547, June 1991.

[133] A. Yariv, "Signal-to-noise considerations in fiber links with periodic or distributed optical amplification," *Opt. Lett.*, vol. 15, pp. 1064–1066, Oct 1990.

[134] H. Kogelnik and A. Yariv, "Considerations of noise and schemes for its reduction in laser amplifiers," *Proceedings of the IEEE*, vol. 52, pp. 165–172, Feb 1964.

[135] R. Laming, M. Zervas, and D. Payne, "Erbium-doped fiber amplifier with 54 dB gain and 3.1 dB noise figures," *Photonics Technology Letters, IEEE*, vol. 4, pp. 1345–1347, Dec 1992.

[136] R. Laming and D. Payne, "Noise characteristics of erbium-doped fiber amplifier pumped at 980 nm," *Photonics Technology Letters, IEEE*, vol. 2, pp. 418–421, June 1990.

[137] M. Ebbeni, "Watt-class continuous wave Er^{3+}/Yb^{3+} fiber amplifier," *MS thesis*, 2012.

[138] J. Tuominen, T. Ritari, H. Ludvigsen, and J. Petersen, "Gas filled photonic bandgap fibers as wavelength references," *Optics Communications*, vol. 255, no. 46, pp. 272 – 277, 2005.

[139] "Measured fractional stability of the GPS/Rb oscillator, http://www.ptsyst.com/appnote2.pdf."

[140] K. Knabe, S. Wu, J. Lim, K. A. Tillman, P. S. Light, F. Couny, N. Wheeler, R. Thapa, A. M. Jones, J. W. Nicholson, B. R. Washburn, F. Benabid, and K. L. Corwin, "10 khz accuracy of an optical frequency reference based on 12c2h2-filled large-core kagome photonic crystal fibers," *Opt. Express*, vol. 17, pp. 16017–16026, Aug 2009.

[141] D. Hou, J. Wu, S. Zhang, Q. Ren, Z. Zhang, and J. Zhao, "A stable frequency comb directly referenced to rubidium electromagnetically induced transparency and two-photon transitions," *Applied Physics Letters*, vol. 104, no. 11, pp. –, 2014.

[142] K. A. Tillman, R. Thapa, B. R. Washburn, and K. L. Corwin, "Significant carrier envelope offset frequency linewidth narrowing in a prism-based cr:forsterite frequency comb," in *Conference on Lasers and Electro-Optics/Quantum Electronics and Laser Science Conference and Photonic Applications Systems Technologies*, p. CTuC5, Optical Society of America, 2008.

[143] J. McFerran, W. Swann, B. Washburn, and N. Newbury, "Suppression of pump-induced frequency noise in fiber-laser frequency combs leading to sub-radian f_{ceo} phase excursions," *Applied Physics B*, vol. 86, no. 2, pp. 219–227, 2007.

[144] A. Sennaroglu, H. Nathel, and C. R. Pollock, "Continuous-wave self-mode-locked operation of a femtosecond Cr^{4+}:YAG laser," *Opt. Lett.*, vol. 19, pp. 390–392, Mar 1994.

[145] A. A. Madej, J. E. Bernard, A. J. Alcock, A. Czajkowski, and S. Chepurov, "Accurate absolute frequencies of the $\nu_1+\nu_3$ band of $^{13}C_2H_2$ determined using an infrared mode-

locked Cr:YAG laser frequency comb," *J. Opt. Soc. Am. B*, vol. 23, pp. 741–749, Apr 2006.

[146] C. Chudoba, J. G. Fujimoto, E. P. Ippen, H. A. Haus, U. Morgner, F. X. Kärtner, V. Scheuer, G. Angelow, and T. Tschudi, "All-solid-state Cr:forsterite laser generating 14-fs pulses at 1.3 μm," *Opt. Lett.*, vol. 26, pp. 292–294, Mar 2001.

[147] K. Kim, B. R. Washburn, G. Wilpers, C. W. Oates, L. Hollberg, N. R. Newbury, S. A. Diddams, J. W. Nicholson, and M. F. Yan, "Stabilized frequency comb with a self-referenced femtosecond cr:forsterite laser," *Opt. Lett.*, vol. 30, pp. 932–934, Apr 2005.

[148] X. Liu, X. Zhou, X. Tang, J. Ng, J. Hao, T. Chai, E. Leong, and C. Lu, "Switchable and tunable multiwavelength erbium-doped fiber laser with fiber bragg gratings and photonic crystal fiber," *Photonics Technology Letters, IEEE*, vol. 17, pp. 1626–1628, Aug 2005.

[149] J. Ye, H. Schnatz, and L. Hollberg, "Optical frequency combs: from frequency metrology to optical phase control," *Selected Topics in Quantum Electronics, IEEE Journal of*, vol. 9, pp. 1041–1058, July 2003.

[150] F.-L. Hong, K. Minoshima, A. Onae, H. Inaba, H. Takada, A. Hirai, H. Matsumoto, T. Sugiura, and M. Yoshida, "Broad-spectrum frequency comb generation and carrier-envelope offset frequency measurement by second-harmonic generation of a mode-locked fiber laser," *Opt. Lett.*, vol. 28, pp. 1516–1518, Sep 2003.

[151] B. R. Washburn, S. A. Diddams, N. R. Newbury, J. W. Nicholson, M. F. Yan, and C. G. Jrgensen, "Phase-locked, erbium-fiber-laser-based frequency comb in the near infrared," *Opt. Lett.*, vol. 29, pp. 250–252, Feb 2004.

[152] K. A. Tillman, R. Thapa, K. Knabe, S. Wu, J. Lim, B. R. Washburn, and K. L. Corwin, "Stabilization of a self-referenced, prism-based, Cr:forsterite laser frequency comb using an intracavity prism," *Appl. Opt.*, vol. 48, pp. 6980–6989, Dec 2009.

[153] U. Keller, T. H. Chiu, and J. F. Ferguson, "Self-starting femtosecond mode-locked nd:glass laser that usesintracavity saturable absorbers," *Opt. Lett.*, vol. 18, pp. 1077–1079, Jul 1993.

[154] D. Kopf, F. X. Kärtner, K. J. Weingarten, and U. Keller, "Pulse shortening in a nd:glass laser by gain reshaping and soliton formation," *Opt. Lett.*, vol. 19, pp. 2146–2148, Dec 1994.

[155] L. Xu, T. W. Hänsch, C. Spielmann, A. Poppe, T. Brabec, and F. Krausz, "Route to phase control of ultrashort light pulses," *Opt. Lett.*, vol. 21, pp. 2008–2010, Dec 1996.

[156] K. Holman, R. Jones, A. Marian, S. Cundiff, and J. Ye, "Detailed studies and control of intensity-related dynamics of femtosecond frequency combs from mode-locked Ti: Sapphire lasers," *Selected Topics in Quantum Electronics, IEEE Journal of*, vol. 9, pp. 1018–1024, July 2003.

[157] F. W. Helbing, G. Steinmeyer, U. Keller, R. S. Windeler, J. Stenger, and H. R. Telle, "Carrier-envelope offset dynamics of mode-locked lasers," *Opt. Lett.*, vol. 27, pp. 194–196, Feb 2002.

[158] F. DeMartini, C. H. Townes, T. K. Gustafson, and P. L. Kelley, "Self-steepening of light pulses," *Phys. Rev.*, vol. 164, pp. 312–323, Dec 1967.

[159] N. R. Newbury and W. C. Swann, "Low-noise fiber-laser frequency combs (invited)," *J. Opt. Soc. Am. B*, vol. 24, pp. 1756–1770, Aug 2007.

[160] S. T. Cundiff and J. Ye, "Colloquium: Femtosecond optical frequency combs," *Rev. Mod. Phys.*, vol. 75, pp. 325–342, Mar 2003.

[161] R. W. Fox, B. R. Washburn, N. R. Newbury, and L. Hollberg, "Wavelength references for interferometry in air," *Appl. Opt.*, vol. 44, pp. 7793–7801, Dec 2005.

[162] D. J. Jones, S. A. Diddams, J. K. Ranka, A. Stentz, R. S. Windeler, J. L. Hall, and S. T. Cundiff, "Carrier-envelope phase control of femtosecond mode-locked lasers and direct optical frequency synthesis," *Science*, vol. 288, no. 5466, pp. 635–639, 2000.

[163] S. T. Cundiff, "Phase stabilization of ultrashort optical pulses," *Journal of Physics D: Applied Physics*, vol. 35, no. 8, p. R43, 2002.

[164] R. Thapa, "Cr:forsterite laser frequency comb stabiliazation and develpment of portable frequency refereces inside a hollow optical fiber," *PhD thesis*, 2008.

[165] L. H. Scott A. Diddams and V. Mbele, "Molecular fingerprinting with the resolved modes of a femtosecond laser frequency comb," *Nature*, vol. 445, pp. 627–630, Feb 2007.

[166] A. M. Weiner, "Femtosecond pulse shaping using spatial light modulators," *Review of Scientific Instruments*, vol. 71, no. 5, pp. 1929–1960, 2000.

Appendix A

VIPA Calculation

A.1 Introduction to VIPA

In order to resolve a single comb tooth, a useful tool for high spectral resolution is the virtually-imaged phase array (VIPA) spectrometer. It was invented in 1996 by M. Shirasaki [13]. The inset picture in Figure A.1 shows the basic working principle of the VIPA. Collimated light is focused into a line by a cylindrical lens and enters the VIPA through its window area. At the back surface, light of different wavelengths emerges at different angles.

A more detailed mechanism can be explained from the side view of the VIPA, shown in Figure A.1. It consists of two reflective glass plates, and can be viewed as a modified Fabry-Perot interferometer. The back surface is coated with a partially reflective film (e.g. 95%); the front surface is coated with an almost 100% reflective film except in a window area, which is AR coated. A collimated laser source is focused into this window. Due to the high reflectivity of the front surface, the laser beam experiences multiple reflections back and forth, each reflection having a diverging output beam. These multiple output beams with constant phase difference can interfere with each other. Since this phase difference is frequency-dependent, the direction of the output beam also varies with frequency. Therefore, the VIPA functions as a spectral disperser. The free spectral range of the VIPA is determined

by its thickness and index of refraction. The name of the VIPA comes from the fact that it operates as if there were multiple virtual sources interfering with each other as in a phased array. The direction of the output beam depends on the phase difference between these virtual sources. The major advantage of the VIPA is that the interference of the array can give rise to a large angular dispersion. In combination with a diffraction grating, the spectral resolution can reach GHz level [165], which is 20 times larger than regular optical gratings [13].

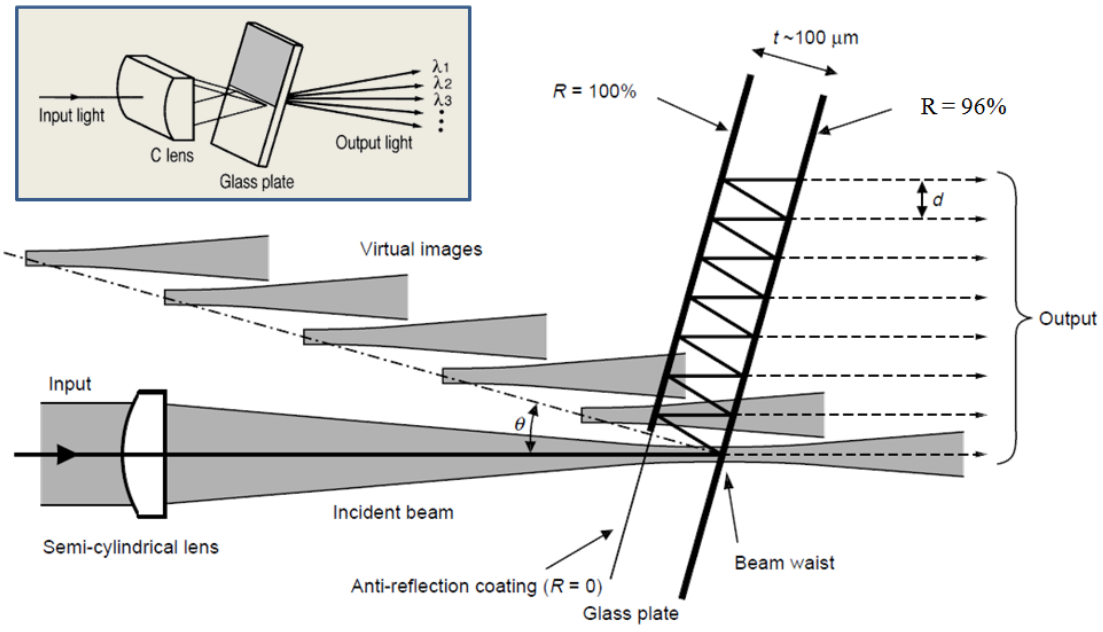

Figure A.1: *Schematic digram of virtually-imaged phase array (VIPA) structure adapted from Figure 1 and 2 from Ref [13].*

Since the dispersion angle is very sensitive to the accumulated phase difference between beam paths, one big challenge for VIPA fabrication is the material index uniformity. A great amount of polishing precision is required to minimize the integrated optical path length error, which results in high cost. For a commercial 50 GHz VIPA (market price $\sim$ \$10,000), the thickness is 1.5 mm with a refractive index $n_r \approx 2$. However, for a 5 GHz VIPA, which we proposed for a potential resolution of sub-100 MHz in combination with a 50 GHz VIPA, the

thickness would be ten times larger. The fabrication of a 5 GHz VIPA is more challenging and beyond the manufacturer's capability at time of our last communication in 2011.

A.2 Resolution calculation for single VIPA

Consider a beam that passes through one VIPA, the intensity distribution of the output beam according to Xiao *et al.* (Opt. Express Vol 12, p2899(2004)) is

$$I_{out}(y,k,\Delta) \propto \exp(-\frac{2f_c^2y^2}{f^2W^2}) \times \frac{1}{(1-Rr)^2+4(Rr)\sin^2(k\Delta/2)} \tag{A.1}$$

In this equation, y is the displacement in y direction on detector plane. f_c and f are the focal lengths of the cylindrical and imaging lenses, W is the incident beam radius, R and r are the high and partial reflectivities of VIPA surfaces, and $k = 2\pi/\lambda$ is the wave number of the beam. Δ is the parameter that determines VIPA dispersion and is given by

$$\Delta(y,\lambda,\theta(\nu)) = 2tn_r\cos\theta_\nu - 2t\frac{\tan\theta_\nu\cos\theta_{i\nu}y}{f} - \frac{t\cos\theta_\nu y^2}{n_r(\lambda)f^2} \tag{A.2}$$

Here, t is the etalon thickness, n_r is the index of refraction, $\theta_{i\nu}$ is the incident angle of the focused beam on the VIPA, and θ_ν is the propagation angle of the beam inside the VIPA. The incident and internal propagation angles of beam are related according to Snell's law

$$n_r(\lambda)\sin\theta_\nu = \sin\theta_{i\nu} \tag{A.3}$$

According to Eqn A.1, constructive interference happens when the phase-matching condition is satisfied

$$k\Delta = 2m\pi \tag{A.4}$$

Here m is the mode order of VIPA transmission. This is derived as spectral dispersion law for the VIPA by Xiao *et al.* We know that maximum intensity occurs when $\sin^2(k\Delta/2)$

reaches the minimum value of zero when

$$\frac{1}{(1-Rr)^2+4(Rr)\sin^2(k\Delta/2)} = \frac{1}{(1-Rr)^2} \tag{A.5}$$

At the same position y_0, the transmitted intensity I_{out} is reduced from $I_{\max}$ to $I_{\max}/2$ when

$$(1-Rr)^2 = 4(Rr)\sin^2(k\Delta/2) \tag{A.6}$$

This is equivalent to

$$\sin^2(\frac{k\Delta}{2}) = \frac{(1-Rr)^2}{4(Rr)} = constant \tag{A.7}$$

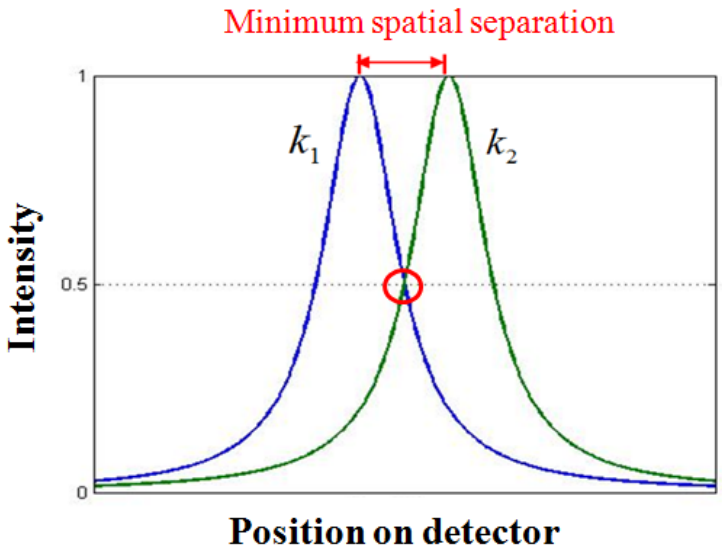

Figure A.2: *Definition of "resolution" for two Lorenzian modes. Here, k_1 and k_2 are the two wave vectors.*

For a frequency comb input, "resolution" is defined as the separation of two adjacent comb teeth with wave number k_1, k_2 when they overlapped at the FWHM point, as shown in Figure A.2. This overlapping point belongs to both curves. So now we will let k_1, k_2

satisfy this condition and then solve for the separation $|k_1 - k_2|$.

$$\sin^2(\theta_1) = \frac{(1-Rr)^2}{4Rr} \;\; and \;\; \sin^2(\theta_2) = \frac{(1-Rr)^2}{4Rr} \tag{A.8}$$

where

$$\theta_1 = \frac{k_1\Delta}{2} \;\; and \;\; \theta_2 = \frac{k_2\Delta}{2} \tag{A.9}$$

Lets define

$$\alpha = \frac{k\Delta}{2} = \pm \arcsin \frac{1-Rr}{2\sqrt{Rr}} \tag{A.10}$$

Since $\dfrac{1-Rr}{2\sqrt{Rr}} \approx 0$, so α is a small angle close to zero. A possible solution to Eqn A.8 is when the separation is twice of the angle α, that is

$$\theta_1 - \theta_2 = \alpha - (-\alpha) = 2\alpha \tag{A.11}$$

This is equivalent to say

$$\frac{\Delta}{2}(k_1 - k_2) = 2\alpha, \;\; or \;\; k_1 - k_2 = \frac{4\alpha}{\Delta}. \tag{A.12}$$

Recall that $k = \omega/c$, where the angular frequency $\omega = 2\pi f$. Substitute both relations into Eqn A.12. We have the resolution

$$\Delta f = f_1 - f_2 = \frac{4\alpha}{\Delta} \times \frac{c}{2\pi} = \frac{2\alpha c}{\pi\Delta} \tag{A.13}$$

which is the minimum frequency separation that a VIPA can resolve. As a final result,

$$\text{VIPA resolution} = \frac{2\arcsin\dfrac{1-Rr}{2\sqrt{Rr}} \times c}{\pi \times \Delta} \tag{A.14}$$

From Eqn A.14 and Eqn A.2, we can see the VIPA resolution depends on three parameters:

highly reflectivity, partial reflectivity and output angle, which determines the dispersion parameter Δ. Calculation shows that VIPA resolution is not sensitive to the output angle but very sensitive to the coating reflectivity. Table A.1 lists a few calculation results.

FSR = 50 GHz					
Highly Reflectivity	99.5%	100%	99.5%	99.5%	99.5%
Partial Reflectivity	96%	96%	95%	96%	96%
Incident angle	2°	2°	2°	10°	0.1°
VIPA Resolution @ 0° output angle	729.7 MHz	649.9 MHz	896.5 MHz	732.4 MHz	729.6 MHz
VIPA Resolution @ 5° output angle	731 MHz	651 MHz	898 MHz	735.8 MHz	730.3 MHz
AVG Resolution	730 MHz	650 MHz	897 MHz	734 MHz	730 MHz

Table A.1: *A 50 GHz VIPA resolution under various parameters. The resolution of a 5 GHz VIPA is 10% of that of 50 GHz VIPA under the same parameter setting.*

A.3 Derivation of grating equation for cross-VIPA

Based on the calculation above, the 5 GHz VIPA has a calculated resolution of less than 100 MHz. Using the combination of 5 GHz and 50 GHz VIPA in an orthogonal configuration, as shown in Figure A.3, we could possibly spectrally resolve individual comb teeth in a two-dimensional manner.

The first cylindrical lens focuses a collimated beam from a frequency comb with a repetition rate of 100 MHz into a 5 GHz VIPA. The second cylindrical lens is used to focus the light emerged at the first VIPA into the input window of the second VIPA. At this point, each individual comb tooth is focused into a line spatially separated from adjacent teeth, but only up to 5 GHz, which is limited by the free spectral range of the first VIPA. For an input with spectral bandwidth greater than 5 GHz, the output modes are spatially superimposed on the previous resolved lines. The second 50 GHz VIPA has a resolution smaller than 5 GHz, thus is capable of resolving these overlapped modes. As a result, the

cross-VIPA spectrometer is acting as a frequency comb "brush" as in ref [165] to map out an array of dots on the detector, representing individual comb tooth.

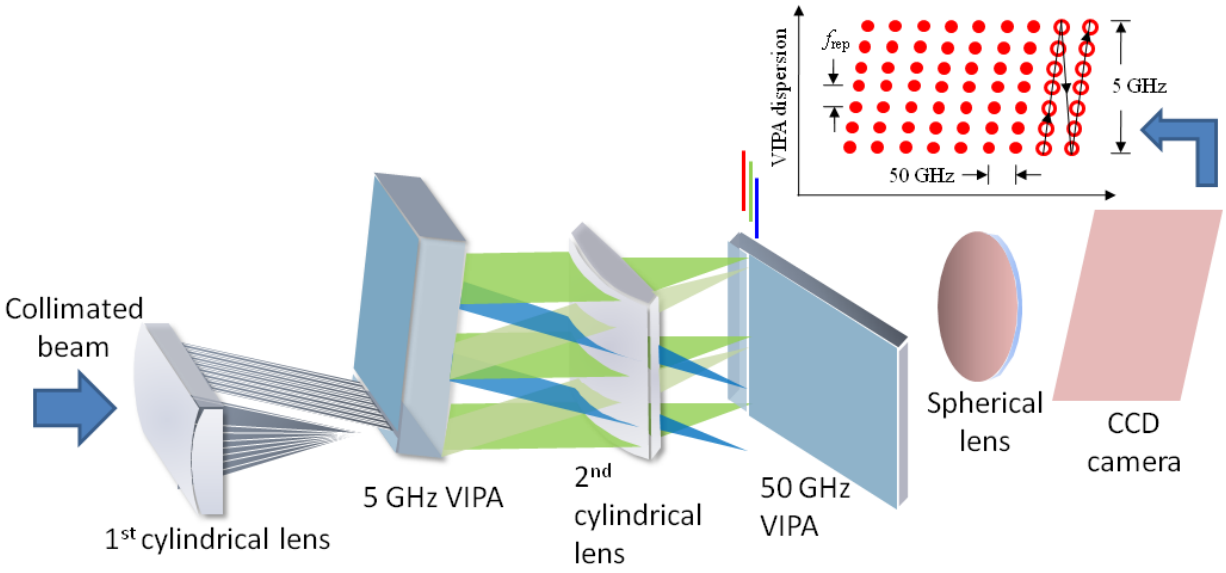

Figure A.3: *Proposed Cross-VIPA setup for sub 100 MHz spectral resolution.*

In this section, I will derive the dispersion equation for the crossed-VIPA spectrometer. The following calculation is for an air-spaced VIPA under the plane wave approximation. Figure A.4 (a) shows that light of different wavelengths (or k vectors) enters the first VIPA through the window, as indicated by arrows of different colors. All k vectors lie on the same plane which is perpendicular to the VIPA surface. At the first VIPA output, light of different wavelengths emerges at different angles, with all k vectors still in the same plane and perpendicular to the cylindrical lens. Figure A.4 (b) and (c) show with different k vector is focused by the cylindrical lens into a line incident on the window of the second VIPA. Because different k vectors have different input angle with respect to the front surface of the second VIPA, light travels in different planes inside the second VIPA. As shown in Figure A.4 (b) and (d), the green light travels on a plane that is parallel to the bottom surface of the VIPA, while the blue light travels on a plane that has an angle with respect to the bottom surface of VIPA.

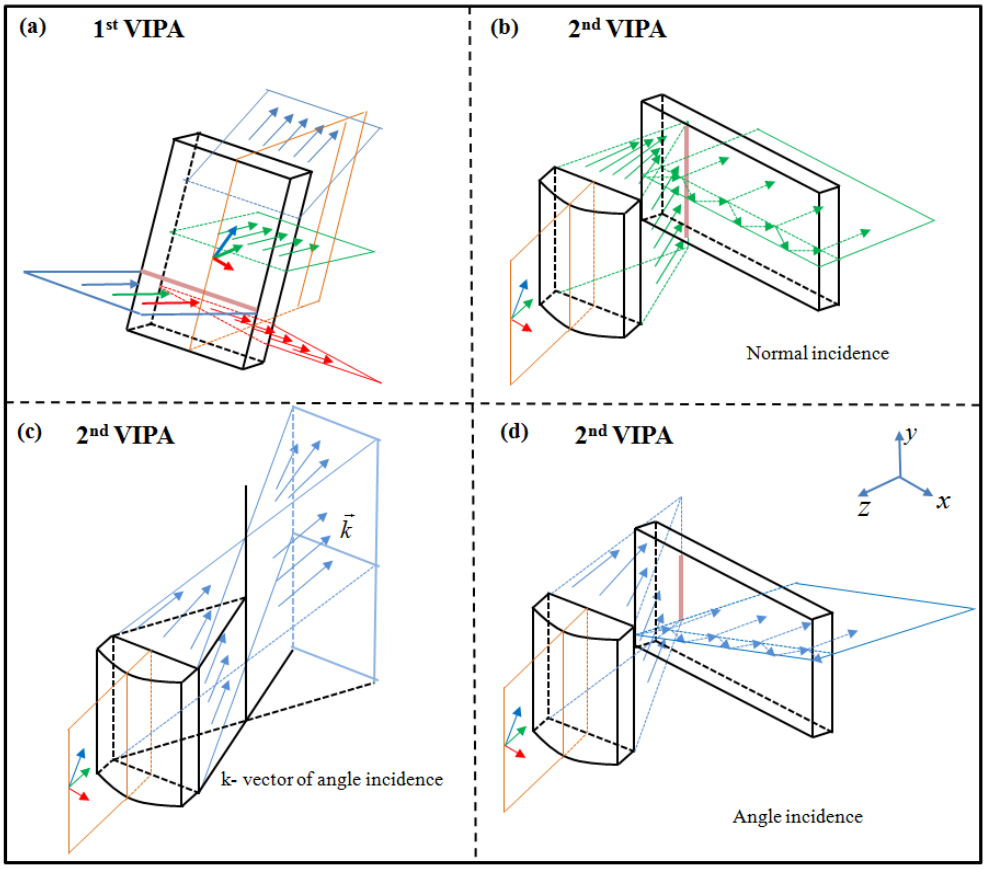

Figure A.4: *The ray tracing diagram illustrating how light of different wavelengths (or k vectors, represented by arrows in different colors in the graph) propagates before and after the two VIPAs.*

In order to derive the grating equation for this cross-VIPA configuration, we need to figure out the path length difference between two successive light paths for an arbitrary k vector. Figure A.5 (a) shows the 3D ray tracing diagram for an arbitrary k vector travelling inside the second VIPA on plane $OCGF$. $\overrightarrow{CH}$ is the input k vector, while $\overrightarrow{HE}$ is one of the paths for the output beam, with θ_{out} being the output angle. Here we define two angles θ and ϕ for the input k vector projected on the zx and yz plane:

$$\theta = \angle OCA, \text{ and } \phi = \angle OCB \tag{A.15}$$

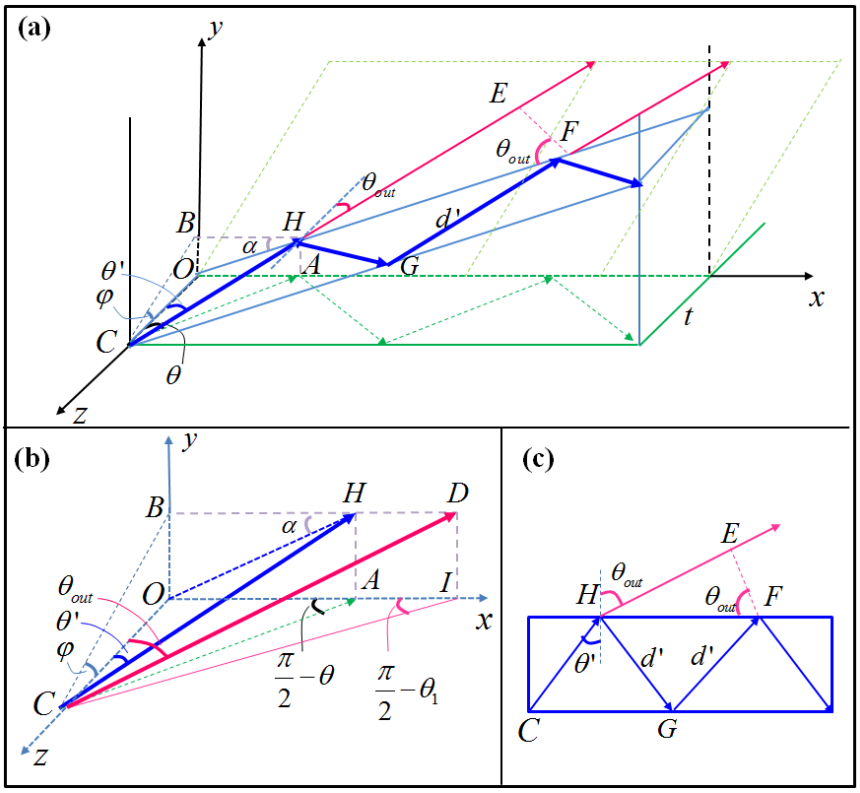

Figure A.5: *(a) The ray tracing diagram for an arbitrary k vector (blue arrow) travelling inside the second VIPA. (b) Zoom in of (a). (c) The top view of plane CGFH in (a).*

The incident angle is

$$\theta_{\text{inc}} = \angle OCH \tag{A.16}$$

If we move the output vector $\overrightarrow{HE}$ to be coincident with the input vector $\overrightarrow{CH}$, Figure A.5 (b) shows the zoomed-in picture of the geometrical relationship. In this picture, the VIPA thickness is represented by $|OC| = t$. We define the first travel distance for k as $d' = |CH|$. Therefore,

$$d' = |CH| = \sqrt{|OC|^2 + |OH|^2} = \sqrt{|OC|^2 + |OB|^2 + |BH|^2} \tag{A.17}$$

Using the relationship $|OB| = |OC| \tan\phi$, and $|BH| = |OA| = |OC| \tan\theta$, Equation B.3 becomes

$$d' = |CH| = t\sqrt{1 + \tan^2\theta + \tan^2\phi} \tag{A.18}$$

Therefore, the incident angle can be expressed in terms of θ and ϕ.

$$\sin\theta_{\text{inc}} = \frac{|OH|}{|CH|} = \frac{|OB| + |BH|}{d'} = \frac{\sqrt{\tan^2\theta + \tan^2\phi}}{\sqrt{1 + \tan^2\theta + \tan^2\phi}} \tag{A.19}$$

Figure A.5 (c) is the top view of plane $CGFH$. $|HF|$ can be written as

$$|HF| = 2d' \sin\theta_{\text{inc}} = 2t\sqrt{\tan^2\theta + \tan^2\phi} \tag{A.20}$$

Therefore, the path length difference is

$$\Delta = 2d' - |EH| = 2t(\sqrt{1 + \tan^2\theta + \tan^2\phi} + \sqrt{\tan^2\theta + \tan^2\phi}\sin\theta_{\text{out}}) \tag{A.21}$$

Now we need to express θ_{out} in terms of θ and ϕ. We know that the input angle $\theta_{\text{inc}} = \theta_{\text{inc}}(\theta, \phi)$. Similarly, the output angle $\theta_{\text{out}} = \theta_{\text{out}}(\theta_1, \phi)$, where θ_1 is the projection angle of θ_{out} on the zx plane angle (Figure A.5 (b)), which is

$$\theta_1 = \angle OCI \tag{A.22}$$

Similar to Equation B.5, we have

$$\sin\theta_{\text{out}} = \frac{\sqrt{\tan^2\theta_1 + \tan^2\phi}}{\sqrt{1 + \tan^2\theta_1 + \tan^2\phi}} \tag{A.23}$$

If we define the dispersion angle θ_λ to be the difference between the two projected angles by θ_{inc} and θ_{out} on the zx plane, that is

$$\theta_\lambda = \theta_1 - \theta \tag{A.24}$$

We can rewrite Equation B.6 in terms of θ, ϕ and θ_λ. That gives us the dispersion equation

for cross-VIPA:

$$\begin{aligned}\Delta &= 2t(\sqrt{1+\tan^2\theta+\tan^2\phi}+\sqrt{\tan^2\theta+\tan^2\phi}\frac{\sqrt{\tan^2(\theta_\lambda+\theta)+\tan^2\phi}}{\sqrt{1+\tan^2(\theta_\lambda+\theta)+\tan^2\phi}}) \\ &= m\lambda\end{aligned} \tag{A.25}$$

where θ, ϕ and θ_λ are defined by Equation B.1 and A.24.

Appendix B

Transmission Grating Calculation

B.1 Introduction to Gratings

A grating spectrometer consists of a diffraction grating, an imaging lens and a detector, as shown in Figure B.1. To calculate the expression for the grating spectral resolution, we will first introduce several properties of a grating spectrometer.

For a typical diffraction grating, the incident angle θ_i and diffraction angle θ_d is related by the grating equation

$$m\lambda = d(\sin\theta_d - \sin\theta_i) \tag{B.1}$$

where m is the order of the diffracted light, λ is the wavelength for the incident light, and d is the grating period (inverse of the # of lines/mm). The diffraction angle is then

$$\theta_d = \arcsin(\frac{m\lambda + d\sin\theta_i}{d}) \tag{B.2}$$

In order to find the expression for the grating spectral resolution, we need to know the frequency-dependent spatial intensity distribution of light in the detector plane, which is given by Ref [166]

$$I_{\text{det}}(x,\omega) \propto I_{\text{in}}(\tilde{\omega})\exp\frac{-2(x-\alpha\tilde{\omega}^2)}{w_0^2} \tag{B.3}$$

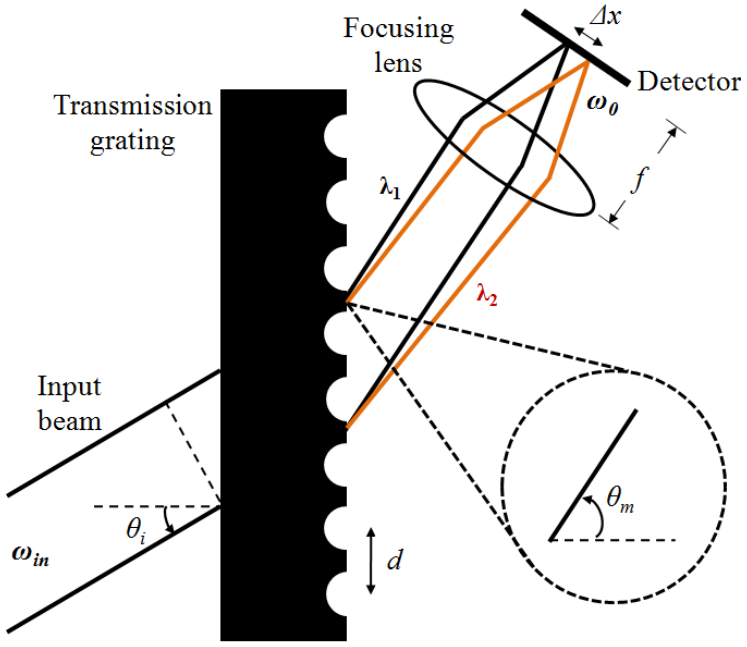

Figure B.1: *A transmission grating spectrometer setup.*

where x is the one dimensional displacement on the detector, $\tilde{\omega} = \omega - \omega_0$ is the offset from the central angular frequency ω_0 of the detector, I_{in} is the input spectrum, and α is the spatial dispersion with units of $cm(rad/s)^{-1}$, also called the grating parameter. Assuming diffraction order m=1,

$$\alpha = \frac{dx}{d\omega} = \frac{\lambda^2 f}{2\pi c d \cos\theta_d}, \tag{B.4}$$

where w_0 is the $1/e^2$ beam waist at the detector, expressed as

$$w_0 = \frac{\cos\theta_i}{\cos\theta_d}\frac{f\lambda}{\pi w_{\text{in}}}. \tag{B.5}$$

where w_{in} is the input beam radius before the grating. Based on the intensity distribution (Eqn B.3), if we choose the resolution condition to occur when the two spots are separated by a $1/e^2$ beam diameter, the spatial separation on the detector between two resolved comb teeth is:

$$\Delta x = 2 \times \omega_0 \tag{B.6}$$

Using the grating parameter derived in B.4, the corresponding frequency separation between these two resolved teeth is:

$$\Delta\omega = \frac{\Delta x}{\alpha} \tag{B.7}$$

Plug B.4, B.5 and B.6 into B.7. We can have the maximum spectral resolution for first-order diffraction as

$$\Delta\nu_{\text{res}} = \Delta\omega = \frac{2cd\cos\theta_i}{\pi w_{\text{in}}\lambda} \tag{B.8}$$

B.2 Spectral Resolution

To choose an appropriate grating for high spectral resolution, I will show a few calculation results, which help illustrate the guidelines. In the end of this section, I will show the experimental result of 22 GHz resolution we have achieved using a transmission grating.

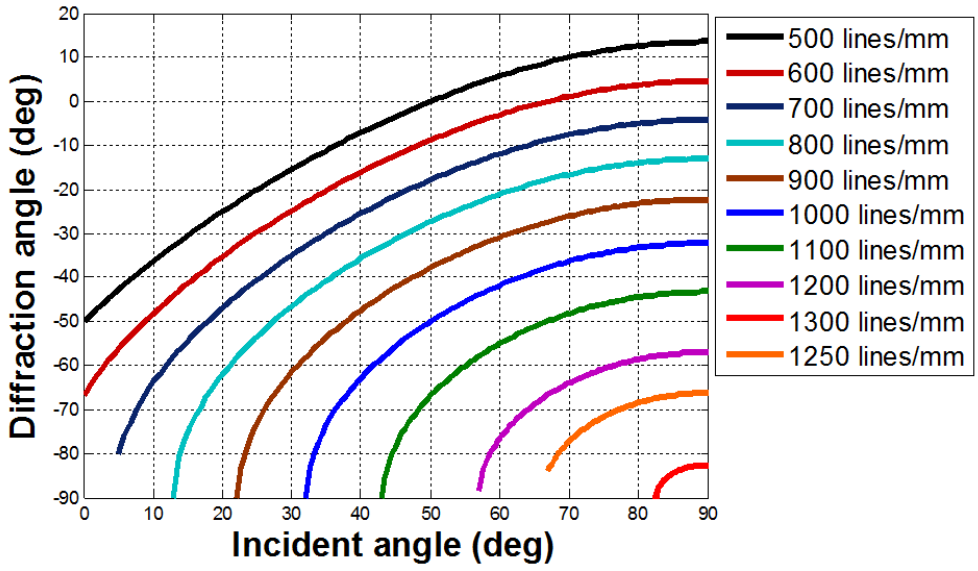

Figure B.2: *The diffraction angle for a reflection grating as a function of incident angle for different groove densities. Diffraction order m = -1. θ_i means normal incidence.*

The spectral resolution of a diffraction grating depends on a number of factors: (1) the incident angle, (2) the diffraction order number m, (3) the groove density, and mostly im-

portantly (4) the beam size. For grating efficiency considerations, the first order diffraction $m = \pm 1$ is preferred in most cases, but it does not necessarily give the best resolution. A low groove density grating could have a better spectral resolution than a high groove density grating, if proper incident angle and beam size are used. But in general, a large beam size would result in a better resolution. It is noteworthy that the spectral resolution is not affected by the focusing lens after the grating, which only determines the spatial resolution, as well as the focused beam size on the detector.

The first step of selecting a grating is to calculate usable incident angles at the wavelength of interest for all possible groove densities, based on the grating equation. Figure B.2 shows all possible incident angles for the first-order diffraction for different groove density at wavelength 1532 nm.

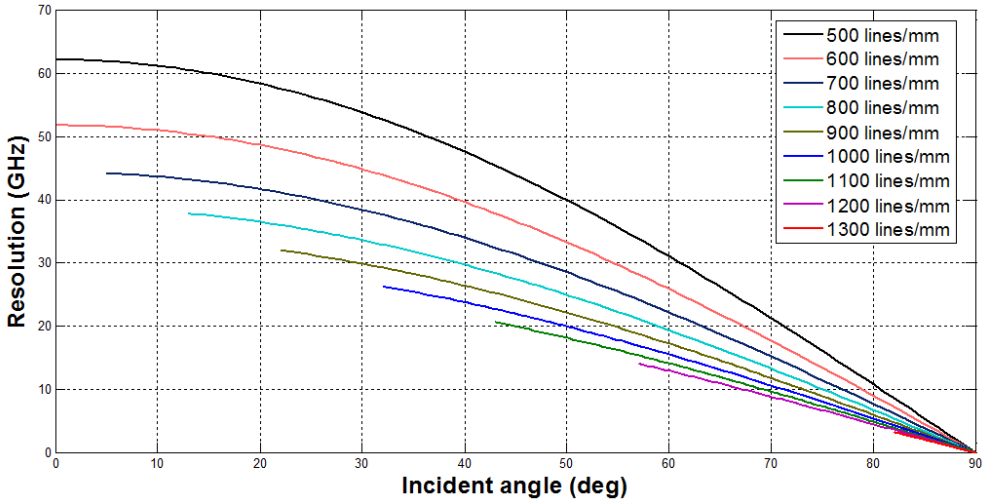

Figure B.3: *The calculated spectral resolution for a reflection grating as a function of incident angle for different groove densities. Diffraction order m = -1, $1/e^2$ (13%) input beam diameter is 4 mm, focal length 150 mm.*

With a constant $1/e^2$ beam diameter of 8 mm, the spectral resolution of gratings for different groove densities is calculated in Figure B.3. The calculation shows a limited range of useful incident angles for each curve. This is because for high groove density, low incident angles give un-defined diffraction angles based on the grating equation B.2, as shown in

Figure B.2. Keep in mind that the $1/e^2$ criteria is 13% of the maximum intensity. To achieve 1% of max beam intensity, the actual beam size will be much larger than the beam size calculated based on the $1/e^2$ critiria. In this case, the actual beam size is about 12 mm.

Angular dispersion is an important parameter that most grating companies will provide on the grating spec sheet. It is determined by : m $\times$ N/cos(diffraction angle), where m is the order number, N is the groove density. Angular dispersion has different units of rad/nm, nm/mrad, deg/nm, nm/deg. Figure B.4 gives the angular dispersion calculation for different groove densities.

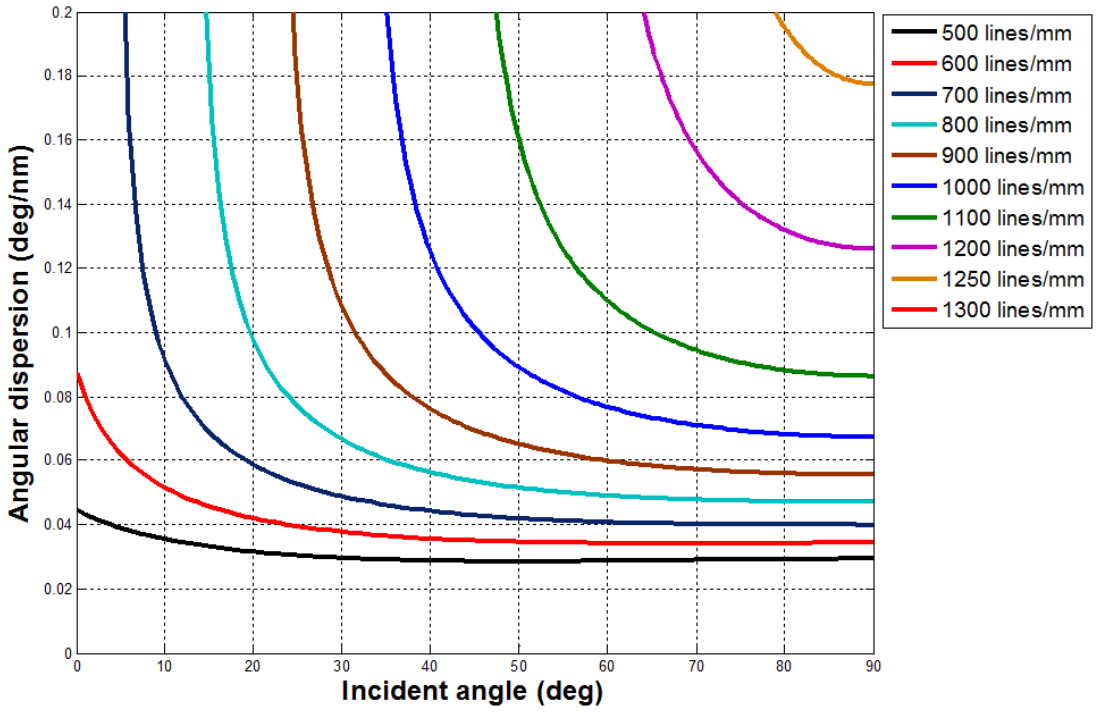

Figure B.4: *[The calculated angular dispersion for a transmission grating as a function of incident angle for different groove densities. Diffraction order m = -1.*

The transmission grating we bought is from Kaiser Optics Systems Inc. with 940 lines/mm, coating size 12.5 mm $\times$ 20 mm. Figure B.5 shows the experimental setup for spectral filtering using this grating. The output beam from the Fabry-Perot cavity containing a 2 GHz comb is collimated and directed into free space, followed by a beam expander

to enlarge the beam size to about 4 mm in waist, before it incidents on the transmission grating at a 45° angle. The diffracted beam is then focused into a line of dots on a focal plane by a 40 mm focusing lens. Implementing a movable slit at the focal plane allows the selection of only a limited number of dots to be coupled back into the output fiber.

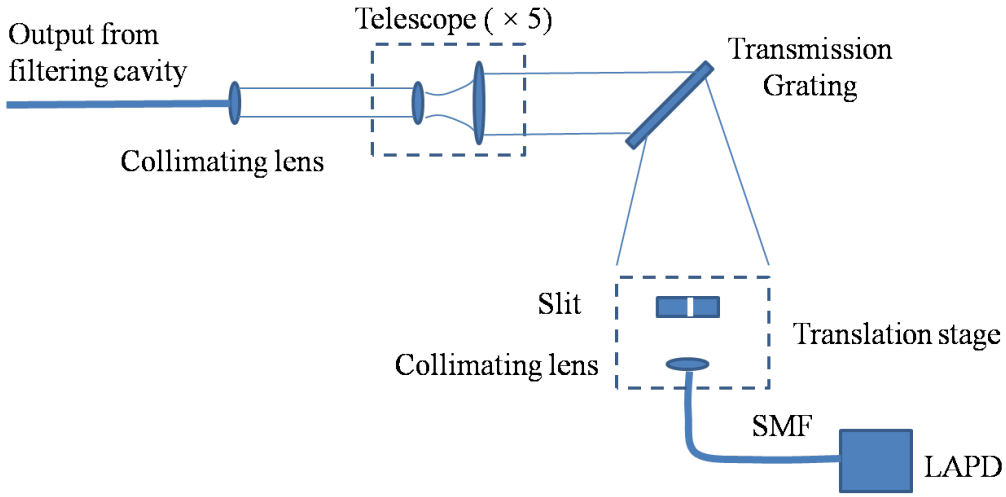

Figure B.5: *Schematic setup for transmission grating. LAPD: large-area photodetector.*

Figure B.6 shows the optical spectrum obtained at the output. It shows a minimum spectral bandwidth of 22 GHz, measured based on the resolution of the spectrum analyzer, which is 6 GHz shown in the grey dashed curve in Figure B.6. This result matches well with the calculated resolution of 23.3 GHz from B.5 using the following parameters: 4 mm input beam waist, 45° incident angle, groove density of 940 lines/mm and wavelength of 1532.8 nm.

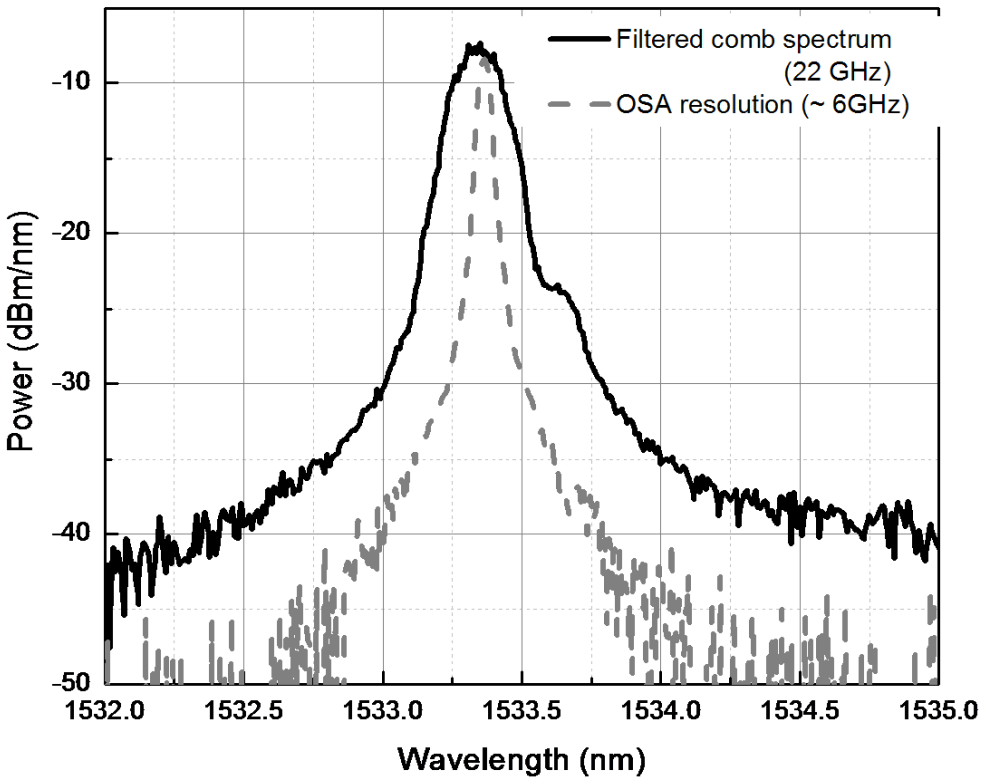

Figure B.6: *Measured optical spectrum of a 2 GHz frequency comb spectrally filtered by the "transmission grating + slit" spectrometer, representing the spectral resolution of the transmission grating. The dashed grey curve is the optical spectrum from a kHz linewidth fiber laser, which represents the OSA resolution.*

Appendix C

Permission for Cited Figures

C.1 Permission for Figure 2.6 and Figure 2.7

From: Shridhar, Lakshmi Priya (ELS-CHN) [l.shridhar@elsevier.com]

Sent: Friday, September 26, 2014 12:47 AM

To: Wu, Shun

Subject: RE: Request permission for using figures in my PhD dissertation

Dear Shun Wu

We hereby grant you permission to reprint 2 figures at no charge in your thesis subject to the following conditions:

1. If any part of the material to be used (for example, figures) has appeared in our publication with credit or acknowledgement to another source, permission must also be sought from that source. If such permission is not obtained then that material may not be included in your publication/copies.

2. Suitable acknowledgment to the source must be made, either as a footnote or in a reference list at the end of your publication, as follows:

This article was published in Publication title, Vol number, Author(s), Title of article, Page Nos, Copyright Elsevier (or appropriate Society name) (Year).

3. Your thesis may be submitted to your institution in either print or electronic form.

4. Reproduction of this material is confined to the purpose for which permission is hereby given.

5. This permission is granted for non-exclusive world English rights only. For other languages please reapply separately for each one required. Permission excludes use in an electronic form other than submission. Should you have a specific electronic project in mind please reapply for permission.

6. This includes permission for UMI to supply single copies, on demand, of the complete thesis. Should your thesis be published commercially, please reapply for permission.

Regards

Lakshmi Priya
Global Rights Department

Elsevier
(A division of Reed Elsevier India Pvt. Ltd.)

International Tech Park — Crest 12th Floor — Taramani Road — Taramani — Chennai 600 113 — India
Tel: +91 44 42994660 — Fax: +91 44 42994701
E-mail: l.shridhar@elsevier.com — url: www.elsevier.com

——Original Message——

From: Wu, Shun [mailto:wshun@phys.ksu.edu]

Sent: Thursday, September 25, 2014 8:38 PM

To: Rights and Permissions (ELS)

Subject: Request permission for using figures in my PhD dissertation

To whom it may concern:

I am completing a doctoral dissertation at Kansas State University entitled "Direct fiber laser frequency comb stabilization via single tooth saturated absorption spectroscopy in hollow-core fiber." I would like your permission to reprint in my dissertation excerpts from the following paper, along with a complete citation of the original material in my dissertation:

T. Hansch and B. Couillaud, "Laser frequency stabilization by polarization spectroscopy of a reflecting reference cavity," Optics Communications, vol. 35, pp. 441-444, Dec 1980.

The excerpts to be reproduced are: Figure 2, and truncated figure 3 from this paper.

The requested permission extends to any future revisions and editions of my dissertation, including the prospective publication of my dissertation by a future publisher. The publisher may produce small quantities of my dissertation on demand and may make my dissertation available for free internet download. These rights will in no way restrict republication of the material in any other form by you or by others authorized by you.

Please let me know if this arrangement meets your approval by replying to this email. Thank you very much.

Sincerely,

Shun Wu

****

Shun Wu

PhD candidate

Physics Department, Cardwell Hall

Kansas State University, Manhattan KS 66502

****

C.2 Permission for Figure 2.20

From: Jeffrey.Coyne@newport.com [Jeffrey.Coyne@newport.com]

Sent: Thursday, September 25, 2014 11:09 AM

To: Wu, Shun

Subject: Newport Corporation - Copyright Request and Authorization Form

Hi Shun,

I received your voice mail attached is the form. Please complete and sign it and send it back to me (PDF is fine) I will sign it and return it to you. If you have any questions, please feel free to call me.

Best regards,

Jeff

Jeffrey B. Coyne

Senior Vice President & General Counsel

Newport Corporation

Experience — Solutions

1791 Deere Avenue

Irvine, California 92606

Direct: 949.437.9885

Fax: 949.253.1221

Email: jeffrey.coyne@newport.com

NEWPORT CORPORATION
REQUEST AND AUTHORIZATION TO USE COPYRIGHTED MATERIAL

Newport

A. REQUEST *(to be completed by Requestor)*

Requester Name:	Shun Wu
Description of requested material (the "Material"): ☐ *(attach additional pages if necessary and check this box if additional pages are attached)*	Operating manual LB1005 High-speed servo controller http://assets.newport.com/webDocuments-EN/images/LB1005OperatingManualP2102297revA.pdf The excerpt to be reproduced is: Figure 8 on Page 14 of the manual
Requested Use (the "Permitted Use"):	I would like to reprint in my doctoral dissertation at Kansas State University entitled "Direct fiber laser frequency comb stabilization via single tooth saturated absorption spectroscopy in hollow-core fiber."
Requested Period of Use (the "Period of Use") *(check appropriate box)*:	☒ Single Use ☐ 6 months ☐ Other: _____ ☐ 90 days ☐ 1 year

B. AUTHORIZATION AND ACKNOWLEDGMENT

1. **Proprietary Rights.** Requester acknowledges that Newport Corporation and/or its subsidiaries (collectively, "Newport") holds certain intellectual property rights in the Material, and that all such rights shall be retained by Newport. Requester shall receive only those rights to use the Material as expressly stated herein.

2. **Grant of Permission.** Newport hereby grants to the Requester a non-exclusive, revocable and non-transferable license to use the Material for the limited purpose of the Permitted Use stated above, specifically subject to the limitations set forth in Section 5 below.

3. **Term.** This Authorization shall be effective on the date signed by Newport and shall expire at the end of the Period of Use stated above (the "Term").

4. **Termination.** This Authorization may be terminated by either party at any time and for any reason upon providing written notice to the non-terminating party. This Authorization shall terminate without notice from Newport if the Requester fails to comply with any provision contained herein. Upon termination of this Authorization, for whatever reason, the Requester agrees to immediately cease any use, including any Permitted Use, of the Material. The Requester agrees to return to Newport all Material upon termination of this Authorization. If this Authorization is terminated for any reason, Newport will not be liable because of such termination for damages relating to the loss of prospective profits, anticipated sales, goodwill, or for expenditures, investments or commitments made in connection with this Authorization.

5. **Limitations on Use.** The Requester may not remove any copyright or other proprietary notices contained on the Material. The Requester further agrees to include the following credit line in a prominent location for each Permitted Use:

"Permission to use granted by Newport Corporation. All rights reserved."

The Requester may not modify or alter the Material in any way, other than by the incorporation of the Material into another original work. The Requester shall not use the Material in any manner that would be unlawful, defamatory, or detrimental to Newport's business or reputation, cause confusion, mistake or deception, or imply affiliation with, or endorsement or sponsorship by, Newport.

6. DISCLAIMERS AND LIMITATION ON LIABILITY.

(a) **DISCLAIMER OF WARRANTIES.** THE MATERIALS ARE PROVIDED "AS IS," AND NEWPORT MAKES NO REPRESENTATIONS OR WARRANTIES, EXPRESS OR IMPLIED, OF ANY KIND WITH RESPECT TO THE MATERIAL. NEWPORT DISCLAIMS ALL REPRESENTATIONS AND WARRANTIES, INCLUDING, WITHOUT LIMITATION, WARRANTIES OF MERCHANTABILITY, FITNESS FOR A PARTICULAR PURPOSE, TITLE AND NON-INFRINGEMENT.

(b) **DISCLAIMER OF ACCURACY.** NEWPORT DOES NOT REPRESENT OR WARRANT THAT THE MATERIAL IS ACCURATE, COMPLETE OR CURRENT. THE MATERIAL COULD CONTAIN TYPOGRAPHICAL ERRORS OR TECHNICAL INACCURACIES. NEWPORT RESERVES THE RIGHT TO MODIFY THE MATERIAL OR ANY PART THEREOF WITHOUT NOTICE.

(c) **LIMITATION ON LIABILITY.** NEITHER NEWPORT NOR ANY OF ITS OFFICERS, DIRECTORS, EMPLOYEES OR OTHER REPRESENTATIVES WILL BE LIABLE FOR DAMAGES ARISING OUT OF OR IN CONNECTION WITH THE USE OF THE MATERIAL EVEN IF ADVISED OF THE POSSIBILITY THEREOF. THIS IS A COMPREHENSIVE LIMITATION OF LIABILITY THAT APPLIES TO ALL DAMAGES OF ANY KIND, INCLUDING, WITHOUT LIMITATION, DIRECT, INDIRECT, SPECIAL AND CONSEQUENTIAL DAMAGES, LOSS OF DATA, INCOME, PROFIT OR GOODWILL, LOSS OF OR DAMAGE TO PROPERTY AND CLAIMS OF THIRD PARTIES.

ACKNOWLEDGED AND AGREED:

REQUESTER:		NEWPORT CORPORATION	
By:	Shun Wu	By:	
Title:	Graduate research assistant	Title:	VP - General Counsel
Date:	9/25/2014	Date:	9/29/2014

C.3 Permission for Figure A.1

From: pubscopyright [copyright@osa.org]

Sent: Monday, September 29, 2014 1:47 PM

To: Wu, Shun

Subject: RE: Request permission for using figures in my PhD dissertation

Dear Shun Wu,

Thank you for contacting The Optical Society.

OSA considers your requested use of its copyrighted material to be Fair Use under United States Copyright Law. It is requested that a complete citation of the original material be included in any publication.

Let me know if you have any questions.

Kind Regards,

Susannah Lehman

Susannah Lehman

September 29, 2014

Authorized Agent, The Optical Society

——Original Message——

From: Wu, Shun [mailto:wshun@phys.ksu.edu]

Sent: Friday, September 26, 2014 11:07 AM

To: pubscopyright

Subject: Request permission for using figures in my PhD dissertation

To whom it may concern:

I am completing a doctoral dissertation at Kansas State University entitled "Direct fiber laser frequency comb stabilization via single tooth saturated absorption spectroscopy in hollow-core fiber." I would like your permission to reprint in my dissertation excerpts from the following paper, along with a complete citation of the original material in my dissertation:

M. Shirasaki, "Large angular dispersion by a virtually imaged phased array and its application to a wavelength demultiplexer" OPTICS LETTERS, Vol 21, NO 5, page 366-368 (1996).

The excerpts to be reproduced are: Figure 1, and figure 2 from this paper.

The requested permission extends to any future revisions and editions of my dissertation, including the prospective publication of my dissertation by a future publisher. The publisher may produce small quantities of my dissertation on demand and may make my dissertation available for free internet download.

Below is my contact info:

My cellphone: 785-236-0743

My mailing address: 1604 Hillcrest Drive Apt U24, Manhattan KS 66502

Please let me know if this arrangement meets your approval by replying to this email. Thank you very much.

Sincerely,

Shun Wu